JOINT TRANSPORTATION
RESEARCH PROGRAM
INDIANA DEPARTMENT OF TRANSPORTATION
AND PURDUE UNIVERSITY

# Repair and Strengthening of Bridges in Indiana Using Fiber Reinforced Polymer Systems:

## Volume 2–FRP Flexural Strengthening and End Region Repair Experimental Programs

William B. Rich, Robert R. Jacobs,
Christopher S. Williams, Robert J. Frosch

SPR-4122 • Report Number: FHWA/IN/JTRP-2021/10 • DOI: 10.5703/1288284317310

## RECOMMENDED CITATION

Rich, W. B., Jacobs, R. R., Williams, C. S., & Frosch, R. J. (2021). *Repair and strengthening of bridges in Indiana using fiber reinforced polymer systems: Volume 2–FRP flexural strengthening and end region repair experimental programs* (Joint Transportation Research Program Publication No. FHWA/IN/JTRP-2021/10). West Lafayette, IN: Purdue University. https://doi.org/10.5703/1288284317310

## AUTHORS

**William B. Rich**
Graduate Research Assistant
Lyles School of Civil Engineering
Purdue University

**Robert R. Jacobs**
Engineer I
Bridge Department
HNTB Corporation

**Christopher S. Williams, PhD**
Assistant Professor of Civil Engineering
Lyles School of Civil Engineering
Purdue University
csw@purdue.edu
(765) 494-5828
*Corresponding Author*
*Principle Investigator*

**Robert J. Frosch, PhD, PE**
Senior Associate Dean of Engineering for
Facilities & Operations
Professor of Civil Engineering
Lyles School of Civil Engineering
Purdue University
*Principle Investigator*

## ACKNOWLEDGEMENTS

The authors would like to thank the Indiana Department of Transportation (INDOT) and the Joint Transportation Research Program (JTRP) for their support of the research presented in this document. Furthermore, the support provided by the INDOT Project Administrator, Prince Baah, and Business Owner, Jeremy Hunter, is greatly appreciated. The authors are also grateful for the guidance and input offered by the members of the Study Advisory Committee: Jennifer Hart, Greg Klevitsky, Jose Ortiz, Stephanie Wagner, and Pete White, in addition to the assistance of Tim Wells. Special thanks are expressed to Sika Corporation, Pilgrim Permacoat, Dayton Superior, and Owens Corning for their assistance with acquiring materials for the experimental programs.

## JOINT TRANSPORTATION RESEARCH PROGRAM

The Joint Transportation Research Program serves as a vehicle for INDOT collaboration with higher education institutions and industry in Indiana to facilitate innovation that results in continuous improvement in the planning, design, construction, operation, management and economic efficiency of the Indiana transportation infrastructure. https://engineering.purdue.edu/JTRP/index_html

Published reports of the Joint Transportation Research Program are available at http://docs.lib.purdue.edu/jtrp/.

## NOTICE

# TECHNICAL REPORT DOCUMENTATION PAGE

| | | |
|---|---|---|
| **1. Report No.**<br>FHWA/IN/JTRP-2021/10 | **2. Government Accession No.** | **3. Recipient's Catalog No.** |
| **4. Title and Subtitle**<br>Repair and Strengthening of Bridges in Indiana Using Fiber Reinforced Polymer Systems: Volume 2–FRP Flexural Strengthening and End Region Repair Experimental Programs | | **5. Report Date**<br>February 2021<br>**6. Performing Organization Code** |
| **7. Author(s)**<br>William B. Rich, Robert R. Jacobs, Christopher S. Williams, and Robert J. Frosch | | **8. Performing Organization Report No.**<br>FHWA/IN/JTRP-2021/10 |
| **9. Performing Organization Name and Address**<br>Joint Transportation Research Program<br>Hall for Discovery and Learning Research (DLR), Suite 204<br>207 S. Martin Jischke Drive<br>West Lafayette, IN 47907 | | **10. Work Unit No.**<br>**11. Contract or Grant No.**<br>SPR-4122 Vol 2 |
| **12. Sponsoring Agency Name and Address**<br>Indiana Department of Transportation (SPR)<br>State Office Building<br>100 North Senate Avenue<br>Indianapolis, IN 46204 | | **13. Type of Report and Period Covered**<br>Final Report<br>**14. Sponsoring Agency Code** |
| **15. Supplementary Notes**<br>Conducted in cooperation with the U.S. Department of Transportation, Federal Highway Administration. | | |


**16. Abstract**

For bridges that are experiencing deterioration, action is needed to ensure the structural performance is adequate for the demands imposed. Innovate repair and strengthening techniques can provide a cost-effective means to extend the service lives of bridges efficiently and safely. The use of fiber reinforced polymer (FRP) systems for the repair and strengthening of concrete bridges is increasing in popularity. Recognizing the potential benefits of the widespread use of FRP, a research project was initiated to determine the most appropriate applications of FRP in Indiana and provide recommendations for the use of FRP in the state for the repair and strengthening of bridges. The details of the research are presented in two volumes.

Volume 1 provides the details of a study conducted to (1) summarize the state-of-the-art methods for the application of FRP to concrete bridges, (2) identify successful examples of FRP implementation for concrete bridges in the literature and examine past applications of FRP in Indiana through case studies, and (3) better understand FRP usage and installation procedures in the Midwest and Indiana through industry surveys.

Volume 2 presents two experimental programs that were conducted to develop and evaluate various repair and strengthening methodologies used to restore the performance of deteriorated concrete bridge beams. The first program investigated FRP flexural strengthening methods, with a focus on adjacent box beam bridges. The second experimental program examined potential techniques for repairing deteriorated end regions of prestressed concrete bridge girders. Externally bonded FRP and near-surface-mounted (NSM) FRP were considered in both programs.


| | | | |
|---|---|---|---|
| **17. Key Words**<br>fiber reinforced polymer, FRP, bridge repair, flexural strengthening, shear strengthening, case studies, industry survey, end region repair, box beams, externally bonded, near-surface-mounted | **18. Distribution Statement**<br>No restrictions. This document is available through the National Technical Information Service, Springfield, VA 22161. | | |
| **19. Security Classif. (of this report)**<br>Unclassified | **20. Security Classif. (of this page)**<br>Unclassified | **21. No. of Pages**<br>141 including appendices | **22. Price** |

Form DOT F 1700.7 (8-72) Reproduction of completed page authorized

# EXECUTIVE SUMMARY

## Introduction

Concrete bridge components experience damage and deterioration due to a variety of sources that range from environmental conditions to vehicle impacts. Such damage and deterioration can lead to reduced structural capacities, necessitating that action be taken to either repair or replace concrete bridge components. Innovative repair and strengthening techniques can provide a cost-effective means to lengthen the service life of bridges, providing cost savings compared to more traditional methods of repair or replacement. Fiber reinforced polymer (FRP) systems are a rapidly emerging solution for such applications. The need to investigate the use of FRP for the repair and strengthening of bridges in Indiana was identified, including the need to study specific applications to structural components that often experience deterioration in the field.

A research project was conducted to develop guidance for the application of FRP systems for the repair and strengthening of bridges in Indiana. To accomplish this objective, a study was first conducted to (1) summarize the current state-of-the-art for the application of FRP to concrete bridge components, (2) identify successful examples of FRP implementation for concrete bridges in the literature and examine past applications of FRP in Indiana through case studies, and (3) better understand FRP usage and installation procedures in the Midwest and Indiana through industry surveys. The details of this study are presented in volume 1. Two experimental programs were then performed to determine the most effective uses of FRP in Indiana for (1) flexural strengthening and (2) girder end region repair. The details of the experimental programs are presented in volume 2.

## Findings

### *Volume 1*

The primary findings of the literature review, case studies, and industry surveys include the following.

- Common FRP strengthening systems include near-surface-mounted (NSM) strips or bars and externally bonded sheets. Prestressed NSM or prestressed externally bonded systems can be implemented to achieve improved serviceability of beams.
- When using externally bonded FRP or near-surface-mounted FRP, proper anchorage or embedment should be provided. A common type of anchorage for externally bonded sheets is the FRP fan anchor, or spike anchor. Its major benefits include compatibility with the FRP strengthening system, ability to anchor flexural or shear strengthening systems, corrosion resistance, and ease of constructability.
- Issues encountered with previously conducted FRP repairs and retrofits in Indiana include inconsistent layering of FRP sheets, premature termination of FRP sheets near support locations or points of intersection of bridge elements, improper epoxy quantities, uneven distribution of epoxy, and inconsistent surface preparation.
- The dominant applications of FRP systems in Midwestern states have included beam shear strengthening and column confinement.

### *Volume 2*

The primary findings of the flexural strengthening and end region repair experimental programs include the following.

#### Flexural Strengthening Experimental Program

- Both externally bonded FRP and NSM FRP are effective techniques for the strengthening of flexural members if properly designed and installed. Appropriate anchorage of the externally bonded FRP must be ensured.
- All FRP-strengthened specimens experienced reduced ductility compared to the specimens without FRP. Furthermore, while the FRP-strengthened specimens achieved post-cracking stiffnesses similar to that of the control specimens without FRP, all FRP-strengthened specimens exhibited significantly higher post-yielding stiffnesses relative to the control specimens.
- Considering the anchorage of externally bonded sheets, specimens with FRP spike anchors only at the ends of the primary FRP sheet consistently gained more capacity than specimens with spike anchors at multiple locations along the length of the primary sheet. The separation and redirection of fibers in the FRP sheet required for the installation of the spike anchors likely contributed to premature rupture at the anchor locations.
- The eccentricity of longitudinal steel reinforcement and the relative placement of NSM strips did not play a significant role in the effectiveness of the strengthening systems or the overall performance of the members.

#### End Region Repair Experimental Program

- The deterioration of the end regions of prestressed concrete girders due to leaking expansion joints can result in significant reductions in strength.
- Restoring the tensile capacity lost due to deteriorated and ineffective prestressing strands in the bottom flange of prestressed concrete girders and ensuring adequate confinement of the repair region are critical factors when designing end region repair systems.
- An externally bonded FRP laminate system proved to be a viable technique for restoring the strength and stiffness of a bridge girder with end region deterioration.
- The use of NSM FRP strips for the repair of the deteriorated end region of a prestressed concrete girder did not provide adequate confinement of the repair region, and therefore, the strength and stiffness of the girder was not restored. If combined with externally bonded FRP laminate, the use of NSM strips may be a viable repair solution.
- Providing a supplemental diaphragm to repair a deteriorated end region of a girder and transfer load to new bearings did not restore the strength of the member. The use of a continuous diaphragm between adjacent girders may provide a more favorable result.

## Implementation

Based on the findings of the research, updates to the *Indiana Design Manual* to allow the use of FRP for strengthening purposes

is recommended. The experimental programs demonstrated that, if properly designed and detailed, FRP systems can be successfully used for flexural strengthening and for the repair and strengthening of deteriorated girder end regions. Past research has demonstrated other successful applications and provide guidance for proper anchorage. Current guidelines available for the design and implementation of FRP systems should be referenced within the *Indiana Design Manual*. Furthermore, special long-term considerations for the inspection of FRP systems are recommended.

Through performing the repairs on the deteriorated end regions during the research program and based on the test results, recommendations for end region repair were developed and delivered to INDOT. Design-related guidance based on the results of both experimental programs is also included in the final report.

To assist with the implementation of the research findings, an FRP guidebook has been developed and provided to INDOT. The document contains general FRP design guidance, key considerations when designing bridge repair systems, suggested language for the *Indiana Design Manual*, and recommendations for FRP installation procedures.

CONTENTS

1. INTRODUCTION . . . 1
1.1 Background . . . 1
1.2 Scope and Objectives . . . 2
2. DETAILS OF FLEXURAL STRENGTHENING EXPERIMENTAL PROGRAM . . . 2
2.1 Introduction . . . 2
2.2 Specimen Design . . . 3
2.3 FRP Strengthening System Details . . . 5
2.4 Material Properties . . . 9
2.5 Summary . . . 11
3. FLEXURAL STRENGTHENING EXPERIMENTAL PROGRAM RESULTS . . . 11
3.1 Introduction . . . 11
3.2 Overview of Experimental Results . . . 11
3.3 Pilot Specimen Test Results . . . 13
3.4 Test Results by Specimen Type . . . 15
3.5 Test Results by Group . . . 28
3.6 Summary . . . 32
4. DETAILS OF END REGION REPAIR EXPERIMENTAL PROGRAM . . . 32
4.1 Introduction . . . 32
4.2 Specimen Background and Details . . . 33
4.3 Repair Details and Rationale . . . 33
4.4 Summary . . . 40
5. END REGION REPAIR EXPERIMENTAL PROGRAM RESULTS . . . 41
5.1 Introduction . . . 41
5.2 Experimental Results . . . 41
5.3 Discussion of Test Results . . . 48
5.4 Summary . . . 51
6. SUMMARY, CONCLUSIONS, RECOMMENDATIONS, IMPLEMENTATION, AND BENEFITS . . . 52
6.1 Summary . . . 52
6.2 Conclusions . . . 52
6.3 Recommendations . . . 53
6.4 Implementation . . . 55
6.5 Benefits . . . 55
REFERENCES . . . 55
APPENDICES
Appendix A. Flexural Strengthening Experimental Program Supplemental Details . . . 57
Appendix B. Flexural Strengthening Experimental Program Supplemental Results . . . 57
Appendix C. INDOT 1961 Standard Drawing—Box Beams . . . 57
Appendix D. Past End Region Repair Research . . . 57
Appendix E. End Region Repair Experimental Program Supplemental Details . . . 57
Appendix F. End Region Repair Experimental Program Externally Bonded FRP Repair System Details . . . 57
Appendix G. Spike Anchor Design Calculations . . . 57

# LIST OF TABLES


| Table | Page |
|---|---|
| **Table 2.1** FRP Strengthening System Components and Design Values | 11 |
| **Table 3.1** Control Specimen Test Results | 15 |
| **Table 3.2** Artificially Deteriorated Specimen Test Results | 17 |
| **Table 4.1** Average Concrete Compressive Strength Obtained from Concrete Cores | 35 |
| **Table 4.2** Text Matrix | 35 |
| **Table 4.3** Externally Bonded FRP Repair System Components and Design Values | 36 |
| **Table 4.4** NSM FRP Repair System Components and Design Values | 39 |
| **Table 4.5** SCC Mixture Design for Supplemental Diaphragm | 41 |
| **Table 5.1** Summary of Load Test Results | 50 |

# LIST OF FIGURES


| Figure | Page |
|---|---|
| **Figure 1.1** Process of deterioration at bottom corners of box beams | 1 |
| **Figure 1.2** Common deterioration patterns (Elkhart, Indiana, Bridge No. 102 CR 35 over Little Elkhart River) | 1 |
| **Figure 1.3** Bridge girders with end region deterioration (INDOT Asset Name I469-01-07020, near Fort Wayne, Indiana) | 2 |
| **Figure 2.1** WS-42 Box beam cross section (INDOT 1961 Standard Set) | 3 |
| **Figure 2.2** General specimen dimensions | 4 |
| **Figure 2.3** Simulated field conditions | 4 |
| **Figure 2.4** Test matrix | 5 |
| **Figure 2.5** Color scheme legend | 5 |
| **Figure 2.6** Specimen identification label | 6 |
| **Figure 2.7** EB.1 strengthening system | 7 |
| **Figure 2.8** EB.2 strengthening system | 8 |
| **Figure 2.9** EB.3 strengthening system | 9 |
| **Figure 2.10** NSM strengthening system | 10 |
| **Figure 3.1** Test results | 12 |
| **Figure 3.2** Applied load, $P$, and midspan deflection, $\Delta$ | 13 |
| **Figure 3.3** Group 0 (pilot) test results | 13 |
| **Figure 3.4** Applied load vs. midspan deflection for Group 0 (pilot) specimens | 14 |
| **Figure 3.5** U-wrap anchor after failure | 14 |
| **Figure 3.6** Partially debonded FRP sheet between anchor points | 15 |
| **Figure 3.7** Applied load vs. midspan deflection for control specimens | 16 |
| **Figure 3.8** Comparison of theoretical and experimental responses for control specimens | 16 |
| **Figure 3.9** Applied load vs. midspan deflection for artificially deteriorated specimens | 17 |
| **Figure 3.10** Artificially damaged specimens after failure | 18 |
| **Figure 3.11** Comparison of theoretical and experimental responses for artificially deteriorated specimens | 19 |
| **Figure 3.12** EB.1 specimen test results | 19 |
| **Figure 3.13** Applied load vs. midspan deflection for EB.1 specimen | 20 |
| **Figure 3.14** EB.1 specimens after failure | 20 |
| **Figure 3.15** Typical FRP sheet rupture at anchor point—EB.1 specimen | 21 |
| **Figure 3.16** EB.2 specimen test results | 21 |
| **Figure 3.17** Applied load vs. midspan deflection for EB.2 specimens | 22 |
| **Figure 3.18** Specimen 0-EB.2 after failure | 23 |
| **Figure 3.19** Specimen 1-EB.2 after failure | 23 |
| **Figure 3.20** Specimen 2-EB.2 after failure | 24 |
| **Figure 3.21** Specimen 3-EB.2 after failure | 24 |
| **Figure 3.22** FRP sheet failure at anchor point (Specimen 1-EB.2) | 25 |
| **Figure 3.23** Test results for all EB specimens | 25 |
| **Figure 3.24** Applied load vs. midspan deflection for EB.1 and EB.2 specimens | 25 |
| **Figure 3.25** Comparison of theoretical and experimental responses for externally bonded specimens | 26 |
| **Figure 3.26** NSM specimen test results | 27 |

**Figure 3.27** Applied load vs. midspan deflection for NSM.1 specimens 27
**Figure 3.28** Applied load vs. midspan deflection for Group 3 NSM specimens 28
**Figure 3.29** FRP strips of specimen 1-NSM.1a 28
**Figure 3.30** Comparison of theoretical and experimental responses for near-surface-mounted specimens 29
**Figure 3.31** Group 1 test results 29
**Figure 3.32** Applied load vs. midspan deflection for Group 1 specimens 30
**Figure 3.33** Group 2 test results 30
**Figure 3.34** Applied load vs. midspan deflection for Group 2 specimens 31
**Figure 3.35** Group 3 test results 31
**Figure 3.36** Applied load vs. midspan deflection for Group 3 specimens 31
**Figure 4.1** Typical in-service condition of girder end regions prior to removal 33
**Figure 4.2** Girders of I-469 bridge selected for experimental program 34
**Figure 4.3** Cross section of test specimens at the original supports 34
**Figure 4.4** Cross section of test specimens 34
**Figure 4.5** Elevation of test specimens 35
**Figure 4.6** Control specimen after failure 35
**Figure 4.7** Damaged specimen after failure 35
**Figure 4.8** Externally bonded FRP details 37
**Figure 4.9** CFRP L-strip plates anchored with CFRP ropes 38
**Figure 4.10** NSM FRP details 39
**Figure 4.11** Supplemental diaphragm details 40
**Figure 5.1** Load configuration 41
**Figure 5.2** Shear vs. deflection at load point for control specimen 42
**Figure 5.3** Control specimen prior to testing 42
**Figure 5.4** Control specimen after failure 42
**Figure 5.5** Shear vs. deflection at load point for damaged specimen 43
**Figure 5.6** Damaged specimen prior to testing 43
**Figure 5.7** Damaged specimen after failure 44
**Figure 5.8** Shear vs. deflection at load point for externally bonded FRP specimen 44
**Figure 5.9** Externally bonded FRP specimen prior to testing 45
**Figure 5.10** Externally bonded FRP specimen after failure 45
**Figure 5.11** Fractured prestressing strands in bottom flange after testing 45
**Figure 5.12** Critical flexural crack of externally bonded FRP specimen after failure 45
**Figure 5.13** Shear vs. deflection at load point for NSM FRP specimen 46
**Figure 5.14** NSM FRP specimen prior to testing 46
**Figure 5.15** NSM FRP specimen after failure 46
**Figure 5.16** Flange separated from NSM FRP specimen 46
**Figure 5.17** Shear vs. deflection at load point for supplemental diaphragm specimen 47
**Figure 5.18** Supplemental diaphragm specimen prior to testing 48
**Figure 5.19** Splitting behavior of supplemental diaphragm 48
**Figure 5.20** Supplemental diaphragm specimen after failure 49

**Figure 5.21** Diagonal cracking of supplemental diaphragm specimen at shear force of 80 kips 49

**Figure 5.22** Shear vs. deflection at load point for all girder specimens 50

**Figure 6.1** Continuous diaphragm details 54

# 1. INTRODUCTION

## 1.1 Background

There are over 600,000 bridges in the United States, and a large percentage of these bridges are nearing the end of their 50-year design life according to the American Road and Transportation Builders Association (ARTBA, 2020). The average age of a non-deficient bridge is 44 years old while the average age of structurally deficient bridges is 69 years old (ARTBA, 2020). As a result, many of these bridges are currently, or soon will be, in need of structural repair or replacement. ARTBA (2020) estimates that 37% of all bridges are currently in need of some type of repair work. While replacing some of these bridges will be necessary, structural repairs are often preferred due to the high economic costs associated with total bridge replacement. The development of efficient and cost-effective repair techniques capable of counteracting a wide variety of structural damage is critically important to the short- and long-term health of America's infrastructure.

A major area of concern for bridges in Indiana and the Midwest is the deterioration of prestressed concrete bridge girders. Due to harsh environmental conditions in the region, the use of deicing salt is required during the winter months. This produces an environment in which chloride-laden water is present, greatly increasing the possibility of corrosion. Two widely observed damaged scenarios caused by this phenomenon are (1) the deterioration of the bottom flanges of adjacent box beams and (2) the deterioration of girder end regions.

When shear keys fail between adjacent box beam girders, chloride-laden water is able to penetrate between the members. When the water reaches the bottom flange, it curls along the bottom surface of the member, initiating corrosion. This process is illustrated in Figure 1.1. Common types of damage resulting from this mechanism include spalling at the bottom corners of the beams and exposed, deteriorated prestressing strands (Frosch et al., 2020a, 2020b). Additionally, water is often found collecting in the voids of the beams, eventually leading to corrosion of the prestressing strands in the bottom flange (Frosch et al., 2020a, 2020b). Examples of common deterioration patterns are shown in Figure 1.2. This type of deterioration is leading to flexural deficiencies and the possibility of structural collapse (Frosch et al., 2020a, 2020b).

Deterioration to the end regions of prestressed concrete bridges is also commonly observed in Indiana. The Indiana Bridge Inspection Application System (BIAS) currently lists 172 prestressed concrete stringer/multi-beam/girder bridges in the state system with a superstructure condition rating of six or less (condition ratings range from zero to nine, with a rating of nine indicating the element is in excellent condition). A condition rating of six indicates that the structural element is in satisfactory condition, but minor deterioration is present (FHWA, 1995). Of these 172 bridges, approximately 55% (96 bridges) either have or show signs of end region deterioration. Failed, leaking expansion joints in the deck or between the deck and approach slab expose girder end regions to the chloride-laden

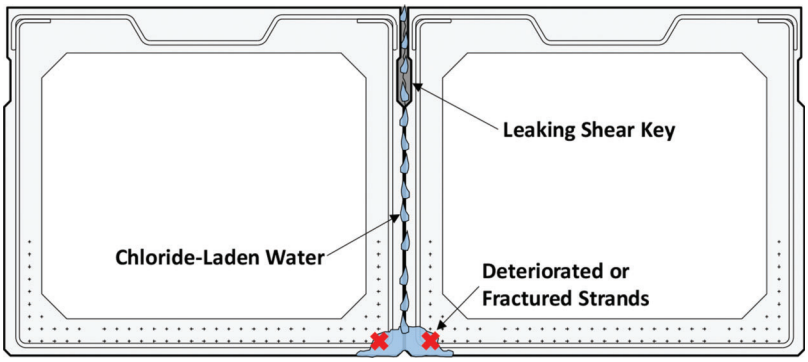


**Figure 1.1** Process of deterioration at bottom corners of box beams.

**Figure 1.2** Common deterioration patterns (Elkhart, Indiana, Bridge No. 102 CR 35 over Little Elkhart River).

(a) Bottom Flange Deterioration (b) Web Deterioration

**Figure 1.3** Bridge girders with end region deterioration (INDOT Asset Name I469-01-07020, near Fort Wayne, Indiana).

water, leading to a corrosive environment in which reinforcement section loss and concrete spalling can occur. An example of a bridge girder with end region deterioration caused by this mechanism is shown in Figure 1.3.

With the high volume of bridges requiring repair, it is necessary to develop techniques that can extend the service life of bridges. One repair technique which could contribute to this effort is fiber reinforced polymer (FRP) systems. FRP systems are rapidly gaining popularity in the concrete infrastructure repair industry due to the many advantages they offer. FRP systems have a high strength-to-weight ratio, are naturally corrosion resistant, come in a variety of materials, have installation flexibility, and can be used for different types of strengthening and repair applications, including shear strengthening, flexural strengthening, and column confinement (ACI Committee 440, 2007). Furthermore, FRP systems can typically be installed relatively quickly, minimizing or eliminating bridge closures (Frankhauser et al., 2015). These characteristics make FRP an appealing material for concrete bridge girder repair.

### 1.2 Scope and Objectives

This report presents details from two experimental programs conducted to better understand the effectiveness and practicality of using FRP systems, and specifically carbon FRP (CFRP) systems, to repair and strengthen prestressed concrete bridge girders. While glass FRP (GFRP) systems have historically been used in Indiana to provided confinement for patched concrete members and environmental protection, CFRP systems are often considered more suitable for structural applications due to their ultimate strengths, stiffnesses, and durability (Kim et al., 2012). One experimental program described in this report examines the use of externally bonded CFRP and near-surface-mounted (NSM) CFRP systems for the flexural strengthening of damaged box beams. The second experimental program focuses on the development of three repair techniques for bridge girders with damaged end regions. These techniques are (1) an externally bonded CFRP system, (2) a near-surface-mounted (NSM) CFRP system, and (3) a concrete supplemental diaphragm. The primary objectives of the two experimental programs described in this document include the following:

- Compare the effectiveness of two CFRP flexural strengthening methods: externally bonded CFRP sheets and near-surface-mounted CFRP strips.
- Assess the ability of the externally bonded CFRP sheets and near-surface-mounted CFRP strips to restore the strength and stiffness of artificially weakened laboratory specimens under flexural loading.
- Evaluate the effects of end region deterioration on the behavior of prestressed concrete bridge girders.
- Determine effective repair techniques for restoring the behavior of prestressed concrete bridge girders with end region deterioration.
- Investigate anchorage techniques for externally bonded FRP sheets.
- Develop and verify installation procedures for CFRP flexural strengthening and end region repair techniques.

The experimental programs described in this document are the final portion of a larger research initiative. The information gathered from each component of the research will contribute to the development of an FRP guidebook for application to Indiana bridges. In volume 1 of this report (Pevey et al., 2021), a state-of-the-art review of FRP was provided along with information gathered from case studies and industry surveys. This current document (volume 2) presents the details of laboratory experiments performed to better understand the behavior of FRP flexural strengthening systems and end region repair techniques applied to existing reinforced concrete members.

## 2. DETAILS OF FLEXURAL STRENGTHENING EXPERIMENTAL PROGRAM

### 2.1 Introduction

An experimental program was developed to compare the performance of two FRP flexural strengthening systems in regard to the increase in strength and stiffness provided to reinforced concrete beam members. Effective anchorage techniques for externally bonded FRP were also investigated. Furthermore, the feasibility of using the strengthening systems on box beam

bridges in the field is considered. A total of 22 beam specimens were fabricated in the laboratory and tested in flexure. For the sake of brevity, the primary details of the experimental program are described within this chapter. Further details of the program are included in Appendix A, including concrete and steel material properties, details of the specimen construction, and strengthening system installation procedures. All specimens were tested in four-point bending (loaded at the third-points of the span). Details of the test setup are also provided in Appendix A.

## 2.2 Specimen Design

As described in Section 1.1, adjacent precast concrete box beam bridges are prone to deterioration that may lead to flexural deficiencies (Frosch et al., 2020a, 2020b). To evaluate the effectiveness of potential flexural strengthening methods for box beams, laboratory specimens were designed and fabricated with common box beam characteristics in mind. To specifically create specimens that are representative of common box beams in Indiana, the specimens were designed to mimic characteristics of the 1960s era WS-42 standard box beam (see Figure 2.1). The WS-42 box beam from INDOT's 1961 standard drawings (see Appendix C) was chosen to provide the general details of typical box beams in the field that are now experiencing deterioration. Although prestressed reinforcement was not used in the test program, other significant variables from the WS-42 box beam were incorporated into the research. Variables such as reinforcement spacing and concrete cover were held constant in order to simulate limitations involved with installing and anchoring the FRP strengthening systems.

The 22 reinforced concrete beam specimens were rectangular in cross section with a depth of 12 in. and a width of 14 in., as shown in Figure 2.2. The specimens were designed with one layer of longitudinal tension (i.e., bottom) reinforcement consisting of No. 3 Grade 60 bars spaced at 1.5 in. The number of bars in each specimen was varied, as described later in this section. Two No. 3 Grade 60 longitudinal reinforcing bars were also included in all of the specimens near the compression face of the member and acted as hanger bars for the stirrups. Each specimen was designed with 20 No. 3 Grade 60 stirrups spaced at 6 in. along the member length. The shear reinforcement ensured that a shear failure would be precluded. It should be noted that a bottom cover dimension of 1 in., longitudinal reinforcement with a diameter of 3/8 in., and a reinforcement grid spacing of 1.5 in. were not only standard for the 1960s WS-42 box beam but were typical for all standard adjacent precast concrete box beams used in that era (see Appendix C). A total length of 120 in. was selected for all specimens based on an approximate scaled ratio of the WS-42 cross-sectional dimensions with consideration of the typical span lengths of adjacent box beam bridges in Indiana (Frosch et al., 2020a). General specimen details are provided in Figure 2.2.

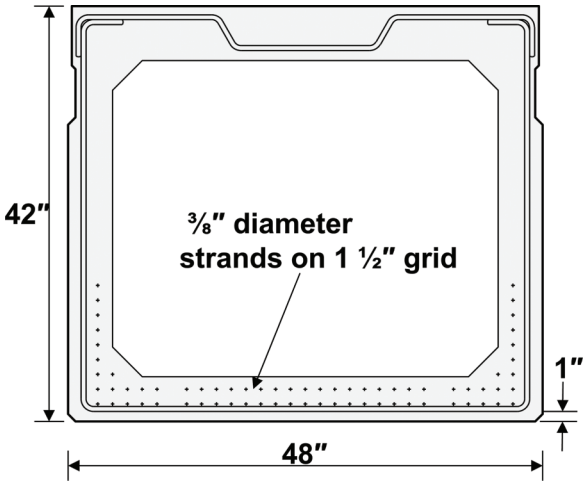


**Figure 2.1** WS-42 Box beam cross section (INDOT 1961 Standard Set).

The experimental program consisted of three primary groups of beams and an additional pilot group of four test beams. For the purposes of this discussion, the state of each specimen at the time of fabrication is referred to as its "simulated field condition" (Figure 2.3). The details of each specimen are summarized in Figure 2.4.

The color scheme used in Figure 2.4 is intended to help highlight similarities between specimen types as well as distinguish variations of each strengthening system. Within the specimen ID column and along the top rows of the table, the colors indicate the specimen simulated field conditions and the strengthening systems used on the specimens. A legend for the established color scheme is shown in Figure 2.5. The specimen details and the color scheme are described in detail next. The color scheme will be used in upcoming figures, tabulated results, and plots for clarity.

As indicated in Figure 2.4, each specimen group contained one full-strength control specimen with seven longitudinal tension reinforcing bars in addition to a number of specimens that were intentionally weakened in a manner that was specific to the group in which they belonged. This intentional weakening of select specimens was designed to simulate the conditions caused by common deterioration patterns experienced by box beams in the field. Therefore, the weakened specimens are referred to as "artificially deteriorated." Artificial deterioration was accomplished by either excluding or cutting longitudinal tension reinforcing bars at the time of fabrication. Excluded reinforcing bars (Types I and III, refer to Figure 2.4 and Figure 2.3) simulated extensively deteriorated reinforcement that is no longer effective in flexure. Cut reinforcing bars (Type II) simulated locally fractured reinforcement. For each cut bar, the location of the cut was at midspan to simulate a worst-case scenario of fractured longitudinal reinforcement due to deterioration. Of the artificially deteriorated specimens in each group, one was tested in its simulated field condition while all others were strengthened prior to testing with either an externally bonded FRP sheet

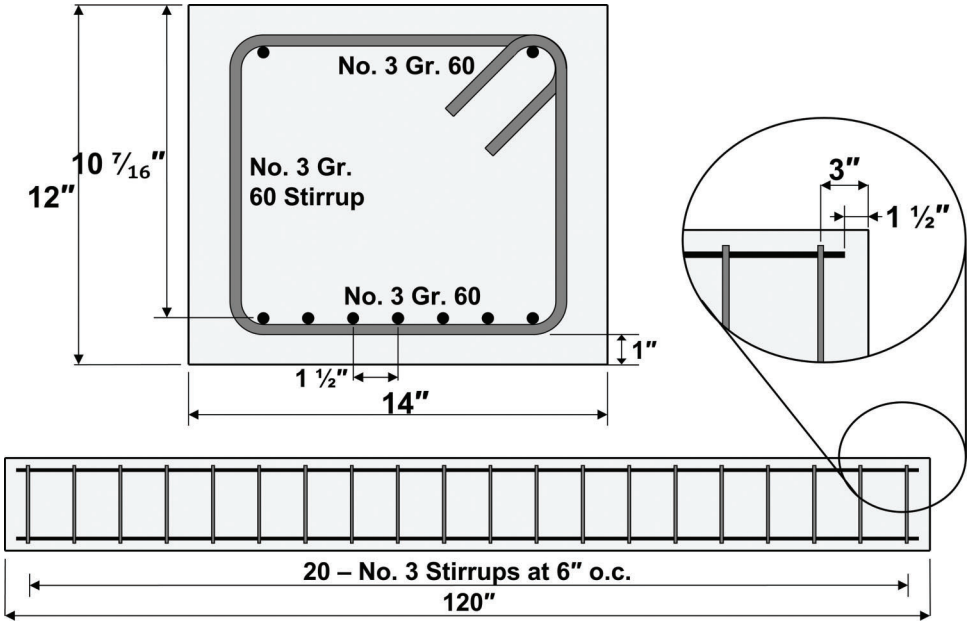


**Figure 2.2** General specimen dimensions.

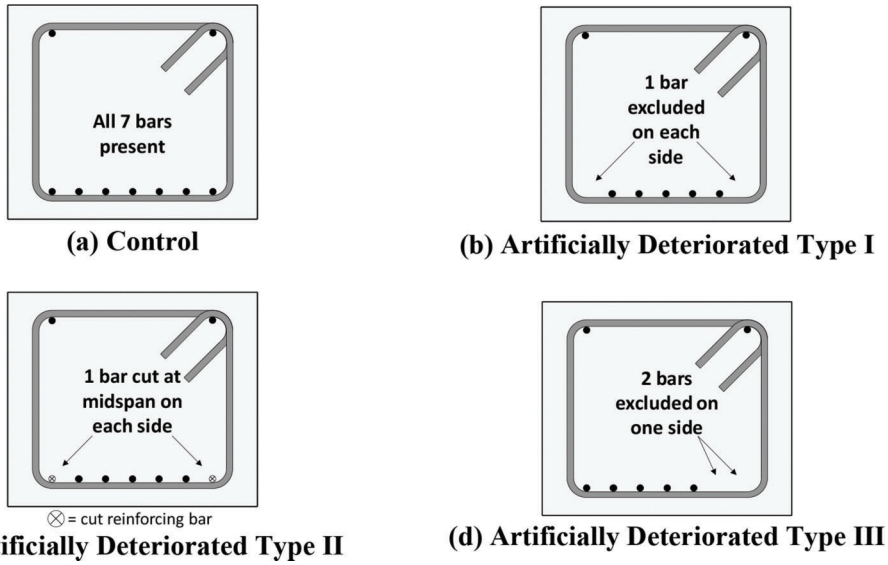


**Figure 2.3** Simulated field conditions.

or near-surface-mounted FRP strips. The strengths provided by the two FRP strengthening systems were determined in accordance with ACI 440.2R-17 with the objective of fully regaining the capacity of the control specimen (ACI Committee 440, 2017). The specimens were designed so that the calculated flexural capacities resulting from each of the two FRP systems are similar, allowing practical comparisons to be made between FRP strengthening systems within each group. ACI 318-19 was used to calculate the capacities of the control specimens and the artificially deteriorated specimens that were left unstrengthened (ACI Committee 318, 2019).

The artificially deteriorated Type I specimens simulated box beams with deterioration near both bottom corners that led to the reinforcement near the corners to be ineffective. For the artificially deteriorated Type III specimens, the objective was to simulate unsymmetrical deterioration of reinforcement with the intention of evaluating how the location of the near-surface-mounted strengthening system, in relation to the excluded reinforcement, affected the overall performance of the specimen. All three types of artificial deterioration were designed to result in the same nominal capacity at midspan in order to facilitate comparisons of similarly strengthened specimens between different groups.

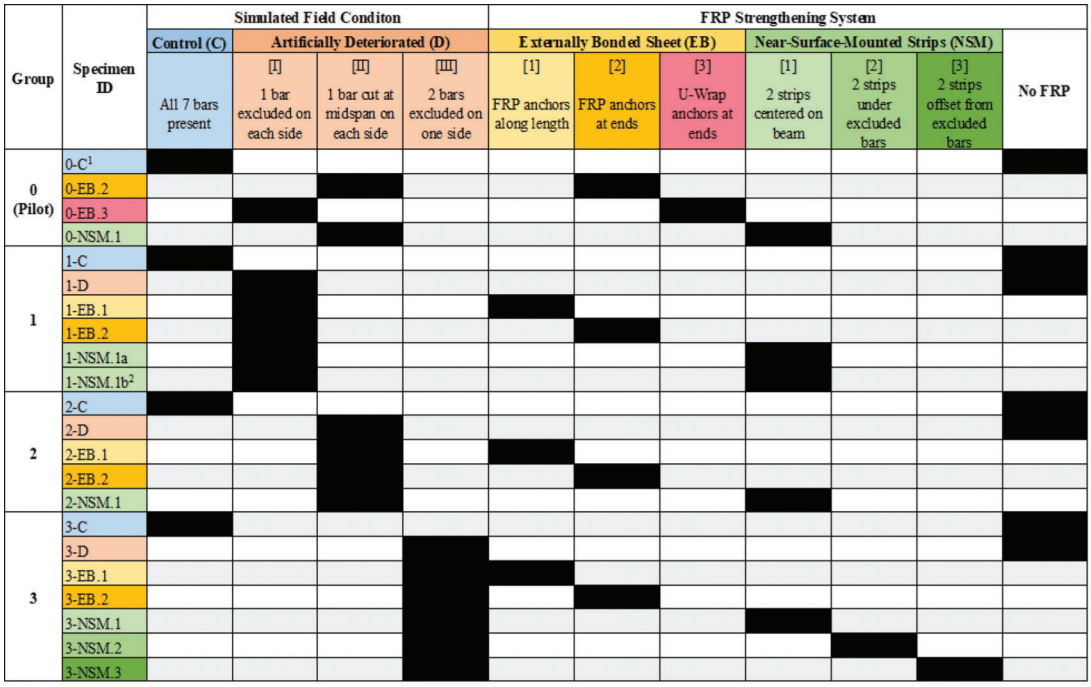


**Figure 2.4** Test matrix.
[1]Pin-roller support condition.
[2]Epoxy grout and NSM strips applied overhead.

| Color | Specimen Details |
|---|---|
| | Control Specimen |
| | Artificially Deteriorated (Unstrengthened) Specimen |
| | Externally Bonded Strengthened Specimen with FRP Spike Anchors Along the Length |
| | Externally Bonded Strengthened Specimen with FRP Spike Anchors at the Ends |
| | Externally Bonded Strengthened Specimen with FRP U-Wrap Anchors at the Ends |
| | NSM Strengthened Specimen with 2 Strips Centered on Beam |
| | NSM Strengthened Specimen with 2 Strips Under Excluded Bars |
| | NSM Strengthened Specimen with 2 Strips Offset from Excluded Bars |

**Figure 2.5** Color scheme legend.

As previously described, a legend for the color scheme used within Figure 2.4 and upcoming tables and figures is provided in Figure 2.5. Within the specimen ID column of Figure 2.4, all control specimens with seven longitudinal tension bars are shown in blue. In the same column, all specimens tested in the weakened, or artificially deteriorated, state are shown in beige. The externally bonded FRP-strengthened specimens are shown in either light yellow or gold, depending on the anchorage configuration. The exception to the color scheme of the externally bonded FRP strengthening system is Specimen 0-EB.3, which is shown in pink and will be discussed further in Section 2.3.1.3. The near-surface-mounted FRP strengthening system is shown in three shades of green, depending on the location of the NSM strips.

Each specimen was given an identification tag that identifies the specimen by group number, specimen type (Control–C, Artificial Deterioration–D, Externally Bonded–EB, Near-Surface-Mounted–NSM), and, if applicable, strengthening system subset number. The strengthening system subset number refers to specific anchorage details for the externally bonded specimens and the location of the strips for the NSM specimens. These details of the strengthening systems are described in Sections 2.3.1 and 2.3.2, respectively. An example of a specimen identification label is provided in Figure 2.6 for Specimen 1-EB.2.

## 2.3 FRP Strengthening System Details

The following subsections present the details of the two FRP strengthening systems included in the experimental program: externally bonded FRP sheets and near-surface-mounted FRP strips. The configuration of each system is described, and the anchorage methodologies evaluated for the externally bonded FRP system are introduced.

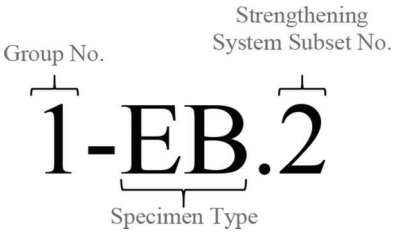


**Figure 2.6** Specimen identification label.

### *2.3.1 Externally Bonded (EB) Sheet Details*

A total of eight specimens received one layer of a unidirectional FRP sheet that was adhered, or externally bonded (EB), to the tension face of the specimen along the longitudinal axis. All sheets were 12 in. wide (2 in. narrower than the beam width) and 96 in. long. As described in volume 1 of this report (Pevey et al., 2021), a variety of anchorage methods can be implemented to anchor the FRP sheet to the concrete substrate and develop the rupture capacity. To further investigate the performance of the EB sheets, three different anchorage methods were evaluated in the experimental program. These anchorage methods are as follows, listed in ascending order of strengthening system subset number:

1. FRP spike anchors along the length of the sheet (EB.1).
2. FRP spike anchors at the ends of the sheet (EB.2).
3. U-wrap anchors at the ends of the sheet (EB.3).

**2.3.1.1 FRP Anchors Along the Length (EB.1)**. Details of the EB.1 strengthening system with FRP spike anchors along the length of the externally bonded sheet are provided in Figure 2.7. Six pairs of anchors were installed at the spacings shown in Figure 2.7(b). The placement of the supports in the test setup, described in Section A.4 of Appendix A, are shown for reference. The support plates were 36-in. by 6-in., which provided a 3-in. gap between the edge of the plate and the termination of the FRP strengthening system. Similar to the experimental tests conducted by Quinn (2009), each of the 12 anchors had a fan length of 6 in. and a fan angle of 60 degrees. The total embedment depth of the anchors measured from the surface of the member was 4 in. Quinn (2009) recommends that the anchor holes extend at least 4 in. into the core of the beam. Furthermore, Kim et al. (2012) and Pudleiner (2016) recommend hole depths of 6 in. However, Pudleiner (2016) suggests that a depth as low as 4 in. may be used if a 6-in. depth is impractical. Achieving a hole depth greater than 4 in. may not be possible within the bottom flanges of adjacent box beams in the field due to the thickness of the flange. Each anchor extended beyond the edge of the sheet by 3/4 in., as indicated in Figure 2.7(b). This dimension also complies with the guidelines from Quinn (2009) that suggest this dimension be at least 0.5 in. Each pair of anchors was covered with two 12-in. by 12-in patches cut from the same FRP sheet as the primary longitudinal sheet. The first patch placed over the anchors had fibers oriented transversely to the longitudinal sheet, and the second patch had fibers oriented parallel to the longitudinal sheet, as recommended by Quinn (2009). The placement of the patches is shown in Figure 2.7(d). It should be noted that choosing a fan length of 6 in. means that adjacent fan anchors did not overlap each other as recommended by Kim (2008). Longer fan lengths would have been required for this detail. The application of the EB.1 strengthening system is discussed further in Sections A.3.1.1 and A.3.1.2 of Appendix A.

**2.3.1.2 FRP Anchors at the Ends (EB.2)**. Details of the EB.2 strengthening system with FRP spike anchors only at the ends of the externally bonded sheet are provided in Figure 2.8. As shown, a pair of anchors was installed 6 in. from each end of the longitudinal sheet. The anchor details were the same as those described for the EB.1 system. Again, two patches with fibers oriented transversely and parallel to the longitudinal sheet were placed over each anchor pair as shown in Figure 2.8(d). The application of the EB.2 strengthening system is discussed further in Sections A.3.1.1 and A.3.1.2 of Appendix A.

**2.3.1.3 U-Wrap Anchors (EB.3)**. Details of the EB.3 strengthening system with U-wrap anchors at the ends of the externally bonded sheet are provided in Figure 2.9. The U-wrap anchor provided at each end of the longitudinal sheet was 12 in. wide, consisted of a single layer of the same FRP fabric used for the longitudinal sheet, and extended over the full depth of the cross section as shown. The fibers of the U-wrap anchors were oriented perpendicular to the fibers of the longitudinal sheet. The application of the EB.3 strengthening system is discussed further in Section A.3.1.3 of Appendix A. It should be noted that the U-wrap anchors were only included for one specimen (0-EB.3) in the pilot group (see Figure 2.4). Due to the relatively inferior performance of the specimen and the fact that U-wraps cannot be installed on adjacent box beams in the field, this anchorage system was not included in the three primary specimen groups of the experimental program. Additional details of the performance of the specimen with U-wrap anchors are presented in Section 3.3.

### *2.3.2 Near-Surface-Mounted (NSM) Strip Details*

A total of seven specimens were strengthened with two near-surface-mounted FRP strips that were inserted into the section along the tension face of the member as shown in Figure 2.10. The cross sections of the rectangular strips had a nominal width of 0.079 in. and a nominal depth of 0.63 in., and each strip was 96 in. long. All strips were inserted to the same depth, centered inside a 0.875-in. deep groove cut into the cross section of the tension face of the specimen (see Figure 2.10(c)). Per ACI 440.2R-17 (ACI Committee 440, 2017), the suggested depth of a groove for a rectangular strip is 1.5 times the largest dimension of

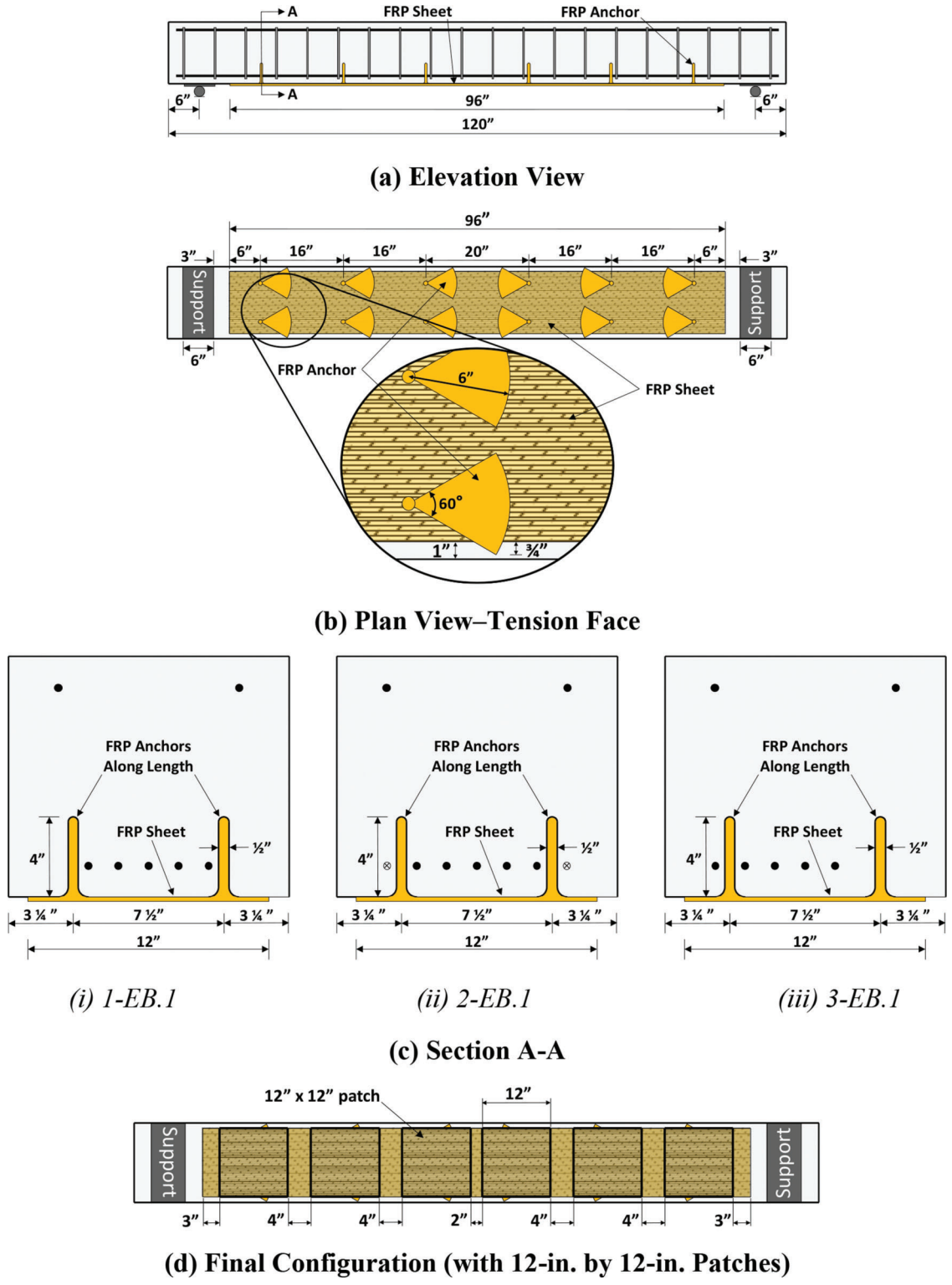


**Figure 2.7** EB.1 strengthening system.

the strip. Therefore, the suggested depth of the grove is 0.945 in. for the NSM strips used in the experimental program. Furthermore, the manufacturer of the epoxy grout used for all NSM specimens except Specimen 1-NSM.1b (see Section 2.4) specifies a minimum grout depth of 1 in. (Pilgrim, n.d.). However, since the specimens had a concrete cover of only 1.0 in., it was decided to test the specimens with strips inserted into a shallower groove with a depth of 0.875 in. to prevent cutting into a stirrup. The clear groove spacing of 1.25 in.

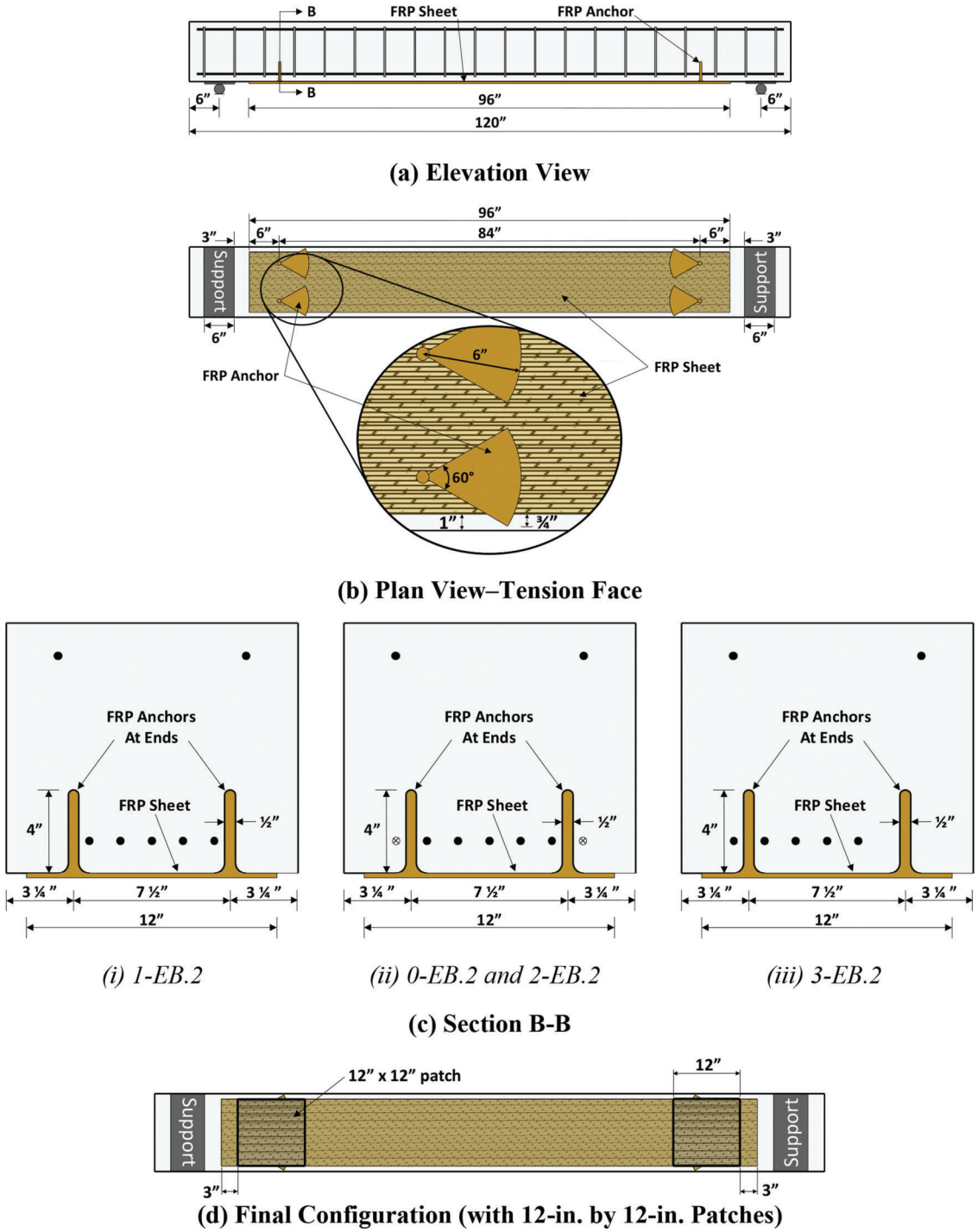


**Figure 2.8** EB.2 strengthening system.

was based on the spacing of the steel reinforcement in the member. It should be noted that this is inconsistent with the suggestions in ACI 440.2R-17 (ACI Committee 440, 2017) that the clear spacing be greater than 2 times the groove depth, or 1.75 in. in this case. All strips were centered on the longitudinal axis of the specimen with the exception of Specimens 3-NSM.2 and 3-NSM.3 (see Figure 2.10(b)). As previously discussed, the artificially deteriorated Type III specimens (see Figure 2.3(d)) were designed to simulate unsymmetrical deterioration of reinforcement to provide the means to evaluate the effects of the placement of NSM strips relative to the missing bars. The variation of the NSM strips relative to the missing bars is intended to simulate a field condition in which it would not be practical to place the NSM strips directly under the deteriorated reinforcement (i.e., insufficient concrete cover or excessive concrete spalling). The

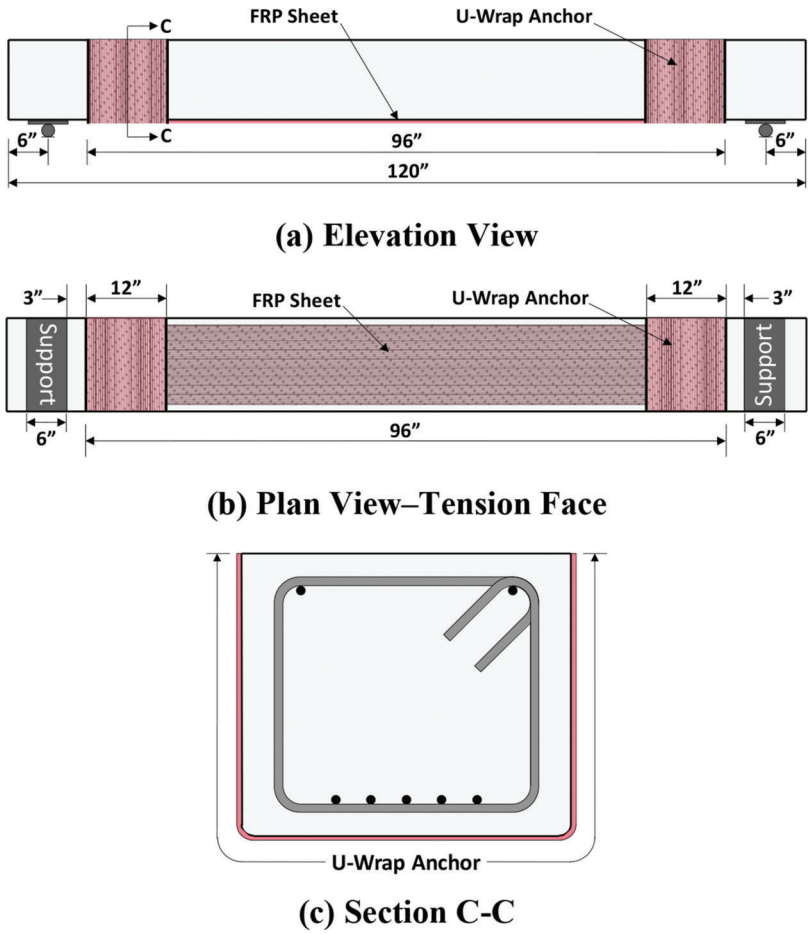


**Figure 2.9** EB.3 strengthening system.

placement of the NSM strips relative to the missing bars of the Type III specimens (3-NSM.1, 3-NSM.2, and 3-NSM.3) is illustrated in Figure 2.10(c). The application of the NSM strengthening system is discussed further in Section A.3.2 of Appendix A.

In Figure 2.4, two specimens with NSM strips are included in Group 1. These specimens (1-NSM.1a and 1-NSM.1b) are essentially identical except for the orientation of the beams when the NSM strips were installed and the type of epoxy used to install the strips. With the exception of Specimen 1-NSM.1b, all strengthened beams in the experimental program were inverted prior to the application of the FRP sheets or strips in order to easily access the tension face. The NSM strips were installed overhead for Specimen 1-NSM.1b. Further details of the epoxy used for the NSM specimens is provided in the next section and in Section A.3.2 of Appendix A.

## 2.4 Material Properties

Each of the two strengthening systems used in the test program consisted of a carbon fiber strengthening component and a constituent material that bonded the component to the concrete substrate. Material properties as reported by the manufacturer of each system are listed in Table 2.1. These values are used for calculating the capacity of the FRP systems. In the table, $A_f$ is the area of the FRP reinforcement, $f_{fu}{}^*$ is the ultimate tensile strength of the FRP reinforcement, $\varepsilon_{fu}{}^*$ is the ultimate rupture strain of the FRP reinforcement, and $E_f$ is the tensile modulus of elasticity of the FRP. This notation and the definitions are consistent with those given in ACI 440.2R-17. The material properties for the externally bonded FRP sheet are given as the properties of the cured laminate consisting of the fabric and epoxy. The design value for the thickness of the cured laminate as reported by the manufacturer is 0.02 in. The FRP rope was used for the FRP spike anchors. The material properties of the FRP rope combined with the cured epoxy are reported with the exception of the ultimate strain, which represents the property for "elongation at break" of the dry fibers as reported by the manufacturer (Sika Corporation, 2015). The material properties listed for the NSM strengthening system consider only the dry carbon fiber strips. The value of $A_f$ given in Table 2.1 for the externally bonded FRP sheet is the total nominal cross-sectional area of the cured laminate installed on the tension face of the EB specimens (EB.1, EB.2, and EB.3). For the FRP rope, the value of $A_f$ is the nominal cross-sectional area of one spike anchor combined with epoxy that is

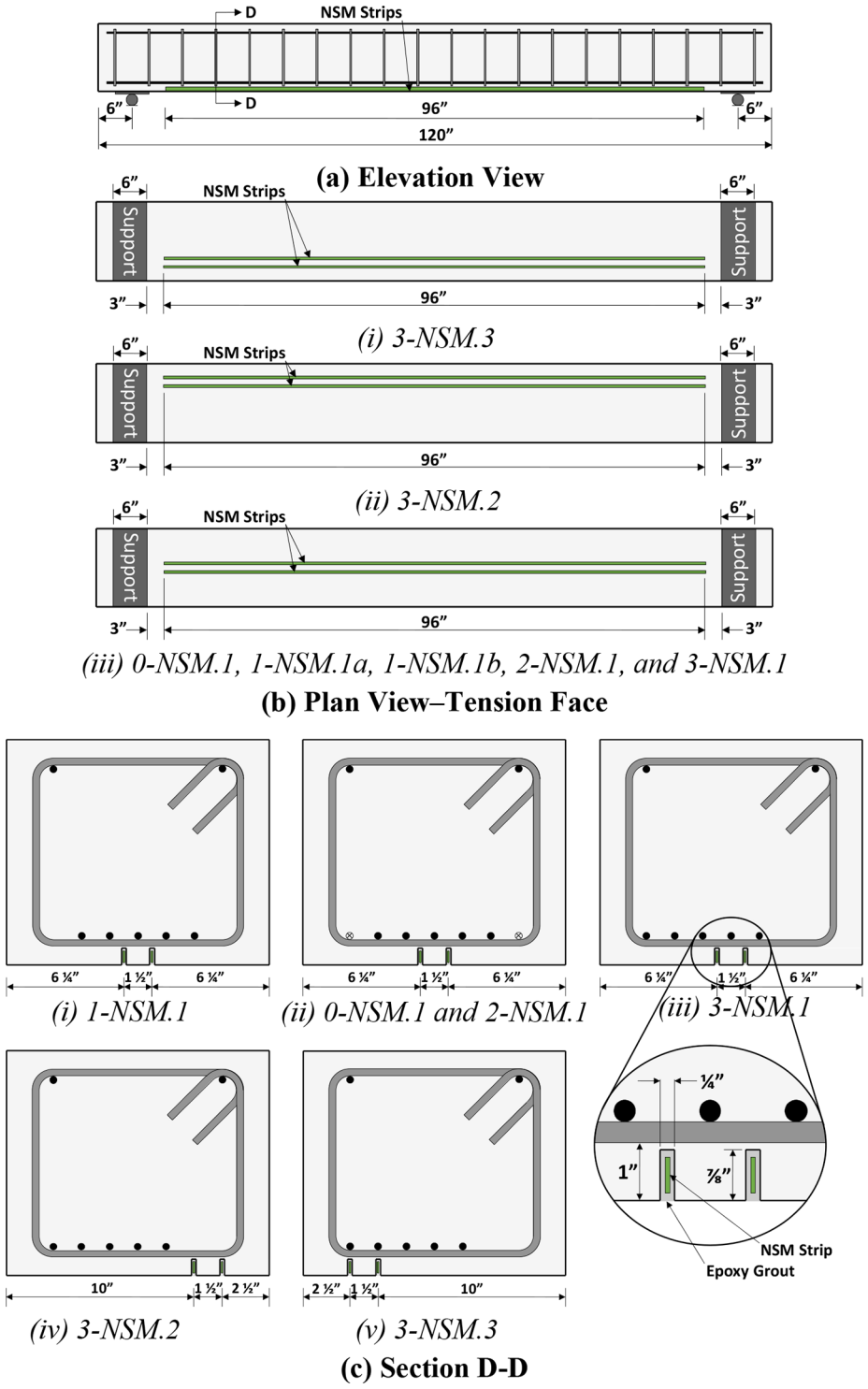


**Figure 2.10** NSM strengthening system.

used in the EB specimens (EB.1 and EB.2). The value of $A_f$ listed for the NSM reinforcement is the nominal cross-sectional area of a single FRP strip.

As indicated in the footnotes to Table 2.1 and previously mentioned, two different epoxies were used in the test program for installing the NSM strips, yet only Specimen 1-NSM.1b received the Unitex Pro-Poxy 400 Anchoring Gel. The relatively high viscosity of the Unitex Pro-Poxy 400 Anchoring Gel allowed for the application process to be performed overhead. Overall, the installation was successful, and once the installation was completed, no sagging of the epoxy from the

TABLE 2.1
**FRP Strengthening System Components and Design Values**

| Strengthening System | Components | Constituent Materials | $A_f$ (in.$^2$) | $f_{fu}^*$ (ksi) | $\varepsilon_{fu}^*$ | $E_f$ (ksi) |
|---|---|---|---|---|---|---|
| Externally Bonded (EB) | FRP Sheet | FRP Fabric[1] + Epoxy[2] | 0.24 | 105 | 0.01 | 8,200 |
| | FRP Anchor | FRP Rope[3] + Epoxy[2] | 0.1 | 304 | 0.016[7] | 33,300 |
| Near-Surface-Mounted (NSM) | NSM Strips | FRP Tape[4] + Epoxy[5,6] | 0.049 | 325 | 0.0181 | 18,000 |

[1]SikaWrap Hex-117C Unidirectional Carbon Fiber Fabric (Sika Corporation, 2018c).
[2]Sikadur Hex-300 Impregnating Resin (Sika Corporation, 2018a).
[3]SikaWrap FX-50 C Unidirectional Carbon Fiber Rope (Sika Corporation, 2015).
[4]Owens Corning Aslan 500 #2 Carbon Fiber Reinforced Polymer Tape (Owens Corning, 2017).
[5]Pilgrim Permocoat Magmaflow Grout-Pak CF Epoxy Grout (Pilgrim, n.d.).
[6]Unitex Pro-Poxy 400 Anchoring Gel (Unitex, 2018).
[7]Based on dry fibers.

grooves was observed. Installation of the NSM strips and use of the two epoxies is described further in Section A.3.2 of Appendix A.

The concrete used for all specimens was a normal weight concrete with a specified 28-day compressive strength of 4,000 psi and target slump of 4 in. All reinforcing steel was Grade 60 (ASTM A615 (ASTM, 2018)). Further details of the concrete mixture and steel reinforcement are provided in Sections A.1.1 and A.1.2 of Appendix A, respectively.

### 2.5 Summary

This chapter outlined the experimental program focused on the flexural strengthening of beam specimens. Details of 22 specimens fabricated in the laboratory were provided. The next chapter discusses the results from the experimental program, and important comparisons between the two FRP strengthening systems are presented to develop conclusions that help fulfill the project objectives.

## 3. FLEXURAL STRENGTHENING EXPERIMENTAL PROGRAM RESULTS

### 3.1 Introduction

Experimental results from the 22 beam tests described in Chapter 2 are presented in this chapter. An overview of the experimental results is first introduced. Details of the behavior of the specimens and the performance of the FRP strengthening systems are then discussed along with comparisons between specimens in terms of strength, stiffness, and ductility. The experimental results are described in the following order:

- Results from pilot tests (Group 0).
- Results by specimen type (Control–C, Artificially Deteriorated–D, Externally Bonded–EB, and Near-Surface-Mounted–NSM).
- Results by group (Groups 1–3).

Lastly, the primary observations from the test program are summarized.

The development of an analysis tool used to create load-deflection plots based on a theoretical model is presented in Section B.1 of Appendix B. The results from the analysis tool are compared to experimental results throughout the chapter.

### 3.2 Overview of Experimental Results

The results from the experimental program are summarized in Figure 3.1. Each specimen is represented in the table by its identification label. The color scheme described in Section 2.2 is used for clarity. The table includes the concrete compressive strength on test day, $f_c$ (reported to the nearest 10 psi per ASTM C39 (ASTM, 2020); maximum load applied during the test, $P_{test}$, and the corresponding moment, $M_{test}$; nominal flexural capacity, $M_n$, and the corresponding applied load, $P_n$; the ratio of the experimental moment capacity to the nominal moment capacity, $M_{test}/M_n$; the ratio of the experimental capacity of a member to the experimental capacity of the corresponding control specimen in the same group, $M_{test}/M_c$; and the midspan deflection at the maximum applied load. The value of $M_n$ was calculated based on nominal flexural strength provisions in ACI 318-19 for the unstrengthened specimens and ACI 440.2R-17 for the specimens strengthened with FRP (ACI Committee 318, 2019; ACI Committee 440, 2017). In both cases, the measured yield stress of the steel reinforcing bars ($f_y$ = 70.2 ksi, refer to Section B.1.1 of Appendix B) was used. It should be noted that the environmental reduction factor, $C_E$, in Section 9.4 of ACI 440.2R-17 is taken as 1.0 throughout this chapter due to the controlled environment in the laboratory. Furthermore, the Whitney stress block was consistently used for all $M_n$ calculations, even for the FRP specimens with capacity governed by rupture or debonding of the FRP. This methodology was determined to provide reasonable strength estimates as noted in ACI 440.2R-17 (ACI Committee 440, 2017). The value of $P_n$ is the magnitude of one of the two point loads that corresponds to $M_n$ at the midspan of the member with consideration of the additional moment imposed at midspan due to both the self-weight of the specimen and the weight of the spreader

| Group | Specimen ID | Concrete Strength, $f_c$ (psi) | $M_{test}$ (kip-ft) | $P_{test}$ (kip) | $M_n$ (kip-ft) | | $P_n$ (kip) | | $M_{test}/M_n$ | | $M_{test}/M_c$ | Midspan Deflection at Max Load, Δ (in.) |
|---|---|---|---|---|---|---|---|---|---|---|---|---|
| | | | | | $\psi_f = 0.85$ | $\psi_f = 1.0$ | $\psi_f = 0.85$ | $\psi_f = 1.0$ | $\psi_f = 0.85$ | $\psi_f = 1.0$ | | |
| 0 (Pilot) | 0-C[1] | 6370 | 59.59 | 19.11 | 45.92[4] | | 14.56 | | 1.30 | | 1.00 | 3.29 |
| | 0-EB.2 | 6110[3] | 79.96 | 25.90 | 47.08[5] | 49.65[5] | 14.94 | 15.80 | 1.70 | 1.61 | 1.34 | 1.76 |
| | 0-EB.3 | 6120[3] | 62.95 | 20.23 | 47.09[5] | 49.65[5] | 14.94 | 15.80 | 1.34 | 1.27 | 1.06 | 1.30 |
| | 0-NSM.1 | 6140[3] | 77.11 | 24.95 | 50.07[5] | 53.17[5] | 15.94 | 16.97 | 1.54 | 1.45 | 1.29 | 1.61 |
| 1 | 1-C | 6820 | 59.80 | 19.18 | 46.11[4] | | 14.62 | | 1.30 | | 1.00 | 3.23 |
| | 1-D | 6560 | 44.68 | 14.14 | 33.88[4] | | 10.54 | | 1.32 | | 0.75 | 3.63 |
| | 1-EB.1 | 6920 | 54.91 | 17.55 | 47.33[5] | 49.91[5] | 15.02 | 15.88 | 1.16 | 1.10 | 0.92 | 0.81 |
| | 1-EB.2 | 6680 | 71.71 | 23.15 | 47.26[5] | 49.84[5] | 15.00 | 15.86 | 1.52 | 1.44 | 1.20 | 1.63 |
| | 1-NSM.1a | 6490 | 70.81 | 22.85 | 50.20[5] | 53.31[5] | 15.98 | 17.02 | 1.41 | 1.33 | 1.18 | 1.72 |
| | 1-NSM.1b[2] | 7030[3] | 58.54 | 18.76 | 50.38[5] | 53.51[5] | 16.04 | 17.08 | 1.16 | 1.09 | 0.98 | 1.10 |
| 2 | 2-C | 6020 | 59.41 | 19.05 | 45.77[4] | | 14.50 | | 1.30 | | 1.00 | 3.45 |
| | 2-D | 6000 | 45.40 | 14.38 | 33.67[4] | | 10.47 | | 1.35 | | 0.76 | 1.63 |
| | 2-EB.1 | 6630 | 60.10 | 19.28 | 47.25[5] | 49.82[5] | 15.00 | 15.86 | 1.27 | 1.21 | 1.01 | 0.68 |
| | 2-EB.2 | 6800 | 72.79 | 23.51 | 47.29[5] | 49.87[5] | 15.01 | 15.87 | 1.54 | 1.46 | 1.23 | 1.25 |
| | 2-NSM.1 | 6390 | 82.87 | 26.87 | 50.16[5] | 53.28[5] | 15.97 | 17.01 | 1.65 | 1.56 | 1.39 | 1.82 |
| 3 | 3-C | 6330 | 56.83 | 18.19 | 45.90[4] | | 14.55 | | 1.24 | | 1.00 | 2.88 |
| | 3-D | 6680 | 44.47 | 14.07 | 33.92[4] | | 10.55 | | 1.31 | | 0.78 | 3.63 |
| | 3-EB.1 | 7270 | 58.36 | 18.70 | 47.42[5] | 50.00[5] | 15.05 | 15.91 | 1.23 | 1.17 | 1.03 | 0.96 |
| | 3-EB.2 | 7210 | 71.62 | 23.12 | 47.40[5] | 49.98[5] | 15.05 | 15.91 | 1.51 | 1.43 | 1.26 | 1.69 |
| | 3-NSM.1 | 6750 | 68.56 | 22.10 | 50.29[5] | 53.41[5] | 16.01 | 17.05 | 1.36 | 1.28 | 1.21 | 1.62 |
| | 3-NSM.2 | 6570 | 69.25 | 22.33 | 50.23[5] | 53.35[5] | 15.99 | 17.03 | 1.38 | 1.30 | 1.22 | 1.56 |
| | 3-NSM.3 | 6620 | 65.50 | 21.08 | 50.25[5] | 53.36[5] | 16.00 | 17.04 | 1.30 | 1.23 | 1.15 | 1.43 |

**Figure 3.1** Test results.
[1]Pin-roller support condition.
[2]Epoxy grout and NSM strip applied overhead.
[3]Estimated concrete strength (see Section A.1.1 of Appendix A).
[4]Calculated in accordance with ACI 318-19 (ACI Committee 318, 2019).
[5]Calculated in accordance with ACI 440.2R-17 (ACI Committee 440, 2017).

beam. In other words, the moment due to $P_n$ plus the moments due to the specimen self-weight and spreader beam weight add together to equal $M_n$. The value of $P_{test}$ is the maximum load applied to the specimen during the test and corresponds to one of the two point loads applied to the member as indicated by the load cell (see Section A.4 of Appendix A. The value of $M_{test}$ is the total moment at midspan when $P_{test}$ is applied. It therefore includes the moment from $P_{test}$ plus the moments due to the specimen self-weight and spreader beam weight.

In Figure 3.1, two values of $M_n$ and $P_n$ are given for all specimens strengthened with FRP. The two strength values correspond to $\psi_f$ values of 0.85 and 1.0. In ACI 440.2R-17, $\psi_f$ is a reduction factor applied to the FRP within the equation for $M_n$. The value recommended for $\psi_f$ within ACI 440.2R-17 is 0.85 (ACI Committee 440, 2017). For a thorough comparison of calculated and experimental strengths, the values of $M_n$ and $P_n$ were calculated with the inclusion of the recommended value and also with the value of $\psi_f$ taken as 1.0.

As explained in Section A.4 of Appendix A, the deflection of the test beams was measured at midspan and at each load point. For the Group 3 specimens, the deflection was measured at each of these three locations using two linear potentiometers at each side of the member. For these specimens, the midspan deflection at the maximum applied load listed in Figure 3.1 and subsequent tables in this chapter is the average reading from the two potentiometers at midspan. The test results presented in Figure 3.1 will be discussed in detail within the following sections.

Throughout this chapter, the behavior of the specimens is presented in load-displacement ($P$-Δ) plots. In the plots, the applied load, $P$, represents one of the point loads applied to the beam (see Figure 3.2) and is shown on the y-axis consistently from 0 to 60 kips. The midspan deflection, Δ, is shown on the x-axis from 0 in. to 2 in., 0 in. to 4 in., or 0 in. to 6 in. depending on the ductility of the specimens. In general, the FRP-strengthened specimens were loaded at least until the FRP ruptured (EB specimens) or slipped (NSM specimens), resulting in a reduction in the load-carrying capacity of the member. The specimens not strengthened with FRP (i.e., C and D specimens) were loaded until extensive concrete crushing was observed along with a reduction in

load-carrying capacity. The specimen response is plotted at least until a reduction in load-carrying capacity was experienced after the peak load was reached. Any residual capacity captured beyond this point is not shown. For the plots showing test results of specimens from multiple test groups, all specimens from Group 0 are plotted in purple. Similarly, all specimens from Group 1 are plotted in red, Group 2 in green, and Group 3 in blue. Furthermore, in plots displaying the response curves for a specific specimen type, a red dotted line is provided to show the load $P_n$ corresponding to the calculated nominal flexural strength for that specimen type, which is calculated using the greatest measured concrete compressive strength of the specimens represented in the plot. For the plots showing test results by group, the color scheme described in Section 2.2 is used in conjunction with illustrative cross sections inset within the plots in order to easily match the specimen to its response curve.

### 3.3 Pilot Specimen Test Results

As explained in Chapter 2, a group of four pilot beam tests were conducted in order to better understand the behavior of the FRP strengthening systems and to use the results to refine the experimental program to best achieve the specified objectives. The intention of the first beam tested, Specimen 0-C, was to verify that the testing configuration and associated instrumentation would perform as predicted. This test was conducted similar to all other tests except the beam supports consisted of a pin and a roller as opposed to two rollers. During the test on Specimen 0-C, it was noted that the tensile face of the beam elongated only in the direction of the roller, causing the hydraulic cylinder to slightly tilt towards the roller support due to the friction between the hydraulic cylinder and the spreader beam. It was then decided to change the support conditions to what is shown in Figure 3.2. The pilot tests for Specimens 0-EB.2, 0-EB.3, and 0-NSM.1 were intended to verify the general behavior of the FRP strengthening systems before continuing with the planned experimental program. The results from the four pilot tests are presented in Figure 3.3 and Figure 3.4. The control specimen (Specimen 0-C) failed due to crushing of the concrete in the compression region after the longitudinal steel yielded and entered the strain-hardening range. Specimens 0-EB.2 and 0-EB.3 failed due to rupture of the FRP sheet. Specimen 0-NSM.1 is believed to have failed due to slip of the FRP within the epoxy (see Section 3.4.5). Specimens 0-NSM.1 and 0-EB.2 experienced some concrete crushing prior to failure of the FRP.

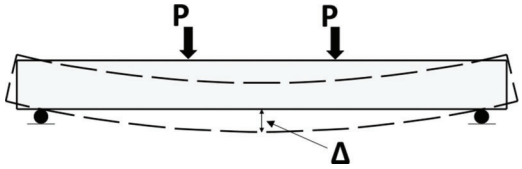


**Figure 3.2** Applied load, $P$, and midspan deflection, Δ.

As explained in Section B.1 of Appendix B, for the strengthened specimens that did not include cut reinforcing bars, the estimated stress in the FRP from the analysis tool that corresponds to the maximum applied load during the experiments, $f_{f\_max}$, is reported in Figure 3.3 and subsequent tables in this chapter. The estimated stress in the steel reinforcement, $f_s$, corresponding to the maximum applied load based on the analysis tool is also provided for all specimens except those with cut bars. The value of $f_{fu}$* in Figure 3.3 is the ultimate tensile strength of the FRP reinforcement as reported by the manufacturer (see Table 2.1), and $f_{fe}$ is the effective stress in the FRP reinforcement at nominal flexural strength calculated in accordance with ACI 440.2R-17 (ACI Committee 440, 2017). Columns for the ratios $f_{f\_max}/f_{fe}$ and $f_{f\_max}/f_{fu}$* are also included in the table. These ratios are convenient values for evaluating the efficiency of the FRP systems. For the FRP-strengthened specimens in Figure 3.3, Specimens 0-EB.2 and 0-NSM.1 contained cut reinforcement bars and, therefore, could not be accurately modeled using the analysis tool.

The longitudinal reinforcing bars in the FRP-strengthened pilot specimens differed among the beams. As indicated in Figure 2.4 and the inset cross sections in Figure 3.4, Specimens 0-EB.2 and 0-NSM.1 included a bar cut at midspan on each side while Specimen 0-EB.3 had one bar excluded on each side. Therefore, direct comparisons between all three of the FRP-strengthened pilot specimens is not possible. Nevertheless, it is observed that the strengthened specimens had similar

| Specimen ID | $M_{test}$ (kip-ft) | $M_n$ (kip-ft) | | $M_{test}/M_n$ | | $M_{test}/M_c$ | Steel Stress, $f_s$ (ksi) | Rupture Stress, $f_{f\_max}$ (ksi) | $f_{fu}$* (ksi) | Effective Stress, $f_{fe}$ (ksi) | $f_{f\_max}/f_{fu}$* | $f_{f\_max}/f_{fe}$ | Midspan Deflection at Max Load, Δ (in.) |
|---|---|---|---|---|---|---|---|---|---|---|---|---|---|
| | | $\psi_f = 0.85$ | $\psi_f = 1.0$ | $\psi_f = 0.85$ | $\psi_f = 1.0$ | | | | | | | | |
| 0-C[1] | 59.59 | 45.92[2] | | 1.30 | | 1.00 | 88.47 | - | - | - | - | - | 3.29 |
| 0-EB.2 | 79.96 | 51.00[3] | 54.28[3] | 1.57 | 1.47 | 1.34 | - | - | 105 | 73.8 | - | - | 1.76 |
| 0-EB.3 | 62.95 | 51.00[3] | 54.28[3] | 1.23 | 1.16 | 1.06 | 73.88 | 117.18 | 105 | 73.8 | 1.12 | 1.59 | 1.30 |
| 0-NSM.1 | 77.11 | 50.36[3] | 53.53[3] | 1.53 | 1.44 | 1.29 | - | - | 325 | 228.1 | - | - | 1.61 |

**Figure 3.3** Group 0 (pilot) test results.
[1]Pin-roller support condition.
[2]Calculated in accordance with ACI 318-19 (ACI Committee 318, 2019).
[3]Calculated in accordance with ACI 440.2R-17 (ACI Committee 440, 2017).

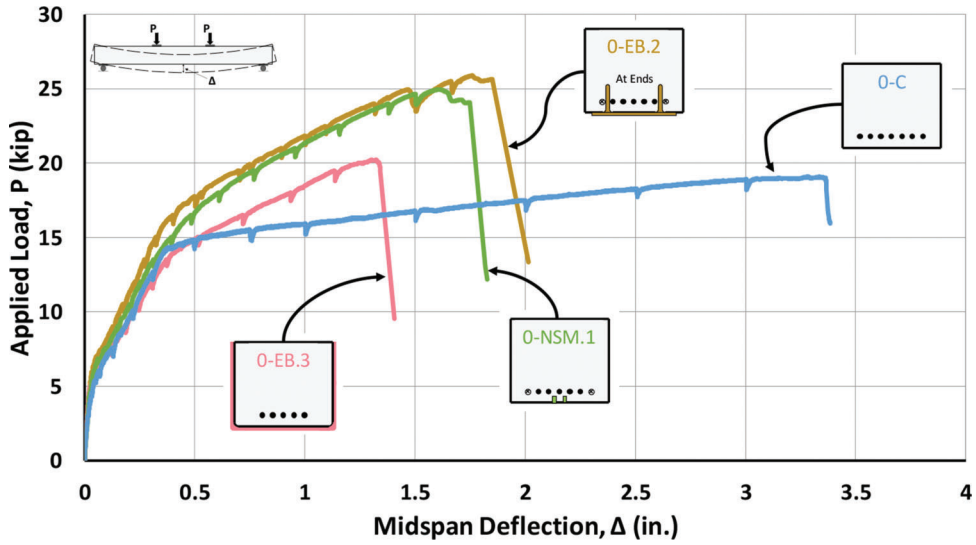


**Figure 3.4** Applied load vs. midspan deflection for Group 0 (pilot) specimens.

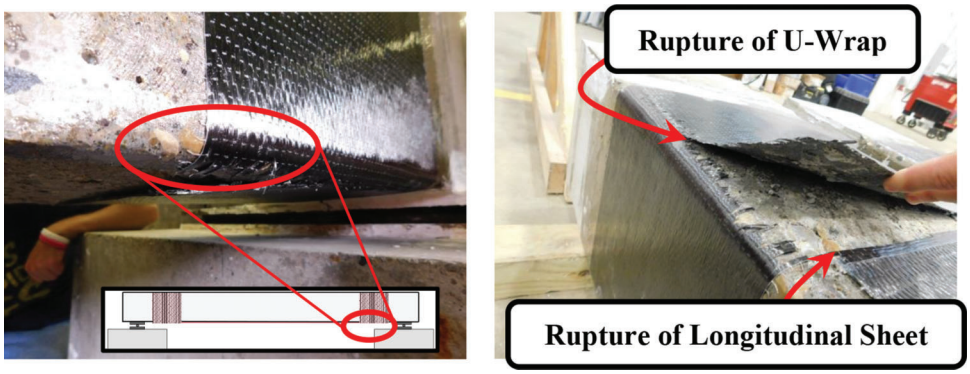


**Figure 3.5** U-wrap anchor after failure.

nominal moment capacities, $M_n$, as indicated in Figure 3.3 and all three of the strengthened specimens exceeded the strength of the control specimen. Further comparisons of the behavior of beams strengthened using various FRP systems and control specimens are provided in later sections of this chapter.

Although comparisons between the performance of the pilot test specimens with externally bonded sheets (0-EB.2 and 0-EB.3) cannot be directly compared, some valuable knowledge was gained during the pilot group testing based on how the strengthening systems behaved under load. As explained in Chapter 2, the externally bonded longitudinal sheet of Specimen 0-EB.2 was anchored at its ends with FRP spike anchors, while the longitudinal sheet of Specimen 0-EB.3 was anchored at its ends with U-wrap anchors. Due to the observed behavior of Specimen 0-EB.3 and consideration of the feasibility of applying strengthening solutions to adjacent box beams, it was decided to forego the U-wrap anchor design to allow for the testing of a different and possibly more viable anchorage configuration.

Comparing the performance of the three strengthened specimens as presented in Figure 3.4, the specimen with U-wrap anchors resulted in lower strength and ductility. This observation must be made with the understanding that the longitudinal reinforcement details differed among the specimens. Nevertheless, the difference in behavior contributed to the decision to explore other anchorage options. Moreover, the application of U-wrap anchors to adjacent box beams in the field, a particular focus of this research, is not possible.

Another notable observation was made after investigating the condition of Specimen 0-EB.3 after failure. It was apparent that the U-wrap anchor reached its rupture strain during the test. As shown in Figure 3.5, the longitudinal sheet also ruptured at the location of the U-wrap. It should be noted that a small number of fibers along the edge of the sheet ruptured prior to the sudden rupture over the entire width of the longitudinal sheet. Nevertheless, the interaction between the longitudinal sheet and U-wrap anchor at failure is unclear. However, it is believed that the U-wrap anchor resulted in a reduction in strength and ductility relative to the other strengthened pilot specimens. It is important to note that using U-wrap anchors with increased cross-sectional area may have provided different results.

The estimated stress in the longitudinal FRP sheet at midspan, $f_{f\_max,}$ for the specimen with U-wrap anchors is 117.18 ksi as indicated in Figure 3.3. This value can be compared to the values of $f_{f\_max}$ calculated for similar specimens of the test program that are introduced in detail later. Specimens 1-EB.2 and 3-EB.2 were both detailed with two excluded steel reinforcing bars and were strengthened with an externally bonded FRP sheet anchored at its ends using FRP spike anchors. The values of $f_{f\_max}$ for Specimens 1-EB.2 and 3-EB.2 are 148.19 ksi and 147.27 ksi, respectively (see Figure 3.16). The values provide evidence that the U-wrap anchors may have led to a premature failure compared to the use of FRP spike anchors at the ends of the sheets.

During the tests on Specimens 0-EB.2 and 0-EB.3 of the pilot group, an important observation was made in regard to the behavior of the longitudinal FRP sheet as the applied load was increased. The FRP sheet started to debond from the concrete surface (see Figure 3.6). This apparent debonding was recognized by a crackling sound which was assumed to be the epoxy breaking its bond with the concrete substrate. The crackling sounds began to be observed sometime after the specimen had reached the cracking moment. To attempt to mitigate this debonding, specimens without U-wraps but with several FRP spike anchors along the length of the longitudinal sheet were added to the test program. This adjustment to the experimental program allowed the effect of the location of the FRP spike anchors on the performance of the strengthening system to be investigated. Complete details of the resulting specimens included in the experimental program are illustrated in Figure 2.7. The modification to the test program allowed for a more realistic solution to be tested in order to meet the objective of flexurally-strengthening adjacent box beam bridges. The strengthening system with FRP sheets anchored with FRP spike anchors does not require access to the sides of the box beam members.

Overall, the test results for Specimen 0-NSM.1 of the pilot group were satisfactory. No alteration was made to the design of the other NSM specimens in the experimental program as a result of the pilot tests.

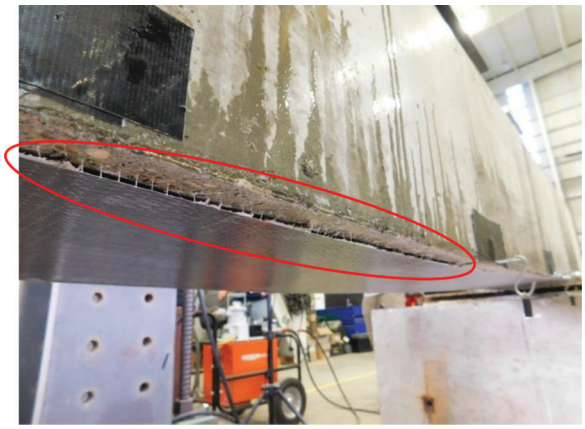

**Figure 3.6** Partially debonded FRP sheet between anchor points.

## 3.4 Test Results by Specimen Type

### *3.4.1 Introduction*

Direct comparisons between specimens of the same type (i.e., Control–C, Artificial Deterioration–D, Externally Bonded–EB, and Near-Surface-Mounted–NSM) are presented in this section. The behavior of the specimens with each strengthening system is also discussed. The test results help to identify reliable FRP systems for flexural strengthening.

### *3.4.2 Control (C) Specimens*

A control specimen with seven No. 3 longitudinal tension bars was cast for each group of the test program. The results of the tests on the control specimens are summarized in Table 3.1. The corresponding response curves are provided in Figure 3.7. Despite the specimens being cast on different days (except for Specimens 0-C and 1-C) and slight differences in the concrete strengths at the time of testing, consistency of the results for all four specimens is clearly evident. The specimens exhibited ductile behavior with failure

TABLE 3.1
**Control Specimen Test Results**

| Specimen ID | $M_{test}$ (kip-ft) | $M_n$ (kip-ft) | $M_{test}/M_n$ | Steel Stress $f_s$ (ksi) | Midspan Deflection at Max Load, Δ (in.) |
|---|---|---|---|---|---|
| 0-C[1] | 59.59 | 45.92[2] | 1.30 | 88.47 | 3.29 |
| 1-C | 59.80 | 46.11[2] | 1.30 | 88.32 | 3.23 |
| 2-C | 59.41 | 45.77[2] | 1.30 | 88.81 | 3.45 |
| 3-C | 59.83 | 45.90[2] | 1.24 | 84.07 | 2.88 |
| | | Mean: | 1.29 | | |
| | | Minimum: | 1.24 | | |
| | | Maximum: | 1.30 | | |

[1]Pin-roller support condition.
[2]Calculated in accordance with ACI 318-19 (ACI Committee 318, 2019).

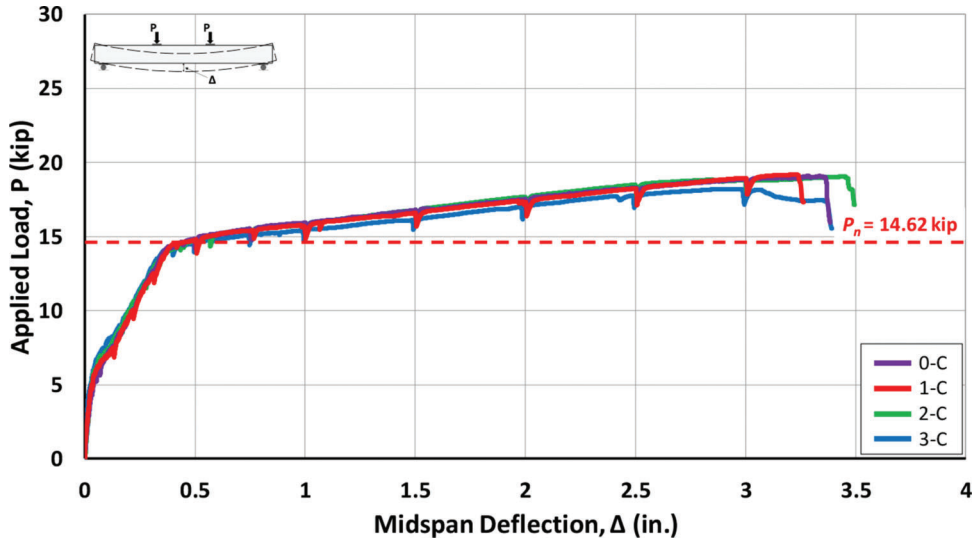


**Figure 3.7** Applied load vs. midspan deflection for control specimens.

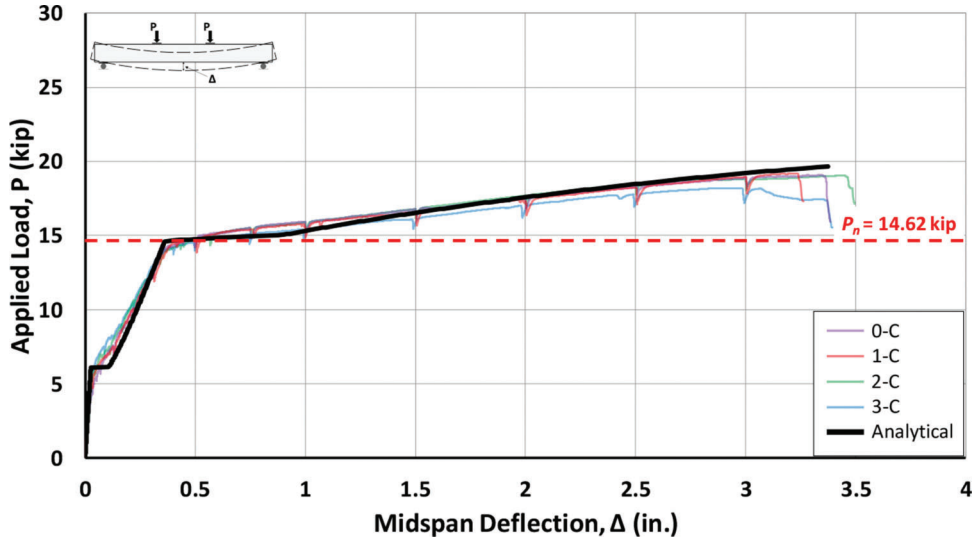


**Figure 3.8** Comparison of theoretical and experimental responses for control specimens.

characterized by crushing of concrete in the compression region. Due to the relatively low reinforcement ratio of the specimens ($\rho = A_s/b_w d = 0.53\%$), the strain in the longitudinal tension reinforcement entered the strain-hardening range for the steel. For this reason, $M_{test}$ was on average 29% greater than $M_n$ based on ACI 318-19, which was calculated using the measured yield stress of the bars ($f_y$ = 70.2 ksi, refer to Section B.1.1 of Appendix B).

The theoretical load-deflection response developed by the analysis tool (see Section B.1 of Appendix B) for the control specimens ($f'_c$ taken as 6,820 psi) is compared to the experimental curves in Figure 3.8. The theoretical load-deflection response is plotted up to the point corresponding to a concrete compressive strain of 0.0038 at the top fiber of the member. The response curve from analysis matches the experimental plots well, providing evidence of the suitability of the analysis tool to model reinforced concrete members under flexure.

### *3.4.3 Artificially Deteriorated (D) Specimens*

The test results for the three artificially deteriorated specimens that were left in their simulated field condition (i.e., not strengthened with FRP) are described in this section. Test data and experimental response curves are provided in Table 3.2 and Figure 3.9, respectively. Although each specimen had a different reinforcement layout (Artificial Deterioration Types I–III, refer to Figure 2.3), the three specimens were calculated to have approximately the same nominal capacity because the

TABLE 3.2
**Artificially Deteriorated Specimen Test Results**

| Specimen ID | $M_{test}$ (kip-ft) | $M_n$ (kip-ft) | $M_{test}/M_n$ | Steel Stress, $f_s$ (ksi) | Midspan Deflection at Max Load, Δ (in.) |
|---|---|---|---|---|---|
| 1-D | 44.68 | 33.88[1] | 1.32 | 89.17 | 3.63 |
| 2-D | 45.40 | 33.67[1] | 1.35 | – | 1.63 |
| 3-D | 44.47 | 33.92[1] | 1.31 | 88.67 | 3.63 |
| | | Mean: | 1.33 | | |
| | | Minimum: | 1.31 | | |
| | | Maximum: | 1.35 | | |

[1]Calculated in accordance with ACI 318-19 (ACI Committee 318, 2019).

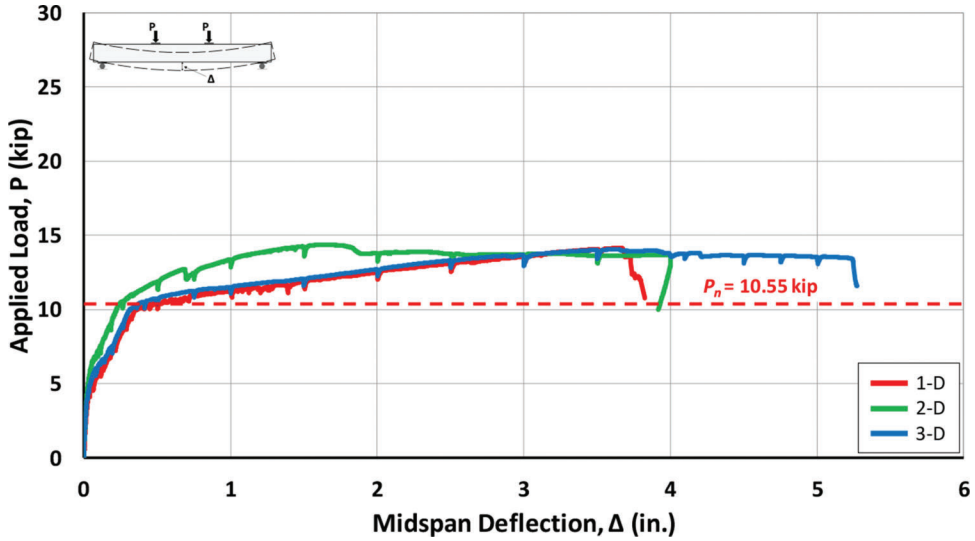


**Figure 3.9** Applied load vs. midspan deflection for artificially deteriorated specimens.

cut longitudinal reinforcing bars in Specimen 2-D were assumed to be ineffective at the location of the critical section for flexure (i.e., at midspan). The small variations in calculated values of $M_n$ in Table 3.2 are only due to slight differences in the measured concrete compressive strengths. The flexural failure of each specimen was characterized by crushing of concrete in the compression region. Although the experimental moment capacities were very similar, Specimen 2-D with the two cut reinforcing bars exhibited the initiation of concrete crushing, accompanied by the opening of a wide flexural crack, considerably earlier compared to the other two specimens. As with the control specimens, the longitudinal reinforcing bars in the artificially deteriorated specimens entered the strain-hardening range during the tests.

The behavior of Specimen 2-D represented in Figure 3.9 is notably different compared to the other specimens with two excluded reinforcing bars. This behavior was due to the concentration of curvature at the location of the cut bars (i.e., at midspan). A wide flexural crack developed at this location as the beam was loaded. The concentration of strain at the location of the crack caused the concrete in the compression region to begin to crush at a lesser deflection compared to the other two specimens. Each of the three artificially deteriorated specimens after failure are shown in Figure 3.10. The relatively large flexural crack at the midspan of Specimen 2-D is evident in Figure 3.10(b) in relation to the other artificially deteriorated specimens, which experienced a more uniform cracking pattern.

It is also observed that Specimen 2-D had higher post-cracking stiffness relative to the two other specimens due to the presence of the two cut reinforcing bars (see Figure 3.9). This higher relative stiffness of the specimen with cut reinforcement bars is important to note in this comparison in which the only variable was cut versus excluded bars. The difference in stiffness among the artificially deteriorated specimens can be used to explain some variations between the stiffnesses of FRP-strengthened specimens that are described in later sections of this chapter.

The load-deflection response obtained from the analysis tool (see Section B.1 of Appendix B) for the artificially deteriorated specimens ($f'_c$ taken as 6,680 psi) is compared to the experimental load-deflection curves

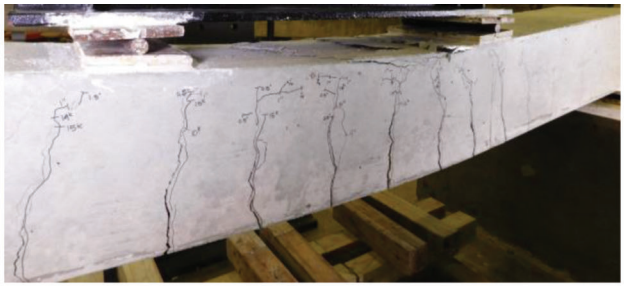

(a) Specimen 1-D

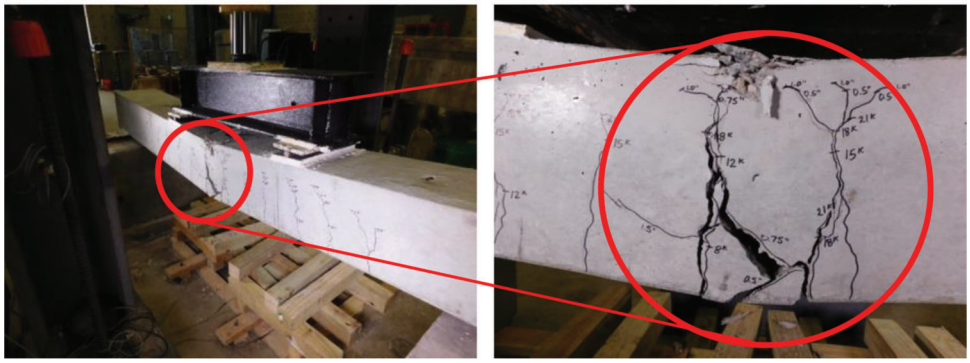

(b) Specimen 2-D

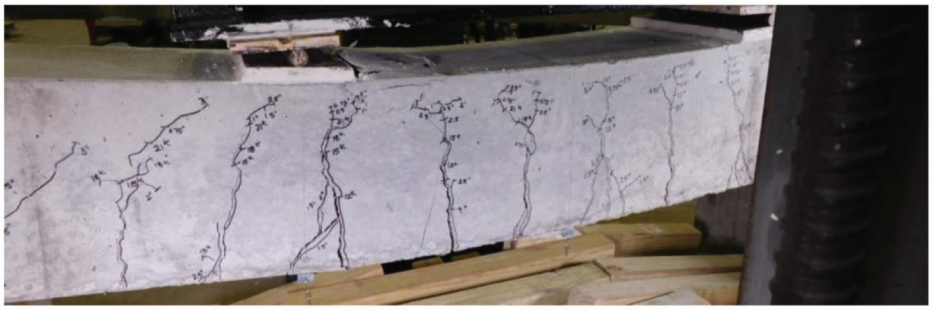

(c) Specimen 3-D

**Figure 3.10** Artificially damaged specimens after failure.

for the beams with excluded reinforcing bars in Figure 3.11. Here, the theoretical curve is plotted to the point corresponding to a concrete compressive strain of 0.0038. Again, the theoretical response curve closely corresponds to the experimental response curves.

### *3.4.4 Externally Bonded (EB) FRP Sheet Specimens*

The test results for the specimens with externally bonded FRP sheets show consistent differences in moment capacity between the two FRP spike anchor configurations (EB.1 with anchors along the length vs. EB.2 with anchors only at the ends). The results from the tests of both anchor configurations are described in the following subsections. Other than Specimen 0-EB.2 which experienced crushing of the concrete prior to FRP rupture, all EB specimens failed by rupture of the FRP sheets prior to concrete crushing regardless of the anchorage details. Important differences between the behaviors resulting from the anchorage details are described in Section 3.4.4.3.

**3.4.4.1 FRP Anchors Along the Length of the FRP Sheet (EB.1)**. The calculated strengths and experimental data for the EB.1 specimens are summarized in Figure 3.12. All three EB.1 specimens exceeded their calculated nominal moment capacity and experienced relatively similar failure moments. However, Specimen 1-EB.1 did not achieve the strength of the corresponding control specimens (Specimen 1-C). It should be noted that the midspan deflection at the maximum applied load for each of the three beams is much lower compared to the deflections of the corresponding unstrengthened specimens (at least approximately 58% less considering the strengthened and unstrengthened specimens from each group, see Table 3.2). Failure by rupture of the FRP

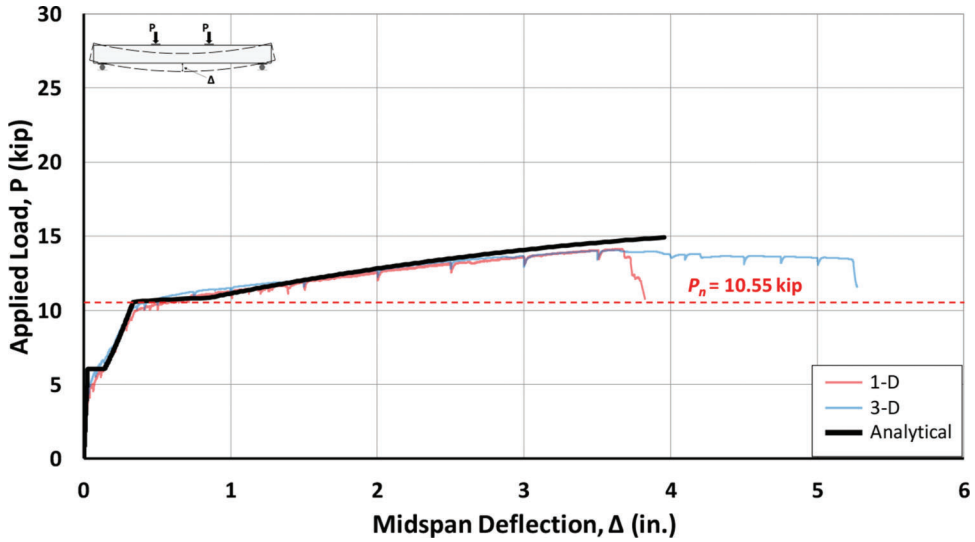


**Figure 3.11** Comparison of theoretical and experimental responses for artificially deteriorated specimens.

| Specimen ID | $M_{test}$ (kip-ft) | $M_n$ (kip-ft) | | $M_{test}$ / $M_n$ | | $M_{test}$ / $M_c$ | Steel Stress, $f_s$ (ksi) | Rupture Stress, $f_{f\_max}$ (ksi) | $f_{fu}$* (ksi) | Effective Stress, $f_{fe}$ (ksi) | $f_{f\_max}$ / $f_{fu}$* | $f_{f\_max}$ / $f_{fe}$ | Midspan Deflection at Max Load, Δ (in.) |
|---|---|---|---|---|---|---|---|---|---|---|---|---|---|
| | | $\psi_f$ = 0.85 | $\psi_f$ = 1.0 | $\psi_f$ = 0.85 | $\psi_f$ = 1.0 | | | | | | | | |
| 1-EB.1 | 54.91 | 51.29[1] | 54.58[1] | 1.07 | 1.01 | 0.92 | 70.60 | 88.19 | 105 | 73.8 | 0.84 | 1.19 | 0.81 |
| 2-EB.1 | 60.10 | 51.19[1] | 54.48[1] | 1.17 | 1.10 | 1.01 | - | - | 105 | 73.8 | - | - | 0.68 |
| 3-EB.1 | 58.36 | 51.40[1] | 54.70[1] | 1.14 | 1.07 | 1.03 | 71.97 | 100.00 | 105 | 73.8 | 0.95 | 1.36 | 0.96 |
| | | | Mean: | 1.13 | 1.06 | | | | | | | | |
| | | | Minimum: | 1.07 | 1.01 | | | | | | | | |
| | | | Maximum: | 1.17 | 1.10 | | | | | | | | |

**Figure 3.12** EB.1 specimen test results.
[1]Calculated in accordance with ACI 440.2R-17 (ACI Committee 440, 2017).

sheet greatly reduced the ductility of the specimens. Figure 3.12 again includes columns for steel reinforcement and FRP stress values. Specimen 2-EB.1 contained two cut reinforcing bars and estimated stress values are therefore not included in the figure as it is difficult to accurately quantify the contribution of the two cut bars.

The response curves of the EB.1 specimens are provided in Figure 3.13. For each specimen, individual fibers of the longitudinal FRP sheet began to rupture once the applied load, P, reached approximately 15 kips. As can be seen by a larger initial drop in load, a larger amount of fibers ruptured at the maximum load for Specimens 1-EB.1 and 2-EB.1 while Specimen 3-EB.1 experienced a more gradual rupturing of the FRP sheet. Individual fibers continued to rupture with increasing applied load until the FRP fully ruptured across the width of the beam and all capacity from the FRP was lost. The plots in Figure 3.13 extend until this point. As expected based on the behavior of the artificially deteriorated specimens, Specimen 2-EB.1 with bars cut at midspan exhibited a greater stiffness compared to the other two specimens after the initial flexural cracking of the concrete occurred. The specimen also exhibited a slightly larger failure moment (9.45% greater than Specimen 1-EB.1) and reduced ductility compared to the beams with missing bars. Unlike the other EB.1 specimens, the flexural cracking behavior of Specimen 2-EB.1 was more closely related to Specimen 2-D compared to the other artificially deteriorated (D) specimens due to the relatively large cracks near midspan.

The data in Figure 3.13 can be used to compare the behaviors of Specimen 1-EB.1 with one bar excluded near each corner and Specimen 3-EB.1 with two bars excluded near one corner. The responses of the two specimens are similar up to the significant loss in load-carrying capacity experienced by Specimen 1-EB.1. Specimen 3-EB.1 displayed noticeably more deflection compared to Specimen 1-EB.1 before total rupture of the FRP sheet occurred across the width of the beam. However, this variability is not attributed to the eccentricity of the reinforcement but rather to the general variability of the FRP strengthening system.

From the results in Figure 3.12, it is observed that the estimated stress in the FRP corresponding to the maximum applied load, $f_{f\_max}$, surpassed the effective stress, $f_{fe}$, for both Specimens 1-EB.1 and 3-EB.1. However, for both beams, the value of $f_{f\_max}$ is less than the ultimate tensile strength of the cured FRP laminate,

$f_{fu}$*, reported by the manufacturer. It should be noted that the value of $f_{fe}$ in the moment strength calculations based on ACI 440.2R-17 (ACI Committee 440, 2017) for all specimens represented in Figure 3.12, as well as all other EB specimens of the flexural-strengthening experimental program, is governed by the strain limit of the FRP, and the value of $f_{fe}$ is equal to $0.9E_f\varepsilon_{fu}$ in accordance with ACI 440.2R-17, where $E_f$ and $\varepsilon_{fu}$ are the modulus of elasticity and ultimate rupture strain, respectively, as reported by the manufacturer (see Table 2.1). For the NSM specimens, the value of $f_{fe}$ is equal to $0.7E_f\varepsilon_{fu}$, where the 0.7 factor is recommended in Section 10.1.1 of ACI 440.2R-17 for NSM reinforcement. The theoretical load-deflection curve from the analysis tool (see Section B.1 of Appendix B) is compared to the experimental load-deflection responses in Section 3.4.4.3.

Failure photos for each of the three tests are provided in Figure 3.14. The longitudinal FRP sheet ruptured in a

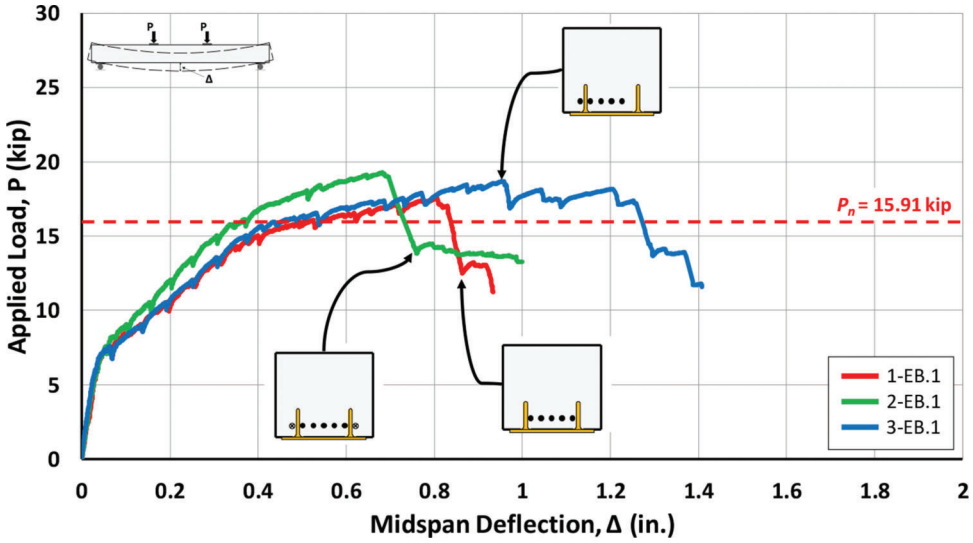


**Figure 3.13** Applied load vs. midspan deflection for EB.1 specimen.

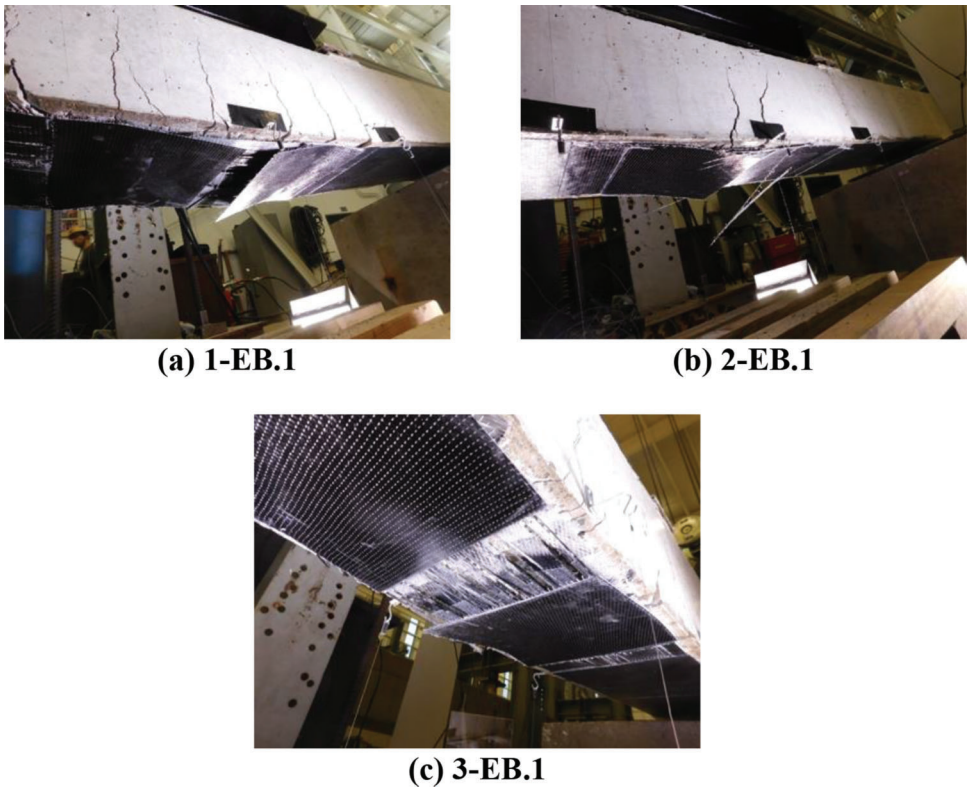


**Figure 3.14** EB.1 specimens after failure.

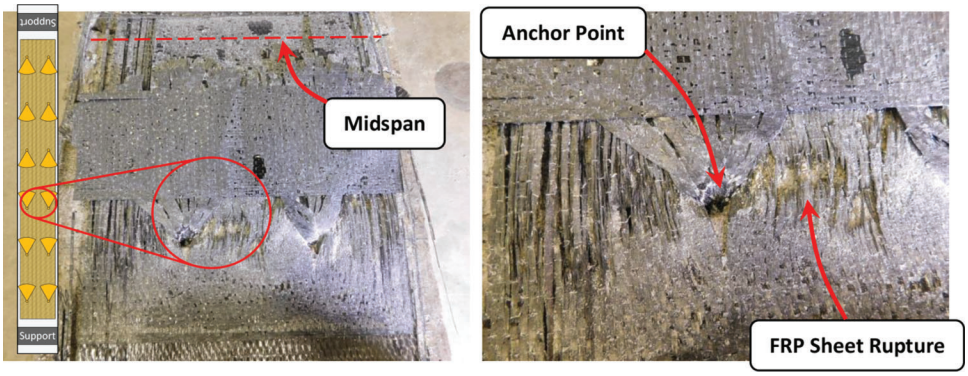


**Figure 3.15** Typical FRP sheet rupture at anchor point—EB.1 specimen.

| Specimen ID | $M_{test}$ (kip-ft) | $M_n$ (kip-ft) | | $M_{test}/M_n$ | | $M_{test}/M_c$ | Steel Stress, $f_s$ (ksi) | Rupture Stress, $f_{f\_max}$ (ksi) | $f_{fu}$* (ksi) | Effective Stress, $f_{fe}$ (ksi) | $f_{f\_max}/f_{fu}$* | $f_{f\_max}/f_{fe}$ | Midspan Deflection at Max Load, Δ (in.) |
|---|---|---|---|---|---|---|---|---|---|---|---|---|---|
| | | $\psi_f = 0.85$ | $\psi_f = 1.0$ | $\psi_f = 0.85$ | $\psi_f = 1.0$ | | | | | | | | |
| 0-EB.2 | 79.96 | 51.00[1] | 54.28[1] | 1.57 | 1.47 | 1.34 | - | - | 105 | 73.8 | - | - | 1.76 |
| 1-EB.2 | 71.71 | 51.21[1] | 54.50[1] | 1.40 | 1.32 | 1.20 | 77.15 | 148.19 | 105 | 73.8 | 1.41 | 2.01 | 1.63 |
| 2-EB.2 | 72.79 | 51.25[1] | 54.54[1] | 1.42 | 1.33 | 1.23 | - | - | 105 | 73.8 | - | - | 1.25 |
| 3-EB.2 | 71.62 | 51.38[1] | 54.68[1] | 1.39 | 1.31 | 1.26 | 77.07 | 147.27 | 105 | 73.8 | 1.40 | 2.00 | 1.69 |
| | | | Mean: | 1.45 | 1.36 | | | | | | | | |
| | | | Minimum: | 1.39 | 1.31 | | | | | | | | |
| | | | Maximum: | 1.57 | 1.47 | | | | | | | | |

**Figure 3.16** EB.2 specimen test results.
[1]Calculated in accordance with ACI 440.2R-17 (ACI Committee 440, 2017).

similar location (near midspan) for all three specimens. After further investigation of the ruptured FRP sheet of the three specimens, it was determined that the location of the rupture was consistently at FRP anchor points located closest to midspan (see Figure 3.15). It could not be visually verified while testing, but it is assumed that the FRP first ruptured near the anchor points due to the increased stress concentration at that location.

**3.4.4.2 FRP Anchors at the Ends of the FRP Sheet (EB.2)**. The results of the tests on the four EB.2 specimens are summarized in Figure 3.16, and the corresponding load-deflection plots are presented in Figure 3.17. In contrast to the three EB.1 specimens that experienced incremental rupturing of the FRP sheet across the width of the sheet, the EB.2 specimens experienced a failure characterized by an abrupt rupture of the longitudinal FRP sheet. In other words, the FRP sheets failed suddenly, with the possible exception of a relatively small number of fibers along the edge of the sheet rupturing prior to this event. As previously noted, Specimen 0-EB.2 experienced crushing of the concrete prior to FRP rupture. Along with the failure behavior of the EB.2 specimens being different from that of the EB.1 specimens, the numerical results were also different. The EB.2 specimens consistently reached larger capacities compared to their EB.1 counterparts and also achieved larger midspan deflections prior to failure.

The increased post-cracking stiffness of the two specimens with cut reinforcing bars (Specimens 0-EB.2 and 2-EB.2) compared to the two specimens with excluded reinforcing bars (Specimens 1-EB.2 and 3-EB.2) is shown by the response curves in Figure 3.17. Another important observation is the variations in ductility and failure loads between Specimens 0-EB.2 and 2-EB.2 presented in this figure. Because the details of these specimens were similar, these differences are assumed to be attributable to variability in the properties of the FRP laminate and sensitivity to small variations in the application process. The relatively large midspan deflection reached by Specimen 0-EB.2 seems to indicate that variations in the ductility of the FRP-strengthened beams may not be dependent on whether longitudinal bars were cut or excluded to create the simulated field conditions of the members. It can also be noted that, with less deflection achieved before the end of the test, the cracking near midspan was less severe for Specimens 0-EB.2 and 2-EB.2 compared to Specimen 2-D of the artificially deteriorated group. It should be noted that cracking patterns after failure cannot be directly compared for all EB.2 specimens since deflections at failure were not all the same, yet general comparisons are still valuable. When comparing the cracking patterns between specimens with cut bars to those with excluded bars, the specimens with cut bars experienced relatively larger cracks near midspan.

The responses of Specimens 1-EB.2 and 3-EB.2 displayed in Figure 3.17 are nearly identical, indicating

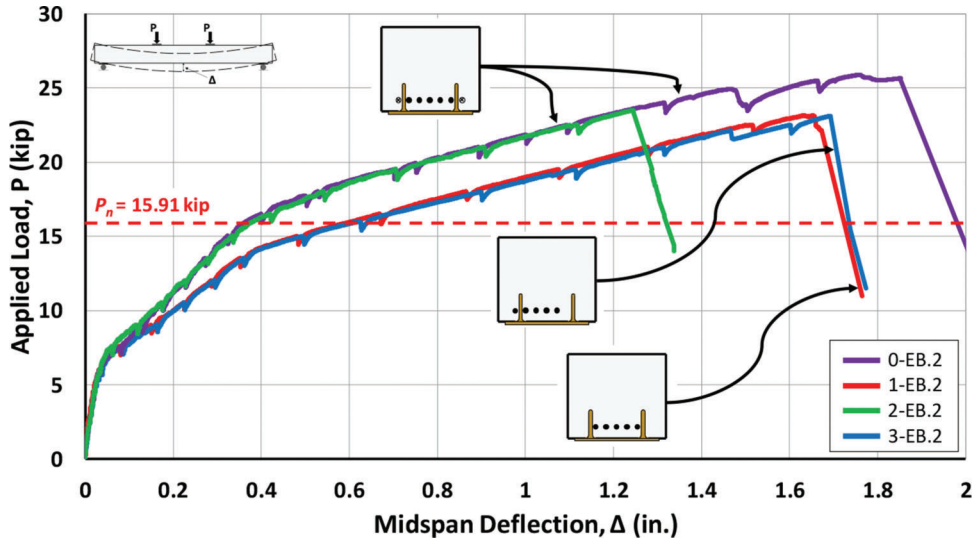


**Figure 3.17** Applied load vs. midspan deflection for EB.2 specimens.

that the eccentricity of the steel reinforcement did not significantly impact the behavior of the specimens. However, a relatively small number of fibers along the edge of the FRP sheet of Specimen 3-EB.2 did rupture early. Nevertheless, as discussed in Section 3.4.4.1, this provides further evidence that the difference in deflections achieved by Specimens 1-EB.1 and 3-EB.1 is likely due to variability of the FRP strengthening system and not due to the eccentricity of the steel.

The two EB.2 specimens with longitudinal bars excluded (Specimens 1-EB.2 and 3-EB.2) were modeled using the analysis described in Section B.1 of Appendix B. Based on this analysis, the FRP sheets for both of these specimens were estimated to have reached a strain value at the maximum applied load, $f_{f\_max}$, that is twice the effective stress, $f_{fe}$, calculated in accordance with ACI 440.2R-17 (see Figure 3.16). Again, the value of $f_{fe}$ is calculated based on failure of the FRP governing the failure of the member. The estimated values of $f_{f\_max}$ also exceed the tensile strength reported by the manufacturer, $f_{fu}$*. The values of the ratio $f_{f\_max}$/ $f_{fu}$* for the specimens are quite large and are again best understood in a relative sense compared to the results of other test specimens rather than as an accurate representation of the actual stress achieved by the FRP. A comparison of the theoretical load-deflection response from the analysis tool is compared to the experimental load-deflection curves in Section 3.4.4.3.

Photos of each EB.2 specimen after failure are provided in Figures 3.18, 3.19, 3.20, and 3.21. While the longitudinal FRP sheet ruptured consistently at one of the FRP anchor points located closest to midspan for all of the EB.1 specimens, the location of the ruptured longitudinal FRP sheet varied between the EB.2 specimens. The FRP sheet on Specimens 0-EB.2 and 1-EB.2 ruptured at the location of the end anchor while the sheet on Specimens 2-EB.2 and 3-EB.2 ruptured near midspan. Considering the data in Figure 3.16 and the plots in Figure 3.17, no correlation is found between the location of the FRP rupture and the overall efficiency (i.e., resulting failure load and ductility) of the strengthening system.

Footage from a high-speed camera was used to capture the failure of Specimen 1-EB.2. An image of the north support for Specimen 1-EB.2 just prior to failure of the FRP sheet (besides a small number of fibers at the edge of the sheet that had ruptured before the image was taken) is provided in Figure 3.22(a). The image in Figure 3.22(b) shows the failure of the longitudinal FRP sheet, potentially due to the stress concentration at the northwest anchor. For this specimen, the fibers of the FRP sheet near the two anchors ruptured, and the rest of the sheet pulled out from under the patches.

**3.4.4.3 Comparison of FRP Anchors Along the Length (EB.1) and at the Ends (EB.2) of the FRP Sheet**. The results from all tests on externally bonded FRP-strengthened beams are summarized in Figure 3.23. In the table, the simulated field conditions refer to the conditions previously discussed and presented in Figure 2.4. The load-deflection responses of the EB.1 and EB.2 specimens are compared in Figure 3.24. The specimens from different groups (see Figure 3.1) are differentiated by color in the figure. The curves for EB.1 specimens are represented by solid lines, and the curves for EB.2 specimens are represented by dashed lines. The plot reveals the consistent ductility and capacity differences between the two strengthening system configurations (EB.1 vs. EB.2).

Several important comparisons can be made from the data in Figure 3.23 and Figure 3.24. Comparing the specimens from Groups 1, 2, and 3 with the same simulated field conditions, the experimental moment capacity, $M_{test}$, is 25% greater on average for the EB.2 specimens compared to the EB.1 specimens. Similarly, the midspan deflection at the maximum applied load is 87% greater on average for the EB.2 specimens compared to the EB.1 specimens from Groups 1, 2, and

(a) South End

(b) North End

(c) Crack Pattern

**Figure 3.18** Specimen 0-EB.3 after failure.

(a) South End

(b) North End

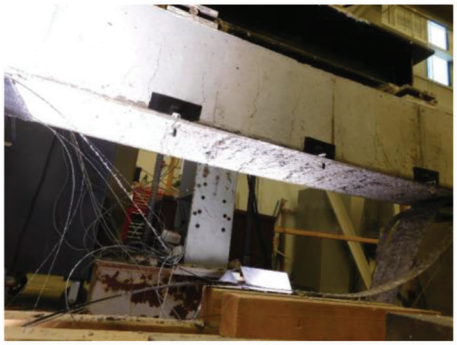

(c) Crack Pattern

**Figure 3.19** Specimen 1-EB.2 after failure.

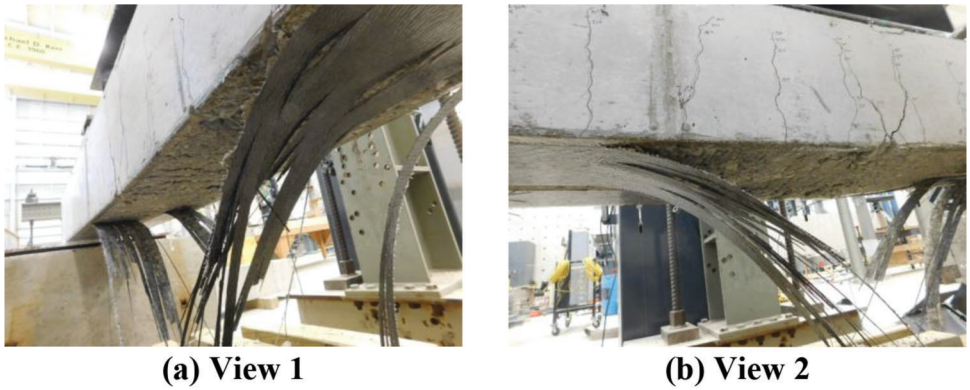

(a) View 1 (b) View 2

(c) View 3 (Beam Inverted)

**Figure 3.20** Specimen 2-EB.2 after failure.

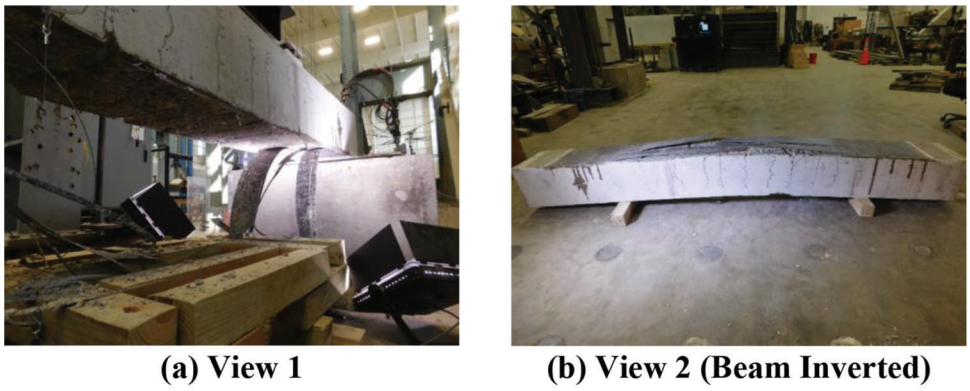

(a) View 1 (b) View 2 (Beam Inverted)

(c) View 3 (Beam Inverted)

**Figure 3.21** Specimen 3-EB.2 after failure.

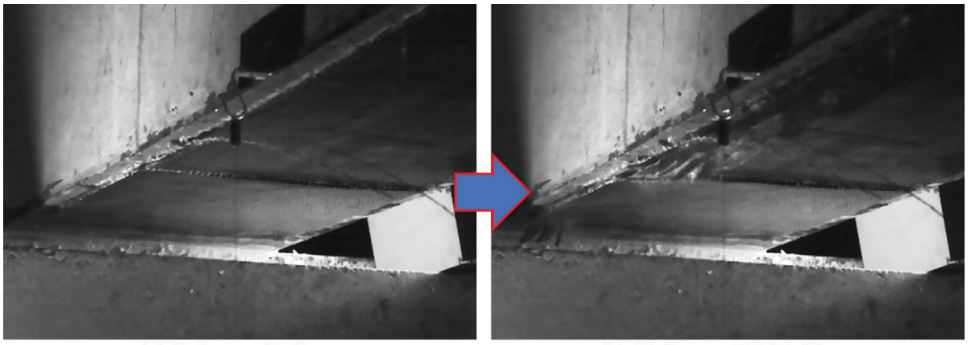

(a) Prior to Failure (b) Failure of FRP Sheet

**Figure 3.22** FRP sheet failure at anchor point (Specimen 1-EB.2).

| Specimen ID | Simulated Field Condition | $M_{test}$ (kip-ft) | $M_n$ (kip-ft) | | $M_{test}/M_n$ | | Steel Stress, $f_s$ (ksi) | Rupture Stress, $f_{f\_max}$ (ksi) | $f_{fu}$* (ksi) | Effective Stress, $f_{fe}$ (ksi) | $f_{f\_max}/f_{fu}$* | $f_{f\_max}/f_{fe}$ | Midspan Deflection at Max Load, Δ (in.) |
|---|---|---|---|---|---|---|---|---|---|---|---|---|---|
| | | | $\psi_f = 0.85$ | $\psi_f = 1.0$ | $\psi_f = 0.85$ | $\psi_f = 1.0$ | | | | | | | |
| 0-EB.3 | D[I] | 62.95 | 47.09[1] | 49.65[1] | 1.34 | 1.27 | 73.88 | 117.18 | 105 | 73.8 | 1.12 | 1.59 | 1.30 |
| 1-EB.1 | | 54.91 | 51.29[1] | 54.58[1] | 1.07 | 1.01 | 70.60 | 88.19 | 105 | 73.8 | 0.84 | 1.19 | 0.81 |
| 1-EB.2 | | 71.71 | 47.26[1] | 49.84[1] | 1.52 | 1.44 | 77.15 | 148.19 | 105 | 73.8 | 1.41 | 2.01 | 1.63 |
| 2-EB.1 | D[II] | 60.10 | 51.19[1] | 54.48[1] | 1.17 | 1.10 | - | - | 105 | 73.8 | - | - | 0.68 |
| 2-EB.2 | | 72.79 | 47.29[1] | 49.87[1] | 1.54 | 1.46 | - | - | 105 | 73.8 | - | - | 1.25 |
| 0-EB.2 | | 79.96 | 47.08[1] | 49.65[1] | 1.70 | 1.61 | - | - | 105 | 73.8 | - | - | 1.76 |
| 3-EB.1 | D[III] | 58.36 | 51.40[1] | 54.70[1] | 1.14 | 1.07 | 71.97 | 100.00 | 105 | 73.8 | 0.95 | 1.36 | 0.96 |
| 3-EB.2 | | 71.62 | 47.40[1] | 49.98[1] | 1.51 | 1.43 | 77.07 | 147.27 | 105 | 73.8 | 1.40 | 2.00 | 1.69 |

**Figure 3.23** Test results for all EB specimens.
[1]Calculated in accordance with ACI 440.2R-17 (ACI Committee 440, 2017).

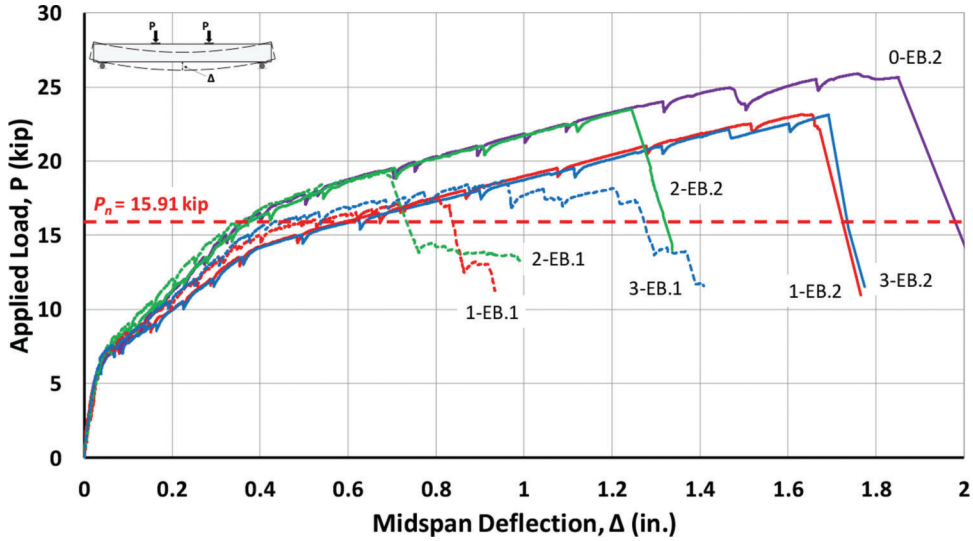


**Figure 3.24** Applied load vs. midspan deflection for EB.1 and EB.2 specimens.

3 with the same simulated field condition. The estimated values of the stress in the FRP sheets at the maximum applied load, $f_{f\_max}$, for corresponding specimens analyzed using the procedure outlined in Section B.1 of Appendix B (1-EB.1 vs. 1-EB.2 and 3-EB.1 vs. 3-EB.2) also provide an important comparison. Assuming the FRP stress can be calculated based on strain compatibility, the value of $f_{f\_max}$ is 68% and 47% greater for the specimens with anchors only at the ends of the sheet compared to the specimens with anchors along their lengths for Groups 1 and 3, respectively. Based on the analysis, the FRP sheets on the EB.2 specimens reached twice the calculated effective stress, $f_{fe}$, while the EB.1 specimens still surpassed the effective stress but only by an average of approximately 28%. Furthermore, the values of $f_{f\_max}$ exceed $f_{fu}$* for the EB.2 specimens but not for the EB.1 specimens. Based on these comparisons along with the observed rupture of the sheets on

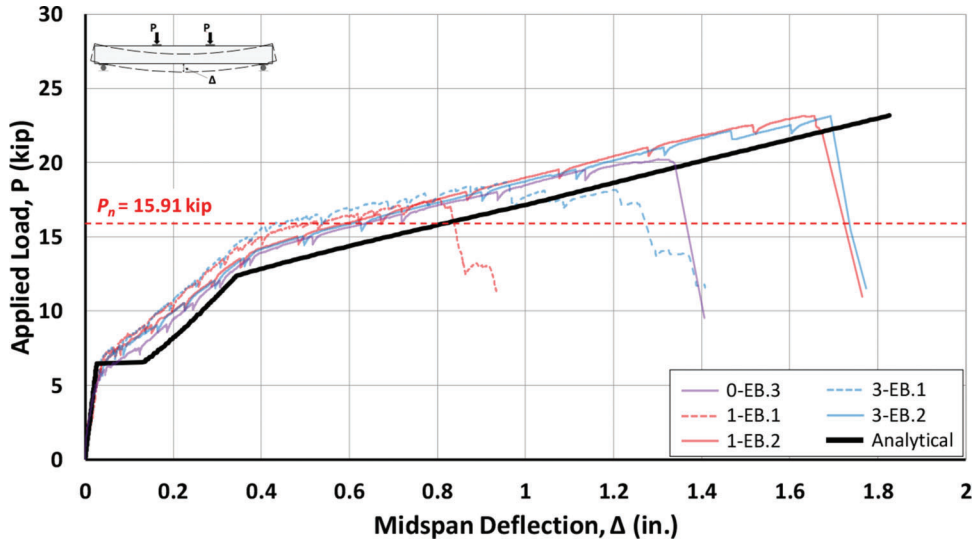


**Figure 3.25** Comparison of theoretical and experimental responses for externally bonded specimens.

the EB.1 specimens occurring at one of the FRP anchor points located closest to midspan, the early failure of the EB.1 specimens is attributed to stress concentrations in the FRP sheets near the anchor points near midspan. It is noted that rupture of the FRP sheet was observed near an anchor at the end of the member for two of the EB.2 specimens. However, the strengths of these specimens do not reflect a premature failure. This is likely because the anchor points were located at a position along the beam at which little bending moment was experienced.

To compare the theoretical load-deflection curve from the analysis tool with the behavior of the test specimens, a plot of the theoretical curve for the externally bonded case ($f'_c$ taken as 7,270 psi) is provided in Figure 3.25 along with the experimental load-deflection plots for the applicable EB specimens. Again, the value of $f_{f\_max}$ for a member is obtained from the analysis tool for the maximum load applied to the experimental specimen during the test.

### *3.4.5 Near-Surface-Mounted (NSM) FRP Strip Specimens*

The test results of the seven near-surface-mounted FRP strengthened specimens are provided in Figure 3.26. The response curves for all NSM.1 specimens are provided in Figure 3.27. The NSM strips were centered on the cross section for these specimens. Three NSM specimens were included in Group 3 to evaluate the effect of the placement of the FRP strips relative to the location of excluded longitudinal reinforcing bars. For clarity, the responses of the Group 3 specimens are shown separately from the other specimens in Figure 3.28. The curve for Specimen 3-NSM.1 is therefore included in both plots. It should again be noted that Specimen 1-NSM.1b was added to the testing program in order to verify the feasibility of applying the FRP strips overhead. A different epoxy was used for this application (see Section 2.4 and Section A.3.2 of Appendix A).

Each NSM specimen surpassed its calculated nominal flexural strength. The load-deflection plots in Figure 3.27 and Figure 3.28 are terminated after a significant loss in load-carrying capacity after reaching the maximum applied load. However, some specimens continued to be loaded after this point and demonstrated several peaks and drops in the applied load. This is thought to be due to incremental slip of the NSM strips within the epoxy. Based on the failure behavior of the specimens, it is believed that each specimen with NSM strips failed by slip of the strips (i.e., bond failure at the epoxy-FRP interface). The only specimen that experienced some concrete crushing prior to a significant loss in load-carrying capacity was Specimen 0-NSM.1. The slight loss in load-carrying capacity corresponding to concrete crushing prior to ultimate failure is evident for this specimen in Figure 3.27.

Several key observations are noted from the load-deflection plots. Consistent with the test results previously presented, the two specimens with cut reinforcing bars (Specimens 0-NSM.1 and 2-NSM.1) exhibited a greater post-cracking stiffness compared to all other NSM specimens. Variations in flexural strengths are also evident, with Specimen 2-NSM.1 achieving a failure load notably greater than other specimens. The differences in strength may be at least partially attributed to variations in material properties or sensitivity to small variations in the installation procedures.

Furthermore, as can be observed from Figure 3.27, the location of the NSM FRP strips in relation to the centroid of the steel reinforcement did not have a significant effect on the response of the specimens. Specimen 3-NSM.3, however, did experience a lower failure load and midspan deflection compared to the other

| Specimen ID | $M_{test}$ (kip-ft) | $M_n$ (kip-ft) | | $M_{test}/M_n$ | | $M_{test}/M_c$ | Steel Stress, $f_s$ (ksi) | Rupture Stress, $f_{f\_max}$ (ksi) | $f_{fu}$* (ksi) | Effective Stress, $f_{fe}$ (ksi) | $f_{f\_max}/f_{fu}$* | $f_{f\_max}/f_{fe}$ | Midspan Deflection at Max Load, Δ (in.) |
|---|---|---|---|---|---|---|---|---|---|---|---|---|---|
| | | $\psi_f = 0.85$ | $\psi_f = 1.0$ | $\psi_f = 0.85$ | $\psi_f = 1.0$ | | | | | | | | |
| 0-NSM.1 | 77.11 | 50.36[2] | 53.53[2] | 1.53 | 1.44 | 1.29 | - | - | 325 | 228.1 | - | - | 1.61 |
| 1-NSM.1a | 70.81 | 50.50[2] | 53.67[2] | 1.40 | 1.32 | 1.18 | 77.79 | 364.58 | 325 | 228.1 | 1.12 | 1.60 | 1.72 |
| 1-NSM.1b[1] | 58.54 | 50.68[2] | 53.86[2] | 1.15 | 1.09 | 0.98 | 72.78 | 252.72 | 325 | 228.1 | 0.78 | 1.11 | 1.10 |
| 2-NSM.1 | 82.87 | 50.46[2] | 53.63[2] | 1.64 | 1.55 | 1.39 | - | - | 325 | 228.1 | - | - | 1.82 |
| 3-NSM.1 | 68.56 | 50.59[2] | 53.77[2] | 1.36 | 1.28 | 1.21 | 76.87 | 343.02 | 325 | 228.1 | 1.06 | 1.50 | 1.62 |
| 3-NSM.2 | 69.25 | 50.53[2] | 53.70[2] | 1.37 | 1.29 | 1.22 | 77.17 | 350.03 | 325 | 228.1 | 1.08 | 1.53 | 1.56 |
| 3-NSM.3 | 65.50 | 50.55[2] | 53.72[2] | 1.30 | 1.22 | 1.15 | 75.67 | 315.71 | 325 | 228.1 | 0.97 | 1.38 | 1.43 |
| | | | Mean: | 1.39 | 1.31 | | | | | | | | |
| | | | Minimum: | 1.15 | 1.09 | | | | | | | | |
| | | | Maximum: | 1.64 | 1.55 | | | | | | | | |

**Figure 3.26** NSM specimen test results.
[1]Epoxy grout and NSM strip applied overhead.
[2]Calculated in accordance with ACI 440.2R-17 (ACI Committee 440, 2017).

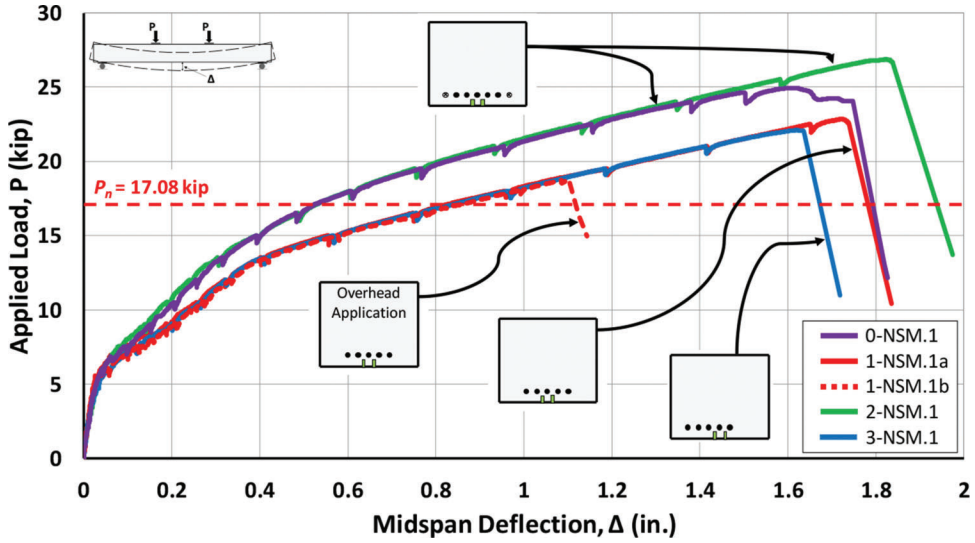


**Figure 3.27** Applied load vs. midspan deflection for NSM.1 specimens.

specimens, with the exception of Specimen 1-NSM.1b, discussed later. As mentioned in Section 3.2 (also see Section A.4 of Appendix A), two linear string potentiometers measured the deflection at each edge of the bottom surface of the Group 3 specimens at midspan and under each of the two load points. No significant differential deflections (i.e., rotation) were measured between the two edges at midspan of the Group 3 specimens with NSM reinforcement (between 0.003 in. and 0.015 in. at the maximum applied load) relative to the differential deflection of the Group 3 control specimen (Specimen 3-C) that had concentric reinforcement (0.024 in. at the maximum applied load). For comparison, the deflections measured at each bottom edge of the Group 3 specimens at midspan are included in Section B.2 of Appendix B. More tests, possibly with larger eccentricities, can be conducted to confirm that placement of NSM strips relative to corroded steel reinforcement has little to no effect on flexural performance.

Specimen 1-NSM.1b for which the NSM strips were installed overhead proved to be an outlier in the data. Although the process of the overhead application of the NSM strips was a success (see Section A.3.2 of Appendix A) and Specimen 1-NSM.1b reached its calculated nominal flexural strength (with the steel reinforcement expected to have increased slightly beyond the yield stress due to strain hardening), it is apparent that the specimen experienced a premature failure compared to the other NSM specimens. The response curve of Specimen 1-NSM.1b follows the trend of other specimens with excluded reinforcing bars closely until the point of this premature failure, which is likely due to a weaker bond between the epoxy and FRP compared to other NSM specimens. More tests on

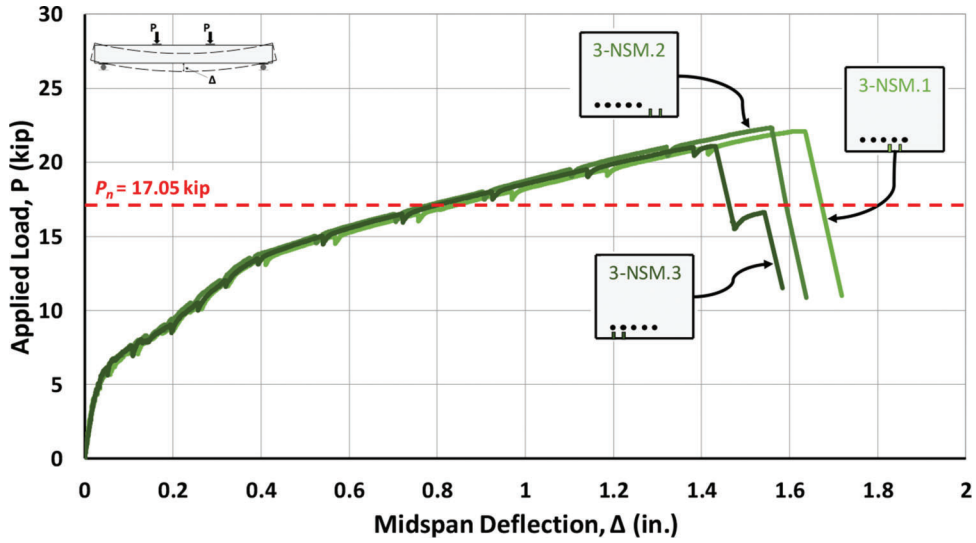


**Figure 3.28** Applied load vs. midspan deflection for Group 3 NSM specimens.

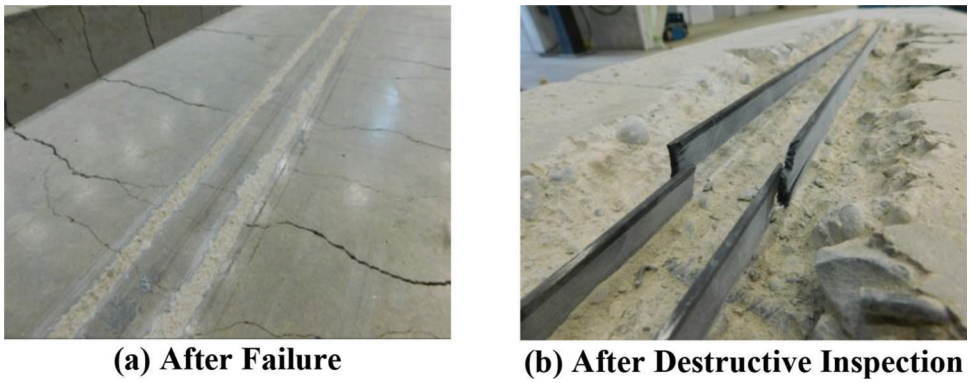


**Figure 3.29** FRP strips of specimen 1-NSM.1a.

specimens with NSM strips installed using the same epoxy as Specimen 1-NSM.1b and additional tests on specimens with strips installed into both overhead and inverted members are needed.

The failure of the NSM specimens was far less explosive than the EB specimens. When each specimen failed, the strips were contained within the epoxy grout, and the slip of the NSM strips within the grout was not externally visible. Specimen 1-NSM.1a was destructively investigated after testing. As shown in Figure 3.29, due to the slip that occurred, the FRP strips failed in compression upon unloading and autopsying the specimen.

As with the specimens with externally bonded FRP sheets, the stress in the NSM strips at failure, $f_{f\_max}$, was estimated and compared to values of $f_{fe}$ and $f_{fu}$* for the specimens without cut steel reinforcing bars (see Figure 3.26). The calculated strengths of the NSM specimens based on ACI 440.2R-17 (ACI Committee 440, 2017) were governed by the strain limit of the FRP. As previous explained, the value of $f_{fe}$ was taken as $0.7E_f\varepsilon_{fu}$, where $E_f$ and $\varepsilon_{fu}$ are the modulus of elasticity and ultimate rupture strain, respectively, as reported by the manufacturer (see Table 2.1). Considering the specimens in Figure 3.26 that did not include cut steel bars, the NSM strips were estimated to have reached a 42% greater stress on average than the calculated value of $f_{fe}$. As expected, the lowest value of $f_{f\_max}$ was calculated for Specimen 1-NSM.1b with strips installed overhead. The value of $f_{f\_max}$ still exceeded $f_{fe}$ by 11%. However, the value of $f_{f\_max}$ for this specimen was only 78% of $f_{fu}$* reported by the manufacturer of the NSM strips.

The theoretical load-deflection curve for the NSM case ($f'_c$ taken as 7,030 psi) is plotted in Figure 3.30 with the load-deflection responses of the five NSM specimens without cut steel reinforcing bars. The plot again demonstrates that a relatively simple analysis tool can provide a reasonable representation of the FRP-strengthened members.

### 3.5 Test Results by Group

Comparisons of specimens within each group, excluding Group 0 (see Section 3.3), are presented in this section. Studying the test results by each group allows the effectiveness of the FRP strengthening systems in regaining the strength and stiffness of the control specimen to be evaluated. Furthermore, direct comparisons can be made between the FRP systems and

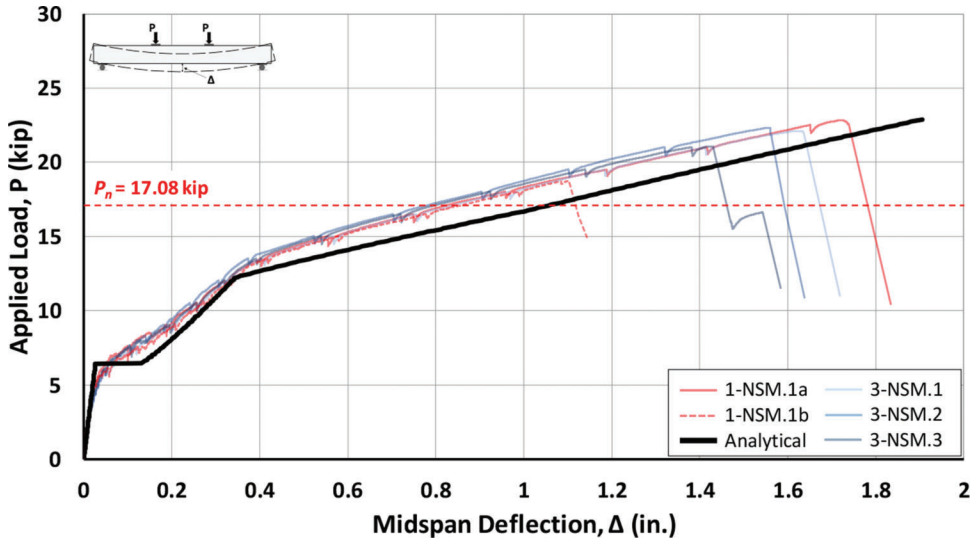


**Figure 3.30** Comparison of theoretical and experimental responses for near-surface-mounted specimens.

| Specimen ID | $M_{test}$ (kip-ft) | $M_n$ (kip-ft) | | $M_{test}/M_n$ | | $M_{test}/M_c$ | $M_{test}/M_D$ | Steel Stress, $f_s$ (ksi) | Rupture Stress, $f_{f\_max}$ (ksi) | $f_{fu}$* (ksi) | Effective Stress, $f_{fe}$ (ksi) | $f_{f\_max}/f_{fu}$* | $f_{f\_max}/f_{fe}$ | Midspan Deflection at Max Load, Δ (in.) |
|---|---|---|---|---|---|---|---|---|---|---|---|---|---|---|
| | | $\psi_f = 0.85$ | $\psi_f = 1.0$ | $\psi_f = 0.85$ | $\psi_f = 1.0$ | | | | | | | | | |
| 1-C | 59.80 | 46.11[2] | | 1.30 | | 1.00 | 1.34 | 88.32 | - | - | - | - | - | 3.23 |
| 1-D | 44.68 | 33.88[2] | | 1.32 | | 0.75 | 1.00 | 89.17 | - | - | - | - | - | 3.63 |
| 1-EB.1 | 54.91 | 47.33[3] | 49.91[3] | 1.16 | 1.10 | 0.92 | 1.23 | 70.60 | 88.19 | 105 | 73.8 | 0.84 | 1.19 | 0.81 |
| 1-EB.2 | 71.71 | 47.26[3] | 49.84[3] | 1.52 | 1.44 | 1.20 | 1.60 | 77.15 | 148.19 | 105 | 73.8 | 1.41 | 2.01 | 1.63 |
| 1-NSM.1a | 70.81 | 50.20[3] | 53.31[3] | 1.41 | 1.33 | 1.18 | 1.58 | 77.79 | 364.58 | 325 | 228.1 | 1.12 | 1.60 | 1.72 |
| 1-NSM.1b[1] | 58.54 | 50.38[3] | 53.51[3] | 1.16 | 1.09 | 0.98 | 1.31 | 72.78 | 252.72 | 325 | 228.1 | 0.78 | 1.11 | 1.10 |

**Figure 3.31** Group 1 test results.
[1]Epoxy grout and NSM strip applied overhead.
[2]Calculated in accordance with ACI 318-19 (ACI Committee 318, 2019).
[3]Calculated in accordance with ACI 440.2R-17 (ACI Committee 440, 2017).

anchorage details used for the strengthening of beams with particular cases of artificial deterioration simulated by cut or excluded reinforcing bars.

### *3.5.1 Group 1*

The test results for the Group 1 specimens are provided in Figure 3.31, and the corresponding response curves are provided in Figure 3.32. In Figure 3.31, the ratios $M_{test}/M_C$ and $M_{test}/M_D$ are listed, where $M_C$ is the experimental flexural capacity of the control specimen (Specimen 1-C) and $M_D$ is the experimental flexural capacity of the artificially deteriorated specimen not strengthened with FRP (Specimen 1-D). It should be noted that the artificial deterioration of the Group 1 specimens was achieved by excluding one reinforcing bar on each side of the member.

As indicated in Figure 3.31, the nominal flexural strengths, $M_n$, for the four specimens strengthened with FRP were relatively similar (average $M_n$ = 51.64 kip-ft for $\psi_f$ = 1.0). The control specimen had a slightly less nominal flexural capacity of 46.11 kip-ft. Despite similar calculated strengths, the actual capacities of the strengthened beams varied. Specimen 1-EB.1 strengthened with an externally bonded sheet with anchors along its length only reached 92% of the strength of the control specimen and failed at a midspan deflection of only 25% of the deflection achieved by the control specimen. The specimen with NSM strips installed overhead (Specimen 1-NSM.1b) approached, but did not achieve, the strength of the control specimen ($M_{test}/M_C$ = 0.98). Specimen 1-EB.2 (externally bonded sheet anchored at its ends) and Specimen 1-NSM.1a (NSM strips installed on inverted beam) behaved similarly to each other and demonstrated the best performance out of the strengthened specimens of Group 1 with $M_{test}/M_C$ values of 1.20 and 1.18, respectively. Nevertheless, even these specimens only achieved a deflection equal to approximately half of the deflection of the control specimen.

The strengthening systems in Group 1 all succeeded in regaining post-cracking stiffness relative to the damaged specimen. The four strengthened specimens regained or nearly regained the full stiffness of the control specimen between first flexural cracking and yielding of the steel reinforcement. These results are consistent with expectations based on the analysis tool described in Section B.1 of Appendix B. After yielding of the steel reinforcement, all FRP-strengthened

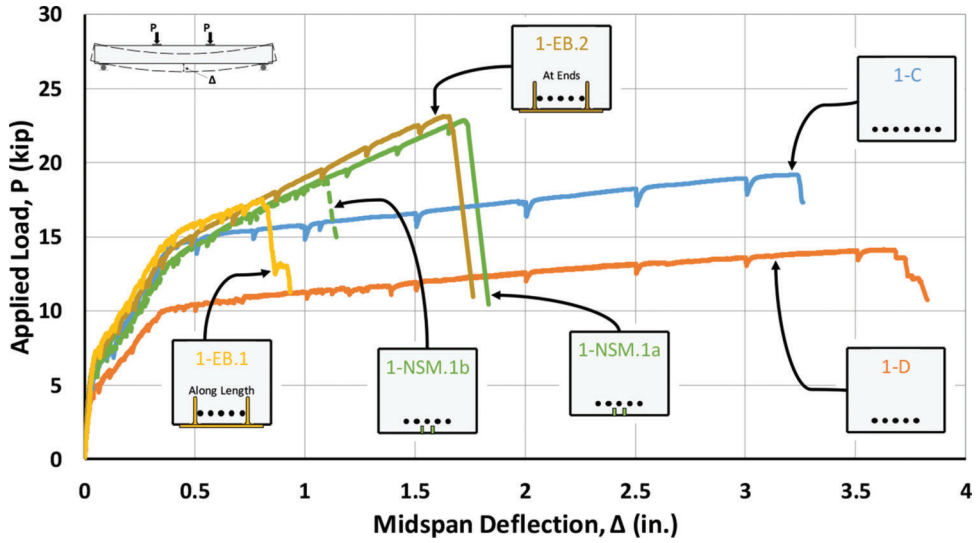


**Figure 3.32** Applied load vs. midspan deflection for Group 1 specimens.

| Specimen ID | $M_{test}$ (kip-ft) | $M_n$ (kip-ft) | | $M_{test}/M_n$ | | $M_{test}/M_c$ | $M_{test}/M_D$ | Steel Stress, $f_s$ (ksi) | Rupture Stress, $f_{f\_max}$ (ksi) | $f_{fu}$* (ksi) | Effective Stress, $f_{fe}$ (ksi) | $f_{f\_max}/f_{fu}$* | $f_{f\_max}/f_{fe}$ | Midspan Deflection at Max Load, Δ (in.) |
|---|---|---|---|---|---|---|---|---|---|---|---|---|---|---|
| | | $\psi_f = 0.85$ | $\psi_f = 1.0$ | $\psi_f = 0.85$ | $\psi_f = 1.0$ | | | | | | | | | |
| 2-C | 59.41 | 45.77[1] | | 1.30 | | 1.00 | 1.31 | - | - | - | - | - | - | 3.45 |
| 2-D | 45.40 | 33.67[1] | | 1.35 | | 0.76 | 1.00 | - | - | - | - | - | - | 1.63 |
| 2-EB.1 | 60.10 | 47.25[2] | 49.82[2] | 1.27 | 1.21 | 1.01 | 1.32 | - | - | 105 | 73.8 | - | - | 0.68 |
| 2-EB.2 | 72.79 | 47.29[2] | 49.87[2] | 1.54 | 1.46 | 1.23 | 1.60 | - | - | 105 | 73.8 | - | - | 1.25 |
| 2-NSM.1 | 82.87 | 50.16[2] | 53.28[2] | 1.65 | 1.56 | 1.39 | 1.83 | - | - | 325 | 228.1 | - | - | 1.82 |

**Figure 3.33** Group 2 test results.
[1]Calculated in accordance with ACI 318-19 (ACI Committee 318, 2019).
[2]Calculated in accordance with ACI 440.2R-17 (ACI Committee 440, 2017).

specimens had a significant increase in stiffness compared to the control specimen.

### *3.5.2 Group 2*

The test results for the Group 2 specimens are summarized in Figure 3.33. The response curves for all specimens in Group 2 are provided in Figure 3.34. The artificial deterioration of the Group 2 specimens was achieved by cutting one reinforcing bar on each side of the member at midspan.

Relative to the corresponding control specimen, the load-deflection plots of the strengthened specimens in Group 2 demonstrate similar behaviors, in terms of strength and maximum deflection, as the strengthened specimens in Group 1 (see Figure 3.32). The primary difference is the discrepancy between the load capacities and maximum midspan deflections of Specimens 2-NSM.1 and 2-EB.2. Although expected to have similar capacities as demonstrated by Specimens 1-NSM.1a and 1-EB.2, Specimen 2-EB.2 seems to have experienced a premature failure. Possible causes of the early failure are sensitivity to small variations in the application of the FRP system and local effects due to concentrated strains at the location of the cut reinforcing bars.

As indicated in Figure 3.33, the three FRP-strengthened specimens in Group 2 all exceeded the strength of the control specimen (Specimen 2-C). However, Specimen 2-EB.1 barely exceeded the strength of Specimen 2-C ($M_{test}/M_C = 1.01$). Similar to Specimen 1-NSM.1a from Group 1, Specimen 2-NSM.1 only reached a deflection equal to approximately half the deflection of the control beam.

As shown in Figure 3.34, the three strengthened specimens adequately regained the stiffness of Specimen 2-C between first flexural cracking and yielding of the steel reinforcement. Furthermore, as expected, the strengthened specimens exhibited a significant increase in stiffness compared to the control specimen after yielding of the steel reinforcement.

### *3.5.3 Group 3*

The test results for the Group 3 specimens are provided in Figure 3.35, and the corresponding response curves are plotted in Figure 3.36. The artificial deterioration of the Group 3 specimens was achieved by excluding two reinforcing bars on one side of the member. The eccentricity of the longitudinal reinforcing bars allowed for three different locations for the NSM strips to be tested. The results of the corresponding specimens

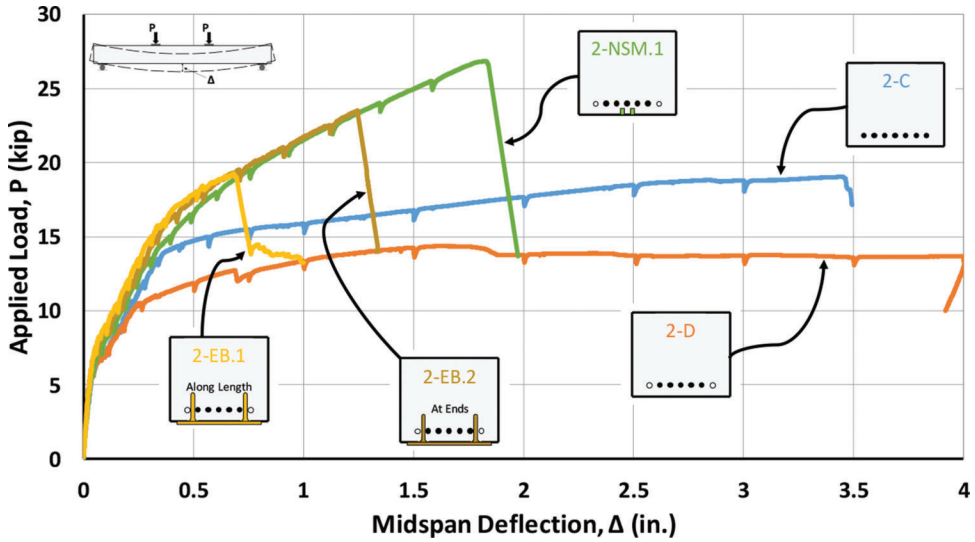


**Figure 3.34** Applied load vs. midspan deflection for Group 2 specimens.

| Specimen ID | $M_{test}$ (kip-ft) | $M_n$ (kip-ft) | | $M_{test}/M_n$ | | $M_{test}/M_c$ | $M_{test}/M_D$ | Steel Stress, $f_s$ (ksi) | Rupture Stress, $f_{f\_max}$ (ksi) | $f_{fu}$* (ksi) | Effective Stress, $f_{fe}$ (ksi) | $f_{f\_max}/f_{fu}$* | $f_{f\_max}/f_{fe}$ | Midspan Deflection at Max Load, Δ (in.) |
|---|---|---|---|---|---|---|---|---|---|---|---|---|---|---|
| | | $\psi_f = 0.85$ | $\psi_f = 1.0$ | $\psi_f = 0.85$ | $\psi_f = 1.0$ | | | | | | | | | |
| 3-C | 56.83 | 45.90[1] | | 1.24 | | 1.00 | 1.28 | 84.07 | - | - | - | - | - | 2.88 |
| 3-D | 44.47 | 33.92[1] | | 1.31 | | 0.78 | 1.00 | 88.67 | - | - | - | - | - | 3.63 |
| 3-EB.1 | 58.36 | 47.42[2] | 50.00[2] | 1.23 | 1.17 | 1.03 | 1.31 | 71.97 | 100.00 | 105 | 73.8 | 0.95 | 1.36 | 0.96 |
| 3-EB.2 | 71.62 | 47.40[2] | 49.98[2] | 1.51 | 1.43 | 1.26 | 1.61 | 77.07 | 147.27 | 105 | 73.8 | 1.40 | 2.00 | 1.69 |
| 3-NSM.1 | 68.56 | 50.29[2] | 53.41[2] | 1.36 | 1.28 | 1.21 | 1.54 | 76.87 | 343.02 | 325 | 228.1 | 1.06 | 1.50 | 1.62 |
| 3-NSM.2 | 69.25 | 50.23[2] | 53.35[2] | 1.38 | 1.30 | 1.22 | 1.56 | 77.17 | 350.03 | 325 | 228.1 | 1.08 | 1.53 | 1.56 |
| 3-NSM.3 | 65.50 | 50.25[2] | 53.36[2] | 1.30 | 1.23 | 1.15 | 1.47 | 75.67 | 315.71 | 325 | 228.1 | 0.97 | 1.38 | 1.43 |

**Figure 3.35** Group 3 test results.
[1]Calculated in accordance with ACI 318-19 (ACI Committee 318, 2019).
[2]Calculated in accordance with ACI 440.2R-17 (ACI Committee 440, 2017).

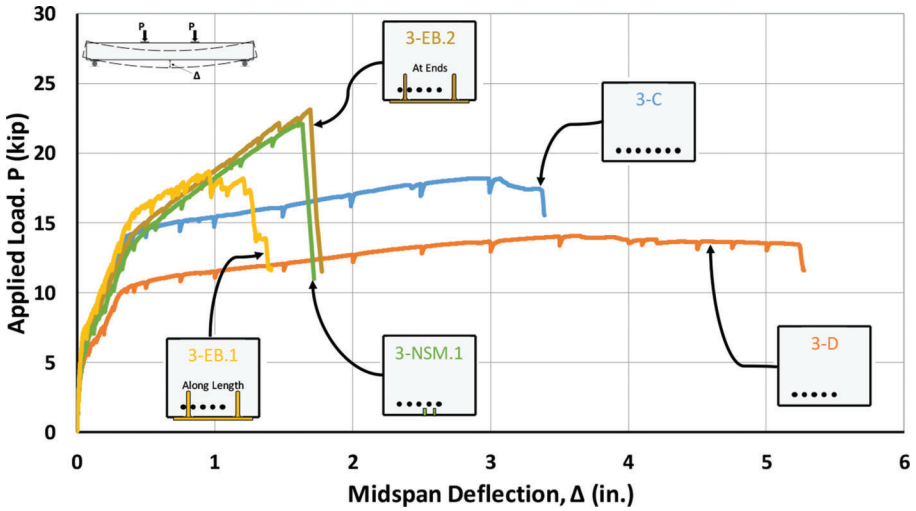


**Figure 3.36** Applied load vs. midspan deflection for Group 3 specimens.

are described in Section 3.4.5. To avoid clutter, the only NSM specimen plotted in Figure 3.36 is Specimen 3-NSM.1. The responses of all three NSM specimens in Group 3 are provided in Figure 3.28.

Again, relative to the corresponding control specimen, the behavior of the strengthened specimens shown in Figure 3.36, in terms of strength and maximum deflection, are similar to the results of the strengthened

specimens in Group 1 (see Figure 3.32). Furthermore, the FRP-strengthened specimens regained or nearly regained the stiffness of the control specimens after cracking and prior to yielding of the steel reinforcement.

All FRP-strengthened specimens in Group 3 surpassed the strength of the experimental control specimen (Specimen 3-C). However, the specimen with an externally bonded sheet with spike anchors along its length again presented a premature failure compared to the other strengthened specimens and only achieved a $M_{test}/M_C$ value of 1.03.

As previously described, displacements at midspan and under the load points were measured on both sides of the Group 3 specimens to capture any differential displacements (i.e., rotation) caused by the eccentricity of the reinforcement. As discussed in Section 3.4.5, the differential displacements measured during the tests were insignificant for the NSM specimens in Group 3. Similarly, the differential displacements at the maximum applied load for the other specimens with eccentric steel reinforcing bars in Group 3 (Specimens 3-D, 3-EB.1, and 3-EB.2) were small (between 0.002 in. and 0.053 in.). The deflections measured at each bottom edge of the Group 3 specimens at midspan are included in Section B.2 of Appendix B.

### 3.6 Summary

The results and observations from 22 beam tests were described in this chapter. In order to best analyze the results and draw substantive conclusions, the tests were compared both by specimen type (Control–C, Artificial Deterioration–D, Externally Bonded–EB, and Near-Surface-Mounted–NSM) and by group (Groups 1–3). The specimens in each group (except the pilot group) were detailed with the same initial simulated field condition.

Both the externally bonded system and the near-surface-mounted system were designed to result in similar calculated nominal flexural strengths as the control specimen in each group. Because control (C) and artificially deteriorated (D) specimens were included, the effectiveness of the FRP strengthening systems were easily evaluated. In general, both FRP strengthening systems were successful in achieving or surpassing the strength of the control specimens. The FRP systems also allowed the strengthened specimens to achieve a flexural stiffness between concrete cracking and yielding of the steel reinforcement that was similar to that of the control specimens. However, the FRP strengthening systems caused a substantial reduction in ductility, which is consistent with the nature of the abrupt failures of FRP materials.

The experimental moment capacities of the specimens with externally bonded sheets anchored at the ends of the member (EB.2 specimens) surpassed the moment capacities of specimens with externally bonded sheets anchored along the length of the member (EB.1 specimens). As noted in Section 3.4.4.3, stress concentrations in the longitudinal FRP sheets near the FRP anchor points likely caused the sheets to be vulnerable to rupture at these locations, leading to premature failure of the EB.1 specimens due to rupture of the sheet near midspan. Although two of the EB.2 specimens (Specimens 0-EB.2 and 1-EB.2) experienced rupture of the FRP sheet near an anchor point, the effect of the stress concentration at the anchors did not seem to significantly affect the strength of the member, likely because the anchor points were located in a region of the beam span experiencing little moment. For the specimens in the experimental program, consistent results led to the conclusion that FRP spike anchors near the end of the FRP sheet provided sufficient anchorage and that installing additional spike anchors along the length of the beam can have a negative impact on the capacity of the member.

The eccentricity of the steel reinforcement in the specimens and the relative placement of NSM strips to the steel reinforcing bars did not result in any clear effect on the behavior of the members. For one specimen, the NSM strips were installed overhead using a different epoxy than the other NSM specimens. This beam experienced a premature failure compared to other test specimens. Further study of various epoxies and installation conditions are needed to better understand their effects.

The analysis tool (see Section B.1 of Appendix B) that was developed for the experimental program proved to be helpful in understanding the behavior of the FRP strengthening systems. The tool demonstrated that a relatively simple analysis procedure can be used to provide reasonable estimates for the load-deflection behavior of FRP-strengthened beams tested in flexure. However, an accurate estimation of the FRP composite failure strain is needed to determine when failure will likely occur along the load-deflection curve.

Overall, from the consideration of the results of the experimental program, both externally bonded and NSM FRP strengthening systems are shown to be viable methods for strengthening flexural members if properly designed and installed.

## 4. DETAILS OF END REGION REPAIR EXPERIMENTAL PROGRAM

### 4.1 Introduction

An experimental program was developed to evaluate the effectiveness of potential techniques for the repair of deteriorated end regions of prestressed concrete bridge girders. More specifically, three repair techniques were studied: externally bonded FRP, NSM FRP, and a concrete supplemental diaphragm. To this end, five decommissioned prestressed concrete bridge girders acquired from the field were tested. Three of the girders were tested after being repaired using the aforementioned repair techniques. This chapter focuses on important background details of the test specimens and details of the repairs evaluated during the test program. Other information related to the test program is included in Appendix E, including concrete and mortar material properties and detailed repair procedures. Each girder was loaded in shear with a short shear span-to-depth

ratio. The girders were supported on elastomeric bearing pads and a point load was applied 45 in. from the support located at the damaged end region. Further details of the test setup are also included in Appendix E. Furthermore, past studies focused on the repair of end regions that influenced many of the details chosen for the current study are summarized in Appendix D.

### 4.2 Specimen Background and Details

Five AASHTO Type I prestressed concrete bridge girders were salvaged from a bridge located on Interstate 469 (I-469) in Allen County near Fort Wayne, Indiana (INDOT Asset Name I469-01-07020, NBI Number 032823). The bridge was constructed in 1988 and received only minimal substructure maintenance until the girders were transported to Bowen Laboratory at Purdue University during the summer of 2018 for the experimental program. However, as shown in Figure 4.1, many of the bridge girders showed signs of significant end region deterioration. Due to the condition of these girders, the bridge superstructure was replaced in 2018. A simple plan view of the original superstructure is shown in Figure 4.2. The girders transported to the laboratory for testing are indicated in the figure.

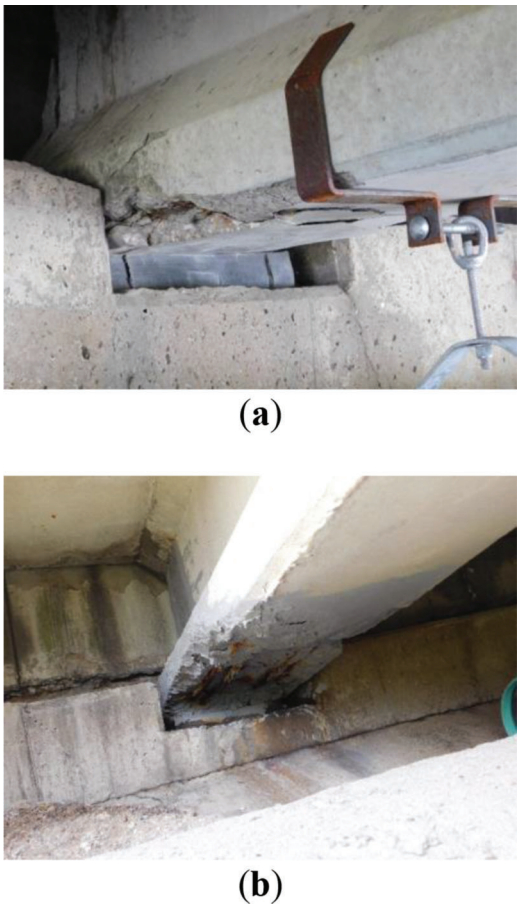


**Figure 4.1** Typical in-service condition of girder end regions prior to removal.

Each of the five test specimens were 38.5-ft long. The cross-sectional dimensions of the girders were in accordance with the standard AASHTO Type I beam, as shown in Figure 4.3 and Figure 4.4. The reinforced concrete composite deck on top of the girders was 8 in. thick as indicated in Figure 4.4. A thin epoxy overlay had been applied to the top surface. As specified in the bridge plans (INDOT, 1987), the girders were prestressed with eight 0.5-in. diameter seven-wire prestressing strands with an ultimate tensile strength, $f_{pu}$, of 270 ksi. As shown in Figure 4.5, four of the eight prestressing strands were straight and were located 2 in. from the bottom surface of the beam. The remaining four strands were harped with harping points located at 1/3 of the girder length from each end. All prestressing strands were initially stressed to 189 ksi, or $0.7f_{pu}$, according to the bridge plans (INDOT, 1987). The stirrups were fabricated from deformed reinforcing bars. The stirrup spacing is shown in Figure 4.5. According to the bridge plans (INDOT, 1987), the specified 28-day concrete compressive strength, $f'_c$, was 5,000 psi. However, after 30 years of service, the actual concrete strength was unknown. As such, 3-in. by 6-in. concrete cores were taken from the webs of the test specimens following testing. The average compressive strength of the cores obtained from each girder is provided in Table 4.1.

When extracting the girders from the bridge, longitudinal cuts were made approximately 2 in. from the edge of the top flange as indicated Figure 4.4. The portion of the deck that remained on the girder was kept in place through the completion of the experimental program. A transverse edge beam was cast along the ends of the girders that were detailed with the 6-in. notch noted in Figure 4.5. A portion of this edge beam remained on all of the test girders except for Girder 17-C as discussed in Section 5.2.4. As observed in Figure 4.1(b), a patch material was applied to the deteriorated end of Girder 20-A while in service. This measure is assumed to have been performed in an effort to mitigate corrosion. Additionally, one side of Girders 20-A and 20-C had been painted. Any paint or patch material remaining on the girders after being transported to the laboratory was removed prior to repairing the specimen.

### 4.3 Repair Details and Rationale

The test matrix for the five girder specimens is shown in Table 4.2. One of the five test girders (Girder 3-C) had an end region in good condition and was used as a control specimen. The other four girders exhibited severe end region deterioration. Girder 20-C received minimal repairs prior to testing as described in Section E.2.2 of Appendix E and was tested to evaluate the performance of a deteriorated girder in its field condition. This girder is referred to herein as the damaged specimen. The remaining three test specimens were repaired using the three techniques indicated in Table 4.2. Repair details are described in Sections 4.3.2 through 4.3.4. Rationale for the selection of each repair technique is provided along with justification for the

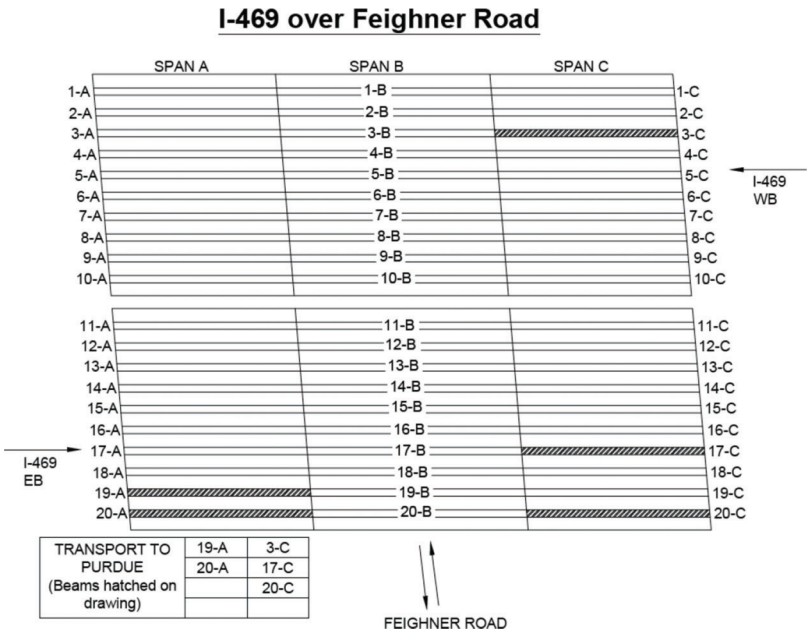


**Figure 4.2** Girders of I-469 bridge selected for experimental program.

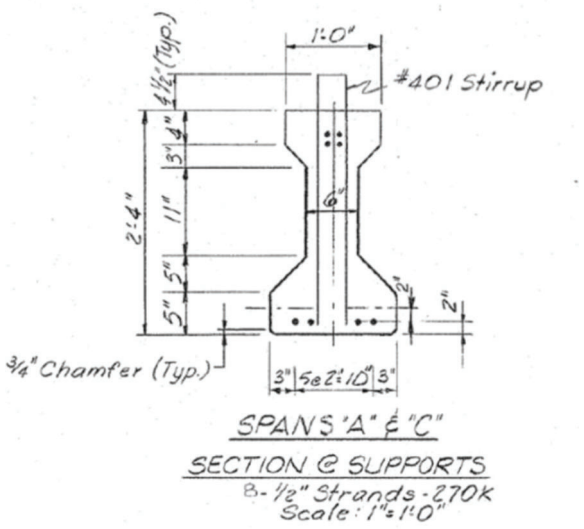


**Figure 4.3** Cross section of test specimens at the original supports (INDOT, 1987).

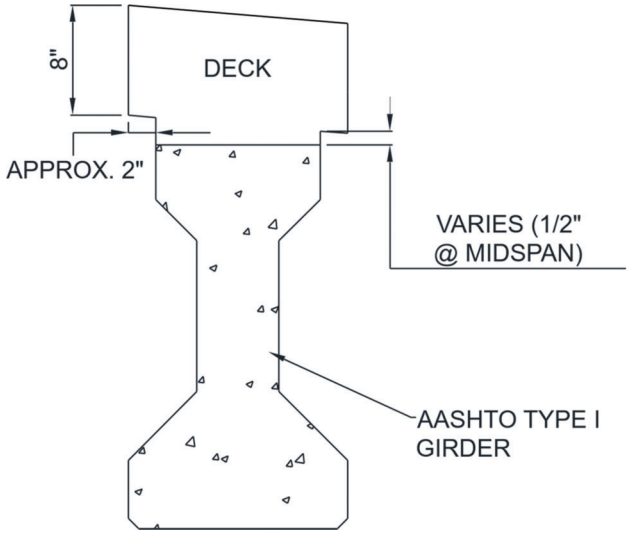


**Figure 4.4** Cross section of test specimens (adapted from INDOT, 1987).

repair details. First, however, the behavior of the control girder and the girder tested in its deteriorated condition is briefly discussed as the rationale for the repairs is related to the test results of these two specimens. Complete details of the test results for all specimens are provided in Section 5.2.

### *4.3.1 Failure Behavior of Control and Damaged Specimens*

Testing of the control and damaged specimens provided insight into the change in behavior caused by the deterioration of girder end regions. As previously described, for each test of the experimental program, load was applied to the girder at a distance of 45 in. from the support located at the end of the girder (further details of the test setup are provided in Section E.3 of Appendix E). For a girder in good condition, the loading was expected to cause the development of a diagonal strut between the applied load and the support. As shown in Figure 4.6, a diagonal strut did develop within the test region of the control specimen. The damaged specimen, however, exhibited a different behavior. The failure behavior of this specimen was controlled by the inability of the prestressing strands to develop tensile forces along the bottom flange. The primary failure crack of the damaged specimen, shown in Figure 4.7, was nearly vertical. A diagonal strut did

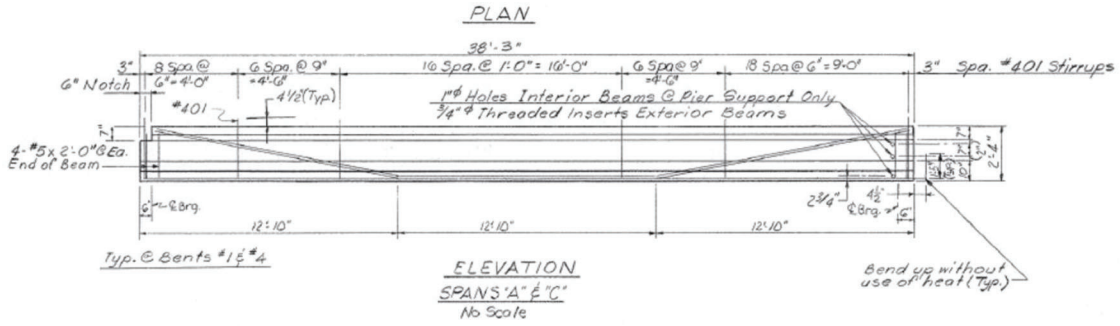


**Figure 4.5** Elevation of test specimens (INDOT, 1987).

TABLE 4.1
**Average Concrete Compressive Strength Obtained from Concrete Cores**

| Girder | Average Compressive Strength (psi) |
|---|---|
| 3-C | 7,270 |
| 20-C | 9,240 |
| 19-A | 7,440 |
| 17-C | 9,070 |
| 20-A | 7,850 |

TABLE 4.2
**Text Matrix**

| Girder | End Region Condition | Repair Technique |
|---|---|---|
| 3-C | Good | Control |
| 20-C | Deteriorated | Tested in Deteriorated Condition |
| 19-A | Deteriorated | Externally Bonded FRP |
| 17-C | Deteriorated | NSM FRP |
| 20-A | Deteriorated | Supplemental Diaphragm |

not form within the test region due to the inability of the corroded prestressing strands to develop adequate tensile capacity in the bottom flange at the end of the member. The behaviors of the control and damaged specimens led to the observation that restoring the tensile capacity along the bottom flange is key to a successful repair. This observation influenced the details of the repair techniques included in the experimental program.

### *4.3.2 Externally Bonded FRP Repair System*

For the externally bonded FRP repair of the experimental program, carbon fiber sheets were used. Carbon reinforcing fibers were selected because they offer a greater ultimate tensile strength and elastic modulus than either glass or aramid fibers (ACI Committee 440, 2017). As a result, carbon fibers are often chosen for strengthening applications (Pevey et al., 2021). Furthermore, carbon fiber spike anchors were used to ensure that the FRP sheets were properly anchored to the concrete. For the FRP sheets, a wet-layup installation method was used. After considering

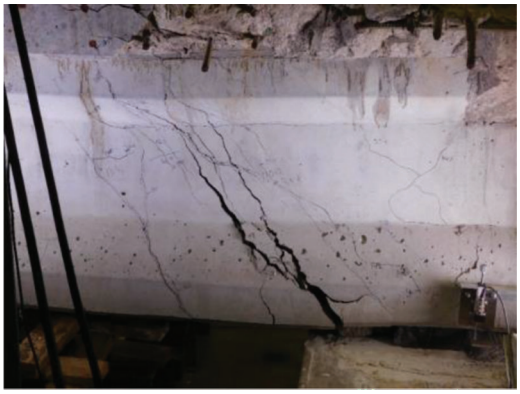

**Figure 4.6** Control specimen after failure.

**Figure 4.7** Damaged specimen after failure.

both pre-saturated sheets and dry sheets that are saturated by the installer, the latter option was chosen due to concerns about the interaction between pre-saturated FRP sheets and FRP spike anchors saturated in the field. Based upon the above decisions, an FRP sheet product (SikaWrap Hex-103C (Sika Corporation, 2019)) was selected, which requires saturation by the installer using the wet-layup procedure. The resin specified by the manufacturer for saturating sheets of this type is an epoxy resin (Sikadur Hex-300). To improve the tack of the concrete surface during vertical and overhead applications, the manufacturer suggested using a different epoxy resin (Sikadur-330 (Sika Corporation, 2018b)) to prime and seal the concrete.

TABLE 4.3
**Externally Bonded FRP Repair System Components and Design Values**

| Repair System | Constituent Materials | Nominal Ply Thickness/Cross-Sectional Area | $f_{fu}$* (ksi) | $\varepsilon_{fu}$* | $E_f$ (ksi) |
|---|---|---|---|---|---|
| Externally Bonded FRP Sheet | FRP Fabric[1] + Epoxy[2] | 0.04 in. | 160.9 | 0.0145 | 10,390 |
| FRP Anchor | FRP Rope[3] + Epoxy[2] | 0.1 in.[3] | 304 | 0.016[4] | 33,300 |

[1]SikaWrap Hex-103 C (Sika Corporation, 2019).
[2]Sikadur Hex-300 Impregnating Resin (Sika Corporation, 2018a).
[3]SikaWrap FX-50 C Unidirectional Carbon Fiber Rope (Sika Corporation, 2015).
[4]Based on dry fibers.

The FRP spike anchors used for the end region repair were cut from a premanufactured FRP rope (Sika Wrap FX-50 C Unidirectional Carbon Fiber Rope (Sika Corporation, 2015)). The applicable design properties of the externally bonded FRP sheets and rope as reported by the manufacturer are provided in Table 4.3. The properties reported in the table are for the cured laminate with the exception of the ultimate strain of the FRP rope, which represents the property for "elongation at break" of the dry fibers as reported by the manufacturer (Sika Corporation, 2015).

The details of the externally bonded FRP system for the end region repair are shown in Figure 4.8. The repair system is composed of three layers of FRP. The first layer consists of FRP sheets that were cut into strips and applied with the fibers running longitudinally (Figure 4.8(a)). The ends of the strips are anchored with spike anchors as shown. The second layer consists of FRP sheets with fibers oriented vertically on the side surfaces of the girder (Figure 4.8(b)). Spike anchors are also used to anchor these sheets. Two of these sheets are U-wraps as indicated. The third layer of FRP consists of externally bonded FRP patch sheets (Figure 4.8(c)). Detailed drawings of the externally bonded system with complete dimensions are provided in Appendix F.

Because of the importance of restoring the tensile capacity of the girder along the bottom flange as explained in Section 4.3.1, the longitudinal FRP strips were installed as the first layer of FRP with the second layer aiding in the anchorage of these strips. As shown in Figure 4.8(a), one longitudinal strip was applied directly to the web of the specimen. Longitudinal strips were also applied directly to both the vertical and sloped surfaces of the bottom flange of the girder. The primary purpose of the longitudinal strips applied to the bottom flange was to regain the tensile capacity lost due to the deteriorated condition of the member. In contrast, the primary purpose of the longitudinal FRP strips in the studies examined in Sections D.1.2 and D.1.3 of Appendix D (Andrawes et al., 2018; Petty et al., 2011) was to provide anchorage to vertically-oriented FRP sheets. The longitudinal strip applied to the vertical surface of the bottom flange and the strip applied to the girder web each consisted of one continuous strip, wrapping around the end of the girder, providing improved anchorage for the longitudinal strip. These strips also provided additional confinement to the mortar used to repair the end region (see Section E.2.3 of Appendix E). The longitudinal strips applied to the sloped surface of the bottom flange were two discrete strips on either side of the girder. Due to the surface being sloped, wrapping the strip around the end of the test specimen was not possible. The longitudinal FRP strips were extended 17.5 in. past the termination of the vertically-oriented FRP sheets. The longitudinal strips applied to the vertical surface of the bottom flange and the strip applied to the girder web were anchored at the ends using FRP spike anchors, as discussed later in this section. The longitudinal strip installed along the sloped surface of the bottom flange was not anchored, as there would be a high risk of hitting prestressing stands when drilling the anchor hole perpendicular to the surface.

The second FRP layer of the repair system consists of sheets with fibers oriented vertically on the side surfaces of the girder (Figure 4.8(b)). The sheet closest to the end of the girder is a face-bonded sheet (i.e., not a U-wrap) to simulate limitations during in-field installations near the support bearing. The second and third FRP vertically-oriented sheets from the end of the member were installed in a U-wrap configuration, as access to the bottom surface of the girder would not be limited in the field. Per the recommendations of the manufacturer, a space was left between all the externally bonded FRP sheets. A space of at least 1 in. was selected based on the research conducted by Andrawes et al. (2018). The vertically-oriented U-wrap sheets were 10 in. wide. This sheet width was selected based on practical limits. While narrower sheets result in a more uniform strain profile over the width of the sheet (Pudleiner, 2016), they require more sheets to be installed along the repair area, thus increasing the labor required for installation. However, increasing the sheet width over 10 in. can make handling the sheet during installation difficult. Because the layout of the internal steel at the end of the girder dictated the locations of the spike anchors, the width of the face-bonded sheet was reduced to 5 in. and the space between the face-bonded sheet and the first U-wrap was increased to 2.25 in. This FRP layout allowed the spike anchors to be located concentrically on the vertical FRP sheets.

A total of 19 FRP spike anchors were used on each side of the girder to anchor the externally bonded strips/sheets as shown in Figure 4.8(b). Two of these anchors

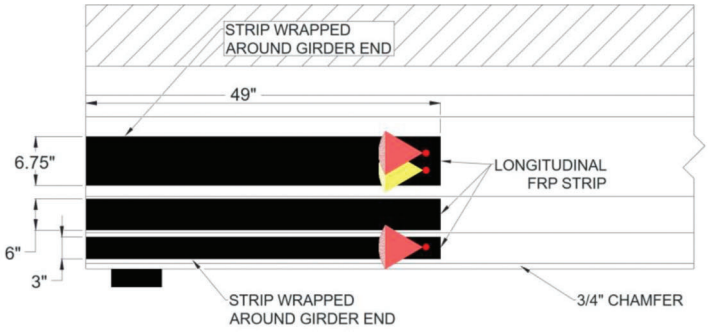


**(a) Layer 1 Detail**

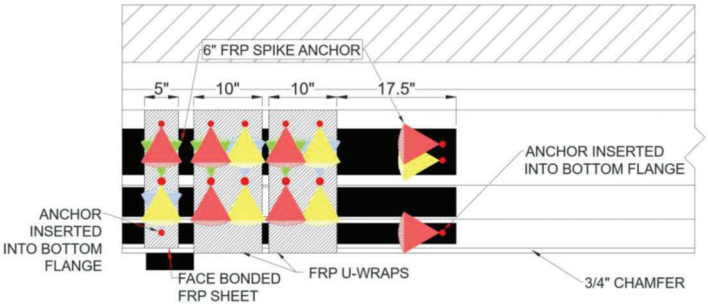


**(b) Layer 2 Detail**

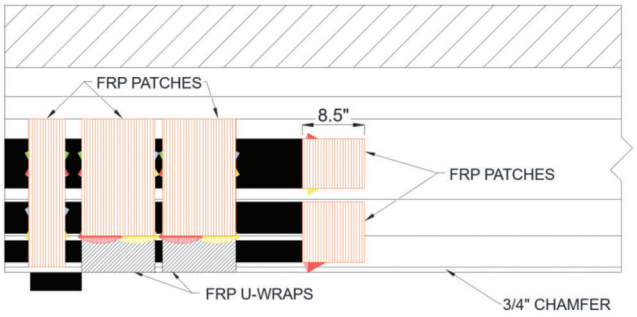


**(c) Layer 3 Detail**


**(d) Location of Anchor Holes within Cross Section of Bottom Flange**

**Figure 4.8** Externally bonded FRP details.

were inserted into 0.875-in. diameter holes drilled horizontally into the bottom flange of the girder. The nominal area of these anchors, in the form of a cured laminate, was approximately 0.31 $in^2$. This area was achieved by combining and folding in half (see Section E.2.3 of Appendix E) 1.6 20-in. long segments of the SikaWrap FRP rope specified in Table 4.3. However, as presented in Appendix G, the amount of material used for each anchor was determined by weight, not by area. The location of the holes relative to the strands in the bottom flange is shown in Figure 4.8(d). The hole was placed such that it would be positioned between the first and second row of strands in the scenario that a girder being repaired in the field contains more than one row of stands on a 2-in. grid pattern. The depth of these holes was 4 in. Deeper holes are recommended

by Orton (2007) and Pudleiner (2016). However, to minimize the risk associated with drilling holes in the bottom flange and considering the successful use of anchors in 4-in. deep holes in the flexural strengthening experimental program, a depth of 4 in. was determined to be sufficient.

Due to the 6-in. web width of the test specimens, it was not feasible to drill separate anchor holes for the anchors installed on each side of the girder. Therefore, a modified spike anchorage system different from what is typically implemented in the field was developed by drilling through the entirety of the web. Continuous anchors cut from the FRP rope were then installed in the holes and used to anchor the FRP on both sides of the girder. The installation process for these anchors is described in Section E.2.3 of Appendix E. A similar type of anchorage system was employed in a study conducted by El-Saikaly et al. (2015). In this study, the authors used CFRP rope to anchor CFRP L-strip plates onto reinforced concrete T-beams as shown in Figure 4.9. The CFRP rope anchorage system significantly increased the ultimate shear capacity of the strengthened specimens and prevented the debonding failure mode (El-Saikaly et al., 2015). For the girder specimens of the end region experimental program, the holes near the bottom of the web had diameters of 1.125 in. to accommodate two anchors, and the remaining holes in the web had diameters of 0.875 in. for a single anchor. The nominal area of the anchors, in the form of a cured laminate, that were inserted through both the 1.125-in. and 0.875-in. diameter holes was approximately 0.31 $in^2$. This area was achieved by combining 3.1 18-in. long segments of the SikaWrap FRP rope specified in Table 4.3. A fan angle of 60° was selected for all spike anchors based on research conducted by Kim (2011) and Pudleiner (2016) as well as its successful use in the flexural strengthening experimental program. For the current experimental program, the remaining spike anchorage detailing, including number of anchors per sheet, required anchorage area, and anchor hole diameter, followed the recommendations and calculations outlined in Pudleiner (2016). See Appendix G for complete spike anchorage detailing calculations.

The third FRP layer of the repair system consists of externally bonded FRP patch sheets applied over the FRP spike anchors as shown in Figure 4.8(c). Research conducted by Kim et al. (2012) was used as guidance for the design of the patch system. Two layers of externally bonded FRP sheets were placed over the anchors. The fibers of the first layer of the patch sheets were orientated perpendicular to the fibers of the externally bonded sheet/strip of interest, while the fibers of the second layer of patch sheets were orientated parallel to the fibers of the externally bonded sheet/strip. Limited guidelines exist for FRP patch sheet geometry, especially for members with complex geometries such as I-shaped beams. Therefore, the patch sheet geometries used in this study were based on a combination of successful geometries from previous FRP research (Kim et al., 2012; Pudleiner, 2016) and engineering judgement. Typically, the patch sheets are taken as the same width as the corresponding externally bonded FRP sheet/strip. The patch sheet widths for the vertically-oriented face-bonded sheets above the bearing support, the U-wrap sheets, and the longitudinal strip along the web of the girder were therefore selected to match the width of each respective sheet or strip. The patch width for the longitudinal strips along the bottom flange of the girder was increased due to the smaller widths of these strips. More specifically, the patch width was increased to cover the entire width of both the longitudinal strip along the vertical surface of the bottom flange and the strip along the sloped surface of the flange.

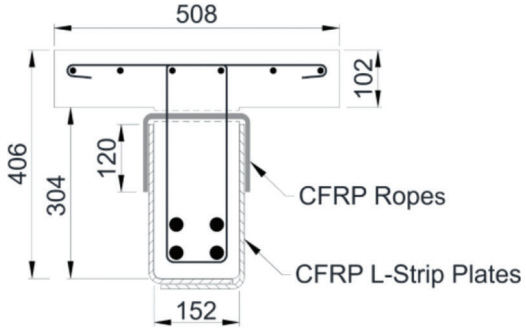


**Figure 4.9** CFRP L-strip plates anchored with CFRP ropes (adapted from El-Saikaly et al., 2015).

The lengths of the patch sheets satisfied the recommendation proposed by Pudleiner (2016) that the patch sheets should extend a minimum of 2 in. beyond the anchorage locations (i.e., beyond the hole into which the anchors are inserted). As such, the patch sheets for the vertically-oriented face-bonded sheets extend over the entirety of the sheets. To meet the recommendation by Pudleiner (2016), the length of the patch sheets corresponding to the U-wraps should extend from the top of the U-wrap sheets to 2 in. beyond the location of the bottom anchor holes. However, because this would result in the patches terminating near a reentrant corner, the patches extend to the end of the sloped surface of the bottom flange as shown in Figure 4.8(c). Finally, the length of the patch sheets at the termination of the longitudinal strips were selected to match the distance from the end of the longitudinal strips to the termination of the splayed fan anchors. The patch sheets are therefore 8.5 in. long.

### *4.3.3 NSM FRP Repair System*

To serve as an alternative FRP repair technique, an FRP NSM repair system was developed. Carbon fiber NSM strips (Owens Corning Aslan 500 #2 Carbon Fiber Reinforced Polymer Tape (Owens Corning, 2017)) were selected because of their availability and overall performance in the flexural strengthening experimental program discussed in Chapters 2 and 3. The results from the flexural strengthening program demonstrated that NSM strips can be an effective repair technique for flexural strengthening of damaged reinforced concrete

TABLE 4.4
**NSM FRP Repair System Components and Design Values**

| Repair System | Constituent Materials | $A_f$ (in.$^2$) | $f_{fu}$* (ksi) | $\varepsilon_{fu}$* | $E_f$ (ksi) |
|---|---|---|---|---|---|
| Near-Surface-Mounted (NSM) Strips | FRP Tape[1] + Epoxy Grout[2] | 0.049 | 325 | 0.0181 | 18,000 |

[1]Owens Corning Aslan 500 #2 Carbon Fiber Reinforced Polymer Tape (Owens Corning, 2017).
[2]Pilgrim Permocoat Magmaflow Grout-Pak CF Epoxy Grout (Pilgrim, n.d.).

beams. Therefore, the same NSM strips were selected to restore the tensile capacity lost in the bottom flange of the deteriorated end region due to ineffective prestressing strands. Furthermore, NSM FRP strips are relatively easy to install compared to externally bonded FRP, decreasing the amount of labor required in the field while also eliminating potential sources of error such as uneven saturation of FRP sheets and air voids trapped beneath the sheets. Pertinent mechanical design values of the NSM strips as reported by the manufacturer are shown in Table 4.4. These values apply to the dry FRP strips alone. The nominal cross-sectional dimensions of the strips are 0.079-in. by 0.63-in.

The details of the NSM FRP repair system used for the experimental program are shown in Figure 4.10. The system consisted of four NSM FRP strips on each side of the girder. Two strips were embedded in the vertical surface of the bottom flange and two strips were embedded in the sloped surface of the flange. Like the longitudinal FRP strips in the externally bonded FRP repair system, the NSM strips were installed to restore the tensile capacity lost due to the deterioration of the prestressing strands in the bottom flange of the girder. The groove depth selected (0.875 in.) allows for the system to be implemented on girders which have a clear cover of 1 in., typical of girders with confinement reinforcement enclosing the pretensioned strands in the bottom flange within the end region of the member. The selected clear spacing between the grooves was 1.25 in. It should be noted that this groove depth is less than the depth (1.5 times the greater dimension of the strip) suggested by ACI 440.2R-17. Furthermore, the manufacturer of the epoxy grout used with the NSM strips specifies a minimum grout depth of 1 in. (Pilgrim, n.d.). However, the strips used to repair the girder end region were also used in 0.875-in. deep grooves during the flexural strengthening test program. Additionally, due to the dimensions of the girder, adhering to the clear spacing (twice the groove depth) and clear edge distance (four times the groove depth) suggested by ACI 440.2R-17 was not practical. The groove width (0.25 in.) is greater than the minimum width (three times the smaller dimension of the strip) suggested by ACI 440.2R-17 (ACI Committee 440, 2017).

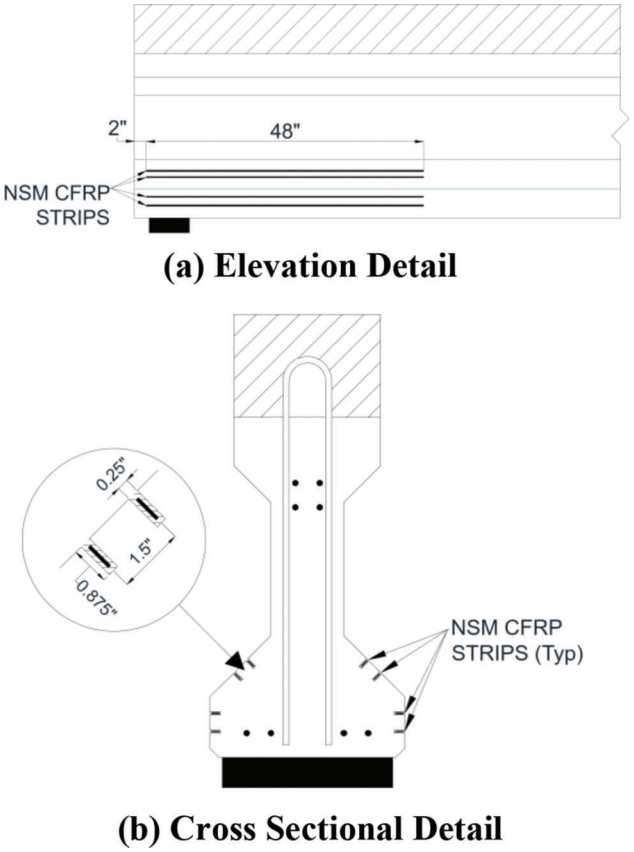


**Figure 4.10** NSM FRP details.

### *4.3.4 Supplemental Diaphragm Repair System*

The supplemental diaphragm repair technique provides INDOT with a repair method that incorporates materials that are more conventional than FRP. The supplemental diaphragm also provides a means to compare the constructability and effectiveness of utilizing traditional materials versus the use of FRP.

The details of the supplemental diaphragm repair system are shown in Figure 4.11. The reinforcement layout was adapted from the reinforcement details utilized in the Needham (2000) and Shield and Bergson (2018) studies presented in Section D.2 of Appendix D. The reinforcing details include two pairs of epoxy-coated No. 3 reinforcing bars (i.e., dowels) inserted through the web to transfer stresses from the original girder to the repair material. No. 3 reinforcing bars were used for this application, as opposed to No. 4 bars, to aid with the required field bend that is noted in Figure 4.11. The remainder of the reinforcing cage consisted of epoxy-coated No. 4 bars arranged in a manner somewhat similar to the details used in the previous studies described in Section D.2 of Appendix D. While designing the diaphragm, the possibility of casting a

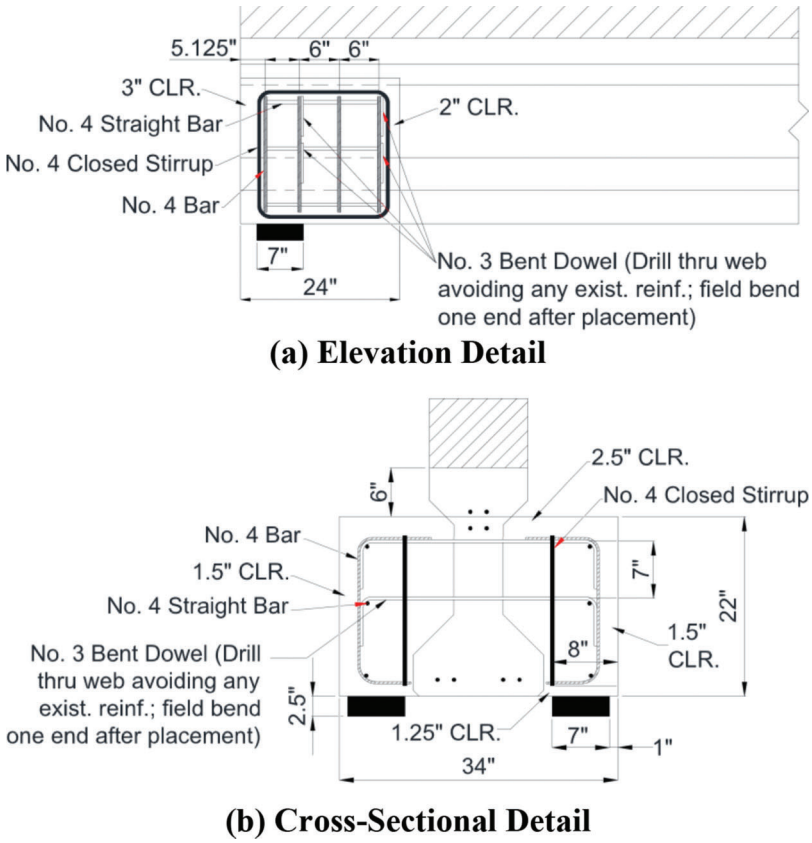


**Figure 4.11** Supplemental diaphragm details.

diaphragm continuously between adjacent girders in the field was kept in mind. Therefore, transverse reinforcement within the diaphragm in the form of closed stirrups was included. More specifically, as shown in Figure 4.11, one epoxy-coated No. 4 closed stirrup was included in the diaphragm on each side of the girder. Lastly, four U-shaped epoxy-coated No. 4 bars with unequal leg lengths (4.25 in. and 7.25 in.) were included in the diaphragm on each side of the girder. As shown in Figure 4.11(b), these bars were oriented in a manner such that the shorter leg was located at the bottom of the reinforcing cage while the longer leg was located at the top of the reinforcing cage. The repair region extended 24 in. along the length of the girder, which was the minimum length needed to repair the portion of the girder that experienced significant section loss. To account for the possibility of severe deterioration around the original bearing location along with potential concrete consolidation issues near the bottom of the original cross section when implementing the repair in the field, a bearing pad was not placed at the original bearing location during testing. Instead, two bearing pads with lengths equal to half the length of the original bearing pad (measured transverse to the longitudinal axis of the girder) were placed 1.0 in. from the edge of the repair area as shown in Figure 4.11(b). All reinforcement used for the repair was Grade 60 (ASTM A615 (ASTM, 2018)).

A self-consolidating concrete (SCC) mixture was used to increase the constructability of the repair. SCC is a flowable concrete that does not require vibration, making it an ideal choice for applications with limited access to the repair region or tightly congested regions. Moreover, SCC is pumpable, giving designers further flexibility when implementing such systems. As a result, a 6-in. clearance was left from the top of the diaphragm to the top surface of the precast girder, allowing for the SCC to be pumped into the forms from below the girder in the field. The mixture design for the SCC is show in Table 4.5. The specified 28-day compressive strength of the concrete was 6,000 psi.

### 4.4 Summary

This chapter detailed the experimental program focused on developing repair techniques for deteriorated end regions of prestressed concrete bridge girders. The details of three repair techniques (an externally bonded FRP system, an NSM FRP system, and a concrete supplemental diaphragm) were presented. Results from the load testing of the five experimental specimens are presented and discussed in Chapter 5.

TABLE 4.5
**SCC Mixture Design for Supplemental Diaphragm**

| Material | Details | Design Quantity | Units |
|---|---|---|---|
| Cementitious Material | Type 1 Cement | 580 | lb/yd$^3$ Concrete |
| | Class F Ash | 145 | |
| Coarse Aggregate | 3/8 in. Pea Gravel | 1,650 | |
| Fine Aggregate | Natural Sand | 1,379 | |
| Water | – | 279.5 | |
| Admixtures | High-Range Water Reducer | 10.00 | oz/cwt Cementitious Material |
| | Viscosity Modifier | 4.00 | |

Note:
Specified $f'_c$ = 6,000 psi.
Water/Cement Ratio = 0.39.
Design Spread = 25.00″ +/- 7.0″.

## 5. END REGION REPAIR EXPERIMENTAL PROGRAM RESULTS

### 5.1 Introduction

The results of the end region repair experimental program outlined in Chapter 4, consisting of tests on one relatively undeteriorated, one deteriorated, and three repaired AASHTO Type I girders loaded to failure, will be presented in this chapter. Additionally, the overall behavior of each of the five test specimens will be discussed. Then, the results and observations obtained from the tests on the three repaired specimens will be used to establish the effectiveness of each repair technique.

### 5.2 Experimental Results

The experimental results for the five girders tested are presented in the following subsections. For each specimen, a load-deflection curve is provided to better understand the specimen behaviors. Each curve is a plot of the shear force caused by the applied load within the 45-in. long test region (i.e., shear span) indicated in Figure 5.1 versus the deflection of the girder measured at the location of the load point (see Section E.3 of Appendix E). For consistency, the range of values along the y-axis for each load-deflection plot is 0 to 220 kips, and the range of values along the x-axis is 0- to 3-in. shear force due to self-weight is not reflected in the load-deflection response curves. The shear force due to self-weight at the middle of the shear span is estimated to be 6.5 kips. It should also be noted that the linear potentiometers positioned to measure the deflection at the support locations (i.e., bearing pads) of the specimens were used to determine the deflection at the load point due to deformation of the bearing pads. As an example, this deflection at the load point was 0.039 in. for the control specimen when the maximum load was applied. This small deflection due to deformation of the bearing pads is not considered in the load-deflection plots provided in the following sections.

#### *5.2.1 Control Specimen*

As explained in Chapter 4, one AASHTO Type I girder (3-C) with an end region in good condition acted as the control specimen, providing a baseline performance to which the repaired specimens were compared. The results of the test on the control specimen allowed for the effectiveness of each of the three repair techniques included in the experimental program to be established. The load-deflection response curve for the control specimen is shown in Figure 5.2. Initial cracking of the specimen was observed at a shear force, $V_{cr}$, of 98 kips (applied load of 110 kips). The first crack observed was a diagonal shear crack that appeared in the web of the specimen. This crack would eventually become one of the primary cracks that characterized the failure of the member. The specimen reached a maximum shear force, $V_{test}$, of 141 kips (applied load of 158 kips).

The condition of the girder prior to testing is displayed in Figure 5.3, and the condition of the girder after failure is shown in Figure 5.4. As discussed in Section 4.3.1, the failure of the control specimen was characterized by the formation of a diagonal strut

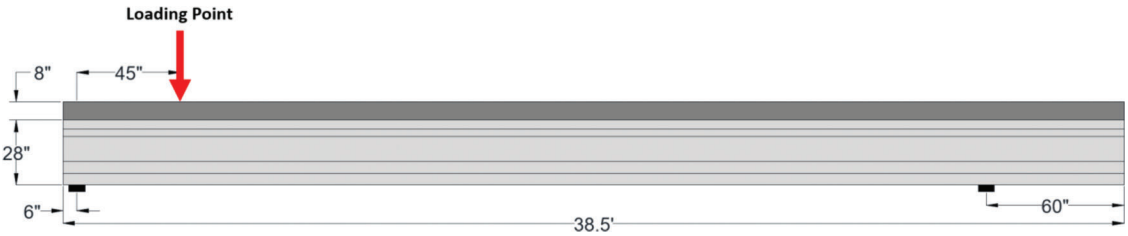


**Figure 5.1** Load configuration.

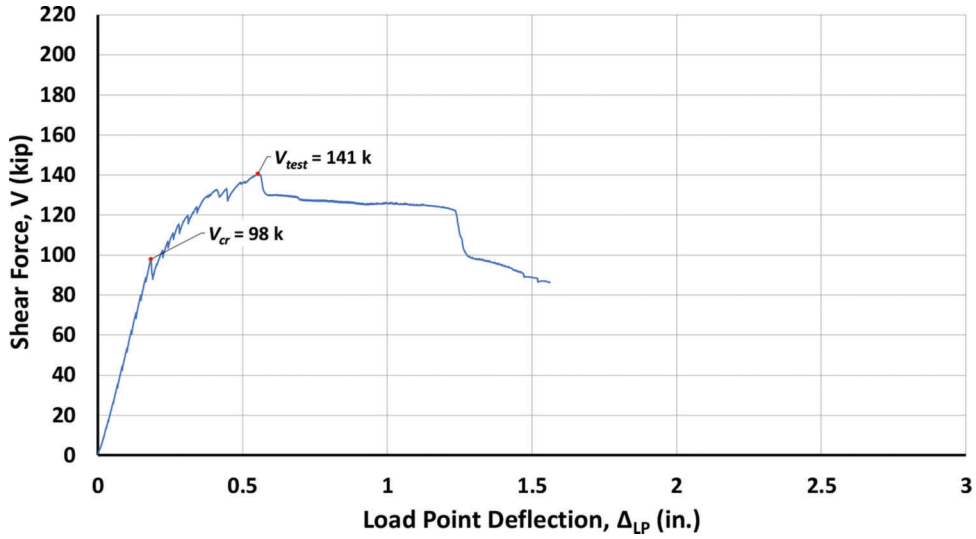


**Figure 5.2** Shear vs. deflection at load point for control specimen.

**Figure 5.3** Control specimen prior to testing.

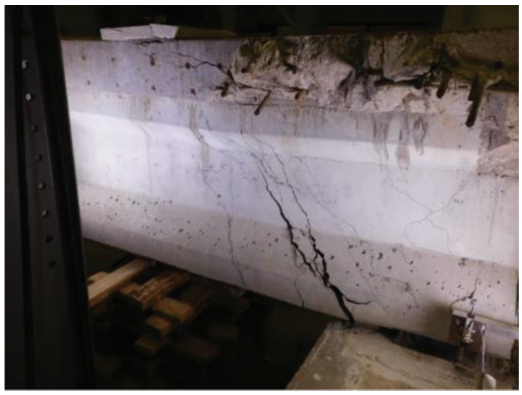

**Figure 5.4** Control specimen after failure.

within the test region, corresponding to a crack angle of approximately 43° measured from the horizontal, as shown in Figure 5.4. The formation of the strut is consistent with D-region shear behavior. Failure of the specimen was defined by a gradual decrease in load-carrying capacity along with the progressive widening of the diagonal cracks that formed along the strut. Furthermore, as the cracks widened and the specimen continued to deflect, the prestressing strands in the bottom flange experienced slippage. The ends of the strands slipped approximately 1.25 in. into the girder by the end of the test, measured using a caliper after completion of the test. The sudden loss in load-carrying capacity shown in Figure 5.2 at a beam deflection of 1.24 in. is believed to be due to strand slip.

### *5.2.2 Damaged Specimen*

To further determine the effectiveness of the three repair techniques described in Chapter 4, Girder 20-C was tested without repairing the damaged end region to better understand the strength and performance of the deteriorated girders in their field condition. The load-deflection response curve for the damaged specimen is shown in Figure 5.5. Due to the existing damage, cracking was observed early in the test within the region of the bottom flange as a portion of the flange separated from the specimen. However, the first crack that developed during the test and corresponded with a notable change in the load-deflection behavior was observed at a shear force of 61 kips (69 kips of applied load). For the purposes of comparing specimen behaviors, this shear force is taken as the cracking shear force, $V_{cr}$, for the girder. This crack became the vertical crack which characterized the failure of the specimen, as discussed in more detail below. The specimen resisted a maximum shear force of 80 kips (90 kips of applied load).

The condition of the specimen prior to testing is shown in Figure 5.6, and the condition of girder following testing is displayed in Figure 5.7. Unlike the control specimen, load was not transferred within the test region through a diagonal strut extending from the load point to the support. Instead, a vertical crack initiated at the bottom of the member approximately 3.5 ft from the end

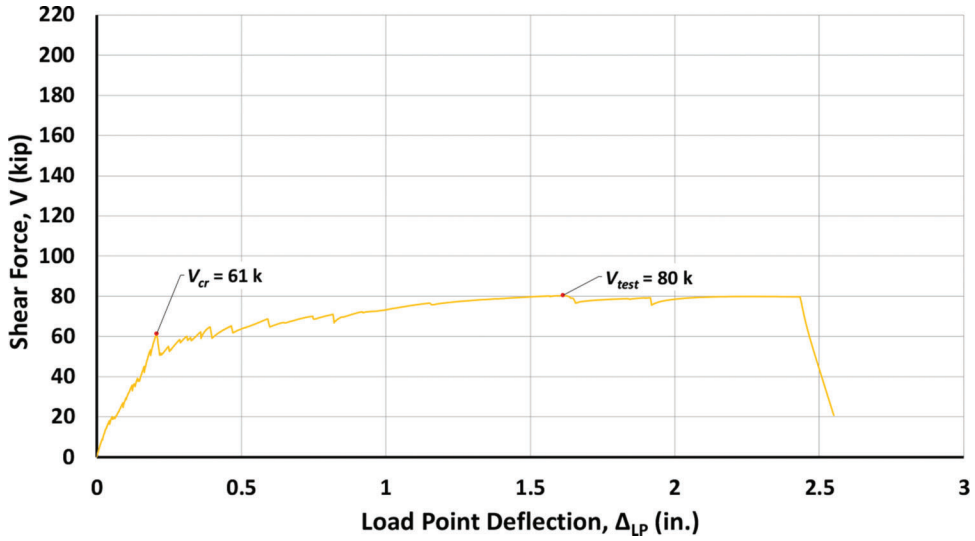


**Figure 5.5** Shear vs. deflection at load point for damaged specimen.

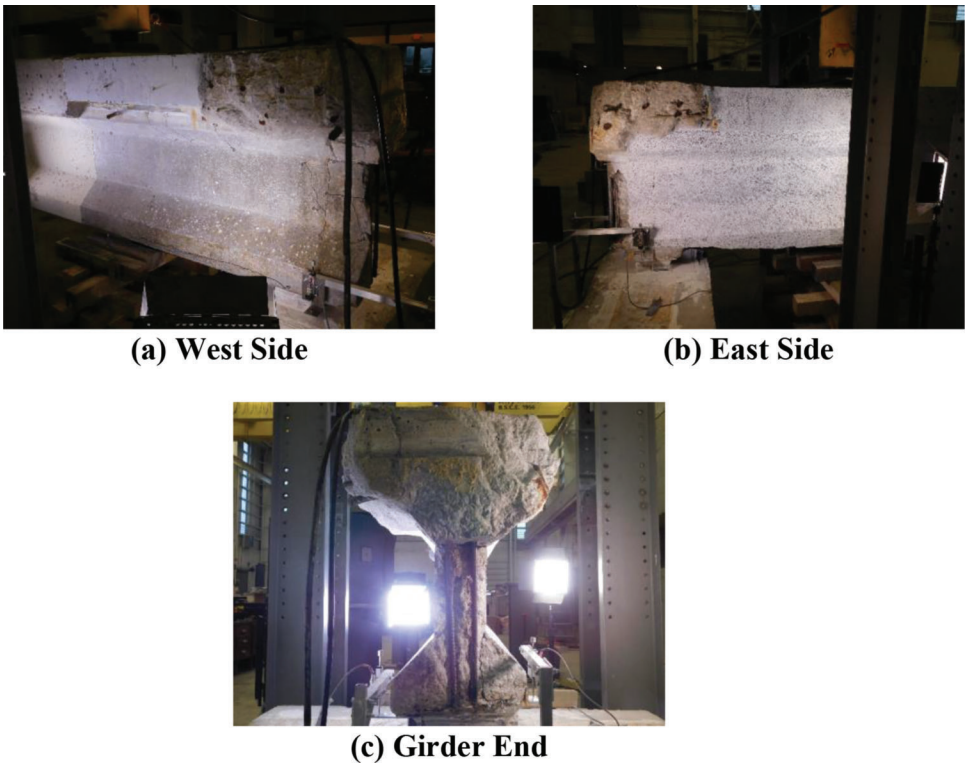


**Figure 5.6** Damaged specimen prior to testing.

of the specimen. Upon further loading, the crack propagated vertically through the web of the member. Then, the crack propagated diagonally through the top flange and deck toward the load point. Additionally, unlike the control specimen, the failure of the damaged specimen was defined by an abrupt drop in the load-carrying capacity. Comparing Figure 5.7(a and b) with Figure 5.4, the failure mechanisms between the control and damaged girders are significantly different, with the primary failure crack(s) oriented at approximately 43° from the horizontal for the control specimen and at approximately 90° for the damaged specimen. The behavior of the damaged specimen was a result of the lost tensile capacity within the bottom flange due to the deteriorated and ineffective prestressing strands. Furthermore, as shown in Figure 5.7(c), the portions of the bottom flange outside of the web detached from the specimen at the support. Through destructive evaluation after the test, it was discovered that the individual wires of one of the harped strands had untwisted from one another.

(a) West Side (b) East Side

(c) Girder End

**Figure 5.7** Damaged specimen after failure.

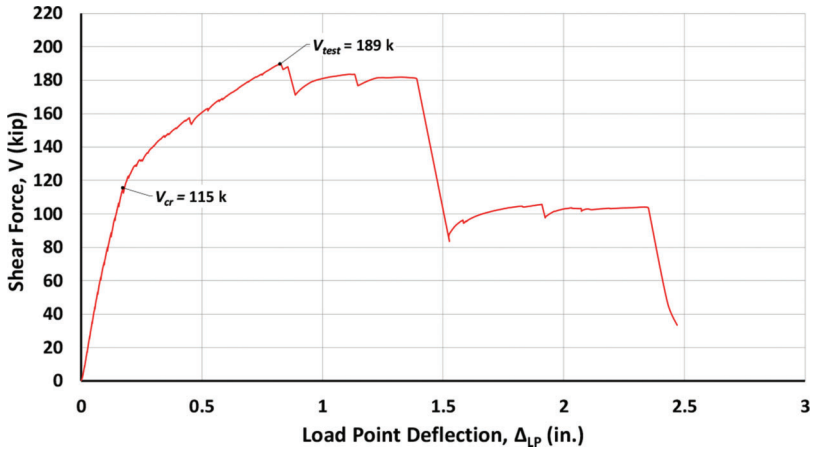


**Figure 5.8** Shear vs. deflection at load point for externally bonded FRP specimen.

*5.2.3 Externally Bonded FRP Repair Specimen*

The first repaired specimen to be discussed is the girder restored with the use of externally bonded FRP. The load-deflection response curve for the specimen is shown in Figure 5.8. The development of the first crack that was visually observed during the test was noted at a shear force of 140 kips (158 kips of applied load). The crack was a flexural crack located at the end of the longitudinal FRP sheets. Due to the brittle nature of FRP, however, a close examination of the specimen was not conducted past a shear force of 106 kips due to safety concerns. Thus, it is probable that a crack formed at a lower shear force. Therefore, for the purposes of comparing specimen behaviors, the cracking shear, $V_{cr}$, of this specimen will be defined by the first notable change in slope of the load-deflection response curve in Figure 5.8. This change in slope occurs at a shear force of 115 kips (130 kips of applied load). The specimen resisted a maximum shear force of 189 kips (214 kips of applied load).

The condition of the specimen prior to testing is presented in Figure 5.9, and the condition of the girder after failure is shown in Figure 5.10. The specimen experienced a flexural failure characterized by the fracture of two prestressing strands in the bottom flange (see Figure 5.11) at the termination of the FRP sheets. The strands fractured at the location of a wide flexural crack at the end of the repaired region as shown in Figure 5.12. The red lines in Figure 5.12 indicate the

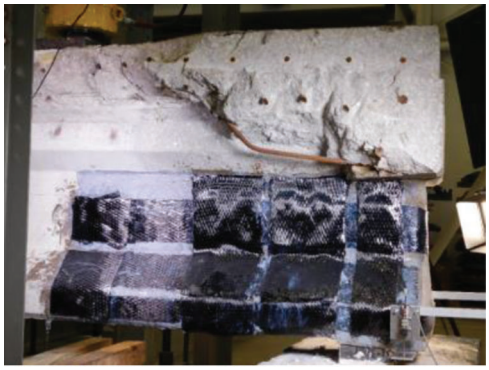

**Figure 5.9** Externally bonded FRP specimen prior to testing.

**Figure 5.10** Externally bonded FRP specimen after failure.

**Figure 5.11** Fractured prestressing strands in bottom flange after testing.

termination of the FRP strips. The sudden loss in load-carrying capacity at a deflection of 1.39 in. is believed to coincide with strand fracture. The specimen continued to be loaded after this event and maintained a shear force of approximately 100 kips until another sudden drop in load-carrying capacity at a deflection of 2.35 in. Concrete crushing was observed in the deck beneath the load point. During the test, minor diagonal cracking was observed near the load point in the region not covered by FRP sheets. The crack was oriented at an angle of approximately 46° from the horizontal. The crack did not widen significantly after formation, however, and the propagation of the crack toward the support is unknown due to the presence of the FRP.

**Figure 5.12** Critical flexural crack of externally bonded FRP specimen after failure.

Considering the failure behavior of the specimen, the repair system restored sufficient shear capacity so that a flexural failure outside of the damaged region occurred. The FRP wrap also provided sufficient confinement to prevent the separation of portions of the bottom flange of the member as observed during the test on the damaged specimen. Furthermore, the confinement provided by the FRP allowed the strands to reach their ultimate capacity within their calculated development length. Based on Equation 5.9.4.3.2-1 of AASHTO LRFD (2020), the development length of the strands is calculated using Equation 5.1. In the calculation, the value of $f_{ps}$ is replaced with the specified ultimate strength of the strands, $f_{pu}$, in consideration of the observed fracture of the strands, and $f_{pe}$ is assumed to be 160 ksi, within the typical range of effective prestress after losses.

$$l_d = \kappa\left(f_{ps} - \frac{2}{3}f_{pu}\right)d_b = 1.6\left[270\,ksi - \frac{2}{3}(160\,ksi)\right](0.5\,in.)$$
$$= 130.7\,in. \qquad \text{(Eq. 5.1)}$$

The strands fractured approximately 49 in. from the end of the member, giving evidence of the benefits provided by the FRP confinement. Based on the observed failure behavior and strength achieved by the specimen, the externally bonded FRP repair system is believed to have effectively restored the tie force in the bottom flange that was assumed to be lost due to deterioration as observed for the damaged specimen.

Minimal FRP delamination was observed during testing, further indicating a successful FRP repair. Indications of delamination were first noted at a shear force of 106 kips when minor popping sounds were heard. At the end of the test, the delamination was confined to the area along the longitudinal strips between the termination of the patch sheets located at the

ends of the strips and the first U-wrap sheet, as indicated by the red areas in Figure 5.10.

### *5.2.4 NSM FRP Repair Specimen*

The focus of the specimen strengthened with NSM FRP strips was the potential benefits of restoring the tensile capacity along the bottom flange of the girder. The load-deflection response curve for the specimen is shown in Figure 5.13. The shear force corresponding to the development of the first crack observed during the test was 31 kips (35 kips of applied load). As explained next, this shear force was also the maximum shear force resisted by the specimen. Therefore, both $V_{cr}$ and $V_{test}$ are shown to be equal to 31 kips (35 kips of applied load) in Figure 5.13.

The condition of the specimen prior to testing is presented in Figure 5.14, and the condition of the specimen following testing is displayed in Figure 5.15. The hairline cracks marked in Figure 5.14 were preexisting. At a shear force of 31 kips, the portion of the web located above the support bearing experienced a splitting crack that effectively caused the end of the specimen to separate from the rest of the member. The splitting crack appeared suddenly along the depth of the member, intersecting with the reentrant corner at the notch located along the top flange of the girder. This produced a sudden loss in load-carrying capacity. Once the end of the member that separated from the beam was no longer effective in transferring load to the bearing, load was primarily transferred to the bearing through the outer portions of the bottom flange in contact with the bearing pad. This resulted in the outer portions of the flange separating from the girder as shown in Figure 5.16, preventing load from being transferred to

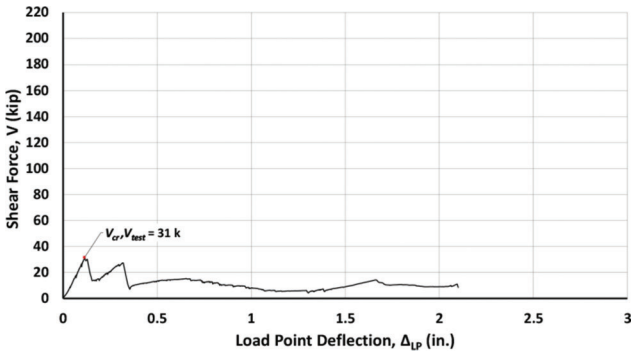


**Figure 5.13** Shear vs. deflection at load point for NSM FRP specimen.

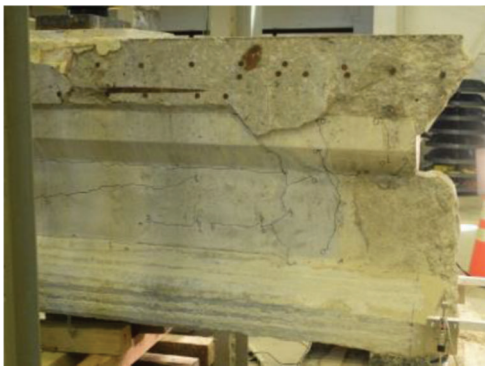

**Figure 5.14** NSM FRP specimen prior to testing.

**Figure 5.15** NSM FRP specimen after failure.

**(a) Elevation View**

**(b) Girder End**

**Figure 5.16** Flange separated from NSM FRP specimen.

the NSM strips. In other words, because of the failure at the end of the girder, the NSM strips were not engaged. As indicated by the load-deflection plot in Figure 5.13, the load carried by the specimen increased after the development of the splitting crack at a shear force of 31 kips, but load-carrying capacity was again lost when portions of the bottom flange of the girder separated from the member at a shear force of 27 kips.

The bridge from which the test girders were extracted included a transverse edge beam located within the notch at the ends of the girders. This edge beam was cast monolithically with the bridge deck. As shown in the previous figures of the specimen with the NSM strips (e.g., Figure 5.14 and Figure 5.15), the transverse edge beam was not intact but separated from the girder at some point during the extraction of the beam from the bridge or during transportation. At least a portion of the edge beam remained intact for the other specimens of the test program. The lack of the edge beam on the specimen with NSM strips may have contributed to the splitting in the vicinity of the notch observed during the test.

### *5.2.5 Supplemental Diaphragm Repair Specimen*

The final specimen to be described is the girder repaired with the addition of a supplemental diaphragm at its end. The load-deflection response curve for this specimen is provided in Figure 5.17. During the test, the first crack observed was within the supplemental diaphragm. The end face of the diaphragm began to experience minor cracking at a shear force of 8.9 kips (10 kips of applied load). At a shear force of 44 kips (50 kips of applied load) cracking had propagated along the entirety of both the end face and the bottom surface of the diaphragm, causing the reduction of stiffness indicated by the load-deflection plot. Therefore, as with the externally bonded FRP specimen, the cracking shear, $V_{cr}$, of this specimen will be defined by the first notable change of slope in the load-deflection curve in Figure 5.17, which corresponds to a shear force of 44 kips (50 kips of applied load). The specimen achieved a maximum shear force of 81 kips (91 kips of applied load).

The condition of the girder prior to the test is shown in Figure 5.18. The hairline cracks marked in the figure were present before testing. As discussed above, at a shear force as low as 8.9 kips, cracking was observed on the end face of the supplement diaphragm, and cracking was observed on the bottom surface of the supplemental diaphragm at a shear force of 35 kips. As shown in Figure 5.19, at a shear force of 44 kips, these cracks had propagated along the entire length of both faces. The formation of the cracks at a relatively low shear force (less than half of $V_{cr}$ for the control specimen) was caused by the transfer of load through the diaphragm to the two bearing pads. In other words, the behavior resulted from the elimination of the original center bearing pad of the girder. Furthermore, the absence of continuous reinforcement near the bottom (i.e., tension face) of the diaphragm caused the splitting of the diaphragm along the cracks shown in Figure 5.19 to quickly increase in severity upon further loading. Such reinforcement is needed to restrain the cracks and provide tensile capacity in order to transfer loads to the two bearing pads. Additionally, as the test continued, the interface between the supplemental diaphragm and the original girder concrete failed (i.e., the supplemental diaphragm separated from the original girder concrete), and rotation of the diaphragm was observed, as shown in Figure 5.20(a through d). The end of the girder after the test is shown in Figure 5.20(e). Outside of the supplemental diaphragm, a diagonal crack (see Figure 5.21) initiated at a shear force of approximately 53 kips. The crack extended from the bottom of the diaphragm toward the load point at an angle of approximately 55° from the horizontal. This indicated the general orientation of compressive stresses in this portion of the member.

Without continuous reinforcement along the bottom of the supplemental diaphragm to help transfer stresses to the two bearing pads and control the splitting cracks, the diaphragm was ineffective. Continuous reinforcement with proper development was identified as being

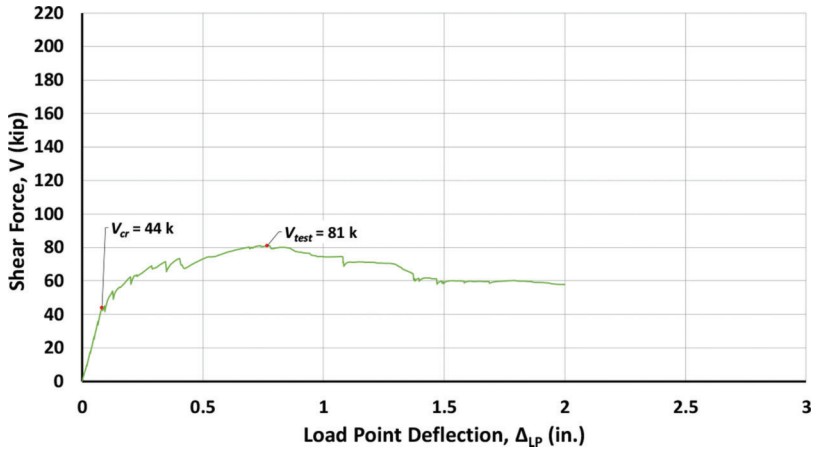


**Figure 5.17** Shear vs. deflection at load point for supplemental diaphragm specimen.

(a) West Side Interface



(b) East Side Interface

(c) West Side

(d) East Side

(e) Girder End

**Figure 5.18** Supplemental diaphragm specimen prior to testing.

(a) Girder End at Shear Force of 44 Kips

(b) Bottom Surface of Diaphragm at Shear Force of 44 Kips

**Figure 5.19** Splitting behavior of supplemental diaphragm.

essential for a successful repair with such a diaphragm. Furthermore, if the supplemental diaphragm were cast continuously between girders in the field, the early failure of the diaphragm observed during the test is expected to be prevented. More detailed suggestions for the implementation of a repair using a continuous diaphragm are provided in Chapter 6.

## 5.3 Discussion of Test Results

Within the following subsections, the results of all five experimental specimens are analyzed and discussed. A summary of the test results is first presented for easy comparison. Then, the results for each of the three repair techniques (externally bonded FRP, NSM FRP, and

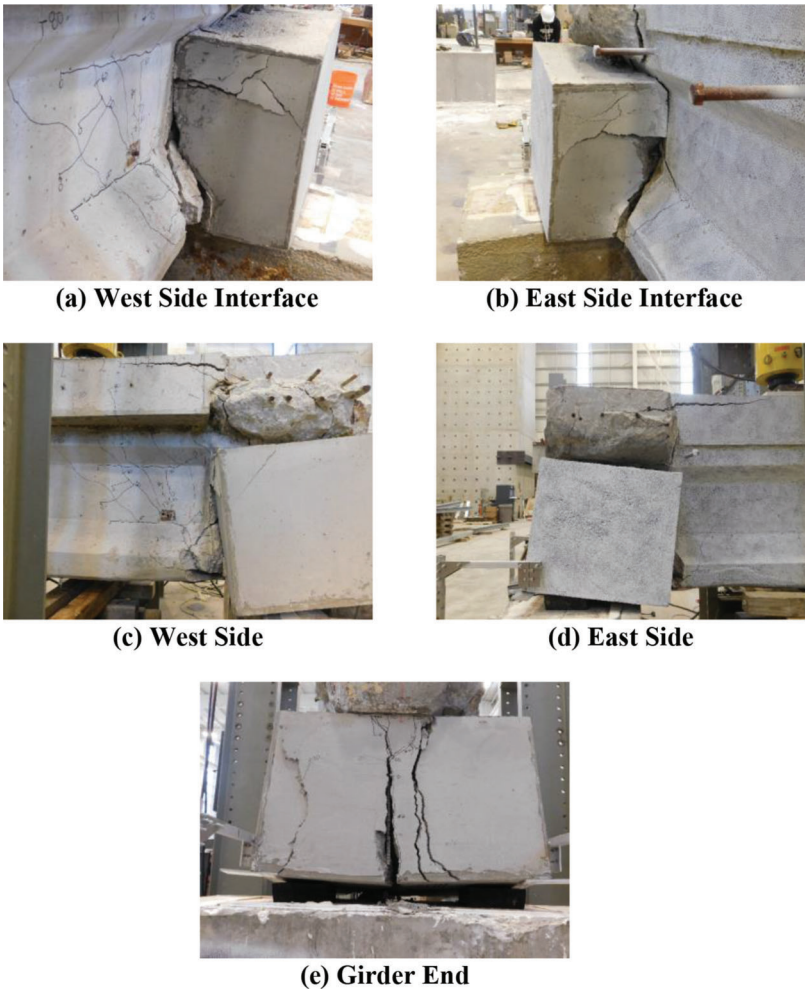


**Figure 5.20** Supplemental diaphragm specimen after failure.

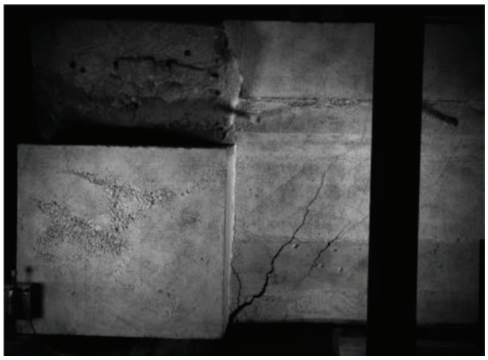

**Figure 5.21** Diagonal cracking of supplemental diaphragm specimen at shear force of 80 kips.

supplemental diaphragm) are compared to the results of the control and damaged specimens to establish the effectiveness and viability of each repair method.

### *5.3.1 Summary of Test Results*

The results of the load tests performed on the specimens are summarized in Table 5.1. In the table, $V_{Control}$ is the maximum shear force resisted by the control specimen, and $V_{Damaged}$ is the maximum shear force resisted by the damaged specimen. The values of $V_{test}/V_{Control}$ and $V_{test}/V_{Damaged}$ are the ratios of the experimental capacity of a specimen to the experimental capacity of the control and damaged specimens, respectively. As observed in Table 5.1, only the externally bonded FRP specimen resisted a higher maximum shear force than the control specimen (34% increase). The damaged, NSM FRP, and supplemental diaphragm specimens achieved peak shear values equal to 57%, 22%, and 57% of the capacity of the control specimen, respectively.

The load-deflection response curves for the five girders are plotted together in Figure 5.22. This plot will be referenced in the following subsections as the performance of the repaired specimens are compared to the performance of the control and damaged specimens.

### *5.3.2 Comparison of Repaired Specimens to Control and Damaged Specimens*

**5.3.2.1 Externally Bonded FRP Repair Specimen.** When the experimental results of the specimen with

TABLE 5.1
**Summary of Load Test Results**

| | $V_{cr}$ (kip) | $V_{test}$ (kip) | $V_{test}/V_{Control}$ | $V_{test}/V_{Damaged}$ |
|---|---|---|---|---|
| Control | 98 | 141 | 1.00 | 1.76 |
| Damaged | 61 | 80 | 0.57 | 1.00 |
| Ext. Bonded | 115 | 189 | 1.34 | 2.36 |
| NSM | 31 | 31 | 0.22 | 0.39 |
| Supplemental Diaphragm | 44 | 81 | 0.57 | 1.01 |

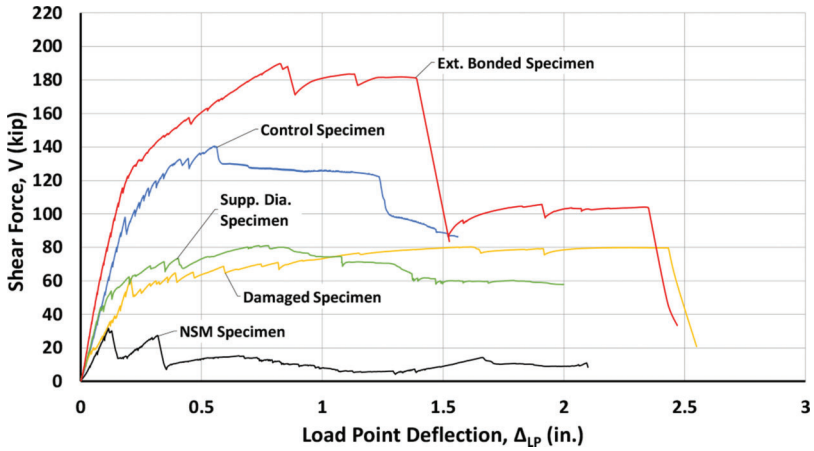


**Figure 5.22** Shear vs. deflection at load point for all girder specimens.

externally bonded FRP are compared to those of the control and damaged specimens, it can be observed that the externally bonded repair system adequately restored the behavior of the damaged end region. As indicated by the load-deflection response curves in Figure 5.22 and the test data in Table 5.1, the maximum shear force, $V_{test}$, resisted by the specimen with externally bonded FRP exceeded that of the control specimen by 34%. Furthermore, the shear force, $V_{cr}$, defined previously, increased by 17% for the repaired specimen compared to the control specimen. It can also be observed from the plots that the externally bonded system resulted in a greater initial stiffness than the control specimen, indicating that, due to the relatively high stiffness of the FRP laminate material, the externally bonded FRP system was able to restore the stiffness lost due to the deterioration of the end region.

As discussed in Section 5.2.3, the specimen repaired with externally bonded FRP failed due to flexure at the termination of the repair. This failure mode differed from the observed failure mode of the control specimen. Considering that the failure of the control specimen can be described as being caused by a combination of D-region shear and strand slip, this change in failure mode indicates that the repair system successfully restored any lost shear capacity due to the deterioration of the end region and resulted in a shear strength greater than that of the control specimen. Furthermore, the confinement provided by the FRP wrap allowed two strands to reach their ultimate strength at the end of the repaired region. With the tensile capacity in the bottom flange effectively restored, the externally bonded FRP system prevented the failure mode experienced by the damaged specimen. Moreover, the repair system helped to prevent the vertical splitting at the end of the member as was observed for the specimen repaired with NSM strips. It should be noted, however, that the presence of the transverse edge beam (see Section 5.2.4) may have also contributed to eliminating this behavior. Lastly, the specimen did not experience the detachment of the portions of the bottom flange from the web as exhibited by the damaged specimen and the specimen with NSM strips. The confinement and tensile resistance provided by the longitudinal FRP strips that wrapped around the end of the girder helped to strengthen the member against vertical splitting at its end and the failure of the bottom flange. The vertically-oriented sheets above the support bearing also likely contributed to confinement at the end of the member. Based on the test results and above comparisons, it can be concluded that the use of externally bonded FRP is a viable repair technique for prestressed girders with end region deterioration. Furthermore, the chosen details for the repair resulted in behavior superior to that of the control specimen.

**5.3.2.2 NSM FRP Repair Specimen**. Unlike the externally bonded repair system, the NSM repair system did not adequately restore the behavior of the member to that of the control specimen. Considering the load-deflection response curves for the control, damaged, and NSM specimens in Figure 5.22 and the

test data in Table 5.1, the maximum shear force, $V_{test}$, resisted by the NSM specimen was only 22% of the shear strength of the control specimen. Furthermore, the maximum shear force was only 39% of the shear force carried by the damaged specimen. The initial stiffness of the NSM specimen was also significantly less than that of the control specimen but was similar to the initial stiffness of the damaged specimen.

As noted in Section 5.2.4, the NSM strips installed in the bottom flange of the girder specimen were not engaged due to the failure mode experienced by the member. Therefore, the behavior of the girder essentially represents a member only repaired with mortar. The low strength exhibited by the specimen provides additional information on the potential strengths of members with deteriorated end regions and emphasizes the need to provide strengthening measures beyond simply restoring the cross section of the girder using a repair material (e.g., mortar).

The NSM specimen failed due to the development of a splitting crack that effectively caused the end of the specimen to separate from the rest of the member. Adequate confinement within the region repaired with mortar, such as that provided by the longitudinal strips that wrapped around the end of the girder in the externally bonded FRP system, is needed to prevent this failure mode. The results indicate that the NSM FRP repair system consisting only of the placement of NSM strips along the vertical and sloped surfaces of the bottom flange is not a reliable repair technique for prestressed girders with end region deterioration. Nevertheless, considering the satisfactory performance of the specimen with externally bonded FRP wrap and the resulting strengths of other test specimens with NSM reinforcement (see Chapter 3), it is believed that a hybrid repair system that includes NSM strips in the bottom flange combined with the confinement, tensile capacity, and stiffness provided by externally bonded FRP sheets may be a viable technique for restoring the strength and stiffness of a deteriorated end region. In this hybrid system, any shear strengthening through the use of FRP sheets that is needed within the end region should be considered.

**5.3.2.3 Supplemental Diaphragm Repair Specimen**. Similar to the NSM FRP system, the supplemental diaphragm repair system was unable to restore the overall behavior of the control specimen. As presented in Figure 5.22 and the test data in Table 5.1, the cracking shear force, $V_{cr}$, for the specimen with the supplemental diaphragm was 72% of the value of $V_{cr}$ for the damaged specimen due to the crack that developed in the diaphragm as it transferred load to the two bearing pads. The maximum shear forces carried by the specimen with the supplemental diaphragm and the damaged specimen only differed by 1 kip. The values of $V_{cr}$ and $V_{test}$ for the repaired specimen were only 45% and 57% of the corresponding values for the control specimen. However, the initial stiffness of the supplemental diaphragm specimen prior to the reduction in stiffness due to cracking was equivalent to the initial stiffness of the control specimen.

As discussed in Section 5.2.5, the failure of the specimen was characterized by the splitting of the supplemental diaphragm, separation of the diaphragm from the original girder concrete, and rotation of the diaphragm. This resulted in the post-cracking behavior of the specimen more closely resembling the behavior of the damaged specimen than the control specimen. Consistent with the discussion in Section 5.2.5, the behavior of the specimen with the supplemental diaphragm was a result of the elimination of the original center bearing pad for the load test and the absence of continuous, transverse reinforcement along the bottom of the diaphragm. If the diaphragm were cast continuously between girders in the field and properly detailed, the observed failure behavior would likely be eliminated. Proposed detailing for a continuously cast diaphragm is provided in Chapter 6. While the experimental results indicate the supplemental diaphragm repair system did not adequately restore the behavior of the girder to that of the control specimen, the precracking behavior did demonstrate the same stiffness as the control specimen. With modifications, the repair system could potentially be a viable technique to restore the behavior of prestressed girders with end region deterioration. Further research, however, is needed to assess the viability of this repair system.

### 5.4 Summary

Five AASHTO Type I girders were loaded to failure according to the experimental program outlined in Chapter 4. One girder in good condition was tested to serve as a control specimen. Another specimen was tested in a damaged state to provide a baseline for the expected behavior of a deteriorated, yet unrepaired, girder. The final three girders were tested after being repaired with either the externally bonded FRP system, the NSM FRP system, or the supplemental diaphragm system described in Chapter 4.

The results and observations from the load tests conducted on the control and damaged specimens influenced the development of the three repair techniques and allowed for the effectiveness of each technique to be established. The comparison of the two specimens indicated that restoring the tensile capacity along the bottom flange of the girder is a key consideration for the development of a successful repair.

The NSM FRP repair system failed prematurely as a result of the formation of a splitting crack in the portion of the web located above the bearing. This behavior emphasized the importance of providing adequate confinement around the repair region when designing repair solutions. In contrast, the externally bonded repair system provided adequate confinement around the repair region and restored the lost tensile capacity, resulting in an overall performance that exceeded that of the control specimen. Based on these results and observations, it was concluded that the externally

bonded FRP repair system is a viable repair technique for prestressed girders with end region deterioration. Lastly, the specimen with a supplemental diaphragm experienced a premature failure due to inadequate detailing and the elimination of the original bearing pad. Nevertheless, providing a continuous diaphragm between adjacent girders in the field could potentially be a viable solution. The recommendations and conclusions gathered during the experimental program are presented in Chapter 6.

# 6. SUMMARY, CONCLUSIONS, RECOMMENDATIONS, IMPLEMENTATION, AND BENEFITS

## 6.1 Summary

To assist INDOT in establishing repair and strengthening techniques for concrete bridge girders with various types of damage and deterioration, two experimental programs were conducted. One experimental program focused on developing and evaluating the effectiveness of FRP flexural strengthening systems. This experimental program consisted of tests on 22 reinforced concrete beams. The details of the beam specimens were selected to specifically evaluate potential flexural strengthening methods for deteriorated adjacent box beam bridges in Indiana. The second experimental program focused on developing and evaluating the effectiveness of various repair techniques for prestressed concrete bridge girders with end region deterioration. The three repair techniques examined in this experimental program were (1) an externally bonded FRP system, (2) a near-surface-mounted (NSM) FRP system, and (3) a concrete supplemental diaphragm. The main objectives of the two experimental programs included:

- Comparing the effectiveness of two FRP flexural strengthening methods: externally bonded FRP sheets and near-surface-mounted FRP strips.
- Assessing the ability of the externally bonded FRP sheets and near-surface-mounted FRP strips to restore the strength and stiffness of artificially weakened laboratory specimens under flexural loading.
- Evaluating the effects of end region deterioration on the behavior of prestressed concrete bridge girders.
- Determining effective repair techniques for restoring the behavior of prestressed concrete bridge girders with end region deterioration.
- Investigating anchorage techniques for externally bonded FRP sheets.
- Developing and verifying installation procedures for FRP flexural strengthening and end region repair techniques.

## 6.2 Conclusions

### *6.2.1 Flexural Strengthening Experimental Program*

The key observations and conclusions from the flexural strengthening experimental program are presented below. The items listed provide insights into viable flexural strengthening methods for box beam bridges as well as other reinforced concrete flexural members.

- Both the externally bonded FRP system and the NSM FRP system are effective techniques for the strengthening of flexural members if properly designed and installed. Appropriate anchorage of the externally bonded FRP must be ensured. The consideration of the bond and development of NSM reinforcement is critical.
- All FRP-strengthened specimens, other than Specimens 1-EB.1 and 1-NSM.1b, regained the experimental moment capacity of the control specimen in their respective group (see $M_{test}/M_C$ column in Figure 3.1).
- Considering the midspan deflection at the maximum applied load during the experimental tests, all FRP-strengthened specimens experienced reduced ductility compared to the specimens without FRP.
- While the FRP-strengthened specimens achieved post-cracking stiffnesses similar to that of the control specimens, all FRP-strengthened specimens exhibited significantly higher post-yielding stiffnesses relative to the control specimens.
- Based on a pilot test conducted on a beam with U-wrap anchors, the particular anchor configuration applied to the member was not the most effective anchorage method for fully developing the capacity of the primary FRP sheet. However, modifications to the anchorage method (e.g., increased cross-sectional area of the anchors) may result in improved behavior. Additional tests are needed to evaluate other configurations.
- Considering the anchorage of externally bonded sheets, specimens with FRP spike anchors only at the ends of the primary FRP sheet (EB.2 specimens) consistently gained more capacity than specimens with FRP spike anchors at multiple locations along the length of the primary sheet (EB.1 specimens). The separation and redirection of fibers in the FRP sheet required for the installation of the FRP spike anchors likely contributed to premature rupture at the anchor locations. The stiffness of the anchors may have also contributed to the high concentration of stresses. Although both anchorage methods may lead to these negative impacts on the primary FRP sheet, the EB.1 specimens were impacted more due to anchors being located in regions of high moment demand along the length of the beam.
- For the specimens in Group 3 of the experimental program, the eccentricity of the longitudinal steel reinforcement and the relative placement of the NSM strips did not play a significant role in the effectiveness of the strengthening systems or the overall performance of the members.
- Between first cracking and yielding of the longitudinal steel reinforcement, the FRP-strengthened specimens with cut bars (Group 2) exhibited greater stiffnesses compared to the FRP-strengthened specimens with excluded bars (Groups 1 and 3). Although the cross sections at midspan were identical, the presence of the cut bars contributed to this increased stiffness. In general, for the specimens with cut bars, cracking was more concentrated at midspan (i.e., where the bars had been cut) relative to the members with excluded bars.
- While the FRP strengthening systems were applied to all other specimens with the member in an inverted position, NSM strips were installed in Specimen 1-NSM.1b from underneath the member as would occur in the field.

A different epoxy with a higher viscosity was also used for Specimen 1-NSM.1b. The overhead installation was successful, and once the installation was completed, no sagging of the epoxy from the grooves was observed. However, the specimen failed at a lower moment capacity compared to the other NSM specimens. The cause of the reduction in strength is not known with certainty but is likely due to a weaker bond between the epoxy and FRP. More tests are needed to determine the potential impact of various epoxies, variations in material properties, and any potential negative effects of overhead applications.

- The experimental moment capacities of all specimens were greater than the calculated moment capacities (see column $M_{test}/M_n$ in Figure 3.1). It should be noted that some of the differences between $M_{test}$ and $M_n$ can be attributed to the strain-hardening of the steel reinforcement, which was not accounted for in the calculated moment capacities.
- The analysis tool that was developed (see Section B.1 of Appendix B) to better understand the behavior of the FRP strengthening systems demonstrated that a relatively simple analysis procedure can be used to provide reasonable estimates for the load-deflection behavior of FRP-strengthened beams tested in flexure.
- The FRP strengthening system installation procedures followed during the experimental program, while advantaged by a controlled laboratory setting, were deemed to be successful. Although care was taken to apply each FRP strengthening system in the same manner, small variations may have contributed to some of the differences in behavior observed during the test program.

### *6.2.2 End Region Repair Experimental Program*

The key observations and conclusions from the end region repair experimental program are listed below.

- The deterioration of the end regions of prestressed concrete girders due to leaking expansion joints can result in significant reductions in strength (43% shear strength reduction considering results of the experimental program).
- Restoring the tensile capacity lost due to deteriorated and ineffective prestressing strands in the bottom flange of prestressed concrete girders is a critical factor when designing end region repair systems. As discussed in Section 4.3.1, the inability of the prestressing strands in the bottom flange to develop tensile forces controlled the failure behavior of the unrepaired specimen. Without adequate tensile capacity in the bottom flange, a diagonal strut could not form between the load and support, resulting in a premature failure mechanism and decreased capacity.
- Ensuring adequate confinement of the repair region is also a critical factor when designing end region repair systems. End confinement, such as the confinement provided by the longitudinal FRP strips included in the externally bonded FRP repair system, is needed to prevent the premature failure mode observed during the test on the specimen with NSM FRP reinforcement. Providing confinement around the repair region also mitigates some concerns about the condition of the concrete at the repair interface and the resulting bond between the original concrete and mortar used to restore the member cross section.
- The externally bonded FRP repair system developed for the experimental program proved to be a viable technique for restoring the strength and stiffness of the prestressed concrete bridge girder with end region deterioration. The repaired specimen achieved a greater shear capacity and a greater initial stiffness than the control specimen. Additionally, minimal FRP debonding was observed during testing.
- The NSM FRP repair system developed for the experimental program did not provide adequate confinement of the repair region, and therefore, the strength and stiffness of the prestressed concrete bridge girder was not restored. The lack of the edge beam on the specimen may have also contributed to the poor performance of the member (see Section 5.2.4). If combined with externally bonded FRP laminate that properly confines the end region, the use of NSM strips may be a viable repair solution.
- The supplemental diaphragm system developed for the experimental program did not restore the strength of the member. The use of a continuous diaphragm between adjacent girders may provide a viable repair technique for restoring the strength and stiffness of prestressed concrete bridge girders. Suggested details are included in the next section.

## 6.3 Recommendations

### *6.3.1 Flexural Strengthening Experimental Program*

Based on observations and results from the flexural strengthening experimental program, recommendations for the design and installation of FRP flexural strengthening systems were generated. These recommendations are as follows:

- Allowing the use of externally bonded FRP and NSM FRP systems in Indiana for the flexural strengthening of concrete bridge members is recommended.
- Proper anchorage or embedment should be ensured. When anchoring externally bonded FRP sheets with spike anchors, the anchors should not be placed along the length of the externally bonded sheet. Anchors should be installed at each end of an FRP sheet and should not be located in regions with high moment demand. Special considerations should also be given to the bond and development of NSM reinforcement to prevent premature debonding/slip failures.
- When applying FRP flexural strengthening systems overhead, care must be taken to ensure adequate bond is achieved. Performing a mock-up prior to installation on the bridge is recommended.

### *6.3.2 End Region Repair Experimental Program*

Based on observations and results from the end region repair experimental program, recommendations for the

design and installation of end region repair techniques were generated. These recommendations are as follows:

- Allowing the use of FRP systems in Indiana for the repair and strengthening of deteriorated end regions of bridge girders is recommended.
- When designing repair systems for prestressed concrete bridge girders with end region deterioration, special attention should be placed on restoring tensile capacity in the bottom flange of the girder and providing confinement to the repair area.
- Considering the success of the externally bonded FRP repair system for restoring the strength and stiffness of the test specimen, similar details as those incorporated into the repair system of the experimental program are recommended when implementing the system in the field. These details include the use of a combination of longitudinal strips and vertical sheets, utilizing FRP spike anchors for the anchoring of both longitudinal and vertical strips/sheets, and wrapping longitudinal strips around the end of the girder. For the vertical sheets, U-wraps should be used where possible.
- Simply restoring the cross section of a girder with end region deterioration using a repair material (e.g., mortar) is an insufficient technique for recovering the overall behavior of the member. As discussed in Section 5.3.2.2, the low strength exhibited by the specimen with NSM FRP reinforcement emphasizes the need to provide strengthening measures beyond restoring the cross section of the girder.
- To prevent the premature failure mode observed during the test on the specimen with the supplemental diaphragm, it is recommended a diaphragm be cast continuously between girders. The details described below are suggested with the understanding that tests have not been conducted to verify the resulting performance of the repair system.

Suggested detailing for a continuously cast diaphragm is shown in Figure 6.1. The details of the diaphragm consist of nine reinforcing bars that extend along the length of the diaphragm. Five of the bars are continuous and are installed through the web of the girders. These bars are mechanically spliced halfway between adjacent girders. Although a mechanical splice is preferred, a lap splice could be used as an alternative if the required lap splice length can be achieved. Two more continuous reinforcing bars are installed below the original bottom surface of the girder and can be spliced as needed. The final two reinforcing bars extend between the bottom flanges of adjacent girders. Closed-cell polystyrene board is placed around and between the bearing pads. Away from the bearing locations, the depth of the diaphragm increases to accommodate the two bars installed below the original bottom surface of the girder. Depending upon the spacing of the girders, multiple bearings may need to be placed between adjacent girders. Pairs of closed stirrups are spaced evenly between the girders. All reinforcing bars in the diaphragm should be epoxy coated.

Based on first-hand experience of conducting the end region repairs of the test girders, recommendations were developed for implementing procedures in the field for the repair of girder end regions. These recommendations are as follows:

- As environmental conditions, such as temperature and humidity, can cause drastic changes in the curing behavior of different materials, a trial batch of the repair material (e.g., mortar) used to restore the cross section of the girder should be cast under similar environmental conditions as those that are expected at the time of the

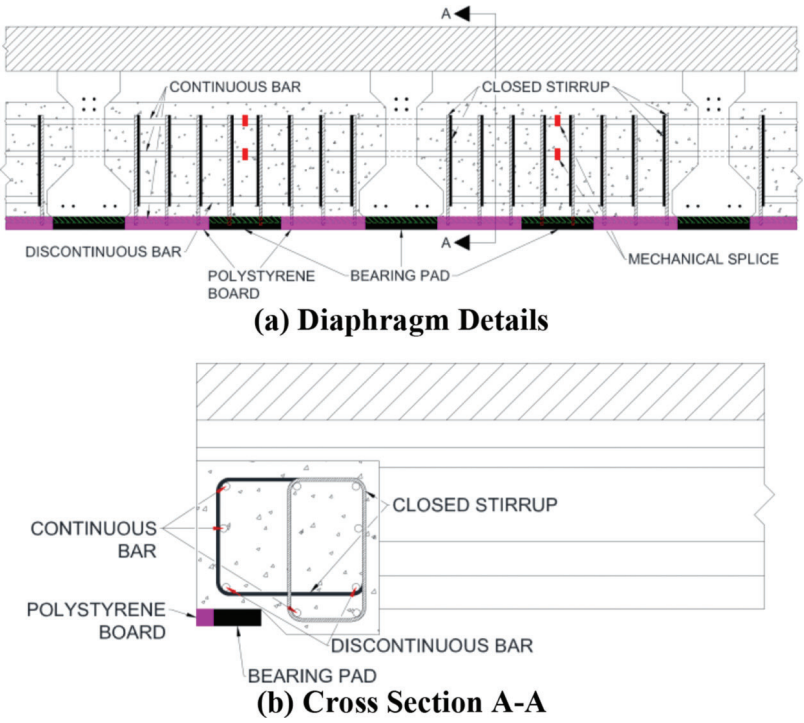


**Figure 6.1** Continuous diaphragm details.

repair. This will provide the installation team a better understanding of the pot life and finish time of the repair material under the expected conditions. The amount of water and set retardant that are used can then be adjusted as necessary for installation.

- When it is necessary to drill a hole through the entire web for the installation of an FRP spike anchor, the hole should be drilled from both sides of the web to avoid concrete breakout. To ensure that a straight hole is drilled, the following steps outline the recommended drilling procedure:

1. Using a drill bit with the desired diameter of the hole, drill through the majority of the web, stopping approximately 0.75 in. short of the other side of the web.
2. From the same side of the girder, use a smaller diameter drill bit to drill through the remainder of the web. This will indicate the location of the hole on the other side of the girder and greatly reduce concrete breakout.
3. From the other side of the girder, use the drill bit with the desired diameter of the hole to finish drilling the hole.

- When installing FRP spike anchors through the entire width of a member, special care should be taken to ensure that the anchor does not pull the FRP sheet away from the concrete surface. As the anchor is inserted into and pushed through the anchor hole on one side of the member, it should be ensured that the anchor does not snag or catch on the FRP sheet on the other side of the member. Prior to fanning and saturating the anchors, check all edges and surfaces on both sides of the member to ensure the FRP sheet has not shifted during installation of the anchor.
- When restoring the cross section of a damaged region located overhead, support for the mortar along the bottom surface of the member is recommended. While it is possible to repair overhead sections without supporting some repair materials, sagging and even total failure of the material prior to curing is common. Furthermore, supporting the material in this manner will decrease the repair time, providing more time to achieve an even finished surface.

### 6.4 Implementation

Based on the findings of the research, updates to the *Indiana Design Manual* to allow the use of FRP for strengthening purposes is recommended. Furthermore, in addition to the recommendation provided in the previous section, an FRP guidebook is being provided to INDOT. The guidebook includes an introduction to FRP systems and viable applications for Indiana bridges, comprehensive guidance for the implementation of FRP systems in Indiana, and recommendations for the *Indiana Design Manual*. The guidebook also directs engineers to the proper published guidelines for the successful design and installation of FRP systems.

### 6.5 Benefits

The benefits of this research are far reaching, as the project aligns with the Economic Competitiveness, Asset Sustainability, and Innovation and Technology strategic priorities of the *Indiana Department of Transportation 2019 Strategic Plan* (INDOT, 2019). The information contained in this report will help facilitate the implementation of FRP strengthening and repair systems, and the implementation of these systems is expected to result in significant time and cost savings. The establishment of proven repair procedures will reduce installation errors in the field, saving labor time and reducing material costs. Additionally, the development of effective repair techniques will provide INDOT with sustainable and cost-effective alternatives to replacing aging and deteriorated bridges. The application of FRP for the strengthening of Indiana bridges introduces an innovative technique to increase the service life of bridge infrastructure.

## REFERENCES


AASHTO. (2020). *AASHTO LRFD bridge design specifications* (9th ed.). American Association of State Highway and Transportation Officials.

ACI Committee 318. (2019). *ACI 318-19: Building code requirements for structural concrete (ACI 318-19): Commentary on building code requirements for structural concrete (ACI 318R-19)*. American Concrete Institute.

ACI Committee 440. (2007, September 1). *ACI-440R-07: Report on fiber-reinforced polymer (FRP) reinforcement for concrete structures*. American Concrete Institute.

ACI Committee 440. (2017). *ACI 440.2R-17: Guide for the design and construction of externally bonded FRP systems for strengthening concrete structures*. American Concrete Institute.

Andrawes, B., Shaw, I. D., & Zhao, H. (2018, February). *Repair & strengthening of distressed/damaged ends of prestressed beams with FRP composites* (Illinois Center for Transportation Report No. FHWA-ICT-18-001). University of Illinois at Urbana-Champaign. https://doi.org/10.36501/0197-9191/18-001

ASTM. (2018). *A615/A615M-18: Standard specification for deformed and plain carbon-steel bars for concrete reinforcement*. ASTM International. https://doi.org/10.1520/A0615_A0615M-18

ASTM. (2020). *ASTM C39/C39M-20: Standard test method for compressive strength of cylindrical concrete specimens*. ASTM International. https://doi.org/10.1520/C0039_C0039M-20

ARTBA. (2020). *2020 ARTBA bridge report*. The American Road & Transportation Builders Association.

El-Saikaly, G., Godat, A., & Chaallal, O. (2015, August). New anchorage technique for FRP shear-strengthened RC T-beams using CFRP rope. *Journal of Composites for Construction*, *19*(4). https://doi.org/10.1061/(asce)cc.1943-5614.0000530

FHWA. (1995, December). *Recording and coding guide for the structure inventory and appraisal of the nation's bridges* (Report No. FHWA-PD-96-001). U.S. Department of Transportation Federal Highway Administration. https://www.fhwa.dot.gov/bridge/mtguide.pdf

Frankhauser, W., Jr., Elkaissi, J., Kahl, S., McMillan, S., Potter, W., Rister, D., Wilson, D., & O'Connor, J. (2015, July). *Scan 13-03: Advances in fiber-reinforced polymer (FRP) composites in transportation infrastructure (NCHRP Project 20-68A)*. American Association of State Highway

and Transportation Officials. http://onlinepubs.trb.org/onlinepubs/nchrp/docs/NCHRP20-68A_13-03.pdf

Frosch, R. J., Williams, C. S., Molley, R. T., & Whelchel, R. T. (2020a). *Concrete box beam risk assessment and mitigation: Volume 1—Evolution and performance* (Joint Transportation Research Program Publication No. FHWA/IN/JTRP-2020/06). West Lafayette, IN: Purdue University. https://doi.org/10.5703/1288284317117

Frosch, R. J., Williams, C. S., Molley, R. T., & Whelchel, R. T. (2020b). *Concrete box beam risk assessment and mitigation: Volume 2—Evaluation and structural behavior* (Joint Transportation Research Program Publication No. FHWA/IN/JTRP-2020/07). West Lafayette, IN: Purdue University. https://doi.org/10.5703/1288284317118

INDOT. (1987). *Bridge plans for spans over 20 feet on State Road No. 24* (Project No. MAF-170-1). Indiana Department of Transportation.

INDOT. (2019). *Indiana Department of Transportation 2019 strategic plan*. Indiana Department of Transportation. www.in.gov/indot/files/INDOTStrategicPlan.pdf

Kim, S. (2008). *Use of CFRP to provide continuity in existing reinforced concrete members subjected to extreme loads* [Doctoral dissertation, The University of Texas at Austin]. Texas Scholar Works. http://hdl.handle.net/2152/17915

Kim, Y. G. (2011). *Shear behavior of reinforced concrete T-beams strengthened with carbon fiber reinforced polymer (CFRP) sheets and CFRP anchors* [Doctoral dissertation, The University of Texas at Austin]. Texas Scholar Works. https://repositories.lib.utexas.edu/handle/2152/ETD-UT-2011-12-4398

Kim, Y., Quinn, K., Satrom, N., Garcia, J., Sun, W., Ghannoum, W. M., & Jirsa, J. O. (2012, February). *Shear strengthening of reinforced and prestressed concrete beams using carbon fiber reinforced polymer (CFRP) sheets and anchors* (Center for Transportation Research Report No. 0-6306-1). University of Texas at Austin. https://ctr.utexas.edu/wp-content/uploads/pubs/0_6306_1.pdf

Needham, D. E. (2000, January 6). *Prestressed concrete beam end repair (final report)* (Michigan Department of Transportation Report No. R-1380). Michigan Department of Transportation. https://www.michigan.gov/documents/mdot_c&t_r-1380_67568_7.pdf

Orton, S. L. (2007). *Development of a CFRP system to provide continuity in existing reinforced concrete buildings vulnerable to progressive collapse* [Doctoral dissertation, The University of Texas at Austin]. Texas Scholar Works. http://hdl.handle.net/2152/3241

Owens Corning. (2017, June). *Aslan™ 500 carbon fiber reinforced polymer (CFRP) tape for structural strengthening* (Product Data Sheet Pub. 10022291). Owens Corning.

Petty, D. A., Barr, P. J., Osborn, P. G., Halling, M. W., & Brackus, T. R. (2011, October). Carbon fiber shear retrofit of forty-two-year-old AASHTO I-shaped girders. *Journal of Composites for Construction*, *15*(5), 773–781. https://doi.org/10.1061/(ASCE)CC.1943-5614.0000208

Pevey, J. M., Williams, C. S., Frosch, R. J., & Rich, W. B. (2021). *Repair and strengthening of bridges in Indiana using fiber reinforced polymer systems–Volume 1: Review of current FRP repair systems and application methodologies*. West Lafayette, IN: Purdue University. https://doi.org/10.5703/1288284317309

Pilgrim. (n.d.). *Magmaflow Grout-Pak CF*. Pilgrim Permocoat, Inc. http://www.pilgrimpermocoat.com/assets/product_pdf/Magmaflow_Grout-Pak_CF.pdf

Pudleiner, D. K. (2016). *Design consideration based on size effects of anchored carbon fiber reinforced polymer (CFRP) system* [Master's thesis, The University of Texas at Austin]. Texas Scholar Works. http://hdl.handle.net/2152/39031

Quinn, K. T. (2009). *Shear strengthening of reinforced concrete beams with carbon fiber reinforced polymer (CFRP) and improved anchor details* [Master's thesis, The University of Texas at Austin]. Texas Scholar Works. http://hdl.handle.net/2152/ETD-UT-2009-12-508

Shield, C., & Bergson, P. (2018, February). *Experimental shear capacity comparison between repaired and unrepaired girder ends* (Minnesota Department of Transportation Report No. MN/RC 2018-07). University of Minnesota. http://www.dot.state.mn.us/research/reports/2018/201807.pdf

Sika Corporation. (2015). *Product data sheet SikaWrap® FX-50C: Carbon fiber rope for structural connection and anchoring of SikaWrap strengthening systems* (Edition 5.16.2015). Sika Corporation. https://usa.sika.com/content/dam/dms/us01/0/pds-cpd-SikaWrap-FX-50-C-us.pdf

Sika Corporation. (2018a, October). *Product data sheet Sikadur® Hex-300: High-modulus, high-strength, impregnating resin* (Version 01.01). Sika Corporation. https://usa.sika.com/content/dam/dms/us01/f/sikadur_hex-300.pdf

Sika Corporation. (2018b, August). *Product data sheet Sikadur® Hex-330: High-modulus, high-strength, impregnating resin* (Version 03.01). Sika Corporation. https://usa.sika.com/content/dam/dms/us01/0/sikadur_-330.pdf

Sika Corporation. (2018c, November). *Product data sheet Sikawrap® Hex-117C: Carbon fiber fabric for structural strengthening* (Version 01.01). Sika Corporation. https://usa.sika.com/content/dam/dms/us01/k/sikawrap_hex-117c.pdf

Sika Corporation. (2019, March). *Product data sheet Sikawrap® Hex-103C: Carbon fiber fabric for structural strengthening* (Version 01.04). Sika Corporation. https://usa.sika.com/content/dam/dms/us01/v/sikawrap_hex-103c.pdf

Unitex. (2018). *Technical data sheet Pro-Poxy® 400 epoxy gel anchor*. Dayton Superior.

## APPENDICES

**Appendix A. Flexural Strengthening Experimental Program Supplemental Details**

**Appendix B. Flexural Strengthening Experimental Program Supplemental Results**

**Appendix C. INDOT 1961 Standard Drawing—Box Beams**

**Appendix D. Past End Region Repair Research**

**Appendix E. End Region Repair Experimental Program Supplemental Details**

**Appendix F. End Region Repair Experimental Program Externally Bonded FRP Repair System Details**

**Appendix G. Spike Anchor Design Calculations**

# APPENDIX A. FLEXURAL STRENGTHENING EXPERIMENTAL PROGRAM SUPPLEMENTAL DETAILS

## A.1 Material Properties

The following subsections provide the material properties and other details of the concrete, steel reinforcement, and fiber reinforced polymer systems used during the flexural strengthening experimental program.

### *A.1.1 Concrete*

All concrete used to cast the specimens was delivered to the laboratory by a local ready-mix producer. The concrete mixture design is provided in Table A.1. The concrete was normal weight concrete with a specified 28-day compressive strength of 4,000 psi. The target slump was 4 in.

**Table A.1** Concrete Mixture Design

| Material | Details | Design Quantity | Units |
|---|---|---|---|
| Cementitious Material | Type 1 Cement | 520 | lb/yd$^3$ concrete |
| Coarse Aggregate | #8 Gravel (INDOT) | 1850 | |
| Fine Aggregate | Natural Sand | 1458 | |
| Water | – | 250.5 | |

Note:
Specified $f'_c$ = 4,000 psi
Water/Cement Ratio = 0.482
Design Spread = 25.00″ +/- 7.0″

A total of four casts were required to fabricate all specimens of the experimental program. The specimens within each group were cast from the same concrete batch, with the exception of Specimens 0-C and 1-EB.2 which were cast along with the Group 1 and Group 2 specimens, respectively. During each cast, 6-in. by 12-in. concrete test cylinders were prepared in accordance with ASTM C192 (ASTM, 2019a) and stored in the same conditions as the beam specimens. Generally, the compressive strength for each cast group was tested at 7, 14, and 28 days as well as on the test day of the beam specimens in accordance with ASTM C39 (ASTM, 2020). For Specimens 0-EB.2, 0-EB.3, 0-NSM.1, and 1-NSM.1b, concrete compressive strengths are not available for test day. Therefore, the concrete strengths for the day of the beam tests (see Figure 3.1) were estimated in consideration of strength gains for concrete used for the experimental program. It should be noted that small variations in concrete compressive strength values have only minor effects on the calculated strengths of the specimens. Prior to the compressive strength tests, a concrete cylinder end grinder was used to level the ends of each cylindrical test specimen so that they were parallel and plane. Furthermore, splitting tensile and modulus of elasticity tests were conducted in accordance with ASTM C496 and ASTM C469

(ASTM, 2017, 2019b), respectively, on the day of each flexural test on a beam specimen. For each material test that was conducted, at least two cylinders were tested and the results were averaged. The typical compressive strength gain of the concrete is provided in Figure A.1.

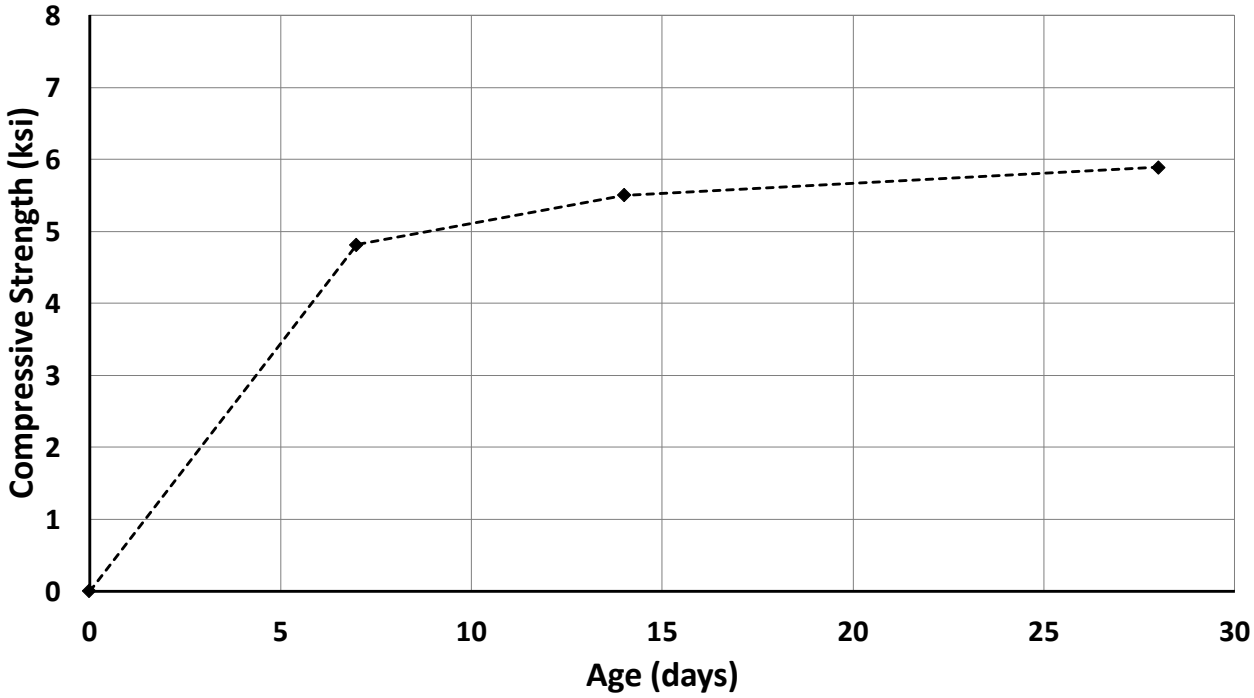


**Figure A.1** Typical concrete strength gain over 28 days.

A.1.2 Steel Reinforcement

ASTM A615 (ASTM, 2018) Grade 60 reinforcing steel was used for both the longitudinal bars and the stirrups. All longitudinal reinforcing steel used in the experimental program was rolled from the same heat. Steel tensile strength tests were performed on three sample coupons from the No. 3 longitudinal reinforcing bars using a universal testing machine. A digital imaging correlation (DIC) system was used to gather strain data and produce stress-strain curves. The resulting curves for each of the three samples are provided in Figure A.2. By considering an average value based on the three sample tests, the yield stress of the longitudinal reinforcement was determined to be 67.5 ksi. Further discussion about the yield stress used in strength calculations and an analysis tool developed for the research program is provided in Section B.1.1 of Appendix B.

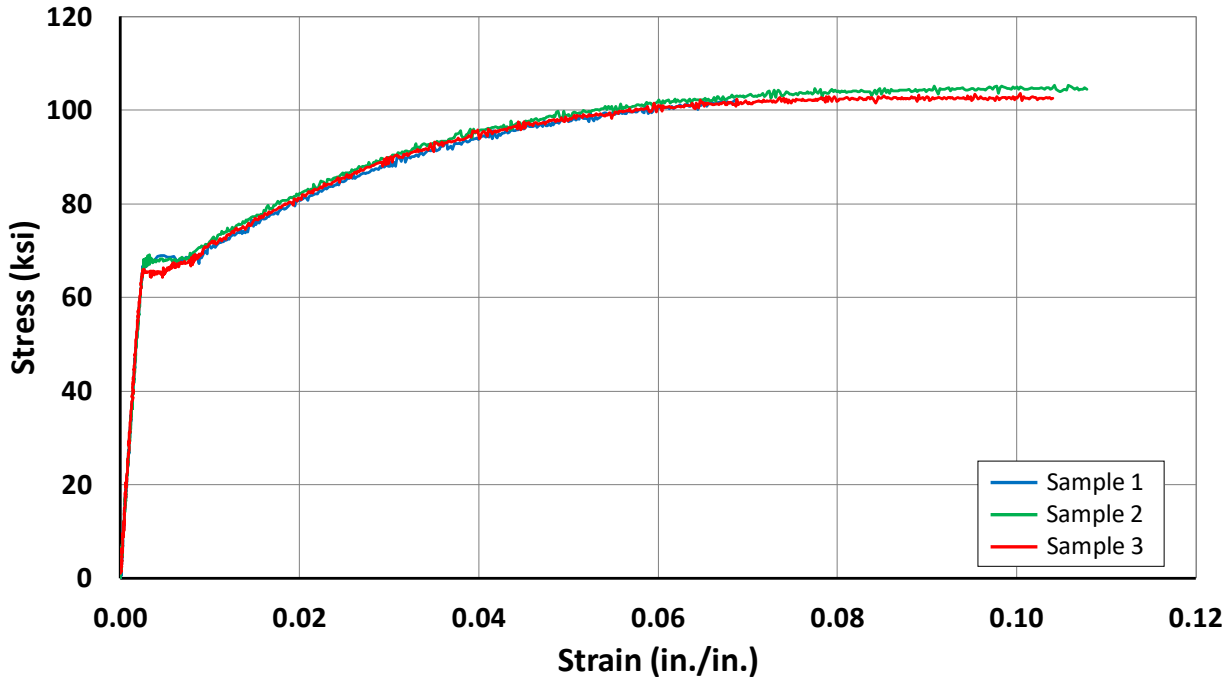


**Figure A.2** Stress-strain response of longitudinal reinforcement samples.

### A.2 Specimen Construction

In order to fabricate the specimens for the experimental program, formwork was first designed and built. Formwork used to cast each specimen was constructed from lumber. Phenolic plywood was used as the casting surface. Phenolic plywood was chosen so that the forms could be cleaned and reused multiple times. Although the number of specimens in each cast group varied, Figure A.3 provides a photograph of a typical set of forms.

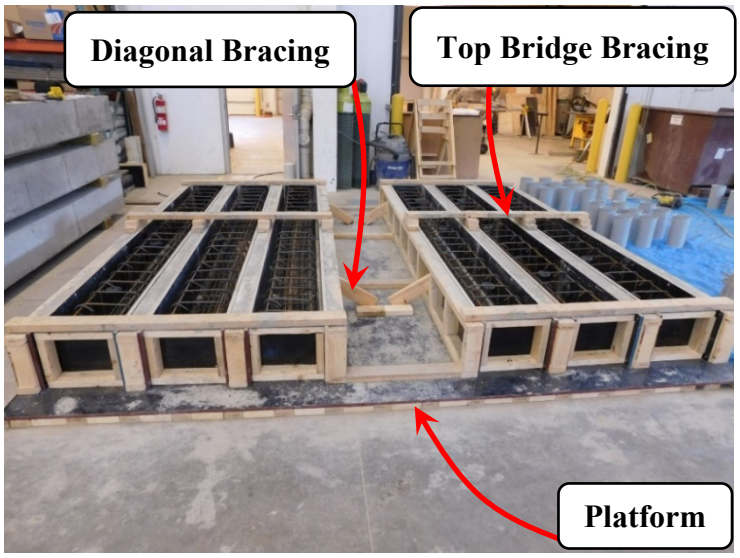


**Figure A.3** Formwork for casting a typical group of specimens.

A completed reinforcement cage installed in one of the forms is shown in Figure A.4. As indicated in the figure, spacer wheels and bar chairs were used to make certain that the reinforcement cages would not shift during casting and ensured the specified cover dimensions were met.

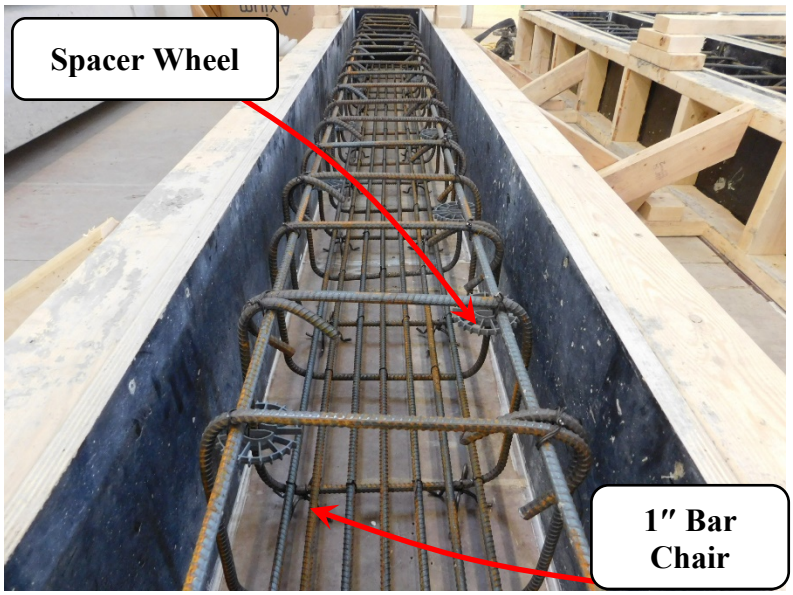


**Figure A.4** Reinforcing cage in forms.

Concrete was poured directly from the concrete truck into the forms. To ensure proper consolidation, concrete immersion vibrators were used as can be seen in Figure A.5(a). Then, the concrete was carefully finished with hand floats (see Figure A.5(b)).


**(a) Vibrating Concrete into Place**

**(b) Finishing Concrete**

**Figure A.5** Casting process.

Before the end of the casting day, the freshly cast specimens were covered with wetted burlap blankets (see Figure A.6(a)), followed immediately by a plastic tarp to contain moisture (see Figure A.6(b)). After seven days, the burlap and tarp coverings were removed and the specimens were removed from the forms.

**(a) Burlap Blankets**

**(b) Plastic Tarp**

**Figure A.6** Curing process.

## A.3 Strengthening System Installation Procedures

The application procedures for the FRP strengthening systems included in the experimental program are described in the following subsections. With the exception of Specimen 1-NSM.1b, the beams were inverted prior to the application of the FRP sheets or strips in order to easily access the tension face. After application of an FRP system was completed, the strengthening system was allowed to cure for a minimum of 7 days before the beam was tested.

### *A.3.1 Externally Bonded Sheets*

#### A.3.1.1 Surface Preparation and FRP Application

For all bond-critical applications of externally bonded strengthening systems, concrete substrate preparation must be performed. As shown in Figure A.7(a), the surface area of concrete to which the FRP was to be applied was first roughened with a grinding wheel to a concrete surface profile (CSP) of 3. Concrete surface profiles, ranging from 1 to 10, are defined by ICRI 310.2R-2013. ICRI 330.2-2016 (ICRI, 2013, 2016) states that concrete surfaces are to be prepared to a surface profile not less than CSP 3 for externally bonded FRP fabric. This is also consistent with ACI 440.2R-17 (ACI Committee 440, 2017). A set of CSP chips were used as a reference to verify adequate surface roughness. Furthermore, as pictured in Figure A.7(b and c), 0.5-in. diameter holes with a depth of 4 in. were drilled into the concrete for the FRP spike anchors at the locations indicated in Figure 2.7(a and b) and Figure 2.8(a and b) to comply with the recommendation from Quinn (2009) stating that anchor holes should be 40% larger than the area of the FRP anchor. To reduce stress concentrations in the FRP at the edges of the holes, a rotary tool was used to round the edges to a minimum radius of 0.5 in., as specified by ICRI 330.2-2016

and ACI 440.2R-17 (ACI Committee 440, 2017; ICRI, 2016) (Figure A.7(d)). Finally, a wire brush and compressed air were used to clean the holes and concrete surface to remove dust and foreign particles before the FRP was applied.

**(a) Grinding Concrete Substrate**

**(b) Drilling Anchor Holes**

**(c) Drilled Anchor Hole Prior to Rounding Edges**

**(d) Rounding Edges of Anchor Holes**

**Figure A.7** Surface preparation for externally bonded strengthening system.

A wet-layup application process was implemented in which the dry carbon fiber fabric was impregnated with epoxy prior to placement onto the prepared and sealed concrete surface. The process of sealing the concrete surface simply involves applying a thin layer of the epoxy onto the surface using a common paint roller to fill any air voids and ridges, resulting in a level resin layer (Figure A.8(a)). Next, spare FRP rope material, saturated with epoxy, was used to prepare the concrete surface inside the pre-drilled anchor holes (Figure A.8(b)). Then, prior to installing the fiber sheet on the specimen, it was impregnated with the same epoxy used to seal the concrete surface (Figure A.8(c)). This process was performed using the same roller type that was used to apply the thin layer of epoxy onto the concrete surface. The sheet was then placed on the tension face of the specimen (Figure A.8(d)). Once in place, plastic laminating rollers were used to ensure the fibers were fully impregnated with epoxy and to smooth out any air pockets (Figure A.8(e)). After fully impregnated, squeegees were used to remove excess epoxy from the sheet (Figure A.8(f)).

**(a) Sealing Concrete Surface**

**(b) Coating Inside of Drilled Holes with Epoxy**

**(c) Saturating FRP Sheet**

**(d) Placing FRP Sheet**

**(e) Rolling FRP Sheet to Eliminate Air Pockets**

**(f) Removing Excess Epoxy with Squeegee**

**Figure A.8** Application of externally bonded sheets.

A.3.1.2 Installation of FRP Anchors and Patches

After the FRP longitudinal sheets were applied, the FRP spike anchors were installed. The details of the anchors are provided in Figure 2.7(b) and Figure 2.8(b). In order to insert the FRP anchors through the longitudinal sheet applied to the beam and into the section of the specimen, a razorblade was used to separate the fibers in the sheet to expose the drilled holes (Figure A.9(a)), resulting in the condition shown in Figure A.9(b). Each spike anchor was cut from the FRP rope

and had a total length of 10 in. consisting of a 4-in. embedment depth and 6-in. fan length (Figure A.9(c)). A steel double loop rebar tie was used to hold the fibers of an individual anchor together near the end that was to be inserted into a hole on the tension face of the beam. Prior to installing an anchor in the beam, the anchor was fully submerged into a container of epoxy. The FRP anchor was then inserted into the hole in the beam (Figure A.9(d)). The rebar tie aided with inserting the spike anchors and was left with the anchor inside the holes. Once inserted, the anchor was fanned out at a 60-degree angle (Figure A.9(e)). As shown in Figure A.9(f), additional epoxy was applied to the anchor using a paint brush with special consideration given to ensuring the fibers toward the center of the bundle were fully saturated.

**(a) Separating Fibers with Razor Blade**

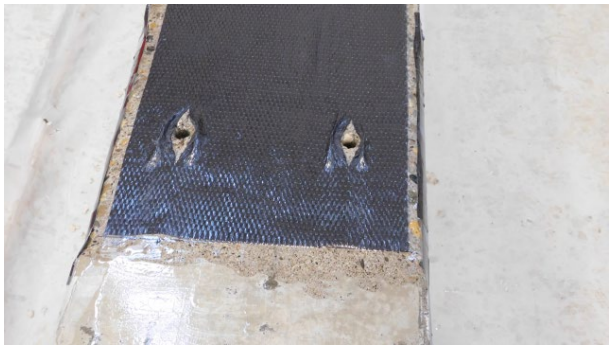

**(b) Exposed Anchor Holes**

**(c) Cut FRP Anchors**

**(d) Inserting Anchor**

**(e) Fanned-Out Anchors**

**(f) Saturating Anchors**

**Figure A.9** Installation of FRP anchors for externally bonded strengthening system.

After the FRP spike anchors were installed, two 12-in. by 12-in. patches, the first with the fibers oriented transversely to the longitudinal sheet and the second with the fibers oriented parallel to the longitudinal sheet, were subsequently placed over the top of the FRP anchors as shown in Figure A.10. The patches were prepared and installed in a similar manner as the longitudinal FRP sheets. The patches were first saturated using a roller (Figure A.10(a)) and then placed over the top of the two anchors (Figure A.10(b)). As with the longitudinal sheets, a plastic laminating roller and squeegee were used to ensure the fibers were fully impregnated with epoxy, smooth out any air pockets, and remove excess epoxy from the patch. A patch with the final anchor configuration is shown in Figure A.10(c).

**(a) Saturating Patch Sheets**

**(b) Placing Patch Sheets**

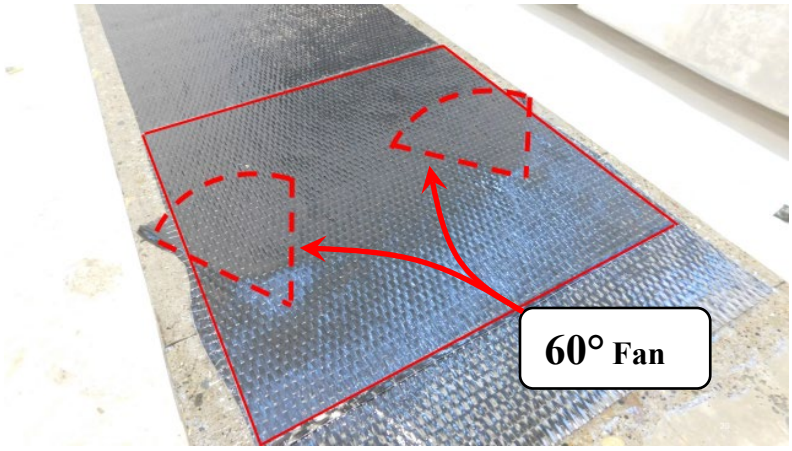


**(c) Patch Sheet with Final Anchor Configuration**

**Figure A.10** Application of patches over FRP anchors.

A.3.1.3 Installation of FRP U-Wrap Anchors (EB.3)

As described in Chapter 3, U-wrap anchors were tested in the pilot group (Specimen 0-EB.3), but FRP spike anchors were determined to be better option compared to U-wrap anchors located near the ends of the longitudinal sheet, especially for adjacent box beams. For installation of the U-wrap anchors, a grinding wheel was used to roughen the concrete substrate along the sides of the specimen where the anchors were to be installed to a concrete surface profile (CSP) of 3 (ICRI,

2013). According to ICRI 330.2-2016 and ACI 440.2R-17 (ACI Committee, 2017; ICRI, 2016), outside corners and sharp edges over which FRP sheets are wrapped should be rounded to a minimum radius of 0.5 in. The grinding wheel was used to round the appropriate edges to the specified radius of 0.5 in. as shown in Figure A.11.

**(a) Rounding Edges** **(b) Verifying Minimum Radius**

**Figure A.11** Additional surface preparation for U-wrap anchors.

Application of the longitudinal FRP sheet on the specimen with U-wrap anchors followed the same wet-layup procedure described in Section A.3.1.1 of Appendix A (Figure A.12(a)). The application of the U-wrap anchors also followed this procedure (Figure A.12(b)).

**(a) Placing Longitudinal Sheet** **(b) Placing U-Wrap Anchor**

**Figure A.12** Application of FRP on specimen with U-wrap anchors.

*A.3.2 Near-Surface-Mounted Strips: Surface Preparation and FRP Application*

The strips of the near-surface-mounted strengthening system are to be completely enclosed in the section of the beam. Grooves were therefore required to be cut along the length of the tension face. A tuckpointing grinder with a 0.25-in. thick diamond cutting blade was used to cut grooves into the specimen that were 0.25-in. wide and 0.875-in. deep. The dimensions of the NSM strips were 0.079-in. wide by 0.63-in. tall. According to ACI 440.2R-17, the suggested depth of a groove for a rectangular strip is at least 1.5 times the largest dimension of the strip (ACI

Committee 440, 2017). Furthermore, the manufacturer of the epoxy grout used for all NSM specimens except Specimen 1-NSM.1b (see Section 2.4) specifies a minimum grout depth of 1 in. (Pilgrim, n.d.). Due to the relatively shallow clear cover at the tension face of the beam members, a depth of 0.875 in. was used to prevent cutting into a stirrup. Similarly, ACI 440.2R-17 suggests that the width of a groove for a rectangular strip be at least 3.0 times the smallest dimension of the strip (ACI Committee 440, 2017). Therefore, the 0.25-in. wide groove meets this suggested dimension because it is larger than 3.0 times 0.079 in., or 0.237 in. The clear groove spacing of 1.25 in. (see Figure 2.10) was based on the spacing of the steel reinforcement in the member. This is inconsistent with the suggestions in ACI 440.2R-17 which would require the clear groove spacing to be 1.75 in. in this case. A steel angle was clamped onto the specimen as shown in Figure A.13 in order to ensure a straight line was cut at a constant depth. Once both of the grooves were cut, compressed air was used to remove any dust and particles before the FRP strips were inserted into the grooves.


**Figure A.13** Cutting NSM grooves.

Next, epoxy grout was poured to fill approximately one quarter of the groove (Figure A.14(a)). Each NSM strip was then put into place by moving it back and forth in a sawing motion to ensure satisfactory bond was achieved between the epoxy grout and the concrete substrate (Figure A.14(b)). The strips were inserted such that they were approximately centered within the depth of the groove. Epoxy grout was then pushed into the groove and leveled to match the surface of the specimen. Excess epoxy grout was removed using a squeegee as shown in Figure A.14(c).

**(a) Filling Groove with Epoxy Grout**

**(b) Inserting NSM Strips**

**(c) Leveling Off Excess Epoxy Grout**

**Figure A.14** Installation of NSM strips.

Specimen 1-NSM.1b was added to the test program in order to verify the feasibility of applying the epoxy overhead. Photographs of the application are provided in Figure A.15. Unitex® Pro-Poxy™ 400 Anchoring Gel (Unitex, 2018) was used in lieu of the Pilgrim Permocoat Magmaflow Grout-Pak CF Epoxy Grout (Pilgrim, n.d.), which was used for all other NSM specimens in the test program. After consulting with the manufacturer of the NSM strips, the Unitex® Pro-Poxy™ was chosen for the overhead application due to its high viscosity. A dispenser gun was used to inject the epoxy into each groove (Figure A.15(a)). Once the groove was roughly halfway filled with epoxy, the NSM strip was inserted such that it was approximately centered within the depth of the groove (Figure A.15(b)). Excess epoxy was squeegeed away and added where needed so that the epoxy was level with the surface of the specimen. Overall, the installation was successful, and once the installation was completed, no sagging of the epoxy from the grooves was observed.

**(a) Filling Groove with Epoxy**

**(b) Inserting NSM Strip**

**Figure A.15** NSM overhead application.

## A.4 Test Setup and Procedure

Each of the 22 beam specimens was monotonically loaded to failure in four-point bending using the loading configuration shown in Figure A.16. The test setup used for the tests is illustrated in Figure A.17, and a photograph of the setup is provided in Figure A.18.

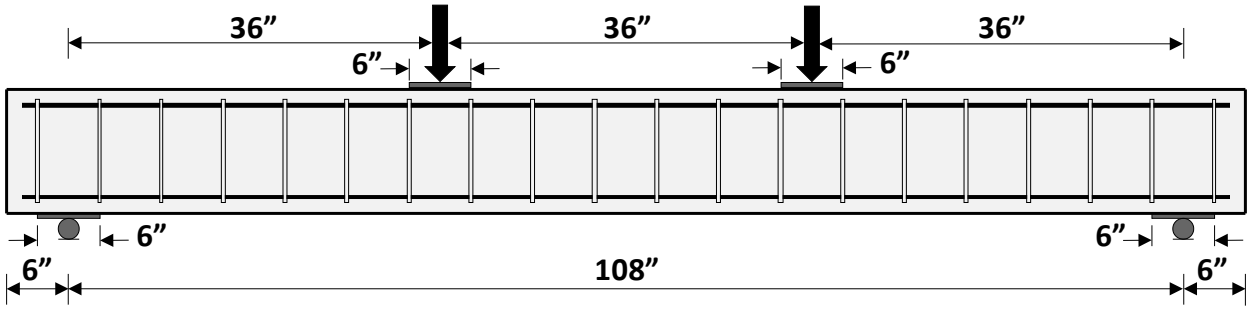


**Figure A.16** Loading configuration.

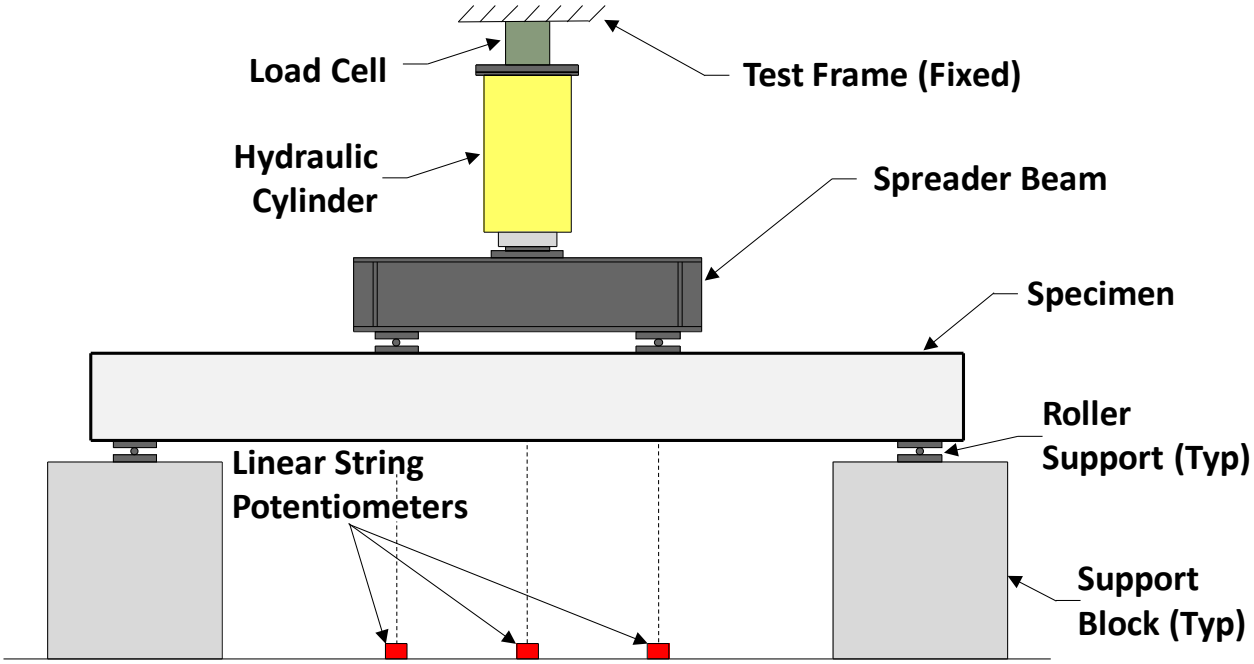


**Figure A.17** Elevation view of test setup.

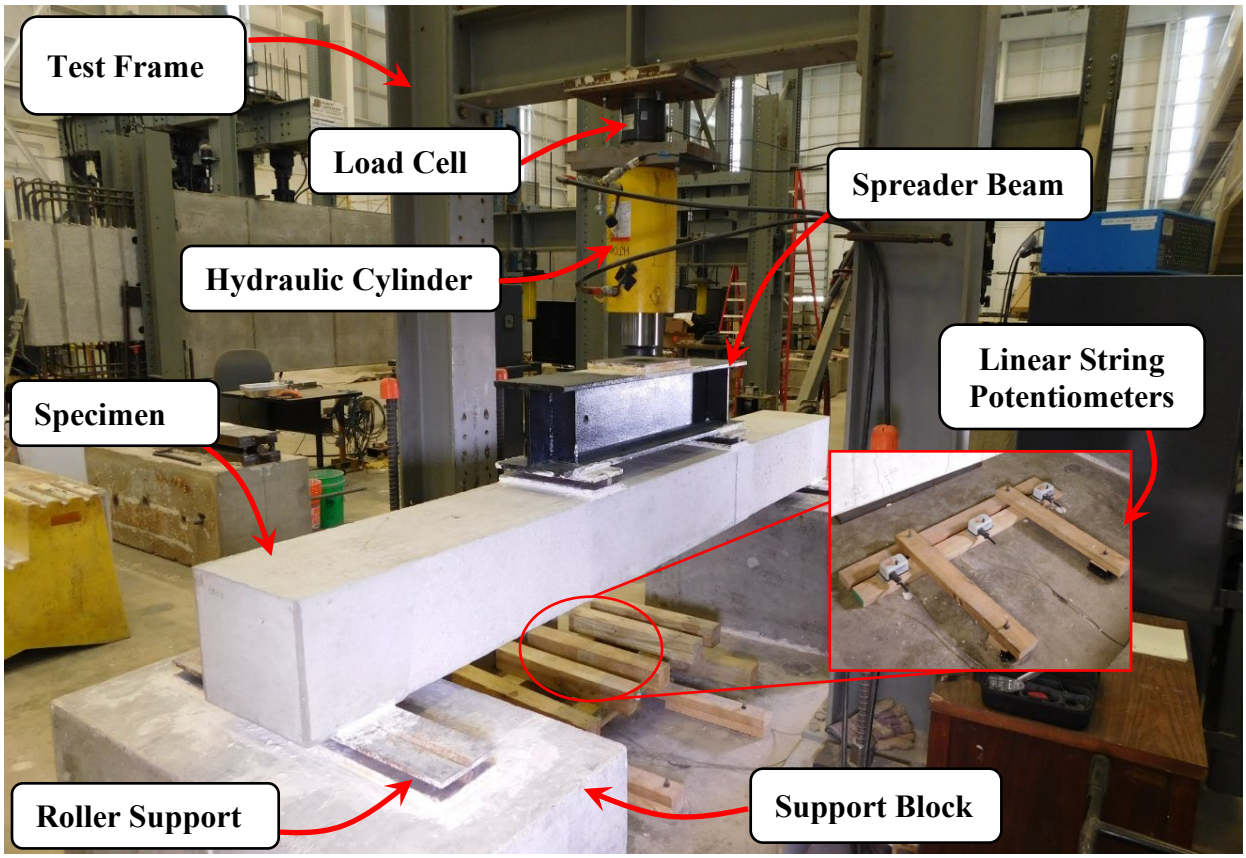


**Figure A.18** Photograph of test setup.

As indicated in Figure A.17 and Figure A.18, a hydraulic cylinder was used to apply load through a spreader beam to the third points of the specimens. A load cell with a 55-kip capacity was installed in series with the hydraulic cylinder in order to directly measure the total load applied to the beam. Rollers were used under the spreader beam at each point of load application to the specimen. The load plates on the specimen extended across the 14-in. width of the member. The specimen was supported on roller supports at both ends to allow for equal elongation of the tension face in both directions, thus producing a symmetric deflected shape. Linear string potentiometers were used to capture displacements at midspan and under the load points by measuring displacements of the bottom edge of one side of the member relative to a stationary point on the ground. For the specimens in Group 3, displacements at these three locations along the length of the member (midspan and under the load points) were measured on both bottom edges of the member in order to capture any differential displacements between the sides due to the eccentric reinforcement within these specimens.

At the beginning of each test, the specimen was loaded to 5 kips (2.5 kips at each load point) followed by 1-kip increments, or load steps, until flexural cracking was observed and marked with felt-tipped markers. The load was then increased to the next multiple of 3 kips and cracks were marked. Additional load was then applied in 3-kip increments until failure occurred. Once yielding was observed in unstrengthened specimens with no FRP, load steps were defined by each additional 0.5 in. of midspan displacement instead of 3-kip load increments until failure occurred. Cracks were marked and photographs were taken at the end of each load step with the exception of the load steps immediately preceding an imminent failure due to safety concerns. Failure of the unstrengthened specimens was characterized by concrete crushing in the compression region, accompanied by a decrease in load-carrying capacity. Failure of the FRP-strengthened specimens occurred when the beams experienced a sudden drop in load-carrying capacity due to the rupture or slip of the FRP. A high-speed camera, capturing images at 4,000 frames per second, was used to better understand failure modes of the specimens with externally bonded FRP (Figure A.19).

**Figure A.19** High-speed camera.

## REFERENCES FOR APPENDIX A


ACI Committee 440. (2017). *ACI 440.2R-17: Guide for the design and construction of externally bonded FRP systems for strengthening concrete structures*. American Concrete Institute.

ASTM. (2017). *ASTM C496/C496M-17: Standard test method for splitting tensile strength of cylindrical concrete specimens*. ASTM International https://doi.org/10.1520/C0496_C0496M-17

ASTM. (2018). *A615/A615M-18: Standard specification for deformed and plain carbon-steel bars for concrete reinforcement*. ASTM International. https://doi.org/10.1520/A0615_A0615M-18

ASTM. (2019a). *ASTM C192/C192M-19: Standard practice for making and curing concrete test specimens in the laboratory.* ASTM International. https://doi.org/10.1520/C0192_C0192M-19

ASTM. (2019b). *ASTM C469/C469M-19: Standard test method for static modulus of elasticity and Poisson's ratio of concrete in compression.* ASTM International. https://doi.org/10.1520/C0192_C0192M-19

ASTM. (2020). *ASTM C39/C39M-20: Standard test method for compressive strength of cylindrical concrete specimens*. ASTM International. https://doi.org/10.1520/C0039_C0039M-20

ICRI. (2013). *ICRI Guideline No. 310.2R: Selecting and specifying concrete surface preparation for sealers, coating, polymer overlays, and concrete repair.* International Concrete Repair Institute.

ICRI. (2016). *ICRI Guide No. 330.2: Guide specifications for externally bonded FRP fabric systems for strengthening concrete structures.* International Concrete Repair Institute.

Pilgrim. (n.d.). *Magmaflow Grout-Pak CF*. Tampa, FL: Pilgrim Permocoat, Inc.

Unitex. (2018). *Technical data sheet Pro-Poxy® 400 epoxy gel anchor*. Dayton Superior.

# APPENDIX B. FLEXURAL STRENGTHENING EXPERIMENTAL PROGRAM SUPPLEMENTAL RESULTS

## B.1 Load-Deflection Behavior from Analysis

An analysis tool was developed in Mathcad 15.0 to create theoretical load-deflection curves for specimens within the experimental program. The beam analyses provided results that allow key comparisons to be made with the experimental results of the test program. More specifically, one of the primary intentions of the analysis tool was to better understand the strains/stresses in the FRP of the test specimens and thus evaluate each strengthening system. Even though two FRP-strengthened specimens (0-EB.2 and 0-NSM.1) experienced some concrete crushing prior to failure of the FRP, all strengthened specimens ultimately failed due to FRP rupture or slip (see Chapter 3). That is, any crushing prior to failure of the FRP did not result in a significant loss in load-carrying capacity. The estimated stress in the FRP at failure obtained from the analysis results is useful in gaining a better understanding of the performance of the strengthening systems. The analysis also allowed the approximate stresses in the steel reinforcement at failure of the specimens to be estimated. Comparisons of the theoretical load-deflection curves to the response curves based on tests demonstrated the viability of using simple models to approximate the flexural behavior of FRP-strengthened members.

### *B.1.1 Input Values*

The analysis tool considered the geometric information of each specimen as well as the stress-strain properties of the following materials: concrete, steel, and FRP. To calibrate the model, some material properties were adjusted based on the experimental data in order to best model the behavior of the strengthening systems.

For concrete in compression, the stress-strain relationship was based on the Hognestad (1951) model, as indicated in Figure B.1 and given as,

$$f_c = f_c' \left[ 2\frac{\varepsilon}{\varepsilon_0} - \left(\frac{\varepsilon}{\varepsilon_0}\right)^2 \right] \qquad \text{Equation B.1}$$

Here, the value of the concrete strain at peak stress, $\varepsilon_0$, was assumed to be equal to,

$$\varepsilon_0 = \left(1 + \frac{\sqrt{2}}{2}\right)\frac{f_c'}{E_c} \qquad \text{Equation B.2}$$

where $E_c$ is taken as $57{,}000\sqrt{f_c'}$ (psi). This formula for $\varepsilon_0$ assumes that $E_c$ is the secant modulus defined by the slope of a line through the origin and the point corresponding to $0.5f'_c$ on the stress-strain curve. The value of the concrete strength, $f'_c$, was input for each specimen based on cylinder tests described in Section A.1.1 of Appendix A. The concrete model assumed an ultimate concrete strain of 0.0038. Unlike the Hognestad (1951) model, which incorporates a

linear descending branch, the parabolic relationship given above was used to define the entire concrete curve in compression.

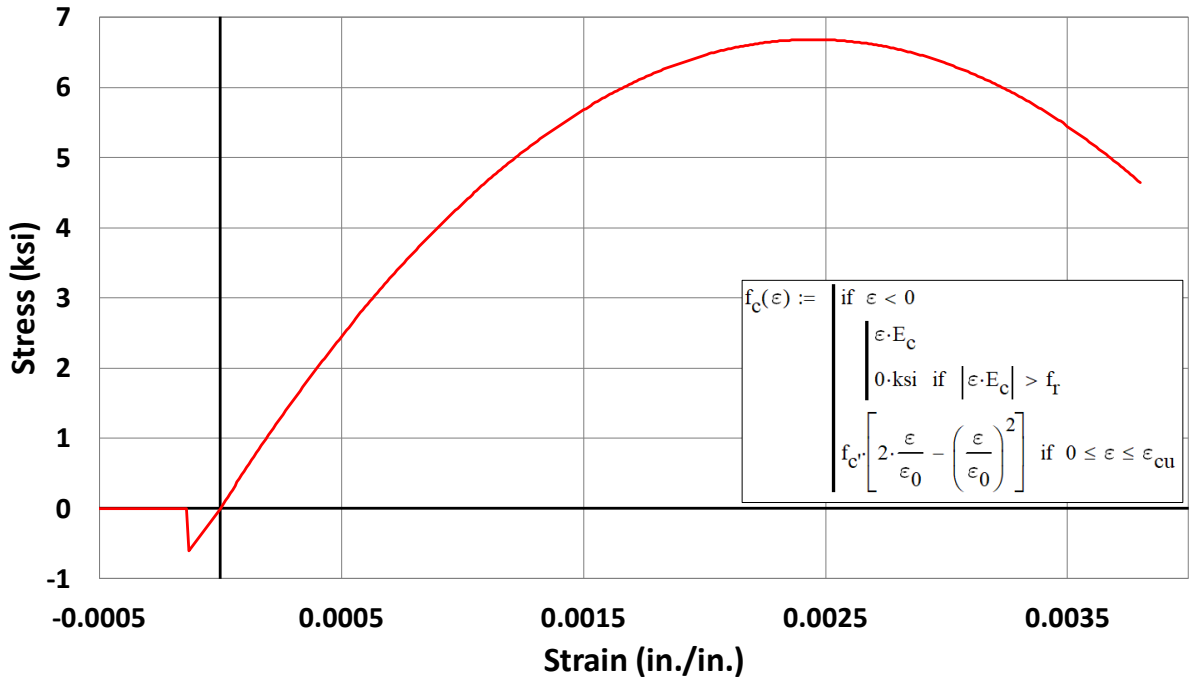


**Figure B.1** Stress-strain model for concrete.

For concrete in tension, the stress-strain curve was assumed to be linear with a slope of $57{,}000\sqrt{f_c'}$ (psi) until the modulus of rupture, $f_r$, was reached, as indicated in Figure B.1. The modulus of rupture was taken as $7.5\sqrt{f_c'}$ (psi).

The stress-strain relationship for the steel reinforcement in tension used in the analysis tool, presented in Figure B.2, was based on the tensile tests conducted on reinforcing bar samples described in Section A.1.2 of Appendix A. With the full response of the bars obtained using DIC, the assumed stress-strain relationship for the analysis was first defined in a manner that followed the responses obtained through the tests. The yield strength, $f_y$, input into the model was calibrated once the load-deflection plots for the specimens output by the analysis tool were compared to results from the beam tests. To better fit the experimental results, it was decided to use the yield strength reported on the mill certificate for the reinforcing bars (70.199 ksi) rather than the average yield strength obtained from the tensile tests utilizing DIC (67.52 ksi). In other words, the yield strength reported on the mill certificate resulted in theoretical load-deflection plots that better matched the responses of test specimens. The assumed stress-strain relationship in the strain-hardening range used in the analysis tool was still based on the strain-hardening behavior of the reinforcement obtained from the DIC results. The stress-strain response from the bar tests are shown in Figure B.2 along with the assumed stress-strain relationship incorporated into the analysis tool. In compression, the stress-strain relationship was assumed to be elastic-perfectly plastic with a yield strength of 70.199 ksi.

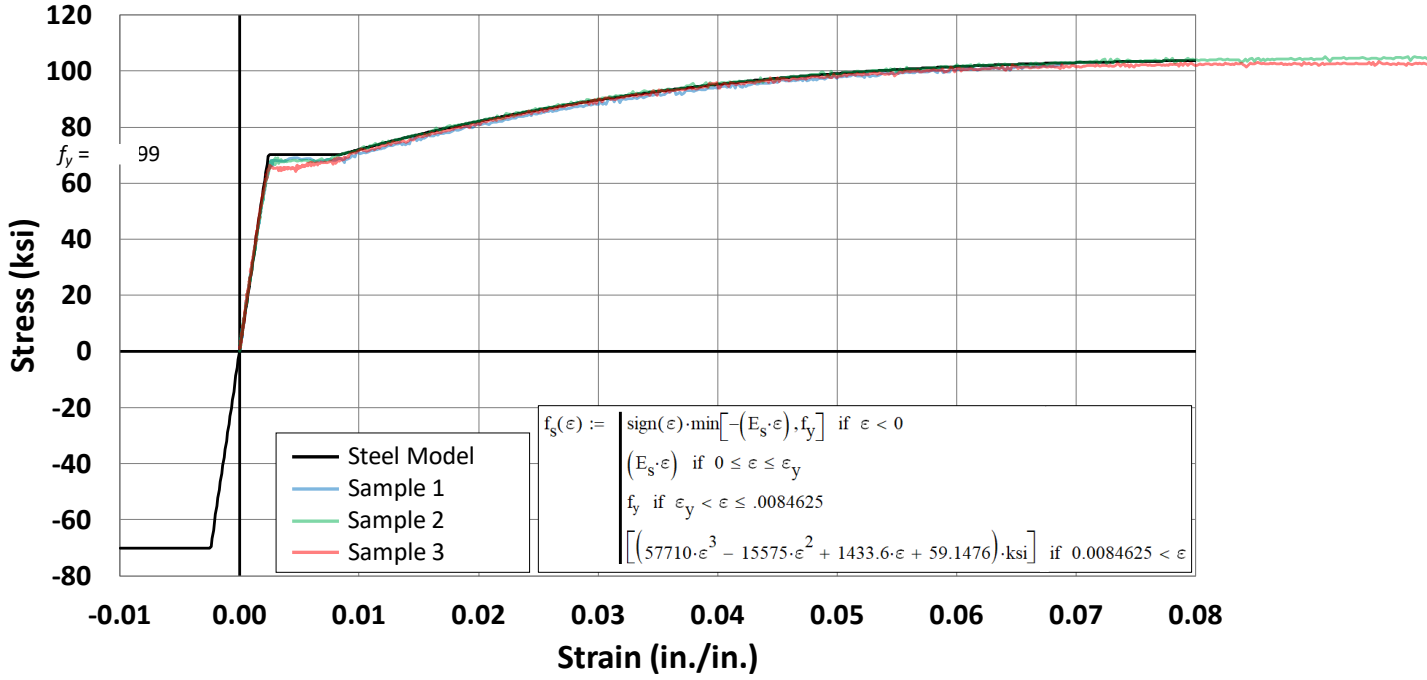


**Figure B.2** Stress-strain model for steel reinforcement.

The stress-strain behaviors of the externally bonded FRP sheets and the near-surface-mounted FRP strips were assumed to be linear. Initially, the input values for the modulus of elasticity were assumed to be equal to the values given on the product data sheets from the manufacturers of both the FRP sheets (8,200 ksi) and strips (18,000 ksi). When the resulting theoretical load-deflection plots were compared to load-deflection plots from the beam tests, it was clear that these assumed stiffness values did not accurately reflect the effective stiffnesses of the FRP reinforcement used to strengthen the specimens. More specifically, the slopes of the theoretical and experimental load-deflection plots after yielding of the reinforcing bars did not correlate well. The values for the modulus of elasticity were therefore calibrated so that the post-yield slopes of the theoretical load-deflection plots and the experimental load-deflection plots are similar. It was determined that the effective stiffnesses of the FRP strengthening systems installed on the beams were greater than the design values initially assumed. The values used in the analysis tool were 8,530 ksi for the externally bonded sheets and 21,000 ksi for the NSM strips (see Figure B.3). Determining the correct stiffness of the FRP is important for estimating the stress in the FRP at failure of the beam specimens, as described in Section B.1.3. Because the analyses were used to estimate the stress in the FRP at failure, the tensile strengths of the FRP materials were selected to ensure that the failure load achieved by the experimental specimen being modeled was reached prior to rupture of the FRP in the analytical model.

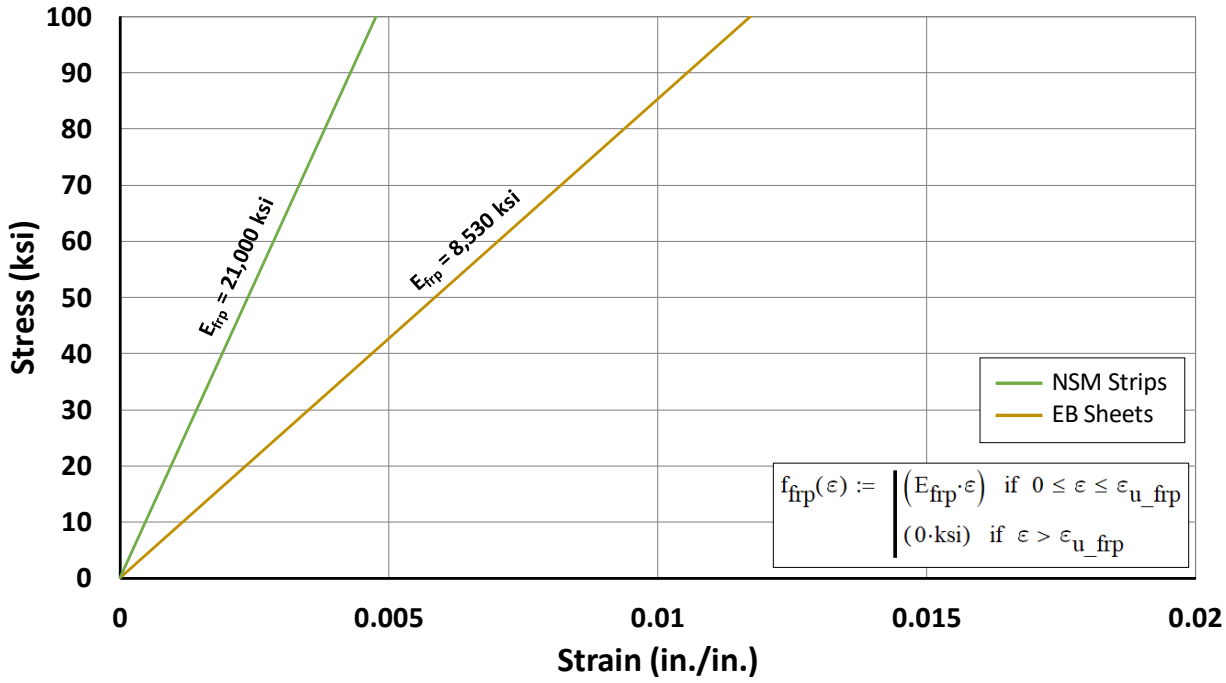


**Figure B.3** Stress-strain model for FRP.

For the steel and FRP reinforcement, nominal areas for the bars, sheets, and strips were used within the analyses.

*B.1.2 Analysis*

To develop a theoretical load-deflection plot for specimens of the test program, the analysis tool first develops a moment-curvature plot considering a cross section of the member. By enforcing internal equilibrium, strain compatibility (i.e., plane sections remain plane and assuming strain compatibility between the concrete and the FRP and steel reinforcement), and the stress-strain responses described in the previous sections, corresponding moment and curvature values are found for increments of the concrete strain at the top fiber of the member ranging from 0 to the ultimate concrete strain. An example moment-curvature plot developed by the analysis tool in Mathcad 15.0 is shown in Figure B.4.

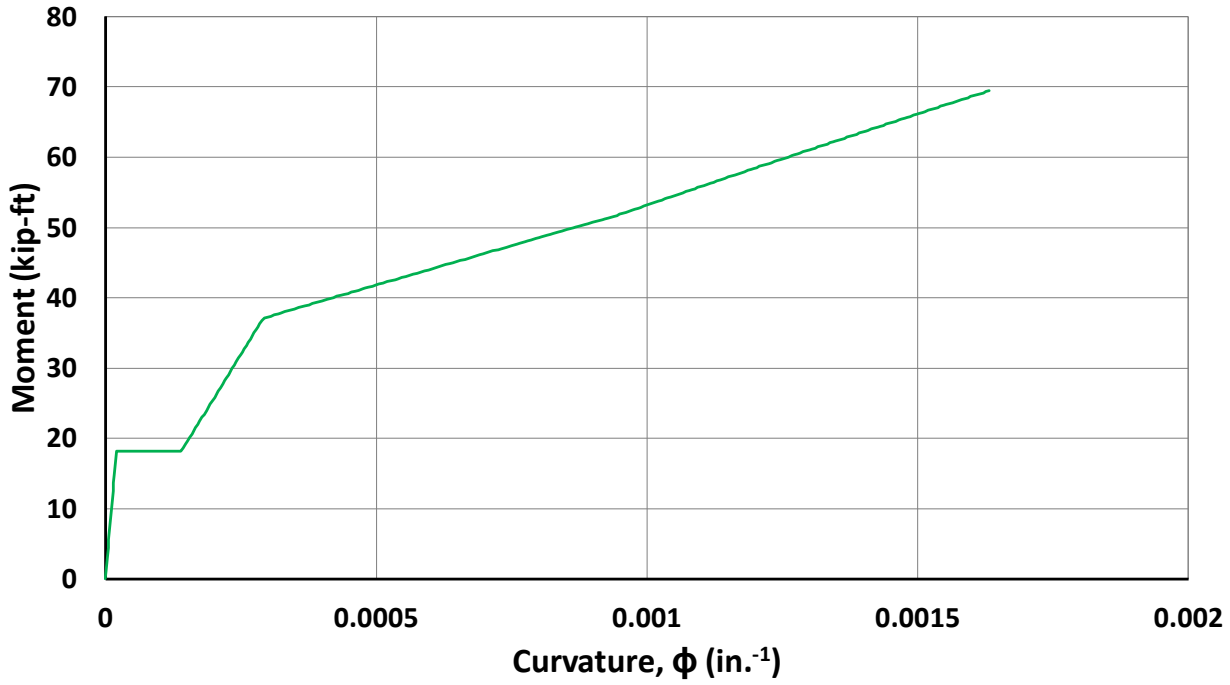


**Figure B.4** Example moment-curvature plot.

Because material strains and stresses at numerous stages are required to develop the moment-curvature plot for a member, the analysis tool can be used to obtain valuable information about the state of stresses and strains in the beam given any applied moment. For example, the tool allows the strain in the reinforcing bars and the strain in the FRP sheets or strips to be easily obtained for any moment acting on the member cross section. Therefore, the tool can be used to determine the estimated state of stress in the FRP strengthening system at the experimentally-determined failure load. This value can then be compared to the effective stress in the FRP, $f_{fe}$, as defined by ACI 440.2R-17 or the tensile strength reported by the manufacturer, $f_{fu}^*$, effectively determining the efficiency of the FRP strengthening system installed on a beam specimen. The value of $f_{fu}^*$ is defined by ACI 440.2R-17 and ACI 440.1R-15 (ACI Committee 440, 2015, 2017) as the average tensile strength of a sample of FRP specimens minus three times the standard deviation. An estimate of the stress in the reinforcing steel at the maximum applied load can also be obtained from the analysis tool. Because the reinforcing steel in the test specimens entered into the strain-hardening range, having an estimate of the actual stress in the steel at failure of the specimen is useful.

Using the moment-curvature plot along with the known bending moment diagram resulting from the three-point bending test configuration, the analysis tool develops a series of relationships describing the curvature over the length of the member for various increments of the applied load. An example of the curvature over the member length is given for Specimen 1-EB.2 under an applied load $P$ of 10 kips in Figure B.5.

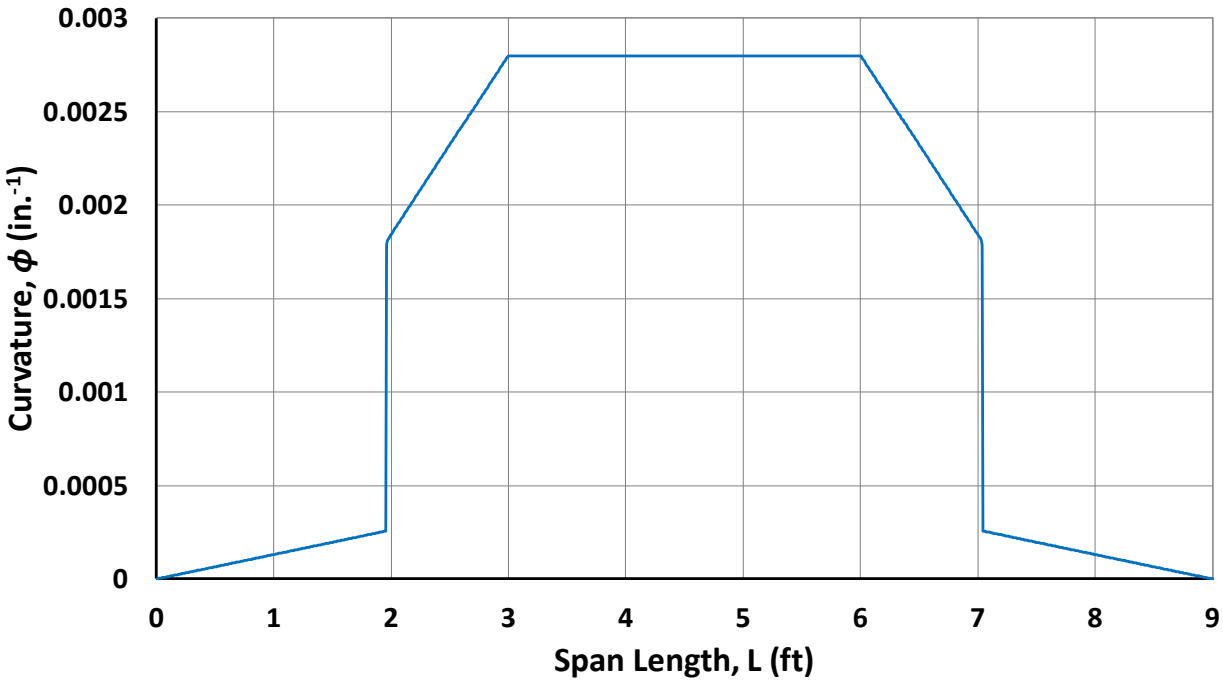


**Figure B.5** Example plot of curvature over member length.

The analysis tool then applies the second moment-area theorem (Hibbeler, 2012) to calculate the midspan deflection of the member being modeled for each increment of the applied load for which the curvature over the member length was determined. The equation used within the tool to calculate the midspan deflection, δ, is,

$$\boldsymbol{\delta = \int_0^{L/2} \phi(x) \cdot x dx} \qquad \text{Equation B.3}$$

where $\phi(x)$ is the curvature along the member length, $x$ is the distance along the member measured from the support, and $L$ is the beam span. It should be noted that the self-weight of the beam and the weight of the spreader beam was neglected within the theoretical analysis for simplicity.

*B.1.3 Results*

For each subsection in Section 3.4, figures are provided that compare the theoretical load-deflection plots from the analysis tool to the experimental load-deflection plots. It should be noted that the specimens with cut bars could not be accurately modeled, and therefore, theoretical load-deflection plots are not provided for these beams. Except for these specimens, the estimated stress in the FRP from the analysis corresponding to the maximum applied load during the experiments, $f_{f\_max}$, is reported within Sections 3.3 and 3.4 along with the estimated stress in the steel reinforcement, $f_s$, corresponding to the maximum applied load.

As an example, both the theoretical and experimental load-deflection plots for Specimen 1-EB.2 are shown in Figure B.6. The theoretical response is shown as a solid line up to the load that corresponds to an FRP stress equal to the effective stress $f_{fe}$ calculated in accordance with ACI 440.2R-17. The response is shown as a dashed line beyond this point and is terminated at the load corresponding to the maximum load applied to the test specimen. Using the analysis tool, the value of the stress in the FRP reinforcement, $f_{f\_max}$, and the stress in the steel reinforcement, $f_s$, corresponding to the maximum applied load is obtained assuming strain compatibility between the concrete and reinforcement. For Specimen 1-EB.2 these values are 148.19 ksi and 77.15 ksi, respectively. It is recognized that a discrepancy does exist between the theoretical and experimental responses as can be expected for most simple analytical models that are compared to results from structural tests. Nevertheless, the stress values obtained from the analysis provide a means to compare results from the tests and better understand the relative performance of the FRP strengthening systems. If the stress values were chosen based on the point in Figure B.6 at which the theoretical curve corresponds to the midspan deflection of the specimen at the maximum load applied during the test, the values of $f_{f\_max}$ and $f_s$ differ by 16.05 ksi and 1.66 ksi, respectively, relative to the values given above (148.19 ksi and 77.15 ksi). The values of $f_{f\_max}$ and $f_s$ provided in Chapter 3 should primarily be used to compare the results between specimens rather than taken as an accurate representation of the stresses reached by the materials.

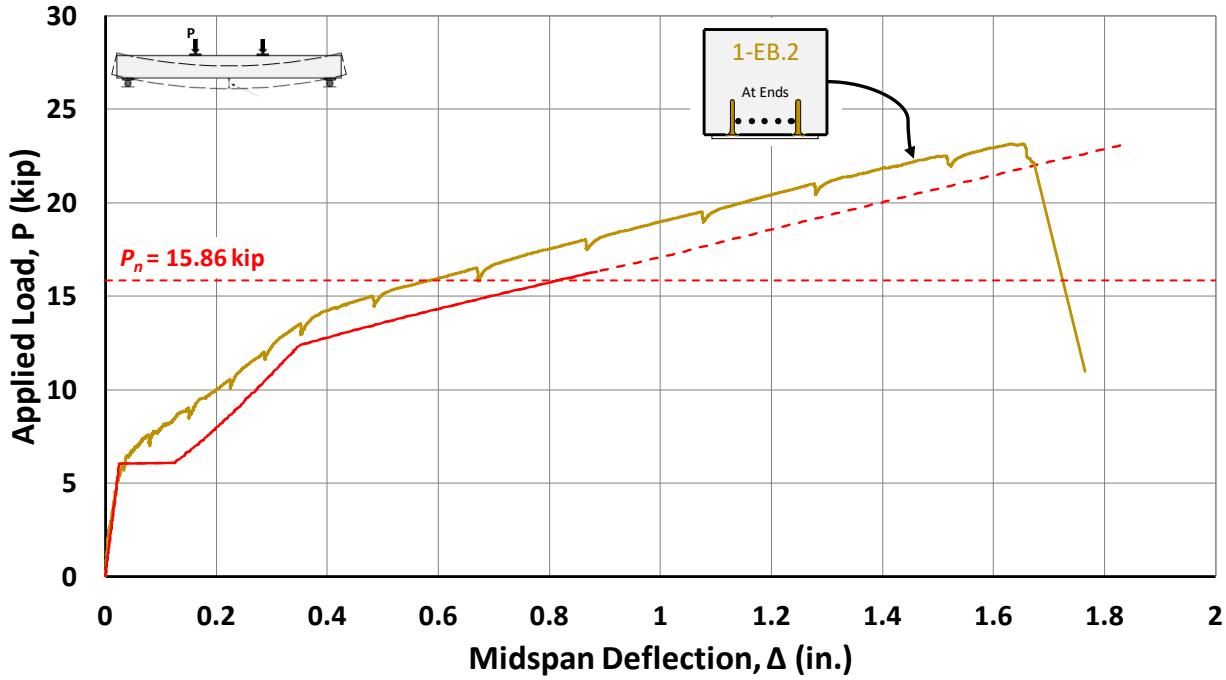


**Figure B.6** Example of comparison of theoretical and experimental responses.

## B.2 Group 3 Midspan Deflection Measurements

| Specimen ID | Avg. Midspan Deflection at Max Load, Δ (in.) | West Edge, Δ (in.) | East Edge, Δ (in.) | Difference (in.) |
|---|---|---|---|---|
| 3-C | 2.88 | 2.896 | 2.872 | 0.024 |
| 3-D | 3.63 | 3.654 | 3.601 | 0.053 |
| 3-EB.1 | 0.96 | 0.958 | 0.956 | 0.002 |
| 3-EB.2 | 1.69 | 1.710 | 1.675 | 0.035 |
| 3-NSM.1 | 1.62 | 1.630 | 1.615 | 0.015 |
| 3-NSM.2 | 1.56 | 1.559 | 1.556 | 0.003 |
| 3-NSM.3 | 1.43 | 1.434 | 1.427 | 0.007 |

**Figure B.7** Group 3 midspan deflection measurements.

## REFERENCES FOR APPENDIX B


ACI Committee 440. (2015). *ACI 440.1R-15: Guide for the design and construction of structural concrete reinforced with fiber-reinforced polymer (FRP) bars.* American Concrete Institute.

ACI Committee 440. (2017). *ACI 440.2R-17: Guide for the design and construction of externally bonded FRP systems for strengthening concrete structures*. American Concrete Institute.

Hibbeler, R. C. (2012). *Structural analysis* (8th ed.). Pearson Education Inc.

Hognestad, E. (1951). *A study of combined bending and axial load in reinforced concrete members: Bulletin 399*. University of Illinois Engineering Experiment Station.

# APPENDIX C. INDOT 1961 STANDARD DRAWING–BOX BEAMS

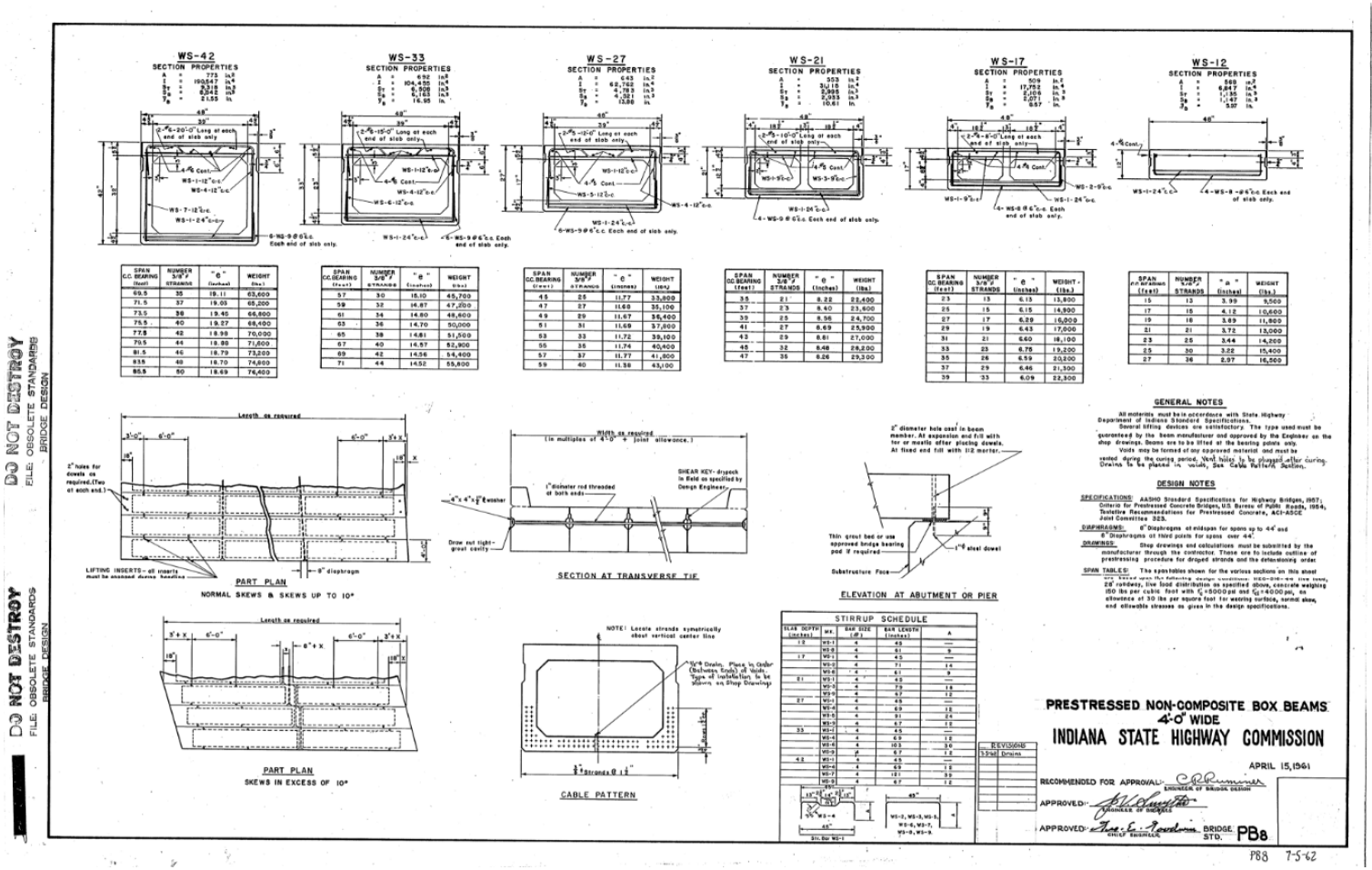

# APPENDIX D. PAST END REGION REPAIR RESEARCH

## D.1 Past Research on End Region Repair Using FRP Systems

While the use of FRP as a repair and strengthening system has been widely researched, only a few studies have been conducted to examine the use of FRP systems for repairing deteriorated end regions of bridge girders. As the damage in these scenarios is largely concentrated at bridge supports, arch action, not beam action, is of primary focus. Research by Kim (2011) and NASEM (2011) concluded that the effectiveness of externally bonded FRP systems decrease as the shear span-to-depth ($a/d$) ratio decreases. Kim (2011) found that externally bonded CFRP strengthened T-beams with $a/d$ ratios of 3.0 achieved shear strength increases up to 50%. In contrast, Kim (2011) also found that identically detailed CFRP-strengthened T-beams with $a/d$ ratios of 1.5 only achieved strength increases up to 15%. Therefore, more research is needed to better understand the behavior of FRP repair systems when arch action controls. The following studies fall into this category, as they examine the behavior of FRP systems used to repair the end region of prestressed concrete bridge girders.

### *D.1.1 Ramseyer and Kang (2012)*

Ramseyer and Kang (2012) examined the effectiveness of glass and carbon FRP repair systems for prestressed concrete bridge girders with deteriorated end sections. Type II AASHTO bridge girders were artificially damaged by failing the girder ends in shear. This damage was meant to simulate in-field corrosion. The end regions were then repaired by (1) removing delaminated concrete, (2) restoring the section using rapid set mortar, (3) epoxy-injecting cracks (only on select specimens), (4) cutting anchorage grooves at the top of the web, (5) applying externally bonded FRP U-wraps onto the repair section, and (6) inserting a metal rod into the groove to anchor the U-wrap. Figure D.1 illustrates the repair process. As Table D.1 shows, the only repair system to regain the shear strength of the undamaged end region was the system with glass FRP U-wraps and epoxy-injected cracks. However, the authors concluded that the carbon FRP systems recovered more stiffness than the glass FRP systems (Ramseyer & Kang, 2012).

**(a) Delaminated Concrete Removed**

**(b) Cross Section Restored**

**(c) Epoxy-Injected Cracks**

**(d) Groove Cut**

**(e) Primed Concrete**

**(f) FRP Repair**

**Figure D.1** Repair procedure for damaged end regions (from Ramseyer & Kang, 2012).

**Table D.1** Shear Test Results (adapted from Ramseyer & Kang, 2012)

| Repair System | Initial Ultimate Shear Load (kip) | Ultimate Shear Load Post-Repair (kip) |
|---|---|---|
| GFRP U-Wraps without Epoxy Injection | 97.9 | 84.1 |
| GFRP U-Wrap with Epoxy Injection | 106.3 | 108.0 |
| CFRP U-Wrap without Epoxy Injection | 99.1 | 81.4 |
| CFRP U-Wrap with Epoxy Injection | 123.5 | 87.9 |

*D.1.2 Andrawes et al. (2018)*

Another study that examined the effectiveness of FRP repair systems for prestressed concrete bridge girders with deteriorated end sections was conducted by Andrawes et al. (2018). The end regions of laboratory-fabricated, half-scale AASHTO Type II I-shaped girders were artificially damaged by removing 0.5 in. of the concrete cover from the webs. Rapid set cement was then used to restore the cross sections of the members. Both glass and carbon side-bonded FRP systems were examined. The side-bonded sheets were anchored using longitudinal FRP strips. As shown in Figure D.2, the anchorage detailing consisted of a single layer of longitudinal strip anchors located at the top of the web, the bottom of the web, and the bottom flange. The longitudinal strip anchors were wrapped around the end of the girder and continued on the other side. An NSM repair system was also tested. Experimental results showed that the carbon FRP system was able to exceed the stiffness and ultimate shear capacity of the control specimen (19.5% and 6.0% increases, respectively), while the glass FRP system exceeded the ultimate shear capacity of the control specimen (2.0% increase) but was unable to restore the stiffness (25.6% decrease). The NSM repair system did not restore the stiffness or the shear capacity of the undamaged specimen (21.4% and 7.5% decrease, respectively).

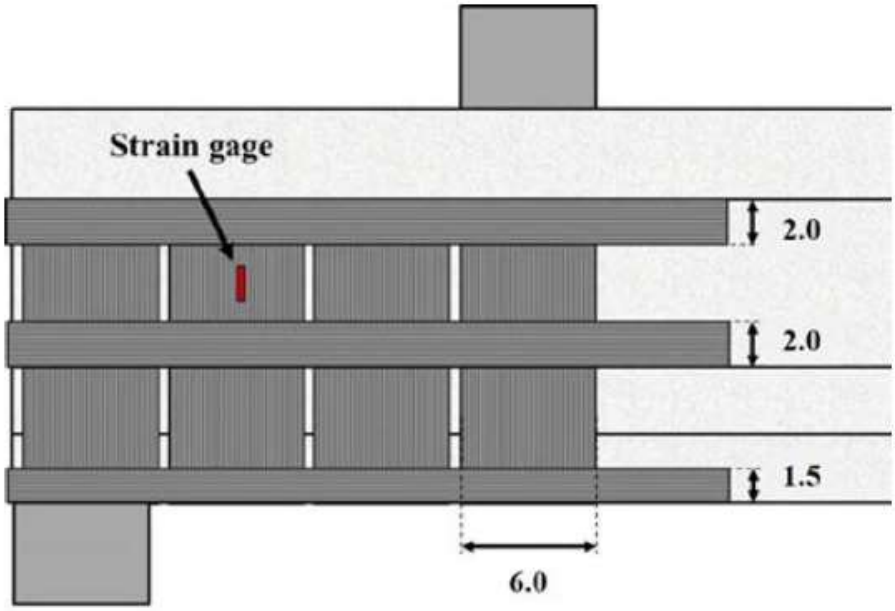


**Figure D.2** Longitudinal FRP strip anchorage detailing for half-scale specimens (from Andrawes et al., 2018).

Based upon the results of the half-scale test specimens, the carbon FRP repair system was selected for full-scale testing on AASHTO Type II I-shaped girders. The full-scale AASHTO Type II I-shaped girders were damaged in a similar manner as the half-scale specimens except that the imposed damaged was continued into the bottom flange. The repair procedure for the full-scale specimens was identical to that of the half-scale specimens except for the FRP detailing. For the full-scale tests, the longitudinal strip anchors were placed at the same locations as the half-scale specimens, but the widths of the anchors were increased to 3 in. each. Additionally, the longitudinal strip anchors were not wrapped around the end of the girder.

Instead, each side of the girder was anchored with longitudinal strips. Figure D.3 displays the anchorage detailing for the full-scale test specimens. As with the half-scale specimens, the carbon FRP repair system was able to exceed the shear capacity of the control specimen (2.6% increase) but did not fully regain the control stiffness (2.3% decrease) (Andrawes et al., 2018).

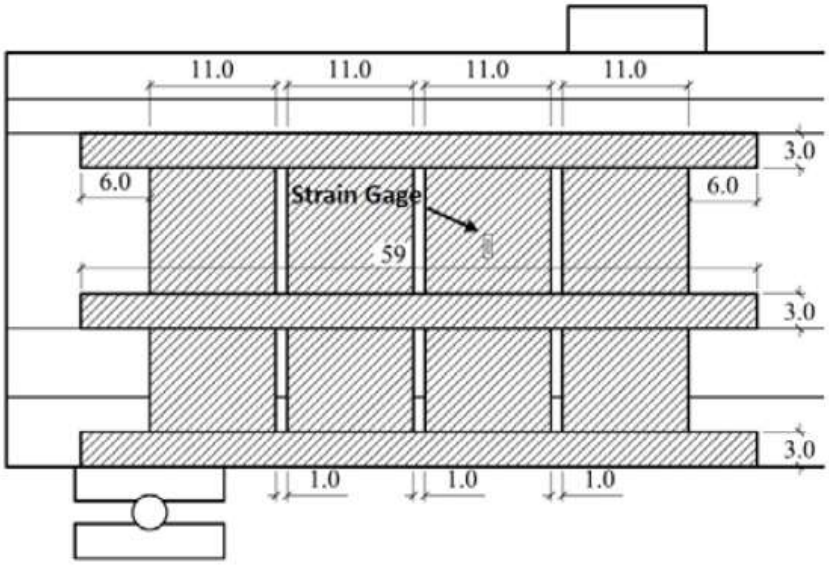


**Figure D.3** Longitudinal FRP strip anchorage detailing for full-scale specimens (from Andrawes et al., 2018).

*D.1.3 Petty et al. (2011)*

Petty et al. (2011) examined the effectiveness of different FRP strengthening systems on deteriorated end regions of I-shaped prestressed concrete bridge girders. Eight AASHTO Type II girders were salvaged from a bridge replacement project for load testing. The following five CFRP repair configuration were implemented: (1) four vertical U-wrap sheets (20 in. wide) anchored with an embedded CFRP laminate along the bottom and top web-flange interfaces, as shown in Figure D.4, (2) six discontinuous, 45° oriented sheets (10 in. wide) with two layers of longitudinal strip anchors (15 in. wide) along the web of the girder, (3) six discontinuous, 45° oriented sheets (10 in. wide) without anchorage, (4) four vertical U-wrap sheets (10 in. wide) anchored with two layers of longitudinal strip anchors (15 in. wide) along the web of the girder, as shown in Figure D.5, and (5) six discontinuous, 45° oriented sheets (10 in. wide) anchored with the detail shown in Figure D.4. Table D.2 shows the results of the experimental program. The authors concluded that the CFRP configuration of vertical U-wrap sheets and longitudinal strip anchors was the most effective design due to its consistent strength increase, ease of installation, and simplistic design. As such, this configuration was used for two additional ultimate shear tests. These tests resulted in strength increases of 16.2% and 15.1%, further displaying the effectiveness of the repair system (Petty et al., 2011).

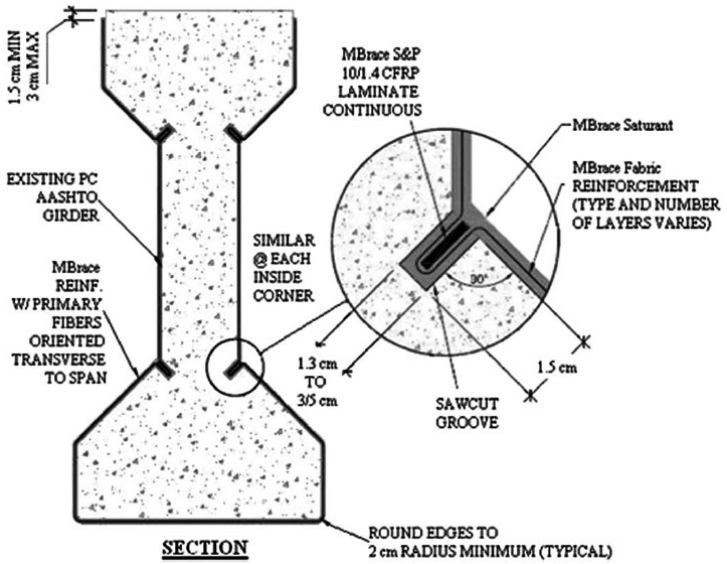


**Figure D.4** Embedded CFRP laminate anchorage system detail (from Petty et al., 2011).

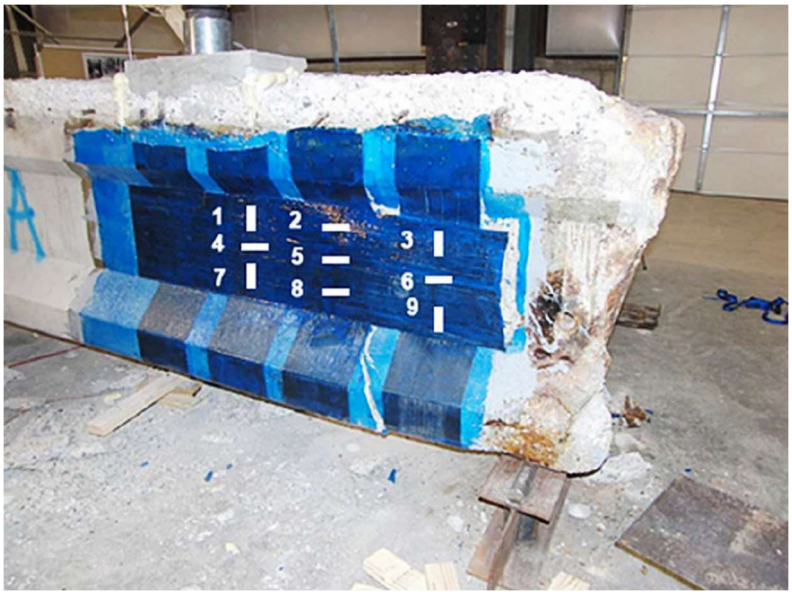


**Figure D.5** CFRP repair system with vertical U-Wrap and longitudinal strip anchorage (from Petty et al., 2011).

**Table D.2** Results from Experimental Program (adapted from Petty et al., 2011)

| CFRP System | Test | Increase in Shear Capacity |
|---|---|---|
| Vertical U-Wrap with Embedded Anchorage | A | 36.0% |
| | B | -0.5% |
| Diagonal Sheets with Longitudinal Strip Anchorage | A | 17.0% |
| | B | 21.9% |
| Diagonal Sheets without Anchorage | A | 8.9% |
| | B | 6.4% |
| Vertical U-Wrap with Longitudinal Strip Anchorage | A | 27.3% |
| | B | 27.3% |
| Diagonal Sheets with Embedded Anchorage | A | 34.1% |
| | B | -7.8% |

## D.2 Past Research on End Block/Supplemental Diaphragm Repair Systems

Two studies in the literature (Needham, 2000, Shield & Bergson, 2018) examined the use of end blocks to repair deteriorated end regions of bridge girders. End block repairs increase the original cross section of the girder and rely on supplemental reinforcement to redistribute stresses from the original member into the repair. As part of the current study described in this report, a similar detail, referred to as a supplemental diaphragm, was considered. The two end block studies served as the design basis for the supplemental diaphragm repair method developed in the current study.

In 2000, the Michigan Department of Transportation (MDOT) published the results of a research project focusing on the repair of I-shaped prestressed concrete bridge girder end regions (Needham, 2000). The project included the development of an end block repair procedure, load testing of the repaired girder, and field installation of the repair on in service girders. The repair procedure was conducted as follows:

1. Deteriorated concrete was removed using either a 15-kg pneumatic chipping hammer or a 7-kg pneumatic chipping hammer around the prestressing strands.
2. The repair limits on the bottom flange of the beam were saw cut to prevent feather edging of the repair material.

3. A 7-kg chipping hammer was used to lightly roughen the surface of the existing sound concrete within the repair limits to improve the bond between the existing concrete and the repair material.
4. Three 13-mm by 25-mm keyways were created in each side of the existing concrete to improve the shear performance of the interface between the existing concrete and the patch material.
5. The supplemental reinforcement was placed, and the concrete forms were set.

A latex modified concrete was used as the patch material. While the repaired girder did not reach the expected shear capacity, it was determined that this was a result of the residual effects of impact damage caused by a vehicle collision when the girder was in service. Additionally, it was concluded that use of the 7-kg pneumatic hammer to roughen the surface of the existing concrete caused too much micro-cracking, and thus an alternative method should be used to prepare the surface. Figure D.7 shows the end block repair details utilized in the study. The repair performed well for 6 months at which time the report was written. Only two minor cracks, caused during the construction of the end block, had appeared despite experiencing several issues during construction. These included accidental cutting of the prestressing strands in the bottom flange, mixing problems with the latex modified concrete, and featheredging at the bottom of the repair area (Needham, 2000).

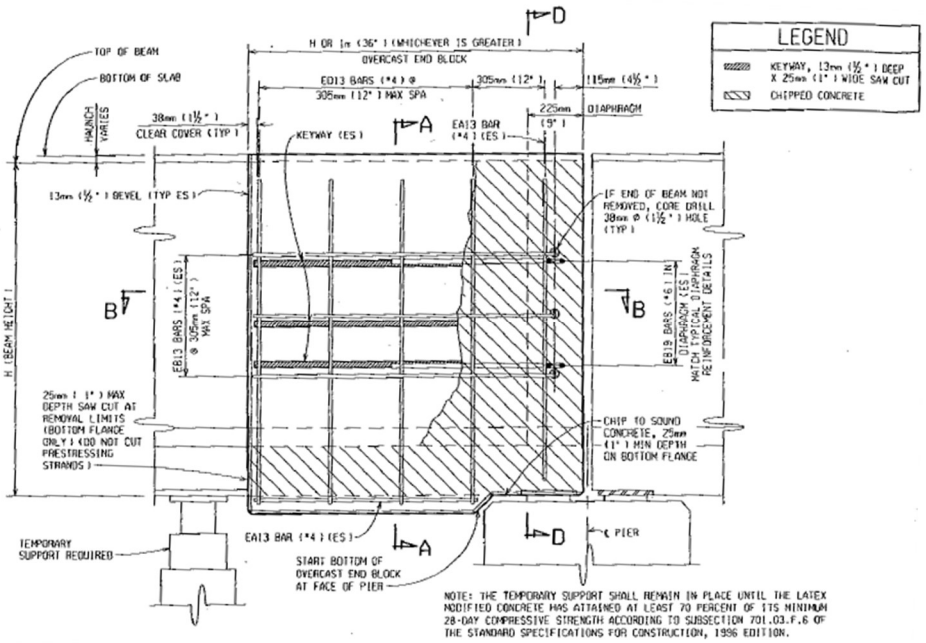


**(a) End Block Repair Elevation Detail**

**Figure D.6** End block repair details (cont.).

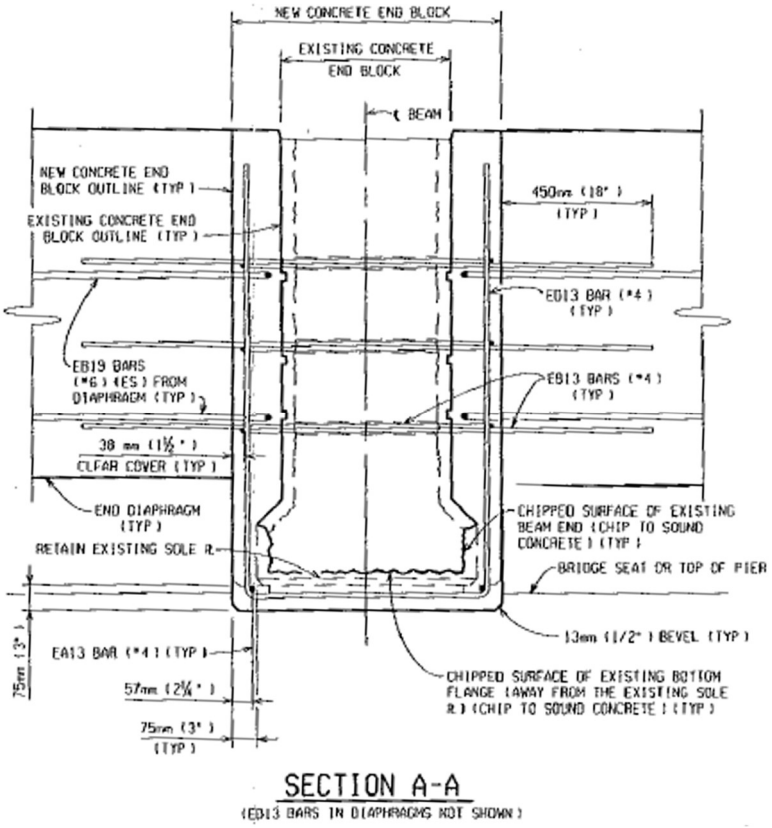


**(b) End Block Repair Cross-Sectional Detail**

**Figure D.7** End block repair details (from Needham, 2000).

Another end block study that influenced the development of the supplemental diaphragm repair was conducted by Shield and Bergson (2018) at the University of Minnesota in collaboration with the Minnesota Department of Transportation (MnDOT). The study examined the performance of shotcrete end block repairs MnDOT performed in 2013 on I-shaped prestressed concrete bridge girders with significant end region deterioration. Figure D.8 shows the condition of the girders prior to and after the repair, and Figure D.9 shows the shotcrete repair details. The shotcrete repair was conducted as follows (Shield & Bergson, 2018):

1. The concrete was sounded to locate hollow sounding areas.
2. Delaminated concrete was removed.
3. Supplemental reinforcement was added to the repair area.
4. The supplemental reinforcement was encased in the shotcrete end block.

In 2017, the bridge which received the shotcrete repair was replaced, and the girders which received the repairs were transported to the University of Minnesota for load testing. Two unrepaired specimens were also tested as control specimens. The end block repaired girders failed at marginally higher loads (1.2% and 3%) than the unrepaired specimens, establishing the effectiveness of the repair (Shield & Bergson, 2018).

**(a) Condition of the Girder Following Removal of Delaminated Concrete**


**(b) Complete Shotcrete Repair**

**Figure D.8** Girder condition prior to and following shotcrete repair (from Shield & Bergson, 2018).

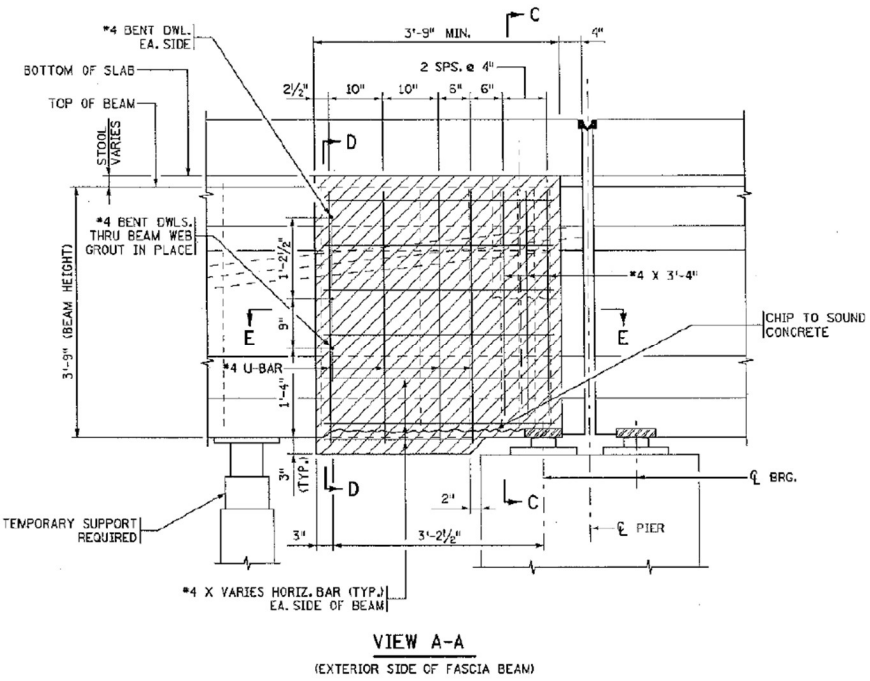


**(a) Shotcrete Repair Elevation Detail**

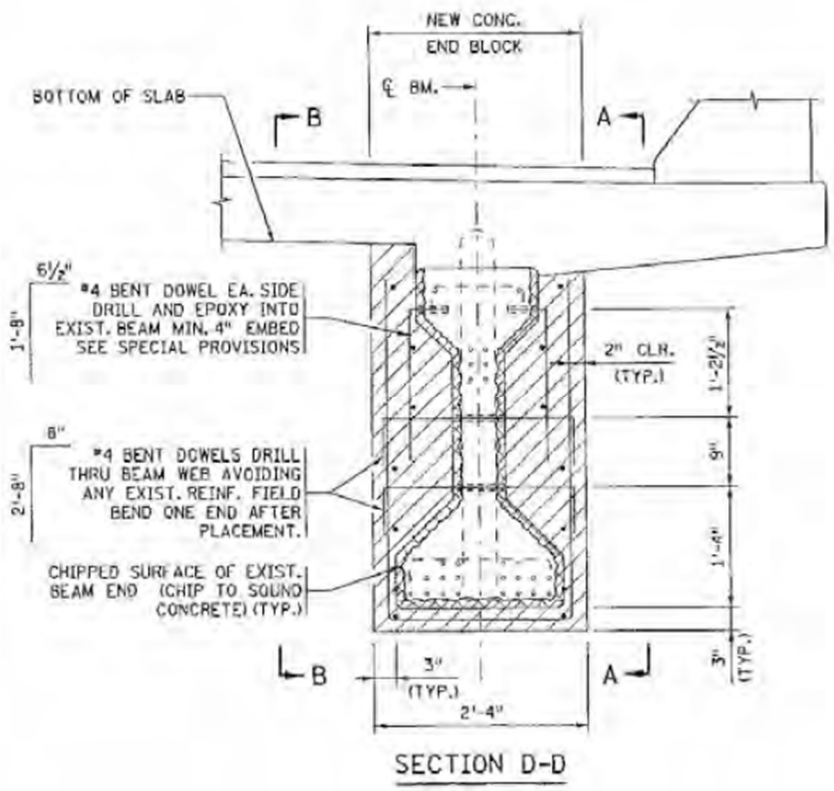


**(b) Shotcrete Repair Cross-Sectional Detail**

**Figure D.9** Shotcrete repair details (from Shield & Bergson, 2018).

## D.3 Summary of Examined Repair Systems

The above sections highlight previously conducted studies examining different repair techniques for end regions of prestressed concrete bridge girders. Ramseyer and Kang (2012), Andrawes et al. (2018), and Petty et al. (2011) examined the effectiveness of different FRP strengthening techniques. Ramseyer and Kang (2012) concluded that the glass FRP U-wrap system with embedded steel rods for anchorage in combination with epoxy-injected cracks was the most effective system for restoring lost shear capacity. However, Andrawes et al. (2018) and Petty et al. (2011) concluded that the carbon FRP systems with longitudinal strips for anchorage provided the best retrofit solution. End block repair solutions were also examined by Needham (2000) and Shield and Bergson (2018). Needham (2000) concluded that the latex modified concrete end block repair provided a cost-effective solution for the repair of prestressed concrete bridge girder end regions, while Shield and Bergson (2018) concluded that the shotcrete end block repair technique that was implemented was also an effective system. Table D.3 summarizes the strength increases achieved by each of these systems. However, caution should be taken when directly comparing the performance of the systems due to differences in repair procedures, repair system detailing, and test specimen configurations.

**Table D.3** Strength Increase for Recommended Repair Techniques from Examined Studies

| Study | Recommended Repair Technique | Average % Increase in Ultimate Shear Capacity |
|---|---|---|
| Ramseyer and Kang (2012) | GFRP U-Wrap with Epoxy Injected Cracks | 1.6% |
| Andrawes et al. (2018) | CFRP Side-Bonded Sheets with Longitudinal FRP Strip Anchorage | 2.6% |
| Petty et al. (2011) | CFRP U-Wrap with Longitudinal FRP Strip Anchorage | 21.5% |
| Shield and Bergson (2018) | Shotcrete End Block | 2.1% |
| Strength data not available for Needham (2000) study. | | |

## REFERENCES FOR APPENDIX D


Andrawes, B., Shaw, I. D., & Zhao, H. (2018). *Repair & strengthening of distressed/damaged ends of prestressed beams with FRP composites* (Illinois Center for Transportation Report No. FHWA-ICT-18-001). University of Illinois at Urbana-Champaign. https://doi.org/10.36501/0197-9191/18-001

Kim, Y. G. (2011). *Shear behavior of reinforced concrete T-beams strengthened with carbon fiber reinforced polymer (CFRP) sheets and CFRP anchors* [Doctoral dissertation, The University of Texas at Austin].

NASEM. (2011). *Design of FRP systems for strengthening concrete girders in shear*. The National Academies Press. https://doi.org/10.17226/14465

Needham, D. E. (2000). *Prestressed concrete beam end repair: final report* (Michigan Department of Transportation Rep No. R-1380). Michigan Department of Transportation. https://www.michigan.gov/documents/mdot_c&t_r-1380_67568_7.pdf

Petty, D. A., Barr, P. J., Osborn, P. G., Halling, M. W., & Brackus, T. R. (2011). Carbon fiber shear retrofit of forty-two-year-old AASHTO I-shaped girders. *Journal of Composites for Construction*, *15*(5), 773–781. https://doi.org/10.1061/(ASCE)CC.1943-5614.0000208

Ramseyer, C., & Kang T. H.-K. (2012). Post-damage repair of prestressed concrete girders. *International Journal of Concrete Structures and Materials*, *6*(3). https://doi.org/10.1007/s40069-012-0019-7

Shield, C., & Bergson, P. (2018). *Experimental shear capacity comparison between repaired and unrepaired girder ends* (Minnesota Department of Transportation Rep No. MN/RC 2018-07). University of Minnesota. http://www.dot.state.mn.us/research/reports/2018/201807.pdf

# APPENDIX E. END REGION REPAIR EXPERIMENTAL PROGRAM SUPPLEMENTAL DETAILS

## E.1 Material Properties

### *E.1.1 Control Specimen*

After testing the girder, 4-in. by 6-in. cores where removed from the web of the specimen to determine the compressive strength of the concrete at the time of testing. As shown in Figure E.1, the test specimen was rotated to allow for the cores to be taken vertically. Cores were removed from an undamaged portion of the web located as close as possible to the test region. This procedure was followed for all five girders of the test program. The four cores from the control specimen were tested in compression in accordance with ASTM C42 and yielded an average compressive strength of 7,270 psi, as provided in Table E.1.

**Figure E.1** Coring web of test specimen.

**Table E.1** Material Compressive Strength Test Results for Control Specimen

| Material | Compressive Strength (psi) |
|---|---|
| Cored Concrete | 7,270 |

### *E.1.2 Damaged Specimen*

As with the control specimen, 4-in. by 6-in. cores were removed from the web of the specimen following testing. Compression tests on three cores yielded an average strength of 9,240 psi. The compressive strength of the concrete used to repair the deck (see Section E.2.1 of Appendix E) was obtained by testing 4-in. by 8-in. cast concrete cylinders. The compressive strength of the

cylinders was determined in accordance with ASTM C39 and yielded an average compressive strength of 7,220 psi on the day of the girder test (97 days after casting). Moreover, mortar cubes were cast in accordance with ASTM C109 (as shown in Figure E.2) to determine the compressive strength of the mortar used to repair the bearing area as described in see Section E.2.2 of Appendix E. The average compressive strength of the mortar cubes on test day (32 days after casting) was 9,130 psi. The compression test results of the concrete cores, concrete cylinders, and mortar cubes for the damaged test specimen are summarized in Table E.2.

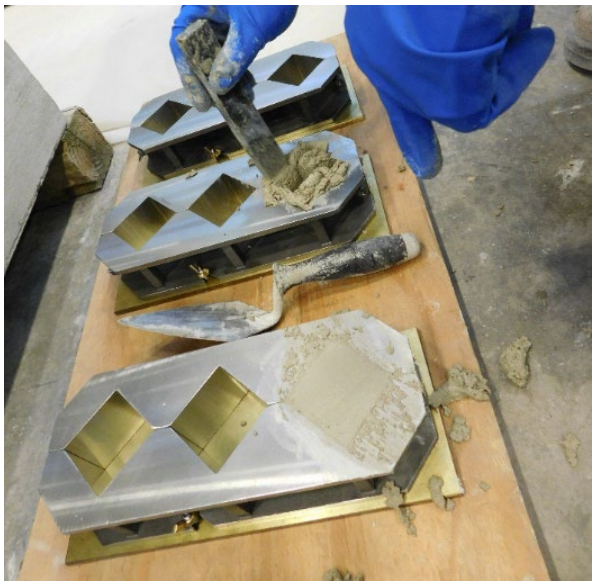

**Figure E.2** Casting mortar cubes.

**Table E.2** Material Compressive Strength Test Results for Damaged Specimen

| Material | Compressive Strength (psi) |
|---|---|
| Cored Concrete | 9,240 |
| Concrete Cylinders (Deck) | 7,220 |
| Mortar Cubes | 9,130 |

*E.1.3 Externally Bonded FRP Repair Specimen*

The compressive strength of the specimen was determined by removing 4-in. by 6-in. cores from the web of the specimen following testing. The average compressive strength of the three cores was 7,440 psi. Mortar cubes were cast to measure the strength of the mortar used to restore the original cross section of the girder. The average compressive strength of the mortar cubes on the day of the girder test (326 days after casting) was 16,100 psi. The average compression test results of the concrete cores and mortar cubes for the specimen with externally bonded FRP are presented in Table E.3.

**Table E.3** Material Compressive Strength Test Results for Externally Bonded FRP Specimen

| Material | Compressive Strength (psi) |
|---|---|
| Cored Concrete | 7,440 |
| Mortar Cubes | 16,100 |

*E.1.4 NSM FRP Repair Specimen*

As with the other specimens, the compressive strength of the girder with NSM strips was determined by removing 4-in. by 6-in. cores from the web of the specimen. The average compressive strength of three cores was 9,070 psi. Like the specimen with externally bonded FRP, mortar cubes were cast to measure the strength of the mortar used to restore the original cross section of the girder. The average compressive strength of the mortar cubes on the day of the girder test (310 days after casting) was 12,170 psi. The average compression test results of the concrete cores and mortar cubes for the specimen repaired with NSM FRP strips are displayed in Table E.4.

**Table E.4** Material Compressive Strength Test Results for NSM FRP Specimen

| Material | Compressive Strength (psi) |
|---|---|
| Cored Concrete | 9,070 |
| Mortar Cubes | 12,170 |

*E.1.5 Supplemental Diaphragm Repair Specimen*

To determine the compressive strength of the girder at the time of testing, 4-in. by 6-in. concrete cores were removed from the web of the specimen for compression tests. The results of test on three cores provided an average strength of 7,850 psi. As with the damaged girder specimen, 4-in. by 8-in. concrete cylinders were cast to determine the compressive strength of the concrete used to repair the deck (see Section E.2.1 of Appendix E). The average compressive strength on the day of the girder test (104 days after casting) of the deck repair concrete cylinders was 6,410 psi. Similarly, 4-in. by 8-in. concrete cylinders were cast to determine the compressive and tensile strengths of the SCC used for the supplemental diaphragm. The average compressive strength on test day (52 days after casting) of the cylinders was 7,070 psi, and the average splitting tensile strength on test day (52 days after casting) was 630 psi. The splitting tensile tests were conducted in accordance with ASTM C496 (ASTM, 2017). The results of the compressive and tensile strength tests are displayed in Table E.5.

**Table E.5** Material Compressive and Tensile Strength Test Results for Supplemental Diaphragm Specimen

| Material | Compressive Strength (psi) | Splitting Tensile Strength (psi) |
|---|---|---|
| Cored Concrete | 7,850 | – |
| Concrete Cylinders (Deck) | 6,410 | – |
| Concrete Cylinders (Diaphragm) | 7,070 | 630 |

*E.1.6 Summary of Test Results*

The measured material strengths corresponding to the five girder specimens of the test program are summarized in Table E.6. All material testing was conducted according to the appropriate ASTM standards. The properties of the FRP systems as reported by the manufacturer are provided in Sections 4.3.2 and 4.3.3. Although some variations in the compressive strengths of the concrete and mortar are evident among the girder specimens, these differences are not believed to be significant in consideration of the failure modes observed during the tests and the overall value provided by the comparisons between the overall performance of the girders.

**Table E.6** Summary of Material Test Results

| | Cored Concrete, $f_c$ (psi)[1] | Deck Concrete, $f_c$ (psi)[2] | Mortar, $f_m$ (psi)[3] | Supp. Dia. Concrete, $f_c$ (psi)[2] | Supp. Dia. Splitting Tensile, $f_t$ (psi)[4] |
|---|---|---|---|---|---|
| **Control** | 7,270 | – | – | – | – |
| **Damaged** | 9,240 | 7,220 | 9,130 | – | – |
| **Ext. Bonded** | 7,440 | – | 16,100 | – | – |
| **NSM** | 9,073 | – | 12,170 | – | – |
| **Supp. Dia.** | 7,850 | 6,410 | – | 7,070 | 630 |

[1]ASTM C42
[2]ASTM C39
[3]ASTM C109
[4]ASTM C496

## E.2 End Region Repair Procedures

In this section, all of the procedures required to prepare the five damaged AASHTO Type I girders for testing are discussed. This discussion includes (1) removal of a drain from the deck of two test specimens and the subsequent repair of the decks; (2) repair of the bearing area on one of the specimens prior to testing; and (3) procedures used to implement the three repair techniques described in Section 4.3.

*E.2.1 Drain Removal and Deck Repair*

Two of the recovered test specimens, Girders 20-C and 20-A, were fascia girders. Because of their location relative to the roadway, stormwater runoff drains were installed in the concrete

deck directly above the girders. As shown in Figure E.3, the proximity of the drains relative to the desired load point for the load tests required that the drains be removed. Concrete was cast to fill the voids left from the removal of the drains.

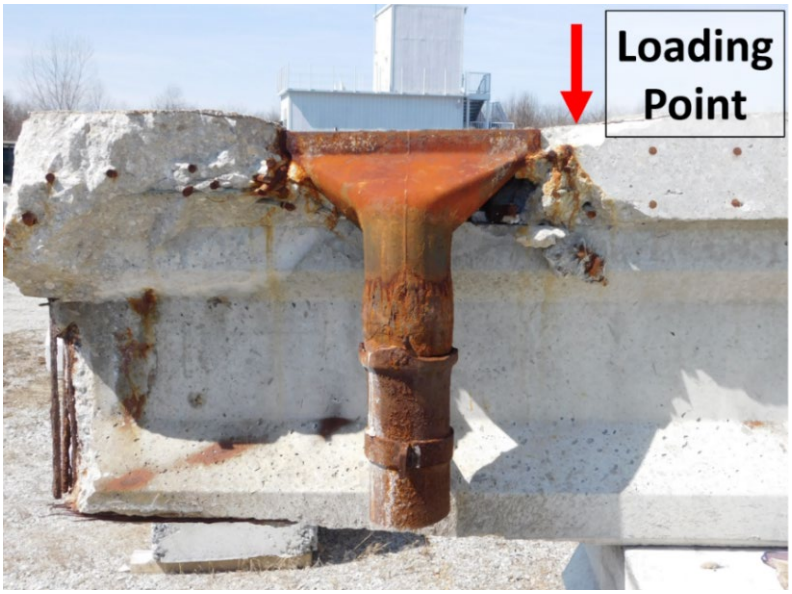


**Figure E.3** Proximity of load point to bridge drain.

The space left within the deck after removal of a drain is shown in Figure E.4(a). After drain removal, approximately 8 in. of concrete deck, measured from the edge of the former location of the drain toward the midspan of the girder, was removed using a concrete saw and chipping hammer (Figure E.4(b and c)). Per ICRI Guideline No. 310.1R-2008, concrete was removed from the deck to form a rectangular repair area. A hammer drill with a 0.875-in. drill bit was used to roughen the concrete surface at the ends of the repair area as shown in Figure E.4(d) to improve the bond between the original deck concrete and the repair concrete.

**(a) Void Left After Drain Removal**

**(b) Sawing Concrete Deck**

**(c) Removing Concrete to Create Rectangular Repair Area**

**(d) Roughened Surface at End of Repair Area**

**Figure E.4** Drain and deck concrete removal and surface roughening.

Next, reinforcement was added to the region being prepared as shown in Figure E.5. The reinforcement pattern matched the reinforcement pattern of the original deck: two layers of No. 5 Grade 60 longitudinal reinforcement with a 3.5-in. vertical center-to-center spacing and two layers of No. 5 Grade 60 transverse reinforcement with a 6-in. spacing measured along the length of the girder. The longitudinal reinforcement consisted of pairs of 24-in. long reinforcing bars with one end of each bar doweled into the original girder at the edge of the repair. Each bar was embedded approximately 3 in. into the deck concrete using an epoxy intended for anchoring reinforcing steel in hardened concrete (Figure E.5(a and b)). This configuration resulted in a 14-in. contact lap splice at the center of the repair area (Figure E.5(c)). The transverse reinforcement spaced at 6 in. was then positioned after the longitudinal bars were in place (Figure E.5(d)). At the drain locations, the portion of two stirrups extending into the concrete deck had been either removed or bent to allow for installation of the drain. As such, supplemental reinforcement (No. 4 Grade 60 bars) was also added to replace the portion of the stirrups extending from the top surface of the precast girder to further improve the bond between the repair concrete and the original girder. The supplemental reinforcement was bent to form a U-shape in order to match

the original stirrups. Each leg of the U-shaped bars was embedded approximately 4.5 in. into the top surface of the precast girder using epoxy (Figure E.5(e and f)).

**(a) Dispensing Epoxy for Anchorage of Longitudinal Reinforcement**

**(b) Inserting Longitudinal Reinforcement**

**(c) Longitudinal Reinforcement After Placement**

**(d) Transverse Reinforcement**

**(e) Installing U-Shaped Bars**

**(f) Completed Reinforcement**

**Figure E.5** Reinforcement installation procedure for deck repair.

Finally, formwork was erected on each side of the repair area (Figure E.6(a)). The formwork was installed such that the top surface of the repair area matched the slope of the original concrete deck. To resist lateral pressure, two 0.25-in. diameter threaded rods where inserted through the sidewalls of the formwork and anchored. Additionally, vertical and diagonal supports were attached to each piece of formwork (Figure E.6(b)). Upon completion of the formwork, a high-slump INDOT Class C concrete was used to fill the repair area. The completed deck repair is shown in Figure E.6(c), and the INDOT Class C concrete mixture design is provided in Table E.7.

**(a) Erected Formwork**

**(b) Formwork Supports**

**(c) Completed Deck Repair**

**Figure E.6** Completion of deck repair procedure.

**Table E.7** High-Slump INDOT Class C Mixture Design for Deck Repair

| Material | Details | Design Quantity | Units |
|---|---|---|---|
| Cementitious Material | Type 1 Cement | 658 | lb/yd$^3$ concrete |
| Coarse Aggregate | #8 Limestone (INDOT) | 1738 | |
| Fine Aggregate | Natural Sand | 1242 | |
| Water | – | 267 | |
| Admixtures | High-Range Water Reducer | 7.00 | oz/cwt cementitious material |

Note:
Specified $f'_c$ = 5,000 psi.
Water/Cement Ratio = 0.41.
Design Slump = 6.50" +/- 1.5″.

*E.2.2 Damaged Specimen Bearing Repair*

One of the girders with a deteriorated end region was tested with minimal repairs to establish the impact of the end region deterioration on the capacity of the bridge girders. Furthermore, by comparing the strengths of the repaired girders to the capacity of this specimen, the test served as a means by which the effectiveness of the three repair techniques could be evaluated. As such, Girder 20-C was tested in a damaged condition. However, minimal repairs were required in order to perform the test.

While extracting the bridge girders and then transporting them from the bridge site, loose concrete fell from the end regions of the member. Therefore, prior to testing Girder 20-C, reestablishing a bearing area for the girder was necessary. The condition of the girder prior to repairs is shown in Figure E.7. As shown in Figure 4.5, the centerline of the bearing pad was located 6 in. from the end the member when the girder was in-service. This left 2.5 in. from the end of the girder to the edge of the pad. Restoring the bearing area at this location, however, would have required substantial repairs. Therefore, the bearing location was shifted 4 in. into the span of the girder for testing.


**(a) Elevation** **(b) Bottom Surface**

**Figure E.7** Condition of Girder 20-C prior to bearing repair.

The bearing area was restored using a fast-setting, low-shrinkage, high-strength mortar (CTS Cement Manufacturing Corp. Rapid Set® Mortar Mix). The mortar repair procedure is shown in Figure E.8. To minimize wasted material, each 55-lb mortar bag was divided into identical 18.3-lb batches. The manufacturer suggested a mixing ratio between 3.0 and 3.75 quarts of water per 55 lbs. After trials were conducted, a mixing ratio of 3.5 quarts of water per 55-lb bag, with the addition of 1/3 of a 25-gram bag of Rapid Set® Set Control® (Figure E.8(a)), yielded the best results. Dust and debris were removed from the repair area by pressurized air prior to mixing the water and mortar. The Rapid Set® Set Control® admixture was combined with the appropriate volume of water and then added to the proportioned mortar. An electric drill with a mixing paddle was used to mix the mortar until a uniform consistency was achieved (Figure E.8(b)). The repair surface was wetted using a spray bottle to assist with the mortar application as the manufacturer suggested. Mortar was then placed and packed by hand until an adequate bearing area was restored (Figure E.8(c)). Relevant properties of Rapid Set® Mortar Mix are displayed in Table E.8.


**(a) Rapid Set® Set Control®**

**(b) Mixing Mortar**

**(c) Placing Mortar**

**Figure E.8** Mortar repair procedure.

**Table E.8** Rapid Set® Mortar Mix Properties (CTS Cement Manufacturing Corp. 2018)

| Property | Value | ASTM Specification |
|---|---|---|
| Initial Set | 15 min | C266 |
| Final Set | 35 min | C266 |
| 1-Hour Compressive Strength[1] | 2,500 psi | C109 Modified |
| 24-Hour Compressive Strength[1] | 5,000 psi | C109 Modified |
| 28-Day Compressive Strength[1] | 6,500 psi | C109 Modified |
| 28-Day Length Change in Air | -0.04 | C157 Modified Per C928 |

[1] Data obtained at flow consistency 100 by ASTM C1437 at 70°F (21°C).

*E.2.3 Externally Bonded FRP Repair System*

Using the details discussed in Section 4.3.2, a repair procedure was developed for the externally bonded FRP repair system. Careful considerations were made to ensure that the repair procedures were conducted in a manner as similar as possible to an in-field installation. To this end, a board was placed approximately 2 in. from the end of the girder to simulate the presence of a mud wall. Furthermore, a bearing pad was supported against the girder at its original location during the repair procedure. The simulated mud wall and placement of the bearing pad are shown in Figure E.9.

**Figure E.9** Simulated mud wall and bearing pad location for externally bonded FRP specimen.

The process followed for repairing the end region with mortar and preparing the specimen for the application of the externally bonded FRP is displayed in Figure E.10. The repair began by removing delaminated concrete from the end region using an electric chipping hammer until sound concrete was reached (Figure E.10(a)). Care was taken to keep the regions from which concrete was removed as rectangular in shape as possible, per ICRI Guideline No. 310.1R-2008. To remove corrosion product and mitigate microcracking caused by the impact hammer, as recommended by ICRI Guideline No. 310.1R-2008, the regions where concrete was removed or

had previously fallen from the specimen were sandblasted by an outside contractor (Figure E.10(b)). The end of the specimen after sandblasting is shown in Figure E.10(c). Next, the original cross section of the girder was restored using Rapid Set® Mortar Mix (Figure E.10(d)). The mortar repair procedure as outlined in Section E.2.2 of Appendix E was again followed. After the mortar cured, the surface of the concrete to which FRP was to be applied was sandblasted to a concrete surface profile (CSP) of 3 per ICRI Guide No. 330.2-2016 and ACI 440.2R-17 (Figure E.10(e)). As in the flexural strengthening experimental program, a set of CSP chips were used as a reference to verify adequate surface roughness. As shown in Figure E.10(f), prior to applying FRP to the concrete surface, a hammer drill with a 0.875-in. diameter drill bit was used to drill anchor holes at the locations indicated in Figure 4.8(b). It is recommended that the anchor holes which require drilling through the entirely through the web be drilled from both sides of the girder to mitigate concrete breakout. Based on a trial-and-error approach, a suggested procedure was developed for this process and is provided in Section 6.3.2 as a recommendation. Per ICRI Guide No. 330-2016 and ACI 440.2R-17, the edges of the anchor holes were rounded to a radius of 0.5 in. using a rotary tool to reduce stress concentrations (Figure E.10(g)). Similarly, the edges of the girder over which the FRP sheet were applied were rounded to a radius of 0.5 in. (Figure E.10(h)).

**(a) Removing Delaminated Concrete**

**(b) Sandblasting to Remove Corrosion**

**(c) Condition After Sandblasting**

**(d) Specimen After Mortar Repair**

**Figure E.10** Mortar repair, surface preparation, and drilling anchor holes.

**(e) Sandblasting for FRP Application**

**(f) Drilling Anchor Holes**

**(g) Rounding Edges of Anchor Hole**

**(h) Rounding Girder Edges**

**Figure E.10** Mortar repair, surface preparation, and drilling anchor holes (cont.).

As discussed in Sections 4.3.2, the externally bonded FRP was installed using a wet-layup application procedure. The steps followed for the girder specimen are presented in Figure E.11. As shown in Figure E.11(a), paint rollers were used to seal the concrete surface with the appropriate epoxy resin (Sikadur-330). Sealing the concrete surface with Sikadur-330 eliminates air voids and ridges in the concrete surface and provides a tack coat to help prevent the fabric from sagging during installation. The longitudinal FRP fabric strips were then saturated with epoxy resin (Sikadur Hex-300) using plastic laminating rollers (Figure E.11(b)). The strips were next applied to the primed concrete surface (Figure E.11(c)) at the locations shown in Figure 4.8(a). Once in place, plastic laminating rollers were used to fully impregnate the longitudinal FRP strips and eliminate air voids (Figure E.11(d)). Squeegees were then used to eliminate excess epoxy (Figure E.11(e)). Once the longitudinal strips were in place, the vertically-oriented face-bonded sheets above the bearing support and the U-wraps were applied in the same manner to the appropriated locations shown in Figure 4.8(b). The end region of the specimen after all externally bonded strips/sheets were applied is shown in Figure E.11(f).

**(a) Sealing Concrete Surface**

**(b) Saturating Longitudinal FRP Strips**

**(c) Placing Longitudinal Strips**

**(d) Rolling FRP to Eliminate Air Pockets**

**(e) Removing Excess Epoxy with Squeegee**

**(f) Externally Bonded Strips/Sheets Applied to Specimen**

**Figure E.11** Application of externally bonded strips/sheets.

The installation procedure for the FRP spike anchors is shown in Figure E.12. For the FRP spike anchors that extended through the entirety of the web, a 1/8-in. wooden dowel was fastened within the spike anchors using zip-ties to aid in the installation process, as shown in Figure E.13. To install the anchors, empty caulk tubes were first filled with the appropriate epoxy resin (Sikadur-330). A razorblade was then used to separate the fibers of the FRP sheets (Figure E.12(a), and the caulk tube was inserted into the anchor hole (Figure E.12(b)). For the anchors that extended through the web, the anchor hole was first filled half-way with epoxy and the spike anchor was then inserted, as shown in Figure E.12(c). Next, the wooden dowel was removed from the anchor (Figure E.12(d)), and the ends of the spike anchors were fanned out at a 60° angle (Figure E.12(e)) on each side of the girder and saturated with epoxy (Figure E.12(f)). Using the filled caulk tube, additional epoxy was injected into the anchor holes to eliminate possible air voids. The same installation procedure was followed for the anchor holes in the bottom flange of the girder, except that the hole was filled entirely with epoxy prior to inserting the anchor and the anchors were folded in half, as shown in Figure E.14, providing a nominal anchor cross-sectional area of approximately 0.31 in.$^2$ (see Section 4.3.2). However, as presented in Appendix G, the amount of material used for each anchor was determined by weight, not by area. Subsequently, the FRP patch sheets were saturated with epoxy (Sikadur Hex-300) (Figure E.12(g)) and installed using the same procedure previously described for the externally bonded strips/sheets. Two FRP patch sheets, the first with the fibers orientated perpendicular to the fibers of the FRP sheets and the second with the fibers orientated parallel to the fibers of the FRP sheets, were applied over the installed anchors at the locations shown in Figure 4.8(c) (Figure E.12(h)). The completed externally bonded FRP repair system installed on the girder specimen is shown in Figure E.12(i).

**(a) Separating Fibers with Razor Blade**

**(b) Injecting Anchor Hole with Epoxy**

**Figure E.12** Spike anchor installation procedure and completed externally bonded FRP repair system.

**(c) Inserting Spike Anchor**

**(d) Removing Wooden Dowel**

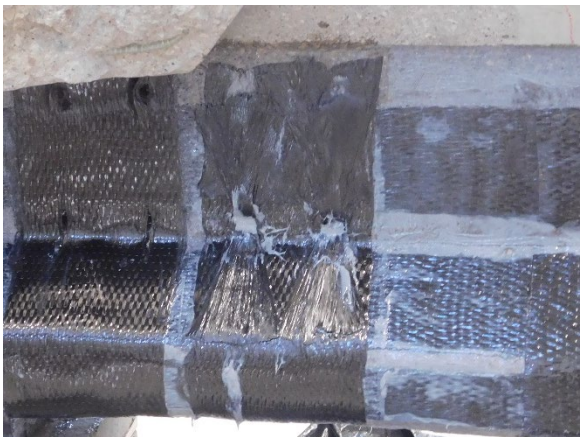

**(e) Fanned-Out Anchors**

**(f) Saturating Anchors**

**(g) Saturating Patch Sheets**

**(h) Placing Patch Sheets**

**Figure E.12** Spike anchor installation procedure and completed externally bonded FRP repair system (cont.).

**(i) Completed Externally Bonded FRP Repair System**

**Figure E.12** Spike anchor installation procedure and completed externally bonded FRP repair system (cont.).

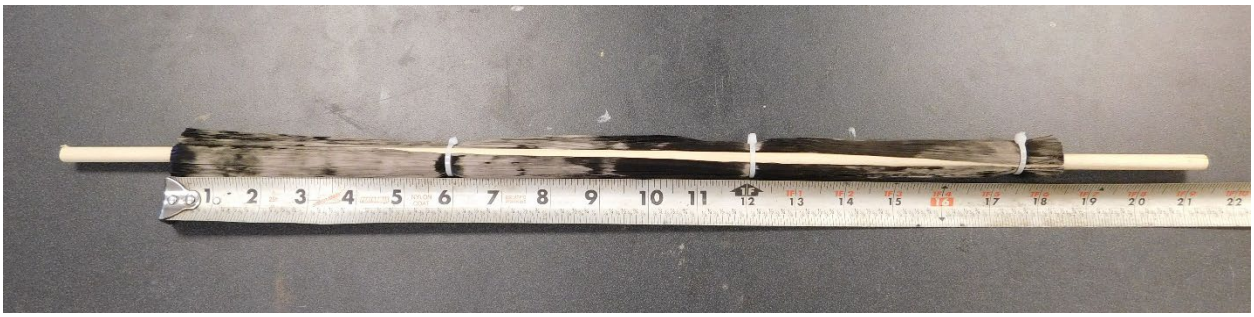

**Figure E.13** Assembled FRP spike anchor for web installation.

**Figure E.14** Assembled FRP spike anchor for bottom flange installation.

*E.2.4 NSM FRP Repair Specimen*

The repair procedure for the specimen tested to evaluate the NSM FRP repair described in Section 4.3.3 consisted of restoring the cross section of the girder with mortar followed by installation of the NSM strips. As with the specimen with externally bonded FRP, a board was placed at the end of the test specimen as shown in Figure E.15 to simulate a mud wall while the specimen was prepared for the mortar repair and while the mortar repair was performed. Furthermore, a bearing pad, also shown in Figure E.15, was placed in its original position during the repair procedures. The procedures that were followed to prepare the end region for the mortar repair and the mortar repair itself were identical to the procedures followed for the specimen

with externally bonded FRP. These procedures are outlined in Section E.2.3 of Appendix E and are shown for the NSM FRP specimen in Figure E.16. The key stages presented in the figure include the removal of delaminated concrete, sandblasting in preparation for the mortar repair, and the end region after the cross section was restored using the same mortar that was previously described. Upon completion of the mortar repair, it was determined that the surface of the repair was too uneven to cut the required grooves at a uniform depth. Therefore, an additional thin layer of mortar was applied over the initial mortar repair to provide a smoother surface.

**Figure E.15** Simulated mud wall and bearing pad location for NSM FRP specimen.

**(a) Removing Delaminated Concrete**

**(b) Sandblasting to Remove Corrosion**

**(c) Condition After Sandblasting**

**(d) Specimen After Mortar Repair**

**Figure E.16** Cross section of NSM FRP specimen.

NSM FRP systems consist of bars or strips that are embedded into a concrete substrate. The process for installing the NSM FRP strips into the girder specimen of the test program is presented in Figure E.17. As shown in Figure E.17(a), a tuckpointing grinder with a 0.25-in. thick diamond cutting blade was used to cut grooves at the locations and with the dimensions specified in Figure 4.10. To ensure the grooves were cut straight and at a constant depth of 0.875-in., a steel angle was clamped onto the test specimen. Prior to installation of the FRP strips, compressed air was used to remove dust and debris from the grooves. Then, the installation of the NSM strips was conducted. This process was performed for two grooves (i.e., a pair of grooves on the same repair surface) at a time. First, approximately one-quarter of the grooves was filled with epoxy grout (Figure E.17(b)). Next, an FRP strip was inserted into each of the two grooves (Figure E.17(c)). To ensure an adequate bond between the epoxy grout, concrete substrate, and FRP strip, the strips were inserted into the grooves using a sawing motion until they were centered at approximately the mid-depth of the grooves. The remainder of each groove was then filled with epoxy grout, and squeegees were used to level the epoxy grout to the surface of the test specimen (Figure E.17(d)). The process was then repeated for the remaining pairs of grooves. The end region of the specimen after the repair was completed is shown in Figure E.17(e).

**(a) Cutting NSM Groove**

**(b) Filling Groove with Epoxy Grout**

**(c) Inserting NSM Strip**

**(d) Leveling Off Excess Epoxy Grout**

**(e) Completed NSM Repair System**

**Figure E.17** Installation of NSM FRP strips.

*E.2.5 Supplemental Diaphragm Repair Specimen*

The repair of the specimen with the supplemental diaphragm described in Section 4.3.4 involved minimal surface preparation and concrete chipping, unlike the specimens repaired with the FRP systems. Because the specimen was a fascia girder, one side of the member had been painted. The paint was removed within the end region of the member using a putty scraper. Furthermore, a patch material that had previously been applied to the bottom flange of the member in the field as a measure to mitigate deterioration was also removed. As indicated in Figure E.18, it was also necessary to remove a large portion of the bottom flange prior to the repair. The portion was only bonded to a single stirrup and had separated from the surrounding concrete. The condition of the girder following the removal of this portion of concrete is shown in Figure E.19.

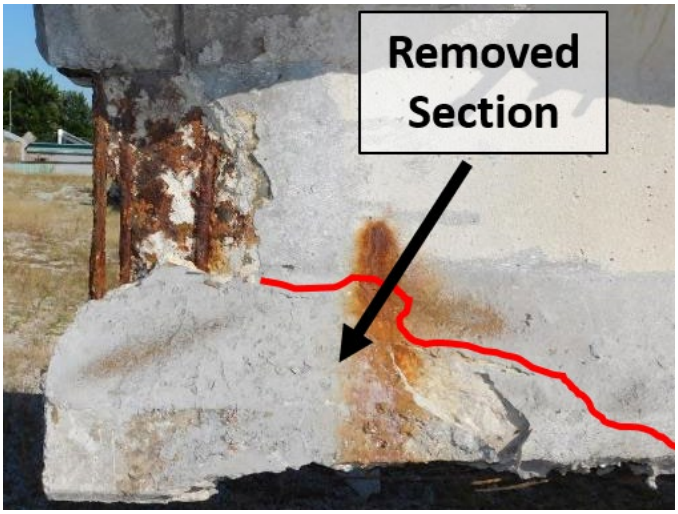


**Figure E.18** Flange portion removed from supplemental diaphragm specimen.

**(a) Elevation – Side 1**

**(b) Elevation – Side 2**

**(c) End View**

**Figure E.19** Condition of specimen prior to supplemental diaphragm repair.

The procedure followed for the construction of the supplemental diaphragm is presented in Figure E.20. It should be noted that some of the photographs illustrate the procedure being conducted near the undamaged end of a girder. However, the procedure used at the damaged end of the test specimen was the same. Assembly of the reinforcing cage for the supplemental diaphragm (Figure 4.11) began with drilling holes for the epoxy-coated No. 3 dowel bars. One end of the bar was pre-bent prior to installation, while the other end was bent after the bar was inserted through the girder web. Using a hammer drill with a 0.5-in. diameter drill bit, holes were drilled through the entire thickness of the web, as shown in Figure E.20(a), at the locations indicated in Figure 4.11. While holding a finger over one end of the hole to plug it, epoxy (Unitex® Pro-Poxy™ 400) was injected into the hole (Figure E.20(b)). With the No. 3 reinforcing bar marked at the termination point of the field bend and one end of the hole still plugged, the unbent end of the bar was inserted into the hole (Figure E.20(c)). When the bar reached the plugged end of the hole, the hole was unplugged, and the bar was pushed through the hole until the mark on the bar was visible (Figure E.20(d)). To bend the bar, the bar was first rotated so that the hook extension at the pre-bent end of the bar was oriented horizontally and pointing toward the end of the girder (Figure E.20(e)). To perform the 90° field bend, a steel pipe was inserted over the unbent end of the bar and, with the end of the pipe touching the concrete

surface of the girder web, the pipe was forced toward the beam (Figure E.20(f)). Once the end of the bar was bent, the position of the bar was adjusted so that the hooked ends of the bar were centered on the beam (Figure E.20(g)). The bar was subsequently cleaned to remove excess epoxy. To eliminate air voids in the hole, more epoxy was injected into both sides of the hole (Figure E.20(h)). The hook extension of the 90° field bend was then cut to the appropriate length (Figure E.20(i)), resulting in the bar shown in Figure E.20(j). After all four No. 3 dowel bars were installed, the remaining epoxy-coated No. 4 reinforcing bars were tied to the No. 3 dowel bars to complete the reinforcing cage, as shown in Figure E.20(k and l). Formwork was then erected around the repair region. A closed-cell polystyrene board was used to form the bottom surface of the diaphragm as shown in Figure E.20(m). When casting such a supplemental diaphragm in the field, a polystyrene board can be placed on the abutment in a similar manner to form the bottom of the diaphragm. The polystyrene board was used in the lab to simulate such field conditions. The completed formwork is shown in Figure E.20(n). The SCC concrete mixture provided in Table 4.5 was poured directly into formwork from the concrete truck (Figure E.20(o)). The completed diaphragm is presented in Figure E.20(p).

**(a) Drilling Holes for No. 3 Bars**

**(b) Injecting Hole with Epoxy**

**(c) Inserting No. 3 Bar Through Web**

**(d) No. 3 Bar Inserted Until Mark is Visible**

**Figure E.20** Supplemental diaphragm repair procedure.

**(e) No. 3 Bar Oriented for Bending Operation**

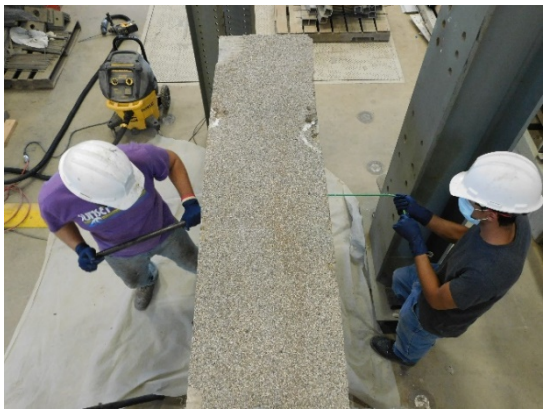

**(f) Bending No. 3 Bar**

**(g) Centering No. 3 Bar**

**(h) Injecting Additional Epoxy**

**(i) Cutting Hook Extension to Length**

**(j) Completed Installation of No. 3 Bar**

**Figure E.20** Supplemental diaphragm repair procedure (cont.).

**(k) Completed Reinforcing Cage**

**(l) Completed Reinforcing Cage**

**(m) Closed-Cell Polystyrene Board**

**(n) Erected Formwork**

**(o) Casting SCC**

**(p) Completed Supplemental Diaphragm Repair System**

**Figure E.20** Supplemental diaphragm repair procedure (cont.).

## E.3 Test Setup and Procedure

The test specimens were loaded to failure using the loading configuration presented in Figure E.21. A specimen in the test frame is shown in Figure E.22. An *a*/*d* ratio of 1.25 (corresponding to a shear span of 45 in. as shown in Figure E.21) was used for all five test specimens. The relatively short shear span was selected based on the observation that direct compressive stresses transferred from the load to the support would be critical for the end regions. Because the short shear span results in an *a*/*d* ratio less than 2.0, the entire test region is defined as a D-region. Thus, the behavior of the test region will be governed by deep beam behavior rather than sectional behavior. The far end of the girder opposite the test region was supported 60 in. from the end of the member to allow a test to performed on the opposite end of the specimen if needed. The original elastomeric bearing pads acquired from the bridge were used to support the specimens. The bearing pads were 14-in. by 7-in. by 2.5-in. For the specimen with the supplemental diaphragm, one of the bearing pads was cut in two, and the member was supported at the supplemental diaphragm as described in Section 4.3.4. A slight modification was made to the test setups for the control and damaged specimens. Although the end region of the control specimen was in relatively good condition, cracking was present in the bottom flange near the end of the member. Therefore, the bearing pad was shifted 3 in. further into the span relative to the original bearing location to avoid the cracks, as shown in Figure E.23. Moreover, as discussed in Section E.2.2 of Appendix E, the bearing pad for the damaged test specimen was shifted 4 in. further into the span to minimize required repairs. However, in both of these cases, the shear span of 45 in. remained consistent as did the stirrup spacing (6 in.) within the test region.

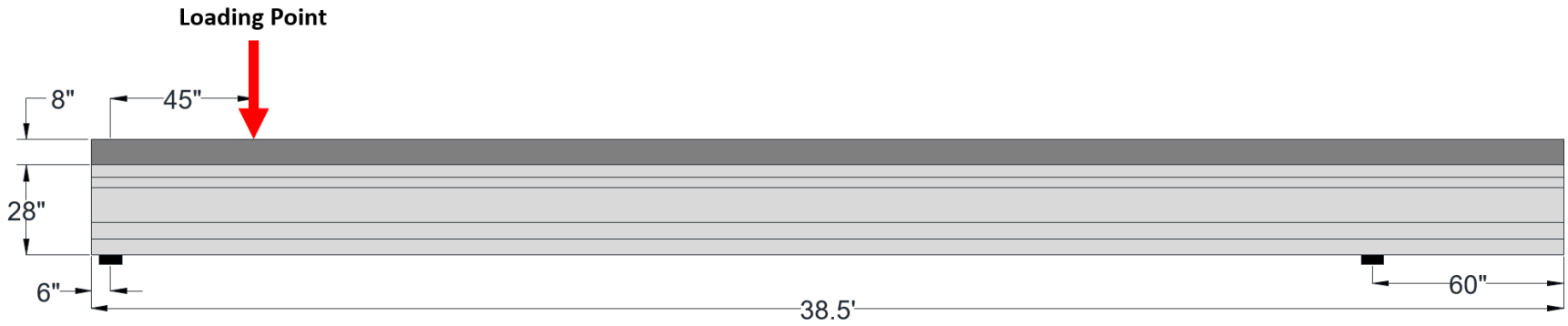


**Figure E.21** Load configuration.

**Figure E.22** Specimen in test frame.

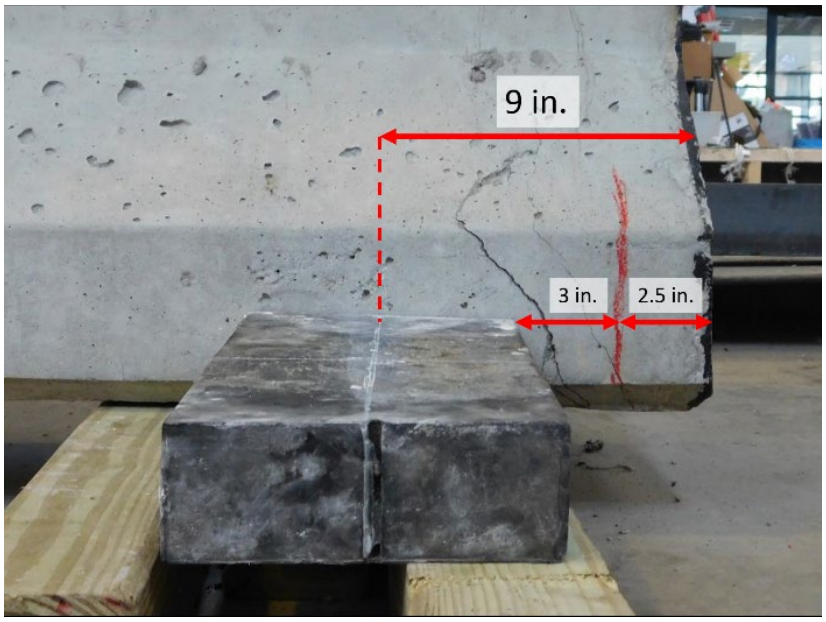


**Figure E.23** Location of the bearing pad for the control specimen.

Due to the sloped top surface of the deck, a gypsum concrete wedge was cast at the load point for each girder as shown in Figure E.24. Using closed-cell polystyrene board, temporary formwork was erected around the loading area. The bottom of the formwork was sealed, and liquid gypsum concrete was poured into the formwork. After self-leveling and curing, the formwork was removed. A 12-in. by 8-in. by 2-in. A36 steel plate was subsequently placed on top of the wedge and centered over the top flange of the test specimen.

**(a) Closed-Cell Polystyrene Formwork**

**(b) Pouring Gypsum Concrete**

**(c) Load Plate on Gypsum Concrete Wedge**

**Figure E.24** Preparing the load point.

A hydraulic ram with a capacity of 250 tons was used to apply load to the test specimens at the load point, and a load cell with a capacity of 300 kips was rigidly connected to the hydraulic cylinder to directly measure the load applied to the beam. This assembly is shown in Figure E.25. At both the load point and at midspan, linear string potentiometers were used to measure displacements throughout each test. At each location, a potentiometer was positioned to measure the displacement at each side of the beam, as shown in Figure E.26. Additionally, a linear potentiometer was placed on each side of both bearing pads to measure deflections at the supports. The average of the readings from the two linear potentiometers at each location was taken as the deflection at that point. Furthermore, an HD video camera was used during each load test to record video of the experiment.

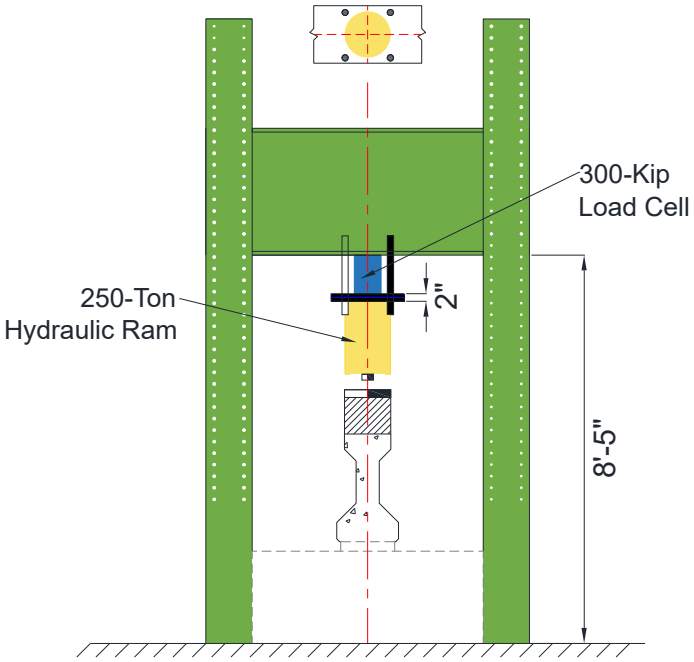


**Figure E.25** Test frame.

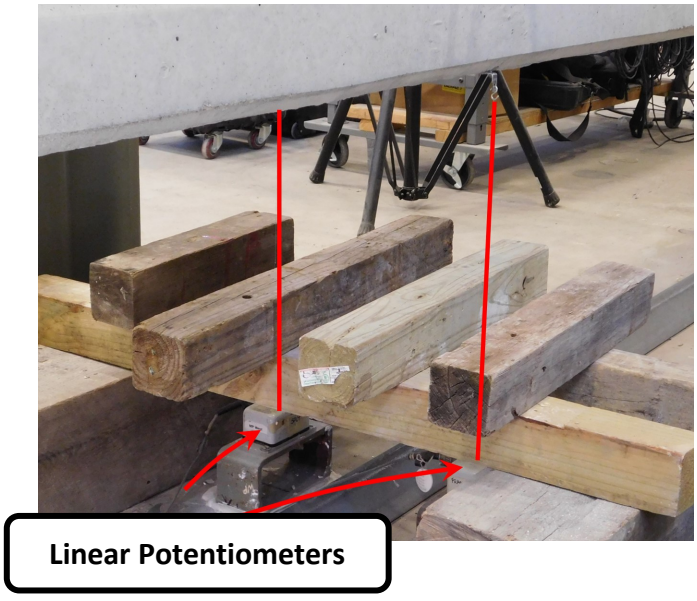


**Figure E.26** Linear potentiometers.

Each specimen was loaded monotonically until failure occurred. The load was increased at 10-kip increments, between which pictures were taken. Cracks were marked with a felt-tipped marker at every load step until failure was imminent, except for the externally bonded FRP specimen due to the presence of the FRP. Failure of the test specimens was defined by either a sudden loss in load-carrying capacity (damaged, externally bonded FRP, and NSM FRP specimens) or when the load-carrying capacity had decreased by 20 kips from its maximum value (control and supplemental diaphragm specimens).

## REFERENCES FOR APPENDIX E


ACI Committee 440. (2017). *ACI 440.2R-17: Guide for the design and construction of externally bonded FRP systems for strengthening concrete structures*. American Concrete Institute.

ASTM. (2017). *ASTM C496/C496M-17: Standard test method for splitting tensile strength of cylindrical concrete specimens*. ASTM International. https://doi.org/10.1520/C0496_C0496M-17

ASTM. (2020). *ASTM C39/C39M-20: Standard test method for compressive strength of cylindrical concrete specimens*. ASTM International. https://doi.org/10.1520/C0039_C0039M-20

ASTM. (2020). *C42/C42M-20: Standard test method for obtaining and testing drilled cores and sawed beams of concrete.* ASTM International. https://doi.org/10.1520/C0042_C0042M-20

ASTM. (2020). *ASTM C109/C109M-20B: Compressive strength of hydraulic cement mortars (using 2-in. or [50-mm] cube specimens).* ASTM International. https://doi.org/10.1520/C0109_C0109M-20B

ICRI. (2008). *ICRI Guideline No. 310.1R: Guide for surface preparation for the repair of deteriorated concrete resulting from reinforcing steel corrosion.* International Concrete Repair Institute.

ICRI. (2016). *ICRI Guide No. 330.2: Guide specifications for externally bonded FRP fabric systems for strengthening concrete structures.* International Concrete Repair Institute.

Rapid Set. (2018). *Mortar mix: high-strength structural repair mortar product datasheet*. Garden CTS Cement Manufacturing Corp.

Sika Corporation. (2018). *Product data sheet Sikadur® Hex-300: high-modulus, high-strength, impregnating resin* (Version 01.01). Sika Corporation.

Sika Corporation. (2018). *Product data sheet Sikadur®-330: high-modulus, high-strength, impregnating resin* (Version 03.01). Sika Corporation.

Unitex. (2018). *Technical data sheet Pro-Poxy® 400 epoxy gel anchor*. Dayton Superior.

# APPENDIX F. END REGION REPAIR EXPERIMENTAL PROGRAM EXTERNALLY BONDED FRP REPAIR SYSTEM DETAILS

The following figures provide detailed drawing of the externally bonded system (see Section 4.3.2) with complete dimensions. It should be noted, however, that the 6-in. fan anchors have been removed from the figures below for clarity.

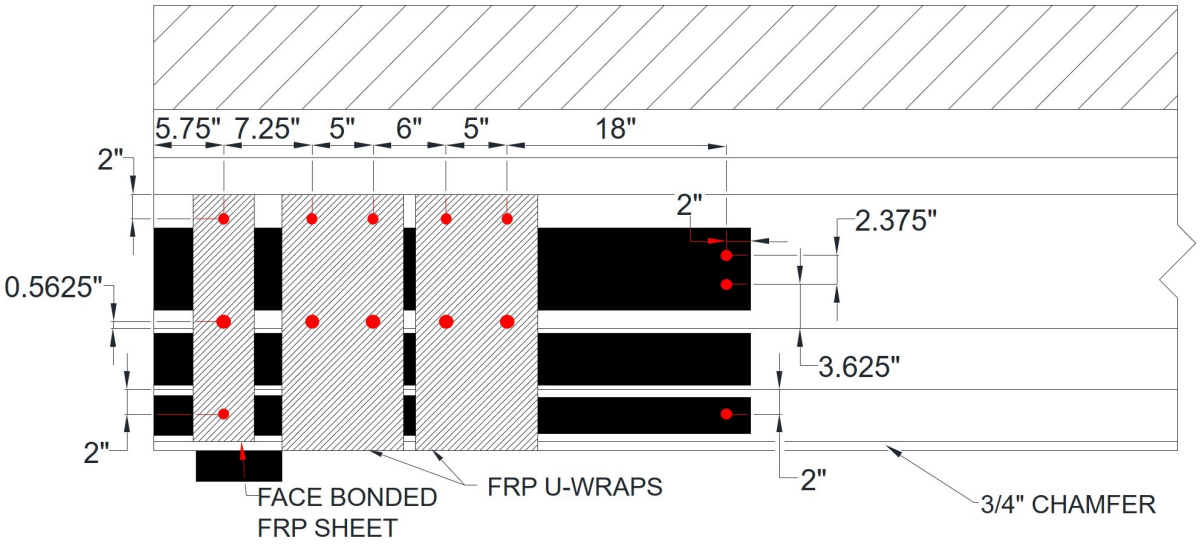


**Figure F.1** Externally bonded FRP repair system hole locations.

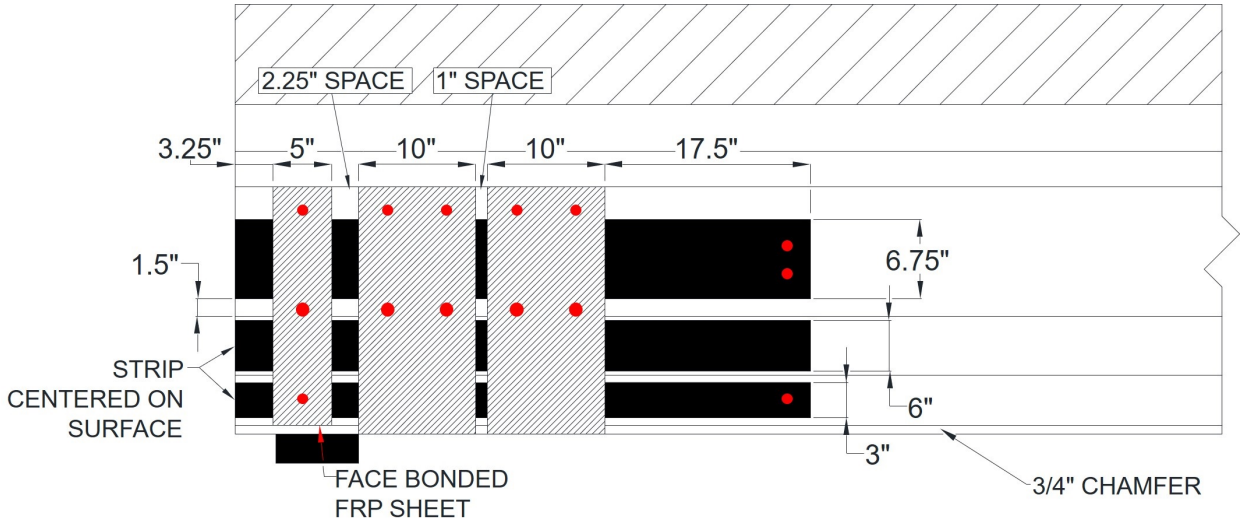


**Figure F.2** Externally bonded FRP repair system FRP dimensions.

# APPENDIX G. SPIKE ANCHOR DESIGN CALCULATIONS

The design procedure and calculations for the FRP spike anchors used in the end region repair experimental program are presented in this appendix. The variable names, procedures, and equations used below follow those developed by Pudleiner (2016).

## G.1 Variable Notation and Definitions

$A_{Eqv}$ = equivalent anchor laminate cross-sectional area, in.$^2$

$AMR_A$ = actual anchor material ratio provided (the ratio, by weight, of fiber material in the anchor to the FRP sheet or strip it is developing)

$AMR_D$ = design anchor material ratio (the ratio, by weight, of fiber material in the anchor to the FRP sheet or strip it is developing)

$d_e$ = embedment depth, in.

$d_h$ = diameter of the anchor hole, in.

$l_{af}$ = fan overlap length, in.

$n_a$ = number of rope segments per hole

$n_A$ = number of anchors per FRP sheet or strip

$n_l$ = number of laminate layers in the FRP sheet or strip

$R_c$ = anchor edge chamfer radius, in.

$t_f$ = specified thickness of the FRP laminate being developed, in.

$w_f$ = width of FRP strip, in.

$w_{f,A}$ = anchor tributary width, in.

$\gamma_{s,Exp}$ = expected fiber weight per surface area of the FRP sheet or strip being developed, oz/in.$^2$

$\gamma_{s,Sp}$ = manufacturer-specified dry fiber weight per surface area of the FRP sheet or strip being developed, oz/yd$^2$

$\lambda_A$ = manufacturer-specified dry fiber weight of the anchor per length, oz/in.

$\lambda_{A,A}$ = actual weight of the anchor fibers provided per anchor hole, oz/in.

$\lambda_{A\text{-}Req}$ = required weight of the anchor fibers per length, oz/in.

$\theta_{anchor}$ = anchor fan angle, degrees

## G.2 Anchorage Design Example

The following design example presents the procedure used to design the anchorage details for the anchors installed in the 0.875-in. diameter holes drilled through the entirety of the web (see Section 4.3.2). However, the same general procedure was used to design all the anchorage details used during the end region repair experimental program. These anchors were designed to provide anchorage for the 10-in. wide externally bonded U-wraps used in the end region repair experimental program.

The material properties of the SikaWrap® Hex-103 C FRP sheet and the SikaWrap® FX-50 C FRP rope needed to carry out the design calculations are:

- SikaWrap® Hex-103 C

  Thickness of the FRP laminate, $t_f$ = 0.04 in.

  Specified dry fiber weight of the FRP sheet or strip per surface area, $\gamma_{s,Sp}$ = 18.0 oz/yd$^2$ = 0.0139 oz/in.$^2$

- SikaWrap® FX-50 C

  Manufacturer-specified dry fiber weight of the FRP anchor per length, $\lambda_A$ = 0.045 oz/in.

To determine the expected dry fiber weight of the externally bonded U-Wraps, $\gamma_{s,Exp}$, Pudleiner (2016) suggests increasing the specified dry fiber weight, $\gamma_{s,Sp}$, by 25% to account for observed underestimates in the weight of the FRP. However, this underestimate in the weight was not observed with the SikaWrap Hex-103 C sheets used. Therefore, this factor was neglected, resulting in $\gamma_{s,Exp} = \gamma_{s,Sp}$ = 0.0139 oz/in$^2$.

As discussed in Section 4.3.2, the design of the externally bonded U-wraps consisted of a single layer ($n_l$ = 1) of FRP, with a sheet width, $w_f$, of 10 in. Based on the recommendations in Pudleiner (2016), it was determined that two anchors would be used to anchor each U-wrap ($n_A$ = 2). Therefore, the anchor tributary width, $w_{f,A}$, was calculated using Equation G.1.

$$w_{f,A} = \frac{w_f}{n_A} = \frac{10 \text{ in.}}{2} = 5 \text{ in.} \qquad \text{Equation G.1}$$

Next, Equation G.2 was used to calculate weight of the anchor fibers needed, $\lambda_{A\text{-}Req}$, to anchor the U-wrap. Per recommendations from Kim et al. (2012) and Pudleiner (2016), a design anchor material ratio, $AMR_D$, of 2.0 was assumed. The number of rope segments required per hole, $n_a$, was then calculated using Equation G.3. Here, a rope segment refers to a piece cut from the continuous FRP rope as received from the manufacturer (SikaWrap® FX-50 C).

$$\lambda_{A-req} = \gamma_{s,Exp}\left(w_{f,A} n_l AMR_D\right) = 0.0139 \text{ oz/in.}^2 * 5.0 \text{ in.} * 1 * 2.0 = 0.139 \text{ oz/in.} \qquad \text{Equation G.2}$$

$$n_a = \frac{\lambda_{A-req}}{\lambda_A} = \frac{0.139 \text{ oz/in.}}{0.045 \text{ oz/in.}} = 3.1 \text{ rope segments}$$ Equation G.3

Once the number of rope segments needed per hole was established, the actual weight of the anchor provided per hole, $\lambda_{A,A}$, was calculated using Equation G.4. Once the actual weight of the anchor fibers provided per hole was determined, the actually anchor material ratio, $AMR_A$, was calculated using Equation G.5, and the equivalent anchor laminate cross-sectional area, $A_{Eqv}$, was calculated using Equation G.6.

$$\lambda_{A,A} = \lambda_A n_a = 0.045 \text{ oz/in.} * 3.1 \text{ rope segments} = 0.139 \text{ oz/in.}$$ Equation G.4

$$AMR_A = \frac{\lambda_{A,A}}{n_l \gamma_{s,Exp} w_{f,A}} = \frac{0.139 \text{ oz/in.}}{1 * 0.0139 \text{ oz/in.}^2 * 5 \text{ in.}} = 2.0$$ Equation G.5

$$A_{Eqv} = t_f AMR_A w_{f,A} n_l = 0.04 \text{ in.} * 2.0 * 5.0 \text{ in.} * 1 = 0.40 \text{ in.}^2$$ Equation G.6

Finally, the diameter of the anchor hole, $d_{h,}$ was calculated using the equivalent laminate area and Equation G.7. Based on this value, an anchor hole diameter of 0.875 in. was selected.

$$d_h = \sqrt{\frac{4 * 1.4 * A_{eqv}}{\pi}} = \sqrt{\frac{4 * 1.4 * 0.40 \text{ in.}^2}{\pi}} = 0.844 \text{ in.}$$ Equation G.7

As discussed in Section 4.3.2, an anchor fan angle, $\theta_{anchor}$, of 60° was used based on recommendations found in Kim (2011) and Pudleiner (2016) as well as its successful application in the flexural strengthening experimental program. This fan angle, combined with the number of anchors per sheet and the width of sheet, necessitated that the fan overlap length, $l_{af}$, be 6 in. for the fan to extend 0.5 in. past the edge of the U-wrap as recommended. Additionally, this was the minimum fan overlap length suggested by Kim et al. (2012). As the anchor holes for the U-wraps were drilled through the entirety of the web, the anchors did not have an embedment depth, $d_e$. A 0.5-in. anchor edge chamfer radius, $R_c$, was used based on the recommendations from Quinn (2009), Kim et al. (2012), and Pudleiner (2016).

## REFERENCES FOR APPENDIX G


Kim, Y. G. (2011). *Shear behavior of reinforced concrete T-beams strengthened with carbon fiber reinforced polymer (CFRP) sheets and CFRP anchors* [Doctoral dissertation, The University of Texas at Austin].

Kim, Y., Quinn, K., Satrom, N., Garcia, J., Sun, W., Ghannoum, W. M., & Jirsa, J. O. (2012). *Shear strengthening of reinforced and prestressed concrete beams using carbon fiber reinforced polymer (CFRP) sheets and anchors* (Center for Transportation Research Report No. 0-6306-1). University of Texas at Austin. https://ctr.utexas.edu/wp-content/uploads/pubs/0_6306_1.pdf

Pudleiner, D. K. (2016). *Design consideration based on size effects of anchored carbon fiber reinforced polymer (CFRP) system* [Master's thesis, The University of Texas at Austin]. http://hdl.handle.net/2152/39031

Quinn, K. T. (2009). *Shear strengthening of reinforced concrete beams with carbon fiber reinforced polymer (CFRP) and improved anchor details* [Master's thesis, The University of Texas at Austin]. http://hdl.handle.net/2152/ETD-UT-2009-12-508

Sika Corporation. (2015). *Product data sheet SikaWrap® FX-50 C: carbon fiber rope for structural connection and anchoring of SikaWrap® strengthening systems* (Edition 5.16.2015). Sika Corporation.

Sika Corporation. (2019). *Product data sheet SikaWrap® Hex-103 C: carbon fiber fabric for structural strengthening* (Version 01.04). Sika Corporation.

## About the Joint Transportation Research Program (JTRP)

On March 11, 1937, the Indiana Legislature passed an act which authorized the Indiana State Highway Commission to cooperate with and assist Purdue University in developing the best methods of improving and maintaining the highways of the state and the respective counties thereof. That collaborative effort was called the Joint Highway Research Project (JHRP). In 1997 the collaborative venture was renamed as the Joint Transportation Research Program (JTRP) to reflect the state and national efforts to integrate the management and operation of various transportation modes.

The first studies of JHRP were concerned with Test Road No. 1—evaluation of the weathering characteristics of stabilized materials. After World War II, the JHRP program grew substantially and was regularly producing technical reports. Over 1,600 technical reports are now available, published as part of the JHRP and subsequently JTRP collaborative venture between Purdue University and what is now the Indiana Department of Transportation.

Free online access to all reports is provided through a unique collaboration between JTRP and Purdue Libraries. These are available at http://docs.lib.purdue.edu/jtrp.

Further information about JTRP and its current research program is available at http://www.purdue.edu/jtrp.

## About This Report

An open access version of this publication is available online. See the URL in the citation below.

Rich, W. B., Jacobs, R. R., Williams, C. S., & Frosch, R. J. (2021). *Repair and strengthening of bridges in Indiana using fiber reinforced polymer systems: Volume 2–FRP flexural strengthening and end region repair experimental programs* (Joint Transportation Research Program Publication No. FHWA/IN/JTRP-2021/10). West Lafayette, IN: Purdue University. https://doi.org/10.5703/1288284317310